

Copyright  
by  
Manuel Antonio Merello Ferrada  
2014

The Dissertation Committee for Manuel Antonio Merello Ferrada certifies that this is the approved version of the following dissertation:

**Study of Galactic clumps with millimeter / submillimeter  
continuum and molecular emission:  
Early stages of massive star formation**

Committee:

---

Neal J. Evans II, Supervisor

---

Daniel T. Jaffe

---

John H. Lacy

---

Milos Milosavljevic

---

Leonardo Bronfman

---

Yancy Shirley

**Study of Galactic clumps with millimeter / submillimeter  
continuum and molecular emission:  
Early stages of massive star formation**

**by**

**Manuel Antonio Merello Ferrada, Licenciado, Magister**

**DISSERTATION**

Presented to the Faculty of the Graduate School of  
The University of Texas at Austin  
in Partial Fulfillment  
of the Requirements  
for the Degree of

**DOCTOR OF PHILOSOPHY**

THE UNIVERSITY OF TEXAS AT AUSTIN

August 2014

Dedicated to my wife Victoria  
and my parents Guido and Verónica.



## Acknowledgments

This dissertation is the result of years of effort and there are many people that I would like to thank for their help during this difficult, although rewarding journey. First, I would like to thank my parents, Guido and Verónica, who taught me that I can accomplish any goal that I follow if I put my mind and my heart to it.

I would like to thank my wife, Victoria, for her immense love and endless patience. You give me every day a reason to smile and feel happy.

I would like to express my gratitude to my advisor, Prof. Neal Evans. It has been a great experience to work with you, and I truly appreciate your guidance and support during all these years.

To the Bolocam Galactic Plane Survey collaboration, Yancy, John, Adam, Cara, Erik, and all of them, for very helpful scientific discussions.

Also, I would like to acknowledge two of my collaborators at Universidad de Chile, Dr. Guido Garay and Dr. Leonardo Bronfman, and my thesis committee, Dr. Dan Jaffe, Dr. Milos Milosavljevic and Dr. John Lacy.

Special thanks to my fellow classmates, to the whole community in the Astronomy Department at University of Texas, and to my friends in Austin. I also thank the help provided during these years from Joel Green, Mike and Miranda Dunham, Rachel Walker and Terry Bruegging .

Finally, I would like to acknowledge support for my graduate studies from a Fulbright-CONICYT scholarship.

**Study of Galactic clumps with millimeter / submillimeter  
continuum and molecular emission:  
Early stages of massive star formation**

Manuel Antonio Merello Ferrada, Ph.D.  
The University of Texas at Austin, 2014

Supervisor: Neal J. Evans II

Massive stars play a key role in the evolution of the Galaxy; hence they are important objects of study in astrophysics. Although they are rare compared to low mass stars, they are the principal source of heavy elements and UV radiation, affecting the process of formation of stars and planets, and the physical, chemical, and morphological structure of galaxies. Star clusters form in dense “clumps” ( $\sim$ few parsecs in size) within giant molecular clouds, while individual stars form in cores (subparsec scale). An important step in the observational study of massive star formation is the identification and characterization of clumps. More detailed studies can then show how these clumps fragment into cores. Studies of clumps in our Galaxy will provide fundamental guidelines for the analysis of other galaxies, where individual clumps and cores cannot be resolved, and provide a catalog of interesting sources for observations of the Milky Way with a new generation of instruments, such as the Atacama Large Millimeter/Submillimeter Array.

Large-scale blind surveys of the Galactic plane at millimeter and submillimeter wavelengths have recently been completed, allowing us to identify star forming clumps and improve our understanding of the early stages of massive stars. One of these studies, the Bolocam Galactic Plane Survey (BGPS), mapped the continuum emission at 1.1 mm over a large region of the northern Galactic plane at a resolution of  $33''$ , identifying 8559 compact sources throughout the Galaxy.

In this dissertation, I present observations of a sample of sources from the BGPS catalog, obtained with the Submillimeter High Angular Resolution Camera II (SHARC-II). I present in this work 107 continuum emission maps at  $350 \mu\text{m}$  at high angular resolution ( $8.5''$ ) toward clump-like sources and construct a catalog of BGPS substructures. I estimate clump properties such as temperatures and multiplicity of substructures, and compare my results with  $350 \mu\text{m}$  continuum maps from the Hi-GAL survey.

I also present a detailed analysis, using molecular line and dust continuum observations, of the region G331.5-0.1, one of the most luminous regions of massive star formation in the Milky Way, located at the tangent region of the Norma spiral arm. Molecular line and millimeter continuum emission maps reveal the presence of six compact and luminous molecular clumps, with physical properties consistent with values found toward other massive star forming sources. This work includes the discovery of one of the most energetic and luminous molecular outflows known in the Galaxy, G331.512-0.103. For this high-speed outflow, I present ALMA observations that reveal a very compact, extremely young bipolar outflow and a more symmetric outflowing shocked shell surrounding a very small region of ionized gas. The source

is one of the youngest examples of massive molecular outflows associated with the formation of a high-mass star.

# Table of Contents

<b>Acknowledgments</b>	<b>v</b>
<b>Abstract</b>	<b>vii</b>
<b>List of Tables</b>	<b>xiii</b>
<b>List of Figures</b>	<b>xiv</b>
<b>Chapter 1. Introduction</b>	<b>1</b>
1.1 Large scale surveys of star forming gas . . . . .	2
1.2 Structures in molecular clouds . . . . .	4
1.3 Temperature characterization . . . . .	5
1.4 Massive star formation . . . . .	7
1.5 Extreme star formation . . . . .	8
1.6 Signatures in the formation of massive stars . . . . .	10
<b>Chapter 2. Temperatures and substructure of Galactic clumps based on 350<math>\mu</math>m observations.</b>	<b>13</b>
2.1 Introduction . . . . .	13
2.2 Observations . . . . .	18
2.2.1 Target selection . . . . .	18
2.2.2 Instrument and Observational Method . . . . .	19
2.3 Data reduction and calibration . . . . .	20
2.3.1 Data reduction . . . . .	20
2.3.2 Calibration . . . . .	21
2.4 Results . . . . .	24
2.4.1 Map description . . . . .	24
2.4.2 Source Extraction . . . . .	25
2.4.3 Source recovery experiments . . . . .	27

2.4.4	Catalog of sources in the 350 $\mu\text{m}$ maps . . . . .	30
2.4.5	Correlation with BGPS sources . . . . .	31
2.4.6	Flux densities of BGPS sources at 350 $\mu\text{m}$ . . . . .	35
2.4.7	Comparison between SHARC-II and <i>Herschel</i> images . . . . .	36
2.5	Analysis . . . . .	38
2.5.1	Temperature determination . . . . .	38
2.5.2	Comparison of temperatures with other surveys . . . . .	41
2.5.3	Comparison between gas temperature from $\text{NH}_3$ and color temperature . . . . .	43
2.5.4	Comparison with tracers of dense gas . . . . .	44
2.5.5	Mass and surface density of substructures . . . . .	46
2.6	Summary and Conclusions . . . . .	50

**Chapter 3. Physical characteristics of G331.5-0.1:  
The luminous central region of a Giant Molecular Cloud 87**

3.1	Introduction . . . . .	87
3.2	Observations . . . . .	90
3.2.1	NANTEN Telescope . . . . .	91
3.2.2	Swedish-ESO Submillimetre Telescope (SEST) . . . . .	92
3.2.2.1	Millimeter continuum . . . . .	92
3.2.2.2	Molecular lines . . . . .	92
3.2.3	Atacama Submillimeter Telescope Experiment . . . . .	93
3.2.4	Atacama Pathfinder Experiment . . . . .	94
3.2.4.1	Millimeter continuum: the ATLASGAL survey . . . . .	94
3.2.4.2	Molecular lines . . . . .	94
3.2.5	Australia Telescope Compact Array . . . . .	95
3.3	Results . . . . .	96
3.3.1	The G331.5-0.1 Giant Molecular Cloud . . . . .	96
3.3.2	The G331.5-0.1 GMC central region . . . . .	99
3.3.2.1	Dust emission: Millimeter continuum observations . . . . .	99
3.3.2.2	Molecular line emission . . . . .	100
3.3.2.3	Mid-infrared and far-infrared emission . . . . .	103

3.3.3	High angular resolution observations of the G331.5–0.1 GMC central region. . . . .	104
3.3.3.1	Radio continuum emission . . . . .	104
3.3.3.2	Maser emission . . . . .	106
3.4	Discussion . . . . .	107
3.4.1	Physical properties of the GMC . . . . .	107
3.4.2	Physical properties of the G331.5–0.1 central region. . . . .	109
3.4.2.1	Spectral energy distributions . . . . .	109
3.4.2.2	Masses and densities . . . . .	111
3.4.2.3	Virial and LTE masses . . . . .	113
3.4.2.4	Rotational temperatures of the G331.512-0.103 outflow . . . . .	115
3.4.2.5	Comparison with other massive star-forming regions . . . . .	117
3.5	Summary . . . . .	118
 <b>Chapter 4. ALMA observations of the massive molecular outflow G331.512–0.103</b>		<b>147</b>
4.1	Introduction . . . . .	147
4.2	Observations and results . . . . .	148
4.3	Discussion . . . . .	152
4.4	Summary and conclusions . . . . .	156
 <b>Chapter 5. Summary and Future Work</b>		<b>163</b>
5.1	Summary . . . . .	163
5.2	Future work . . . . .	166
 <b>Appendices</b>		<b>170</b>
 <b>Appendix A. Calibrators of 350 <math>\mu\text{m}</math> continuum maps of BGPS sources</b>		<b>171</b>
 <b>Appendix B. Complete sample of 350 <math>\mu\text{m}</math> continuum maps</b>		<b>174</b>
 <b>Appendix C. Hi-Gal SPIRE images at 350 <math>\mu\text{m}</math> for <math>l = 30^\circ</math></b>		<b>212</b>
 <b>Vita</b>		<b>229</b>



## List of Tables

2.1	Average calibration factors of SHARC-II maps . . . . .	53
2.2	Observing information of 350 $\mu\text{m}$ continuum maps . . . . .	54
2.2	Observing information of 350 $\mu\text{m}$ continuum maps . . . . .	55
2.2	Observing information of 350 $\mu\text{m}$ continuum maps . . . . .	56
2.3	Properties of sources recovered in the 350 $\mu\text{m}$ maps . . . . .	57
2.4	Sources from BGPS catalog with large number of high-resolution associated substructures. . . . .	58
2.5	Fluxes and estimated temperatures of BGPS sources . . . . .	59
2.5	Fluxes and estimated temperatures of BGPS sources . . . . .	60
2.5	Fluxes and estimated temperatures of BGPS sources . . . . .	61
3.1	Parameters of the molecular line observations of the G331.5 region . .	120
3.2	Parameters of continuum observations of the G331.5 region . . . . .	120
3.3	Observed parameters of dust continuum emission . . . . .	120
3.4	Molecular Lines: Observed Parameters . . . . .	121
3.5	Sizes (FWHM) obtained with CS(7 $\rightarrow$ 6) line . . . . .	122
3.6	Fluxes from continuum observations . . . . .	123
3.7	Observed parameters of radio sources detected towards G331.5–0.1 .	124
3.8	Spectral Energy Distributions . . . . .	125
3.9	Bolometric luminosities of complex and individual clumps . . . . .	125
3.10	Masses and densities derived for the clumps . . . . .	125
3.11	Outflow parameters obtained from rotational diagrams . . . . .	126
4.1	Parameters of the molecular line observations of molecular outflow G331.512–0.103 . . . . .	158
A.1	Calibrators of SHARC-II maps . . . . .	172
A.1	Calibrators of SHARC-II maps . . . . .	173

## List of Figures

2.1	Distribution of $40''$ aperture flux density of the complete sample of 8594 sources from the BGPS V2.1 catalog (blue line), along with those 619 sources contained in the SHARC-II maps (shaded black line). The distribution of the 104 sources considered as representative targets is also shown (red line). . . . .	62
2.2	Error map obtained from CRUSH reduction for L133.71+1.21. The image unit is $\text{Jy beam}^{-1}$ . The measured average noise for the L133.71+1.21 map is $0.338 \text{ Jy beam}^{-1}$ . . . . .	63
2.3	Map at $350 \mu\text{m}$ obtained with SHARC-II toward the region L133.71+1.21. Beam size of image is shown in the bottom left corner. Contour levels represent $3\sigma$ , $6\sigma$ , $10\sigma$ , $15\sigma$ , $30\sigma$ , $50\sigma$ and $100\sigma$ , with a rms noise $\sigma = 338 \text{ mJy beam}^{-1}$ . . . . .	64
2.4	Example of the extraction of sources with <i>Bolocam</i> . Left: Map of L030.70-0.07 with SHARC-II at $350 \mu\text{m}$ (FWHM beam of $8.5''$ ). Right: The same region mapped with Bolocam at $1.1 \text{ mm}$ (FWHM beam of $33''$ ). Some structures of Bolocam have several substructures mapped at the better resolution of SHARC-II. Also, the figure shows BGPS sources with no counterpart in the $350 \mu\text{m}$ map. . . . .	65
2.5	Completeness fraction derived from fake source tests. The tests were performed in nine SHARC-II maps with different noise levels. The plot shows the results of those detections, scaled to the mean noise of the catalog maps ( $0.48 \text{ Jy beam}^{-1}$ ). The fraction of sources recovered is plotted as a function of input source intensity. The vertical dotted lines indicate $\{1, 2, 3, 4, 5, 6\}\sigma$ . The dashed line with diamonds corresponds to fake sources across the whole map, while the continuous line with squares corresponds to sources at a distance $<3.5'$ from the center of the map. The completeness tests indicates that the catalog is complete at the $>99\%$ limit for sources with flux densities $> 6\sigma$ . . .	66
2.6	Recovery of source flux density for simulated resolved sources (FHWM $= 2.7\theta_{beam} = 23''$ ) in SHARC-II maps. The left panel shows the flux recovery in instrument units ( $\mu\text{V}$ ). Right panel shows the results of the calibrated flux recovery in units of Jy. Small differences are found between the $40''$ aperture and the integrated flux, with an under estimation of the integrated flux of $\sim 10\%$ . . . . .	67

2.7	Recovery of source size for simulated observations in SHARC-II maps. The vertical line at $48''$ indicates the largest size recovered for an object in our sample by <i>Boloccat</i> . The largest major-axis recovered is $65''$ , and therefore the plot suggests that source sizes are typically well recovered.	68
2.8	Fraction of blended objects as a function of source pair separation (solid line). The vertical red line shows the FWHM beam size of the $350\ \mu\text{m}$ maps. Smaller sources ( $15''\text{--}24''$ in size) are represented by the dotted line, and large sources ( $24''\text{--}34''$ in size) are represented by segmented line.	69
2.9	Flux distribution for objects identified in the 107 SHARC-II maps. Three methods of flux recovery are represented in the image: aperture photometry at $20''$ (red long dash) and $40''$ (blue short dash) toward the peak, and integrated emission of the source (solid black line).	70
2.10	Distribution of the deconvolved radii and aspect ratio of sources in the SHARC-II maps. The average and median values of the radii distribution are $15''$ and $14''$ , respectively. The average and median values of the aspect ratios are 1.53 and 1.45.	71
2.11	Upper left: Results of <i>Boloccat</i> on the $350\ \mu\text{m}$ map of L133.71+1.21, corresponding to the W3 main region. The different colors indicate the peak signal-to-noise of each source (above $10\sigma$ in red, below that limit in blue). Sources in red are associated with compact and dense core-type structures, the blue sources are related to low emission, field material or possible filamentary structure. Upper right: Grey color scale of the 1.1 mm toward the same region. Black regions show the result of <i>Boloccat</i> on the 1.1 mm map, and red regions the results of <i>Boloccat</i> on the $350\ \mu\text{m}$ map. The central V2.1 source mask shows large number of substructures (both strong and faint). Lower panels are similar to the upper panels for L081.48+0.00, in the Cygnus X region. The comparison of source masks reveal a large population of BGPS V2.1 sources located inside the $350\ \mu\text{m}$ maps, but not associated with any source at high-resolution.	72
2.12	Distribution of $350\ \mu\text{m}$ sources per 1.1 mm source from BGPS. The top panel shows the cumulative number. Half of the 1.1 mm parental clumps are associated with one-or-two substructures identified at high-resolution.	73
2.13	Comparison between integrated flux in $40''$ apertures obtained at $350\ \mu\text{m}$ on SHARC-II and <i>Herschel</i> images toward $l = 30^\circ$ . The points represent the 213 high-resolution sources recovered by <i>Boloccat</i> in SHARC-II maps, and the colors show different limits of peak signal-to-noise on those sources.	74

2.14	<p>Example of the 350 <math>\mu\text{m}</math> continuum emission from SHARC-II (upper left) and <i>Herschel</i>/SPIRE (upper right) toward the region <math>l = 28.95^\circ</math>, <math>b = -0.05^\circ</math>. Beam sizes are shown in the bottom left corner of each map. The contours of the SHARC-II image correspond to <math>3\sigma</math>, <math>6\sigma</math>, <math>10\sigma</math>, <math>15\sigma</math>, <math>30\sigma</math>, <math>50\sigma</math> and <math>100\sigma</math>, with an rms noise <math>\sigma = 514 \text{ mJy beam}^{-1}</math>. Contours of the <i>Herschel</i> image start from <math>10\sigma</math>, with increasing steps of <math>5\sigma</math> (<math>\sigma = 164 \text{ MJy ster}^{-1}</math>). The smaller beam size of SHARC-II images allow us to recover structures not identified by <i>Herschel</i> with lower resolution. Bottom: Convolved SHARC-II image with gaussian kernel of <math>\sigma = 9.9''</math> (6.14 pixels), to match the <math>24.9''</math> FWHM beam size of <i>Herschel</i> image. Contours represent 1, 3, 6, 10, 15, 30 and 50 times the rms noise of the image. The <math>1\sigma</math> contour level resembles the emission observed at the <math>15\sigma</math> white contour level of the <i>Herschel</i> image. The <math>15\sigma</math> level in the <i>Herschel</i> map sets then a limit of the diffuse emission filtered out in the SHARC-II maps. . . . .</p>	75
2.15	<p>Comparison between integrated flux in <math>40''</math> apertures for 350 <math>\mu\text{m}</math> images from SHARC-II and <i>Herschel</i> image on a sample of 102 BGPS sources located toward <math>l = 30^\circ</math>. Both SHARC-II and <i>Herschel</i> were convolved to match the resolution of the Bolocam maps (<math>33''</math>). Unfilled circles represent BGPS sources with no associated source detected at 350 <math>\mu\text{m}</math>, and filled circles show the 1.1 mm parental clumps with only faint objects (black) and with compact substructures (red). The error bars in the flux ratio considered 20% uncertainties in <math>F_{\text{Herschel}}</math>, and 30% in <math>F_{\text{SHARC}}</math>. . . . .</p>	76
2.16	<p>Distribution of the flux ratio between the emission at 0.35 mm and 1.1 mm for our sample of 574 BGPS V2.1 sources with reliable flux values. Nearly 94% of the sources have a flux ratio lower than 70.2 . . . . .</p>	77
2.17	<p>Models of dust temperature as a function of the flux ratio between continuum emission at 350 <math>\mu\text{m}</math> and 1.1 mm, in the optically thin limit. The three models correspond to different opacity laws, <math>\beta = 1.0</math>, <math>\beta = 1.7</math> and <math>\beta = 2.0</math>. The error bars for the <math>\beta = 1.7</math> model show the expected uncertainty in temperature determination when the flux ratio has an error of 10%. . . . .</p>	78
2.18	<p>Distribution of temperatures of the BGPS sources with good fit in the determination of temperature, using the three different opacity models: spectral index <math>\beta=1.0</math> (blue line), <math>\beta=2.0</math> (green dashed line), and <math>\beta=1.7</math> (shaded black line). The vertical red dashed line at <math>T=13.3 \text{ K}</math>, represents the median value for the distribution with <math>\beta=1.7</math>. . . . .</p>	79
2.19	<p>Temperature determined for the BGPS sample of sources as a function of their <math>40''</math> aperture flux, for a spectral index <math>\beta = 1.7</math>. Only sources with good fits in the determination of temperature (<math>T \leq 50 \text{ K}</math>) are shown in this figure. . . . .</p>	80

2.20	Comparison between estimated temperatures with 350 $\mu\text{m}$ and 1.1 mm continuum maps, $T_{SHARC}$ , and temperatures obtained from SED fitting by Battersby et al. (2011), $T_{Herschel}$ , as a function of 40'' aperture flux density at 1.1 mm for a sample of 91 BGPS sources toward $l = 30^\circ$ . The colors shown in the legend represent different ranges for $T_{SHARC}$ . The weighted mean value of the ratio is $0.50 \pm 0.01$ for sources with $T_{SHARC} \leq 50$ K. . . . .	81
2.21	Distribution of the ratio of gas temperature determined from $\text{NH}_3$ observations $T_{gas}$ , and fitted dust temperatures $T_{dust}$ , for the sample of 49 BGPS sources with $T_{gas} < 30$ K and $T_{dust} < 50$ K, ranges in which both values are relatively well determined. The average and median values of this distribution are 0.88 and 0.76, respectively. . . . .	82
2.22	Peak main-beam temperature, as a function of dust temperature, for the sample of BGPS sources from the spectroscopy catalog by Shirley et al. (2013) that are contained in the SHARC-II maps. The number of sources with $\text{HCO}^+$ emission is 250, and the number of sources with $\text{N}_2\text{H}^+$ emission is 199. . . . .	83
2.23	Ratio between the mass estimated using color temperatures determined from 350 $\mu\text{m}$ and 1.1 mm images ( $T_{clump}$ ), and the mass estimated using a single fiducial temperature ( $T_{fix}$ ). For the sample of 514 V2.1 BGPS sources with good fits in the determination of temperature, using $T_{fix} = 20$ K, the average value of the source masses will be underestimated by a factor of $\sim 2.4$ . . . . .	84
2.24	Comparison between the total estimated mass from 350 $\mu\text{m}$ substructures on each clump, and the mass estimated at 1.1 mm for that parental BGPS clump, as a function of dust temperature (left) and the integrated flux of the BGPS sources (right). Black points consider for $M_{substructures}$ the flux contribution from all high-resolution sources in the parental clumps, and have a weighted averaged mass fraction $\Sigma(M_{substructures})/M_{clump}$ of $0.22 \pm 0.01$ . Red points only consider the flux contribution from strong, compact substructures, and the weighted averaged mass fraction of this distribution is $0.19 \pm 0.01$ . . . . .	85
2.25	Estimation of surface density between substructures and parental clumps. Solid line represent the locus of equality between the structures. Black crosses show the bulk of the sources, with temperatures between 10–50 K. Blue marks show sources with low temperature ( $T < 10$ K), likely to overestimating the surface density. Grey marks show sources with high temperature ( $T > 50$ K). Red points show only those compact, core-type substructures found in the parental clumps, with detections above $10\sigma$ . Most of these compact sources have higher surface 2–3 times larger than their parental clump. Several of these compact sources have surface densities above theoretical thresholds of $0.2 \text{ g cm}^{-2}$ (Butler & Tan, 2012) or $1.0 \text{ g cm}^{-2}$ (Krumholz & McKee, 2008) for massive star formation. . . . .	86

3.1	Maps of velocity integrated emission, in the range $-117.7$ to $-73.2$ km $s^{-1}$ , of the G331.5-0.1 GMC. <i>Top</i> : CO(1 $\rightarrow$ 0). Contour levels are drawn from 20% ( $3\sigma$ ) to 90%, in steps of 10%, of the peak intensity (297.6 K km $s^{-1}$ ). <i>Bottom</i> : C <sup>18</sup> O(1 $\rightarrow$ 0). Contour levels are drawn from 20% ( $4\sigma$ ) to 90%, in steps of 10%, of the peak intensity (19.6 K km $s^{-1}$ ). The 50% emission in each map is drawn with a thicker contour. A $7' \times 7'$ red dashed box, oriented in equatorial coordinates, is drawn toward the 70% emission contour in the C <sup>18</sup> O(1 $\rightarrow$ 0) map. This area is considered as the central region of this cloud. . . . .	127
3.2	Average profile of the CO emission over the whole GMC. . . . .	128
3.3	Position-velocity maps of the CO(1 $\rightarrow$ 0) ( <i>top</i> ) and C <sup>18</sup> O(1 $\rightarrow$ 0) emission ( <i>bottom</i> ) integrated between $-0.21$ and $-0.04$ in Galactic Latitude. Contour levels are drawn at 40% to 90%, in steps of 10%, of the peak intensity (11.5 K km $s^{-1}$ for CO and 0.78 K km $s^{-1}$ for C <sup>18</sup> O). The C <sup>18</sup> O shows a clear component between $l = 331.3^\circ$ and $l = 331.6^\circ$ at $\sim -90$ km $s^{-1}$ . . . . .	129
3.4	Map of dust continuum emission at 0.87 mm from ATLASGAL towards the Norma spiral arm tangent region. Overlaid in grey is the contour map of the C <sup>18</sup> O(1 $\rightarrow$ 0) emission integrated over the velocity range from $-117.7$ to $-73.2$ km $s^{-1}$ . Contour levels are from 20% to 90%, in intervals of 10%, of the peak intensity 19.6 K km $s^{-1}$ . The red dashed box, $7' \times 7'$ in size ( $15 \times 15$ pc <sup>2</sup> at a distance of 7.5 kpc) and oriented in equatorial coordinates, shows the defined central region of the G331.5-0.1 GMC. The yellow circles show the position of the RMS sources in this region: G331.0890+00.0163A, G331.0890+00.0163B, G331.0931-00.1303, G331.3865-00.3598, G331.4117+00.0154, G331.4181-00.3546, G331.4904-00.1173, G331.5414-00.0675, G331.5582-00.1206, G331.6035-00.1081, G331.6191-00.0442A, G331.6191-00.0442B, and G331.7953-00.0979. . . . .	130
3.5	Maps of 1.2 mm. (top) and 0.87 mm. (bottom) continuum emission observed with SIMBA and APEX. . . . .	131
3.6	Spectra observed at the peak position of the millimeter clumps MM1 through MM6. The transition is given in the upper right corner. These spectra indicate that the emission arises from two different components: a high velocity component at $v=-88.9$ km $s^{-1}$ , and a low velocity component at $v=-100.8$ km $s^{-1}$ , indicated with vertical dotted lines. Molecular sources associated with millimeter clumps MM2, MM3, MM4 and MM5 are part of a single structure at high velocity that we defined as the complex of clumps. . . . .	132
3.7	SiO and SO spectra observed toward the peak position of clump MM3, which is associated with the high-velocity molecular outflow G331.512-0.103. Transitions are given in the upper right corner. The vertical dotted line indicates the ambient gas velocity. . . . .	133

- 3.8 Contour maps of velocity-integrated emission, in the range from  $-93.9$  to  $-84.4$   $\text{km s}^{-1}$  from the central region of the G331.5-0.1 molecular cloud in four different transitions. For the CS(7  $\rightarrow$ 6) map, the contour levels are drawn at 5%, 10%, 15%, 20%, 25%, 30%, 50% and 70% of the peak flux density  $25.6$   $\text{K km s}^{-1}$ . For CS(2  $\rightarrow$ 1), CS(5  $\rightarrow$ 4) and  $^{13}\text{CO}$ (3  $\rightarrow$ 2) maps, the contours are drawn at 10% to 90%, with interval of 10%, of the peak intensity. For CS(2  $\rightarrow$ 1), CS(5  $\rightarrow$ 4) and  $^{13}\text{CO}$ (3  $\rightarrow$ 2), the peak intensities are 15.3, 5.3 and  $161.7$   $\text{K km s}^{-1}$ , respectively. The red points show the peak positions of the millimeter clumps MM1 through MM6, as is labeled in the CS(7  $\rightarrow$ 6) contour map. Molecular sources associated with millimeter clumps MM2, MM3, MM4 and MM5 are part of a single structure at high velocity that we defined as the complex of clumps. . . . . 134
- 3.9 Contour maps of velocity-integrated emission, in the range between  $-105.4$  and  $-95$   $\text{km s}^{-1}$ , from the central region of the G331.5-0.1 molecular cloud in four different transitions. For the CS(7  $\rightarrow$ 6) map, the contour levels are drawn at 10%, 20%, 30%, 40%, 50%, 70% and 90% of the peak flux density  $14.0$   $\text{K km s}^{-1}$ . For CS(2  $\rightarrow$ 1), CS(5  $\rightarrow$ 4) and  $^{13}\text{CO}$ (3  $\rightarrow$ 2) maps, the contours are drawn at 10% to 90%, with interval of 10%, of the peak intensity. For CS(2  $\rightarrow$ 1), the peak intensity is  $5.2$   $\text{K km s}^{-1}$ . For CS(5  $\rightarrow$ 4), the peak intensity is  $1.4$   $\text{K km s}^{-1}$ . For  $^{13}\text{CO}$ (3  $\rightarrow$ 2), the peak intensity is  $86.7$   $\text{K km s}^{-1}$ . The red points show the peak positions of the millimeter clumps MM1 through MM6, as is labeled in the CS(7  $\rightarrow$ 6) contour map. The emission observed in the CS(7  $\rightarrow$ 6) map at  $\alpha_{2000} = 16^h 12^m 10.13^s$  and  $\delta_{2000} = -51^\circ 28' 37.5''$  (toward the MM3 point) is related with the emission integration on the blue wing of the G331.512-0.103 outflow. . . . . 135
- 3.10 0.87 mm greyscale image of the central region of the G331.5-0.1 GMC, overlaid with CS velocity integrated contour map. The contour levels are drawn at 5%, 10%, 15%, 20%, 25%, 30%, 50% and 70% of the peak flux density  $25.6$   $\text{K km s}^{-1}$ . The red contours show the integrated emission in the high velocity component of the spectra, integrated between  $-93.9$  and  $-84.4$   $\text{km s}^{-1}$ . The blue contours show the low velocity component, integrated between  $-105.4$  and  $-95$   $\text{km s}^{-1}$ . Labels MM1 through MM6 show the associated millimeter clump for each CS source. Molecular sources associated with millimeter clumps MM2, MM3, MM4 and MM5 are part of a single structure at high velocity that we defined as the complex of clumps. . . . . 136



- 3.11 Contour map of the 0.87 mm continuum emission from the G331.5-0.1 region overlaid on a three color image of the mid infrared emission, made using the IRAC filters 1 (3.6  $\mu\text{m}$ , blue), 2 (4.5  $\mu\text{m}$ , green) and 4 (8  $\mu\text{m}$ , red). Contour levels are drawn at 10%, 20%, 30%, 40%, 50% and 90% of the peak flux density 13.8 Jy beam<sup>-1</sup>. Millimeter sources are labeled in the map with MM1, MM2, MM3, MM4, MM5 and MM6. Red crosses mark the positions of the four radio emission components in the central region of the G331.5-0.1 GMC (A, B, C and D). Component B and D are associated with methanol and OH masers. Component C is associated only with OH maser emission. White boxes mark the position of the three RMS sources in the region (G331.4904-00.1173, G331.5414-00.0675 and G331.5582-00.1206). The RMS box sizes are 18'' to account for the beam of MSX observation. 137
- 3.12 Contour maps of the radio emission from the G331.5-0.1 GMC central region at 3.6 cm (*top*) and 6 cm (*bottom*), overlaid on 0.87 mm continuum emission. The contours are drawn at 10%, 30%, 60% and 90% of the peak flux. For the 6 cm map, the peak intensity is 153.0 mJy beam<sup>-1</sup>, rms noise is 1.04 mJy beam<sup>-1</sup>. For the 3.6 cm map, the peak intensity is 159.5 mJy beam<sup>-1</sup>, rms noise is 1.09 mJy beam<sup>-1</sup>. The blue crosses in the 6 cm map show the position of methanol masers in the central region of the G331.5-0.1 GMC. All methanol masers here are associated with OH masers. The yellow cross shows the position of the OH maser, without methanol counterpart, toward the G331.512-0.103 outflow. . . . . 138
- 3.13 Spectral energy distributions at short frequency for each radio component found in the central region of the G331.5-0.1 GMC. For components B and C, the dotted line is a fit of the spectrum using modified blackbody function of the form  $B_\nu(T_e)[1 - \exp(-\tau_\nu)]$ , with  $\tau_\nu \propto T_e^{-1.35}\nu^{-2.1}EM$ . The emission measure  $EM$  is in units of [pc cm<sup>-6</sup>]. The  $T_e$  considered is 10000 K. The spectral index of components B and C are  $0.8 \pm 0.2$  and  $1.2 \pm 0.2$ , respectively. . . . . 139
- 3.14 Spectral energy distribution of the region harboring the G331.5-0.1 complex of clumps. From left to right, the circle marks the SIMBA flux, the triangle the LABOCA, the stars mark IRAS fluxes, filled-squares MSX fluxes, and open-squares SPITZER fluxes. The solid curve is a fit to the spectrum using three modified blackbody functions of the form  $B_\nu(T_e)[1 - \exp(-(\nu/\nu_0)^\beta)]$ , with different temperatures (cold, warm and hot components). The fitted parameters of the cold component (represented as the dotted line) are listed. . . . . 140



3.15	Spectral energy distributions of each millimeter clump in the G331.5–0.1 central region. The symbols are the same as in Fig. 3.14. The solid curve is a fit to the spectrum using two modified blackbody functions of the form $B_\nu(T_e)[1 - \exp(-(\nu/\nu_0)^\beta)]$ , with different temperatures (cold and warm components). In the case of MM1, only one modified black function was considered. The fitted parameters of the cold component (represented as the dotted line) are listed on the upper left.	141
3.16	$L_{bol} - M_{env}$ diagram for the six millimeter clumps (MM1-MM6) in the G331.5–0.1 GMC central region (filled black circles), together with sources from Molinari et al. (2008). From Molinari et al. sample, MM sources are represented as open circles (small representing MM-S sources), IR-P sources are shown in grey filled triangles and IR-S are indicated in crosses.	142
3.17	Observed spectra of the CS(2 →1) line emissions toward the core G331.5–0.1.	143
3.18	Observed spectra of the CS(5 →4) line emissions toward the core G331.5–0.1.	144
3.19	Observed spectra of the CS(7 →6) line emissions toward the core G331.5–0.1.	145
3.20	Observed spectra of the $^{13}\text{CO}(3 \rightarrow 2)$ line emissions toward the core G331.5–0.1.	146
4.1	Integrated spectra observed with ALMA of the G331.512–0.103 molecular outflow. A dashed line is drawn in each spectrum representing the baseline. The dotted vertical line shows the systemic velocity of this source ( $-88.9 \text{ km s}^{-1}$ ).	159
4.2	Channel maps of the SiO(8-7) line emission. The contours are at 3, 6, 12, 18, 24 and 30 times the rms defined for the SiO emission ( $0.14 \text{ Jy beam}^{-1}$ ). The velocity of each channel is indicated in the upper right corner of each box. The channels are separated by $10 \text{ km s}^{-1}$ . In the central channel map, toward the systemic velocity of the source ( $-88.9 \text{ km s}^{-1}$ ), the emission shows a clear ring-type or projected shell structure, with the inner hole well determined at the $18 \sigma$ contour. The ALMA synthesized beam is shown at the bottom left corner in each box. The gray and white crosses define the positions considered in the blue and red lobes to set the symmetry axis of the outflow, represented by the gray dotted line.	160

4.3	<p><i>Top</i> : H<sup>13</sup>CO<sup>+</sup> (4-3) emission (in colors) of the G331.512–0.103 source at a velocity of –91.9 km s<sup>–1</sup>, where the peak of flux density is found. The overlaid contours in black correspond to the SiO(8-7) emission at the same velocity, at 3, 6, 12, 18, 24 and 30 <math>\sigma</math> (with <math>\sigma=0.14</math> Jy beam<sup>–1</sup>). The dashed contour represent the 12 <math>\sigma</math> emission toward the cavity observed in SiO, which is coincident spatially with the ones observed with H<sup>13</sup>CO<sup>+</sup>. The red contour shows the 50% of emission (peak of 158 mJy beam<sup>–1</sup>) of the radio source detected at 8.6 GHz toward this source, presented by Merello et al. (2013). The peak position of the radio continuum observations is inside the cavity described by the SiO and H<sup>13</sup>CO<sup>+</sup> emissions. <i>Bottom</i> : H<sup>13</sup>CO<sup>+</sup> (4-3) emission (in colors), with overlaid black contours of the 0.86 mm continuum emission obtained with ALMA. The contours are at 3, 6, 12, 18, 24, 30 <math>\sigma</math> (with <math>\sigma=0.02</math> Jy beam<sup>–1</sup>). The continuum emission peaks, within errors, in the center of the cavity shown in the H<sup>13</sup>CO<sup>+</sup> emission. . . . .</p>	161
4.4	<p>Position-velocity diagrams of the SiO(8-7) (<i>top</i>) and H<sup>13</sup>CO<sup>+</sup>(4-3) (<i>bottom</i>) emission of the G331.512–0.103 source. The slices are centered at the cavity observed in the SiO map (<math>\alpha_{2000} = 16^h12^m09.985^s</math>, <math>\delta_{2000} = -51^\circ28'37.42''</math>). Slices along the axis of symmetry of the outflow (primary axis), and perpendicular to this (secondary axis), are displayed in gray scale, with 3, 6, 12, 18, 24 and 30 <math>\sigma</math> contours, with a slit of 4.5'' for the SiO emission, and 6'' for H<sup>13</sup>CO<sup>+</sup>. <i>Upper left</i> : Slice of the SiO emission, running along the axis of symmetry (position angle of 102.5°). <i>Upper right</i> : Slice of the SiO emission, running perpendicular to the axis of symmetry (position angle of 12.5°). An additional 16 <math>\sigma</math> contour in red is shown, extending between -111.9 and -63.8 km s<sup>–1</sup>. <i>Bottom left</i> : Slice of the H<sup>13</sup>CO<sup>+</sup> emission, running along the axis of symmetry. <i>Bottom right</i> : Slice of the H<sup>13</sup>CO<sup>+</sup> emission, running perpendicular to the axis of symmetry. . . . .</p>	162
5.1	<p>Spectral windows 0 and 1 observed with ALMA band 7 toward the molecular outflow G331.512-0.103. The numbers indicate the identified line transition. . . . .</p>	168
5.2	<p>Spectral windows 2 and 3 observed with ALMA band 7 toward the molecular outflow G331.512-0.103. The numbers indicate the identified line transition . . . . .</p>	169
B.1	<p>Continuum maps at 350 <math>\mu</math>m of the 107 regions included in our catalog.. Left: Contours are drawn at 3<math>\sigma</math>, 6<math>\sigma</math>, 10<math>\sigma</math>, 15<math>\sigma</math>, 30<math>\sigma</math>, 50<math>\sigma</math>, and 100<math>\sigma</math>. Noise level <math>\sigma_{rms}</math> is indicated in the figure for each map. Right: Recovery of substructures with <i>Bolocat</i> algorithm. Red and blue regions represent the position of dense, compact cores-type sources and faint substructures, respectively. Figures 27.127.107 are available in the online version of the Journal. . . . .</p>	175

B.1 Continuum maps at 350 $\mu\text{m}$ (Continuation) . . . . .	176
B.1 Continuum maps at 350 $\mu\text{m}$ (Continuation) . . . . .	177
B.1 Continuum maps at 350 $\mu\text{m}$ (Continuation) . . . . .	178
B.1 Continuum maps at 350 $\mu\text{m}$ (Continuation) . . . . .	179
B.1 Continuum maps at 350 $\mu\text{m}$ (Continuation) . . . . .	180
B.1 Continuum maps at 350 $\mu\text{m}$ (Continuation) . . . . .	181
B.1 Continuum maps at 350 $\mu\text{m}$ (Continuation) . . . . .	182
B.1 Continuum maps at 350 $\mu\text{m}$ (Continuation) . . . . .	183
B.1 Continuum maps at 350 $\mu\text{m}$ (Continuation) . . . . .	184
B.1 Continuum maps at 350 $\mu\text{m}$ (Continuation) . . . . .	185
B.1 Continuum maps at 350 $\mu\text{m}$ (Continuation) . . . . .	186
B.1 Continuum maps at 350 $\mu\text{m}$ (Continuation) . . . . .	187
B.1 Continuum maps at 350 $\mu\text{m}$ (Continuation) . . . . .	188
B.1 Continuum maps at 350 $\mu\text{m}$ (Continuation) . . . . .	189
B.1 Continuum maps at 350 $\mu\text{m}$ (Continuation) . . . . .	190
B.1 Continuum maps at 350 $\mu\text{m}$ (Continuation) . . . . .	191
B.1 Continuum maps at 350 $\mu\text{m}$ (Continuation) . . . . .	192
B.1 Continuum maps at 350 $\mu\text{m}$ (Continuation) . . . . .	193
B.1 Continuum maps at 350 $\mu\text{m}$ (Continuation) . . . . .	194
B.1 Continuum maps at 350 $\mu\text{m}$ (Continuation) . . . . .	195
B.1 Continuum maps at 350 $\mu\text{m}$ (Continuation) . . . . .	196
B.1 Continuum maps at 350 $\mu\text{m}$ (Continuation) . . . . .	197
B.1 Continuum maps at 350 $\mu\text{m}$ (Continuation) . . . . .	198
B.1 Continuum maps at 350 $\mu\text{m}$ (Continuation) . . . . .	199
B.1 Continuum maps at 350 $\mu\text{m}$ (Continuation) . . . . .	200
B.1 Continuum maps at 350 $\mu\text{m}$ (Continuation) . . . . .	201
B.1 Continuum maps at 350 $\mu\text{m}$ (Continuation) . . . . .	202
B.1 Continuum maps at 350 $\mu\text{m}$ (Continuation) . . . . .	203
B.1 Continuum maps at 350 $\mu\text{m}$ (Continuation) . . . . .	204
B.1 Continuum maps at 350 $\mu\text{m}$ (Continuation) . . . . .	205
B.1 Continuum maps at 350 $\mu\text{m}$ (Continuation) . . . . .	206
B.1 Continuum maps at 350 $\mu\text{m}$ (Continuation) . . . . .	207

B.1	Continuum maps at 350 $\mu\text{m}$ (Continuation)	208
B.1	Continuum maps at 350 $\mu\text{m}$ (Continuation)	209
B.1	Continuum maps at 350 $\mu\text{m}$ (Continuation)	210
B.1	Continuum maps at 350 $\mu\text{m}$ (Continuation)	211
C.1	Left: BGPS maps at 1.1 mm toward $l = 30^\circ$ . The ellipses show the recovered sources from the BGPS catalog. Right: Corresponding 350 $\mu\text{m}$ maps from <i>Herschel</i> SPIRE. Contours start from $10\sigma$ , with increasing steps of $5\sigma$ ( $\sigma=164 \text{ MJy ster}^{-1}$ ) The crosses show the peak position of the high-resolution sources recovered in SHARC-II map. Red and blue crosses show substructures with peak signal-to-noise above and below 10, respectively. The area covered by SHARC-II maps, indicated under each figure, is represented by the thick black contour. Figures 28.128.5 are available in the online version of the Journal.	213
C.1	BGPS maps at 1.1 mm toward $l = 30^\circ$ , with corresponding 350 $\mu\text{m}$ maps from <i>Herschel</i> SPIRE (Continuation)	214
C.1	BGPS maps at 1.1 mm toward $l = 30^\circ$ , with corresponding 350 $\mu\text{m}$ maps from <i>Herschel</i> SPIRE (Continuation)	215

# Chapter 1

## Introduction

Because it is one of the most studied problems in astronomy, it is perhaps surprising that the formation of stars is still far from a complete picture. The basic concept of gravity overcoming pressure leads to the successful paradigm for the formation of individual stars with low mass ( $M \leq 1 M_{\odot}$ ) (e.g., Shu et al., 1987). Observations of nearby clouds (typically at a distance  $< 500$  pc) gives us details on the distribution of star formation, timescales of different stages, and the star formation efficiency, along with constraints on the shape of the initial mass function. However, studies of low mass star formation are not directly applicable to the characterization of star-formation on Galactic scales, because low mass star formation is not observable at large distances.

Regions of massive star formation are found at larger distance, starting at  $\sim 440$  pc in the Orion complex (Hirota et al., 2007). Considering their clustering nature, massive stars are born in cores within harboring, intermediate structures. The study of high-mass star forming regions present a particular challenge, both observational and theoretical, but it is necessary to understand the process of star formation in a Galactic context, which can be used later for comparison with tracers of star formation activity in nearby galaxies.

## 1.1 Large scale surveys of star forming gas

Recent wide-area, unbiased surveys at infrared and millimeter wavelengths have give us a deep view of the dust emission in the Galactic plane. These mm surveys identify a large number of dense gas structures associated with star forming regions at different development stages. Thermal radiation in the infrared is considered a signpost of on-the-spot star formation. For instance, the emission at  $24\ \mu\text{m}$  from MIPS GAL, at a resolution of  $6''$  is associated with dust heated by embedded protostellar objects within the source, and therefore is a signpost of a later evolutionary phase (e.g., Calzetti et al., 2007, 2010). The *WISE*  $22\ \mu\text{m}$  emission, with a resolution of  $12''$  (Wright et al., 2010), provides data less affected by saturation.

Maps in the mm regime probe the Rayleigh-Jeans, optically thin tail of the spectral energy distribution of the cold dust, providing a measure of the mass of gas available for star formation. Since grains in starless cores are colder than in the surrounding lower-density medium, mm-wave studies also allow the identification of sources at very early stages of evolution. Two of these surveys, ATLASGAL (Schuller et al., 2009; Contreras et al., 2013) and the Bolocam Galactic Plane Survey (BGPS Aguirre et al., 2011; Ginsburg et al., 2013), have found a large population of dust structures across the Galactic plane. The ATLASGAL survey mapped  $\sim 153$  square degrees of the Southern part of the plane at  $870\ \mu\text{m}$  at a resolution of  $19.2''$ , using the 12 m APEX telescope, detecting 6639 compact sources. A recent work by Csengeri et al. (2014) presented the latest result from ATLASGAL (total of  $\sim 420$  sq. degree), with a new extraction method that identifies 10861 compact mm sources. The BGPS survey has mapped  $\sim 190$  square degrees of the Northern Galactic Plane in 1.1 mm

continuum emission at a resolution of  $33''$ , detecting a total of 8594 sources.

While ATLASGAL and BGPS surveys at  $\lambda \sim 1$  mm have provided a robust tracer of cold dust and hence the amount of gas available to form star, they lack sufficient angular resolution to match with observations at shorter wavelengths. Interferometric observations can solve this problem, giving mm maps with very high angular resolution, but these studies are limited to a selected group of regions due to small fields of view (some examples toward massive star clusters are Fontani et al., 2008; Beuther et al., 2007; Zhang et al., 2007; Hunter et al., 2006). Another approach is to obtain ground-based bolometric observations at shorter wavelengths with instruments such as SABOCA at APEX ( $350 \mu\text{m}$ ,  $7''$  resolution; Siringo et al., 2010), or SHARC-II at CSO, that have higher angular resolution ( $<10''$ ), but with fields of view that can map arcmin size regions. Ragan et al. (2013), for instance, presented  $350\mu\text{m}$  observations with SABOCA of 10 IRDCs previously observed with *Herschel*, and they found a large number of compact structures within their sources, suggesting a hierarchical structure in them.

In this dissertation, I will present  $350\mu\text{m}$  maps with the SHARC-II instrument of a large sample of BGPS sources. The flux distribution of the sample is comparable with the distribution of the complete BGPS survey (see Chapter 2), and therefore is not biased to a particular evolutionary stage or mass. This sample can give us a wide-view understanding of star forming Galactic clumps. I intend to answer the following questions:

- Do sources identified in Galactic plane surveys present internal structure (sub-

structure) when observed at higher resolution or when background emission is filtered out?

- What fraction of sources present substructures?
- What is the mass and surface density of these substructures compared to their parental sources?

## 1.2 Structures in molecular clouds

Most young stars are formed in large structures of molecular gas called giant molecular clouds (GMCs) or cloud complexes. Their main component is  $H_2$ , and they have typical sizes of  $\sim 50$  pc, masses of  $\sim 10^5 M_\odot$ , average densities  $\langle n_{H_2} \rangle \sim 10^2 \text{ cm}^{-3}$  (e.g., Blitz, 1993), and they are considered as the predominant organizational structures of molecular gas in the ISM (e.g., Scoville, 1990). Molecular clouds are inhomogeneous on a wide range of scales, and Williams et al. (2000) defined structures called “star-forming clumps” as dense and massive regions of molecular gas that will form a star cluster, and “cores” as structures of molecular gas likely to form a single star, or a multiple-star system. Observations show that star-forming clumps are approximately gravitationally bound (Bertoldi & McKee, 1992), have typical masses of 50-500  $M_\odot$ , average densities of  $10^3 - 10^4 \text{ cm}^{-3}$ , and sizes of 0.3 – 3 pc (Bergin & Tafalla, 2007). Cores are necessarily bounded structures, and have masses of 0.5 – 5  $M_\odot$ , average densities of  $10^4 - 10^5 \text{ cm}^{-3}$ , and sizes of 0.03-0.2 pc. These values should be taken nevertheless as rough guidelines for the characteristic values of these structures, considering for example instrumental limitations on the identification of



small scale sources at large distances.

### 1.3 Temperature characterization

The dust temperature of Galactic structures is physically determined by the balance between the heating provided by the interstellar radiation field or embedded star formation, and the cooling by the far infrared thermal radiation of dust grains (Mathis et al., 1983). Observationally, the dust temperature is determined from mm to FIR continuum observations, usually assuming thermal emission from a blackbody model modified by the opacity of the source. The observed intensity of continuum emission is given by  $S_\nu = \Omega_{beam}[1 - e^{-\tau_{\nu d}}]B_\nu(T_d)$ , where  $\Omega_{beam}$  is the beam solid angle,  $\tau_{\nu d}$  is the optical depth of the emitting dust at each frequency and  $B_\nu(T_d)$  is the Planck function at the dust temperature  $T_d$ . The optical depth in the submm to mm regime is proportional to  $\nu^\beta$ , with  $\beta$  the spectral index, and therefore the emission is optically thin at long wavelengths. Multi-wavelengths continuum surveys give us the opportunity to estimate the dust temperature of a statistically significant sample of compact structures, which can be used to improve mass estimates, and to identify warm, active star forming regions, and cold, pre-stellar sources.

Spectral energy fitting analysis is a widely used method in the determination of temperatures and spectral index in star forming regions (e.g., Faúndez et al., 2004). Lately, *Herschel* PACS (70  $\mu\text{m}$ , 160  $\mu\text{m}$ ) and SPIRE (250  $\mu\text{m}$ , 350  $\mu\text{m}$ , 500  $\mu\text{m}$ ) continuum data allow us to perform point-by-point systematic temperature determination over large areas of the Galaxy (e.g., Molinari et al., 2010; Battersby et al., 2011). The limitations of this method include low spatial resolution of *Herschel*

at long wavelengths (FWHM beam size of  $35.2''$  at  $500\mu\text{m}$ ); bias in the emission at shorter wavelengths toward warmer dust ( $\frac{hc}{\lambda k} \sim 29$  K for  $\lambda = 500 \mu\text{m}$ ,  $\frac{hc}{\lambda k} \sim 90$  K for  $\lambda = 160 \mu\text{m}$ ); and uncertainties in the determination of parameters due to temperature gradients within sources. Therefore, we require an approach that includes observations at mm wavelengths to also characterize the emission of cold dust ( $T \sim 10$  K).

Another approach is the determination of temperature by single color measurements in mm and submm wavelengths (e.g., Ward-Thompson et al., 2002; Kramer et al., 2003; Schnee & Goodman, 2005). Shetty et al. (2009) have shown variations and uncertainties due to line-of-sight effects in the determination of physical parameters (temperature and opacity spectral index  $\beta$ ), that can lead to inaccurate determination of parameters when two or more unresolved sources at different temperatures are blended due to low angular resolution. Even more, Shetty et al. showed that the determination of temperature of isothermal sources from two observations at different wavelengths gives good estimation (less uncertainties) of T of cold sources compared to warm sources, under the assumption of a reasonable value of  $\beta$  (flux ratio method, see chapter 2). Also, considering pairs of observations at  $450\text{-}850\mu\text{m}$ , and at  $1200\text{-}2100 \mu\text{m}$ , their analysis showed that for cold sources ( $T \sim 10$  K), the  $450\text{-}850\mu\text{m}$  pair of wavelengths is more accurate in the determination of temperatures. However, no particular analysis was presented for a pair with mm wavelengths ( $\lambda \sim 1$  mm) and submm observations ( $\lambda \sim 350 \mu\text{m}$ ).

I will present in chapter 2 a temperature determination analysis for my sample of BGPS sources. The analysis will answer these question

- How reliable is the single-color method compared with other estimations toward star forming regions?
- What is the temperature distribution of Galactic clumps?

## 1.4 Massive star formation

Massive stars play a fundamental role in Galactic evolution. Stars with masses  $M > 8 M_{\odot}$  and luminosities  $L > 10^3 L_{\odot}$ , corresponding to spectral types B3 or earlier, are the principal source of heavy elements and have a dominant role in feedback and regulation of the interstellar medium through energetic processes as stellar winds and supernova explosions.

These stars form rarely compared with their low mass counterparts. Most of the star-forming gas of the cloud is close to isothermal due to efficient radiative cooling. Isothermal simulations predict that massive structures fragment into clusters of low-mass stars (e.g., Bonnell & Bate, 2006). Krumholz & McKee (2008) asserted that radiative heating from surrounding low-mass protostars can prevent the fragmentation of a high-mass clump, and proposed a threshold on the surface density for structures forming massive stars of  $\Sigma \sim 1 \text{ g cm}^{-2}$ . More recent works suggested a lower threshold on surface density for the formation of massive stars. Wu et al. (2010) obtained properties of a sample of 50 massive, dense clumps with high density molecular tracers, obtaining mean surface densities of  $\sim 0.3 \text{ g cm}^{-2}$  for  $\text{HCN}(J = 1 \rightarrow 0)$  observations. A study by Butler & Tan (2012) of mid-infrared extinction toward a sample of infrared dark clumps suggested a lower limit of  $\Sigma \sim 0.2$

$\text{g cm}^{-2}$  for massive star formation. More work is needed to establish if there are minimum threshold conditions for the formation of massive stars.

In this dissertation I address the following questions:

- What fraction of the mass in Galactic clumps is in dense substructures?
- What fraction of substructures (cores) found in clumps have the conditions needed to form massive stars?
- How do my determination of temperatures compare with other surveys of massive star forming regions?

## 1.5 Extreme star formation

In the framework of these large Galactic surveys at different wavelengths, the identification of complexes of Giant Molecular Clouds with very active massive star formation, is of particular interests. These regions consist of groups of molecular clouds with masses up to  $\sim 10^7 M_{\odot}$  (Rand & Kulkarni, 1990; Rand, 1993; Kuno et al., 1995; Koda et al., 2009), and include regions such as W51 and W49 in our Galaxy. Another of these regions is W43 (e.g., Nguyen Luong et al., 2011, and references within). It is located at the meeting point of the Scutum-Centaurus Galactic arm and the end of the Bar, between  $l = 29^{\circ} - 32^{\circ}$ ,  $|b| < 1$ , at a heliocentric distance of 6 kpc (Nguyen Luong et al., 2011; Carlhoff et al., 2013). It has one of the largest cloud groups in the first Galactic Quadrant, with a total mass of  $\sim 5 \times 10^6 M_{\odot}$  (Dame et al., 1986). W43 contain a well known giant H II region, with a FIR luminosity

of  $\sim 3.5 \times 10^6 L_{\odot}$ , and it harbors a cluster of Wolf-Rayet and OB main-sequence stars (Blum et al., 1999, and references therein), which provide its main ionizing source. Toward its central region lies the ridge W43-MM1, which present a notably efficient burst of high-mass star formation (star formation efficiency of  $\sim 6\%$ , enclosed in  $\sim 8 \text{ pc}^3$ ; Louvet et al., 2014).

W43 is an example of an extreme environment for the formation of massive stars, and it is important to learn if there are more regions like this in the Galactic plane. Their study and characterization will allow us to make meaningful assessment of star formation in the galactic context.

In chapter 3, I will present a thorough multi-wavelength study of the G331.5 GMC, one of the most massive GMCs in the Southern Galaxy. This region is located in the tangent of the Norma spiral arm, at a distance of 7.5 kpc, and radio continuum observations show the presence of an extended region of ionized gas. The region has a FIR luminosity of  $3.6 \times 10^6 L_{\odot}$ , and therefore is an ideal candidate for a region with active high-mass star formation. I will address the following questions:

- Is the G331.5 GMC a region with extreme conditions (or extreme environment) for the formation of massive stars?
- Can we spatially resolve the components of this region?
- What are the physical conditions that characterize this GMC and the resolved structures within?

- Are any of the dense structures inside G331.5 above the threshold for massive star formation presented by Krumholz & McKee (2008)?

## 1.6 Signatures in the formation of massive stars

Some of the main characteristics of a massive star are its highly energetic processes during its formation, which provides significant feedback to their surrounding environment.

The high far-ultraviolet luminosity from a massive protostar,  $10^{47} - 10^{49} \text{ s}^{-1}$  for spectral types B-O, produces regions of ionized gas in the vicinity of these newly formed stars called hyper- and ultra-compact H II regions, with sizes of  $< 0.01 \text{ pc}$  and  $< 0.1 \text{ pc}$ , respectively (Beuther et al., 2007; Hoare et al., 2007). These structures have temperatures of  $10^4 \text{ K}$  and show rising spectral indices at radio wavelengths from their thermal bremsstrahlung emission. An indirect method for the detection of thermal emission include the detection of hydroxyl (OH) masers, which are known to be excellent indicators of ultra compact H II regions (e.g., Garay et al., 1985).

Protostellar winds and molecular outflows are a common phenomena found toward young stars, observed from the earliest stages of star formation until the end of their accretion phase (e.g., Reipurth & Bally, 2001). Outflows can affect the kinematics, density and chemistry of a substantial volume of their parent cores and clouds (Arce & Sargent, 2006), and thus can be important to the turbulent dynamics and energetics of their environment, even affecting the formation efficiency in the cloud (Matzner & McKee, 2000; Nakamura & Li, 2007; Machida & Hosokawa, 2013). Molecular outflows toward star forming regions are traced by molecular lines

at millimeter wavelengths, with high density tracers such as CO and CS (e.g., Beuther et al., 2002, 2004b), and using tracers of shocked material such as SiO and SO (e.g., Hirano et al., 2006; Beuther et al., 2004a; Wakelam et al., 2005). Furthermore, it is often assumed that the driving sources of molecular outflows in massive star forming regions are stellar ionized winds. Reynolds (1986) showed that a collimated, ionized jet has a steeper spectral index ( $\geq 0.9$ ) than that of a spherical, isothermal, stellar wind model ( $\sim 0.6$ ).

The impact of newly formed massive stars is also traced by the formation of “hot cores”, very compact and dense regions ( $\sim 10^7 \text{ cm}^{-3}$ ) surrounding the protostar, with temperatures  $> 100 \text{ K}$  (Garay & Lizano, 1999). These hot cores are characterized by a rich chemical composition, with abundance of hydrogenated species such as  $\text{CH}_3\text{OH}$ , and by increased concentrations of sulfur-bearing molecules, such as SO,  $\text{SO}_2$  and CS (Charnley, 1997).

Therefore, the study of the very early stages of protostellar massive objects and the impact on their surrounding medium requires both continuum and molecular line observations in mm-radio regimes.

An important challenge in the study of these early-stage signatures is that massive stars are usually found at large distances from us, deeply embedded on their host dusty, dense cores. Then, their study require high-angular (and velocity) resolution instruments, which can identify structures at sub-parsec scales. A better characterization of the observational evidence on molecular outflows and other early-stage signatures, and their comparison with hydrodynamical numerical simulations and shock models will lead to a complete picture of protostellar winds, entrainment

processes and their impact on their surrounding medium. While this is best done for nearby low-mass star forming region, we want to know if high-mass stars produce similar outflows.

In chapter 3, I will present the discovery of a high-velocity molecular outflow at the center of the brightest molecular clump of the G331.5 region. In Chapter 4, I will report follow-up high-angular observations of this source with the new Atacama Large Millimeter/Submillimeter Array. The analysis of this region will allow me to answer the following questions:

- What is the structure of a very young embedded massive protostar?
- What are the characteristic physical parameters and kinematics of energetic processes, such as outflow emission and material infall, toward a forming massive star?

In chapter 5, I will summarize the results of this dissertation, and I will discuss plans for future research directions.



## Chapter 2

# Temperatures and substructure of Galactic clumps based on $350\mu\text{m}$ observations.

### 2.1 Introduction

Although high-mass stars play a key role in the structure and evolution of our Galaxy, there are still many questions that need to be answered before we have a paradigm for their formation process (Stahler et al., 2000; Bally& Zinnecker, 2005; Zinnecker& Yorke, 2007; Tan et al., 2014). Adopting the nomenclature of Williams et al. (2000), star clusters form in dense clumps ( $M \sim 50 - 500 M_{\odot}$ , sizes  $\sim 0.3 - 3$  pc) of giant molecular clouds while individual stars form in cores ( $M \sim 0.5 - 5 M_{\odot}$ , sizes  $\sim 0.03 - 0.2$  pc). An important step in the observational study of massive star formation is the identification and characterization of clumps and resolution into cores. Studies of compact structures in our Galaxy will give fundamental “ground truth” for the analysis of nearby galaxies where individual clumps and cores cannot be resolved, and provide source information for observations of the Milky Way with a new generation of instruments, such as the Atacama Large Millimeter/Submillimeter Array.

There are complementary approaches to the study of massive star forming regions. We may consider obtaining molecular line observations, which are a good

diagnostic of line-of-sight motions in a cloud, but variations in tracer abundances due to depletion and complex chemical processing, excitation conditions and the impacts of radiation fields and shocks add uncertainties (Evans, 1999). We may also proceed by mapping the continuum emission toward these sources. Newly formed stars heat the dust of their parental molecular cores and this dust emits in the far infrared and submillimeter wavelengths (Garay & Lizano, 1999). Continuum emission observations at (sub) millimeter wavelengths offer a reliable tracer of the column density and clump masses due to the low optical depth of the dust (e.g. Johnstone & Bally, 2006), and they have made an increasingly significant contribution to the understanding of star formation.

Several studies have made progress toward this goal, but they are usually biased because target selection required existing signposts of massive star formation, including maser emission, IR emission, or the presence of H II regions (Churchwell et al., 1990; Cesaroni et al., 1991; Plume et al., 1992). Therefore, the identification of clumps with a less biased survey will improve our understanding of the early stages of massive stars. Examples include the large scale survey of particular regions, such as the study of the W3 giant molecular cloud with Submillimetre Common-User Bolometer Array (SCUBA) by Moore et al. (2007) or the Cygnus X molecular cloud complex region with MAMBO receiver by Motte et al. (2007). Large-scale blind surveys of the Galactic Plane at far-IR, submm and mm wavelengths have recently been completed. The ATLASGAL survey mapped the Southern part of the plane at 870  $\mu\text{m}$  using the 12 m APEX telescope (Schuller et al., 2009; Contreras et al., 2013). Space borne missions, such as *WISE* (Wright et al., 2010) and

*Spitzer*/GLIMPSE (Benjamin et al., 2003) and MIPS GAL (Carey et al., 2009), have mapped most of the Galactic plane at a resolution of a few to  $10''$ , at wavelengths between 3.6 and  $24\ \mu\text{m}$ . The *Herschel*/Hi-GAL survey (Molinari et al., 2010) covered the entire Galactic plane with resolution between  $6''$  and  $36''$ , in five bands at 70, 160, 250, 350 and  $500\ \mu\text{m}$ . In addition, the 15-m James Clerk Maxwell Telescope is using SCUBA-2  $850\ \mu\text{m}$  and  $450\ \mu\text{m}$  emission to map the Galactic plane and several nearby Gould Belt clouds. These surveys have provided a robust tracer of dust properties (column density and mean grain temperature), for different phases of the interstellar medium.

The Bolocam Galactic Plane Survey (BGPS; Aguirre et al., 2011) is one of the first ground-based surveys to map the continuum emission at 1.1 mm over a large region of the northern Galactic plane. The BGPS coverage region extended from  $l = -10^\circ$  to  $+86.5^\circ$  for  $b = \pm 0.5^\circ$ , at a resolution of  $\sim 30''$ , and it identified 8454 compact sources throughout the Galaxy (Rosolowsky et al., 2010). Depending on their distance, millimeter features may be cores, clumps, or clouds (McKee & Ostriker, 2007), although BGPS sources are mostly clumps (Dunham et al., 2011). An improved reduction and a new version (V2.0) of the BGPS maps and catalog was recently released (Ginsburg et al., 2013), including additional  $\sim 20$  square degree coverage area in the third and fourth quadrant, and  $\sim 2$  square degree in the 1st quadrant. This new reduction shows an improved flux calibration with respect to the former version (V1.0), in agreement with other data surveys on the Galaxy. The characterization of the angular transfer function of the Bolocam pipeline shows that the flux recovery is above 90% for scales between  $33''$  and  $80''$ , with a steep drop

for scales above  $\sim 100''$ . While version 2.0 of the catalog contains 8559 sources, 35 sources were unintentionally excluded, and they were added in a new version (V2.1), for a total of 8594 sources. Figure 2.1 shows the distribution of  $40''$  aperture flux density of V2.1 sources.

We selected a sample of sources from the BGPS catalog, initially from V1.0 and later from V2.1, towards the most crowded and brightest portions of the Galactic Plane including the Galactic Center, the Molecular Ring near  $l = 30^\circ$  and Cygnus-X, and used the Submillimeter High Angular Resolution Camera II (SHARC-II; Dowell et al., 2003) to obtain continuum maps at  $350 \mu\text{m}$  of them. The high resolution of the SHARC-II observations (FWHM beam size of  $8.5''$ ) is in particular very useful when we observe small structures at great distances in the Galaxy, and the comparison of flux densities of sources at  $350 \mu\text{m}$  and  $1.1 \text{ mm}$  will give us constraints on their dust temperatures, hence improving the determination of masses and column densities of the molecular clumps.

SHARC-II has been used before for studying low-mass dense cores from the *Spitzer* Legacy Program “From Molecular Cores to Planet-Formation Disks” (Wu et al., 2007, Suresh et al. in prep.), concluding that observations with this instrument are better to distinguish between starless and protostellar cores than observations at longer wavelengths. While Mueller et al. (2002) studied dense clumps selected for having massive star formation using SHARC at  $350 \mu\text{m}$ , there has not been a comprehensive study of BGPS-selected sources with SHARC-II. A recent study by Ragan et al. (2013) shows how ground-based observations at  $350 \mu\text{m}$  continuum emission of regions of high-mass and cluster formation can give information on substructures

within them. For a set of 11 nearby Infrared-dark clouds (IRDCs), they obtained data on  $350\ \mu\text{m}$  continuum emission with the SABOCA instrument at the APEX telescope, finding a large population of small core-like structures. Higher resolution observations at submm wavelengths allow the study of the complex process of massive star formation from fragmentation of molecular clumps to individual substructures, such as cold and hot cores.

We present a set of 107 continuum emission maps at  $350\ \mu\text{m}$  obtained with SHARC-II toward clump-like sources from the BGPS V2.1 catalog. This paper is organized as follows. Section 2 describes the selection of targets from the BGPS catalog and the SHARC-II instrument. Section 3 describes the data reduction and calibration methods for our set of submm continuum maps. Section 4 presents the results of the extraction of sources in the images, including source recovery tests, a catalog of these sources, the procedure for association between sources in the  $350\ \mu\text{m}$  maps and the 1.1 mm sources, and the comparison between SHARC-II and *Herschel* at  $350\ \mu\text{m}$ . Section 5 describes the determination of color temperatures for BGPS sources found in our set of maps, comparing them with temperature determination from spectral energy distribution (SED) fitting from Hi-GAL and other continuum surveys. Correlations between our dust temperature estimations and high-density molecular tracers are presented, and we explore consequences from our results for mass and surface density estimations of millimeter sources. In section 6, we present conclusions from our analysis.

## 2.2 Observations

Observations were taken in several runs between June 2006 and September 2012 at the Caltech Submillimeter Observatory (CSO<sup>1</sup>). The observations required excellent weather conditions, with a measured optical depth at 225 GHz ranging between 0.030 and 0.094, with an average value of  $\tau_{225 \text{ GHz}} = 0.057$ , corresponding to an optical depth at 350  $\mu\text{m}$  (857 GHz) of  $\tau_{350 \mu\text{m}} = 1.41$ . In general, we observed our targets when they were culminating, and we avoided observing sources below an elevation of 30° or above 80°.

### 2.2.1 Target selection

The targets were initially selected from sources in the BGPS V1.0 catalog. We chose sources with strong emission at 1.1 mm (typically with peak emission above 1 Jy beam<sup>-1</sup>) toward densely populated regions, many of them known as active star forming regions, such as the Galactic Center,  $l = 30^\circ$ , Cygnus-X region, W3 and W5 molecular clouds, GemOB1 region, and others. Several of those targets were extended and they were likely to have unresolved substructure at a resolution of 30". Most of the time the observation fields were centered directly on a V1.0 source, but in some cases we tried to cover several sources in the same field. Starting in December 2009, we added to our list of targets bright sources selected from new Bolocam maps that were later incorporated in BGPS V2.0. Considering that almost all targets from V1.0 catalog are incorporated in V2.1 (Ginsburg et al., 2013), we consider the latest

---

<sup>1</sup>The Caltech Submillimeter Observatory is operated by the California Institute of Technology, until 2013 April 1 under cooperative agreement with the National Science Foundation (AST-0838261)

version of the catalog for our analysis. In just one of our maps, L136.52+1.24, there are three sources marginally detected in V1.0 but not included in subsequent V2.0 or V2.1 catalog versions. We also obtained 350  $\mu\text{m}$  maps of the regions SH2-209, SH2-307 and IRAS 03233+5833, which were not covered by the BGPS survey. These observations are included for completeness.

For a better characterization of our targets with respect to the complete catalog, we consider the brightest V2.1 source in each map as the representative target for that map. In some cases, where adjacent maps share the brightest source, we consider the second brightest source as a representative target. From the 350  $\mu\text{m}$  maps that have a BGPS source in them, we have then a sub-sample of 104 V2.1 sources considered as representative targets. Figure 2.1 shows in red the distribution of flux density in 40'' apertures for our sample of representative targets. The distribution has an average of 2.63 Jy and a median of 1.37 Jy, much higher than the values for the overall BGPS catalog. However, weaker sources were covered in the same fields, so the final flux density distribution of BGPS sources with 350  $\mu\text{m}$  data is closer to that of the full catalog (see black line in Figure 2.1). We found a total of 619 V2.1 sources in our sample of SHARC-II maps, with an average and median flux density of 0.79 Jy and 0.29 Jy, respectively, about twice the values for the complete V2.1 catalog (average of 0.35 Jy and median of 0.16 Jy for 40'' apertures).

### 2.2.2 Instrument and Observational Method

SHARC-II is a background-limited facility camera operating at 350  $\mu\text{m}$  or 450  $\mu\text{m}$ , located at the CSO on Mauna Kea, Hawaii. It consists of a 32 $\times$ 12 array

of doped silicon ‘pop-up’ bolometers and it has a mean beam size of  $8.5''$  at  $350\ \mu\text{m}$ . The array has a full size of  $2.59' \times 0.97'$ , which makes the instrument start to lose sensitivity to emission on scales larger than  $\sim 1'$ . We used the box scan mode of SHARC-II without chopping<sup>2</sup> for mapping regions with sizes significantly larger than the size of the array. In the box scan mode, the scan pattern moves across the rectangular field of view, starting in the center of the array and going straight until the edge of the bounding box, where it changes trajectory emulating the bounce of a ball on a billiard table. The advantage of this scan mode is that it provides better isolation against  $1/f$  noise, with more uniformly distributed noise across the field of view in comparison with the alternative sweep mode with Lissajous scan pattern. Different box sizes were used in our data acquisition, between  $2.5' \times 2.5'$  and  $18' \times 18'$ , although the bulk of our observations were obtained with  $10' \times 10'$  boxes. Column 3 in Table 2.2 shows the size for each map.

For all our observations we used the Dish Surface Optimization System (DSOS)<sup>3</sup> to correct the dish-surface figure for imperfections and gravitational deformations as the dish moves in elevation during observations.

## 2.3 Data reduction and calibration

### 2.3.1 Data reduction

The  $350\ \mu\text{m}$  raw data were reduced using the Comprehensive Reduction Utility for SHARC-II (CRUSH; Kovács, 2006). CRUSH is a Java-based software which

---

<sup>2</sup>See <http://www.submm.caltech.edu/~sharc/>

<sup>3</sup>See [http://www.cso.caltech.edu/dsos/DSOS\\_MLeong.html](http://www.cso.caltech.edu/dsos/DSOS_MLeong.html)



solves a series of iterative models, attempting to reproduce atmospheric and instrumental effects on the observations, removing the sky emission common to all bolometers at first order (e.g., Beelen et al., 2006). We used version 2.10 of CRUSH, publicly accessible from the CSO webpage.

Figure 2.2 shows an example of the error or noise maps that reduction with CRUSH produces for each observed region. In general, all SHARC-II maps are much noisier toward the edges by a factor of  $\sim 4$  with respect to the measured average noise of the image. At a distance of  $\sim 20''$  (twice the beam size) from the edge, the noise is only increased a factor of  $\sim 2$ . Also, when taking multiple scans for a single map at different runs, the orientation of the field of view rotates, and the regions that do not overlap in the integration of the source show a significant increase in the noise. The rest of the map shows some residuals of the pattern used in the box scan mode, but in general the inner parts of these maps are well represented by uniform noise.

### 2.3.2 Calibration

The maps were reduced in instrumental units of  $\mu V$ , and we estimated the flux conversion factors  $C_\theta$  in order to measure the flux densities of the sources in units of Jy. On our analysis, we followed the same method used on SHARC-II maps by Wu et al. (2007), and on SCUBA maps by Shirley et al. (2000), based on aperture calibrations over a given angular size  $\theta$ . Flux estimation obtained from aperture corrected photometry are less sensitive to uncertainties due to effects of sidelobes. The observed flux density for an aperture of diameter  $\theta$  is  $S_\nu(\lambda, \theta) = C_\theta V(\lambda, \theta)$ , with  $V(\lambda, \theta)$  the voltage measured at wavelength  $\lambda$  in an aperture of diameter  $\theta$ .

We used the fluxes from Mars, Uranus and Neptune to obtain the flux conversion factors for two different apertures, 20'' and 40''. We restricted our flux estimation to 40'' considering the limited sensitivity of the instrument to large scale emission. The bulk of the compact structures identified on the maps have sizes below this limit.

To compare the 350  $\mu\text{m}$  data with the 1.1 mm images from BGPS survey, we also convolved the 350  $\mu\text{m}$  to match the 33'' FWHM beam from Bolocam. Therefore, we also estimated the flux conversion factor  $C_{40}^{33''}$  for an aperture of 40'' using the images of the calibration sources convolved to a 33'' beam. The flux densities of sources and calibrators in instrumental units were measured using Starlink's *aperadd* package.

In addition, we estimated the flux conversion factor for one beam,  $C_{beam}$ , which we used to express the peak flux of each source and the  $1 \sigma$  rms of the maps in units  $\text{Jy beam}^{-1}$ .  $C_{beam}$  is obtained from the integrated flux density of the calibrators in one beam and the peak pixel of the map in instrument units. We have then an average value for the conversion  $\mu\text{V}$  to  $\text{Jy pixel}^{-1} = 32.23 \text{ Jy beam}^{-1}$ , for the beam size and pixel scale of the instrument. Therefore, the value of  $C_{\theta}$  will depend of the number of pixels considered. From the maps, the average value of  $C_{beam} = 8.27 \text{ Jy beam}^{-1} \mu\text{V}^{-1}$ , and then

$$\begin{aligned}
 1 \text{ Jy beam}^{-1} &= 503.8 \text{ MJy ster}^{-1} \\
 &= 0.031 \text{ Jy pixel}^{-1} \\
 &= 0.121 \mu\text{V}^{-1} .
 \end{aligned}$$

For the calibration of the images, only the observations of planets were con-

sidered. While the secondary calibrators mentioned in section 2.4.1 are useful to check the pointing when planets are not available, they are not as bright and their flux densities are not as well known as planets. Therefore, we avoided using them to minimize uncertainties in the estimation of calibration factors.

Table A.1 in the Appendix section gives the observation dates (column 1), the planet observed (column 2), the observed opacity at 225 GHz at that date (column 3), the computed values of  $C_{beam}$  (column 4) and  $C_{\theta}$  at different apertures (columns 5 and 6). Column 7 gives the calibration factor for an aperture of  $40''$  obtained for the planet images convolved to a beam of  $33''$ . Table 2.1 shows the average values of  $C_{\theta}$  for the different observation epochs. According to these results, the uncertainties in the calibration of the maps are between 15-20%, consistent with previous observations and calibration estimations for the SHARC-II instrument (Wu et al., 2007).

While some sources may have significant contributions to the broad-band flux density from line emission, it is usually a small fraction of the dust continuum emission (e.g., Groesbeck 1995). The continuum flux measured with SHARC-II (780 - 910 GHz for the  $350 \mu\text{m}$  filter) could in principle be contaminated by the CO(7 – 6) line. Hatchell & Dunham (2009) estimated a contribution less than  $100 \text{ mJy beam}^{-1}$  in the SHARC-II  $350 \mu\text{m}$  band for a CO(7 – 6) integrated intensity of  $100 \text{ K km s}^{-1}$ , which is smaller than the typical sensitivity found in our maps, and they consider that the CO line may contribute  $\sim 20\%$  of the continuum emission in the  $350 \mu\text{m}$  band, a limit also adopted in this work for possible line contamination.

## 2.4 Results

### 2.4.1 Map description

Figure 2.3 shows as an example the 350  $\mu\text{m}$  continuum map of L133.71+1.21, corresponding to the W3 main region (see Rivera-Ingraham et al., 2013; Megeath et al., 2008, and references therein). Besides the two bright infrared sources IRS5 and IRS4 (Wynn-Williams et al., 1972), the small beam size of the 350  $\mu\text{m}$  maps allows us to identify several sources near them, and some elongated, filamentary-like structures and scattered faint sources. These types of features are found recurrently in the 350  $\mu\text{m}$  maps and we characterize their correspondence with 1.1 mm sources later in section 2.4.5.

We obtained a total of 107 maps, with an average noise of 744 mJy beam<sup>-1</sup>, and a standard deviation of 443 mJy beam<sup>-1</sup>. These maps are presented in Figure B.1 in the Appendix. Because the noise increases at the edges of the images (section 2.3.1), we estimated a more representative value of the rms of each map on a region toward the central area. In the 10'×10' maps, the considered area has a diameter of 7'. Column 7 in Table 2.2 shows the representative rms noise of each map. The average 1 $\sigma$  noise value estimated this way is 478 mJy beam<sup>-1</sup>, with a median of 375 mJy beam<sup>-1</sup> and a standard deviation of 298 mJy beam<sup>-1</sup>. Each map has an angular scale of 1.618 arc-seconds per pixel. Table 2.2 lists, for each map observed, the configuration used, the size and center of each map, the date on which the map was taken, and the 1  $\sigma$  noise of the map in units of mJy beam<sup>-1</sup>. Integration time was obtained in blocks of  $\sim 14$  minutes. The pointing was checked on planets such as Mars, Uranus and Neptune, and with secondary objects when the

planets were not available, such as IRAS 16293-2422, K350, G34.3, W75N and CRL 618. The blind pointing uncertainty varied between  $1.8''$  and  $2.1''$  for azimuth and between  $0.8''$  and  $1.6''$  for zenith angle.

## 2.4.2 Source Extraction

To facilitate comparison with the BGPS sources, we used the same algorithm for source extraction as was used for the BGPS catalogs, *Bolocat* (Rosolowsky et al., 2010). *Bolocat* identifies sources based on their significance with respect to the local estimate of the noise in a map, subdividing regions with high significance into individual sources based on local maxima inside that region. Each pixel is assigned to an individual source using a seeded watershed, in a similar way to other source extraction algorithms (*Clumpfind*, Williams et al. 1994; *SExtractor*, Bertin & Arnouts 1996). The source identification process is determined by three parameters:  $P_{amp}$ , the amplitude of the signal compared to a local estimation of the noise  $\sigma(\alpha, \delta)$ ;  $P_{base}$ , the base level of emission at which the identified region is expanded; and the deblending parameter  $P_{deb}$ , used in decomposing regions of emission with multiple local maxima. First, *Bolocat* masks all data above  $P_{amp}$  of a particular image, and extends a region to include all connected regions of emission above  $P_{base}=1\sigma(\alpha, \delta)$  since areas with marginal significance adjacent to regions of emission are probably real. Second, each identified region is examined and subdivided according to the level of contrast between local maxima. For each pair of local maxima in a region, the amplitudes of emission,  $I_1$  and  $I_2$ , are compared with the highest contour of emission containing the local maxima pair,  $I_{crit}$ , and if any  $I_1$  or  $I_2$  is less than  $P_{deb}$  above

$I_{crit}$ , that local maximum is discarded as a subregion. *Bolocat* also avoids recovering sources (and sub-sources from the deblending process) with sizes less than the beam FWHM. A detailed description of the algorithm is presented in Rosolowsky et al. (2010). BGPS catalogs V1.0 and V2.1 used as parameters for the extraction of sources  $P_{amp}=2\sigma(l, b)$ ,  $P_{base}=1\sigma(l, b)$  and  $P_{deb}=0.5\sigma(l, b)$ , with  $\sigma(l, b)$  the local noise estimation, as a function of Galactic coordinates, on the BGPS maps.

We tested *Bolocat* in the SHARC-II maps varying the  $P_{amp}$ ,  $P_{base}$  and  $P_{deb}$  parameters, checking which of them reproduce a “by eye” extraction of sources in those maps. Using the same parameters as BGPS, spurious low brightness sources were recovered across the maps, with several of them toward the noisy edges of the maps, and bright extended sources are sub-divided until the routine reaches small areas, comparable to the beam size of the maps. Better results were obtained considering  $P_{amp}=3\sigma(\alpha, \delta)$ ,  $P_{base}=1\sigma(\alpha, \delta)$  and  $P_{deb}=1\sigma(\alpha, \delta)$ , and these values were used for all 107 maps and the following catalog of BPGS substructures at 350  $\mu\text{m}$ .

Figure 2.4 shows an example of one SHARC-II map and the corresponding image at 1.1 mm obtained from BGPS. The angular scales of SHARC-II and BGPS images are 1.6 arc-seconds per pixel and 7.2 arc-seconds per pixel, respectively. The better angular resolution of SHARC-II reveals substructures within the clumps identified by the BGPS catalogue. Crowded fields and extended clumps identified at 1.1 mm show small components and filaments when they are observed at 8.5'' resolution.

### 2.4.3 Source recovery experiments

We performed similar tests to the ones done for BGPS to assess catalog properties compared with the real distribution of emission on the sky. For these tests, we inserted sources in selected maps that do not have detected sources, or that have just a couple of compact identified sources. The selected maps are those of L030.15+0.00 (2 identified sources), L078.92-0.19 (0), L079.62+0.49 (0), L079.11-0.35 (1), L080.86+0.38 (2), L111.26-0.77 (2), L111.79+0.71 (0), L136.52+1.24 (2), and L137.69+1.46 (0). The median rms noise of these maps is  $667 \text{ mJy beam}^{-1}$ , larger than 83% of the estimated noise in the whole set of maps. This set of maps will be considered as a conservative representation of an emission free SHARC-II map. For those maps that already have identified sources, we flagged the detection of those sources and any input sources near them, and therefore the recovered properties of input sources will not be affected by the emission prior to the test. After the artificial Gaussian objects were added, the maps were reduced in the same standard way as the rest of the SHARC-II maps. Although Gaussian brightness profiles do not quite represent all structures observed in the  $350 \mu\text{m}$  maps, they are still good models of compact sources. Thus, the bulk of sources will be well represented in these tests.

We examined the degree of completeness of the catalog of substructures at different flux density limits. For the nine test maps, we input sources with FWHM of  $9''$  and amplitudes uniformly ranging between  $0.1\sigma_{rms}$  and  $15\sigma_{rms}$ , with  $\sigma_{rms}$  the noise of each map. For  $\sigma_{rms} = 667 \text{ mJy beam}^{-1}$ , this range correspond to sources with flux densities between 0.19 Jy to 28.5 Jy. Taking into account that the edges of

the maps have a larger noise than the central area of the map with uniform noise, we consider the detection fraction of sources across the whole map, and sources inside a central area of  $7'$  in diameter. Figure 2.5 shows the results of the test of completeness. The vertical lines represent 1 to 6 times the average  $\sigma_{rms}$  value of the complete set of SHARC-II maps. For sources inside the central area of the map, the detection is  $>99\%$  complete at the  $6\sigma_{rms}$  level. For sources with amplitude less than  $3\sigma_{rms}$ , the detection fraction is less than  $15\%$ . For the rest of our test, we only considered sources inside a central area of radius  $3.5'$  to avoid noisy edge effects.

The next test we performed was examining the properties recovered by the extracting algorithm for a distribution of input sources. Figure 2.6 shows the comparison between input and extracted flux densities for objects with FWHM equal to  $23''$  (2.7 times the beam size of the  $350\ \mu\text{m}$  maps). The left panel shows the flux recovery in units of  $\mu\text{V}$ , prior to calibration, and the extraction results using apertures of  $20''$  and  $40''$ , and the total integrated flux of the artificial sources in our set of test maps. The integrated flux is estimated from the area of significant emission defined by the watershed extraction. At an aperture smaller than the source size, we just recovered part of the total intensity as expected, and the flux recovery at a larger aperture as  $40''$  is almost coincident with the integrated flux. All the sources extracted in our catalog have a recovered flux density in the range presented in the figure (less than  $3000\ \mu\text{V}$ ). The right panel shows the results of calibrating the sources from the left panel. The integrated emission was calibrated using the  $C_{beam}$  conversion factor, and flux recovery at  $20''$  and  $40''$  was calibrated using  $C_{20}$  and  $C_{40}$ , respectively. The image indicates that the  $40''$  aperture flux density could



be underestimating the amount of flux recovered for input sources, with a difference with respect to the curve of the integrated flux of  $\sim 10\%$ . That difference between integrated and aperture flux density recovery gets bigger for input sources with larger size. For example, for input sources with FWHM equal to 4 times the beam size ( $\sim 30''$ ), the difference between a  $40''$  aperture and the integrated flux is around 35%.

The size recovered with *Boloccat* for input sources with a peak signal of  $50\sigma_{rms}$  is shown in Figure 2.7. The sizes of small sources are well recovered by the algorithm, but they become underestimated for sources larger than  $\sim 60''$ . These results are similar to those found in the BGPS maps, where the radii of recovered sources become underestimated for radii  $\geq 200''$ . The largest source that we found in the  $350\ \mu\text{m}$  maps has a size of  $\sim 48''$ , with a major-axis of  $65''$ , and therefore most of the recovered sizes should be reliable.

Finally, we inspected how the algorithm decomposes sources into individual substructures. We tested how blended sources are identified as a single or as a couple of individual objects, considering pairs of input objects in the set of test maps. Each source of the pair of input fake sources have sizes between  $14''$  and  $34''$ , and peak flux density of  $50\sigma_{rms}$ . Figure 2.8 shows the fraction of blended sources as a function of the separation between pairs of input sources. In general, sources at a distance less than the beam FWHM cannot be recovered individually and they are assigned to the same source in the recovered catalog, and more than 50% of the pairs of input sources are recovered individually at distances larger than  $20''$  (2.4 times the beam size). Figure 2.8 also shows that pairs of input sources with sizes less than  $24''$  are better resolved at shorter distance than pairs with larger sizes than that. Pairs of

sources are resolved more than 50% at separations of  $16''$  for small input sources, and at  $25''$  for larger sources.

#### 2.4.4 Catalog of sources in the $350 \mu\text{m}$ maps

We have recovered from the *Bolocatt* extraction 1386 sources in the  $350 \mu\text{m}$  maps. We name our sources in a similar way as described in the BGPS catalog, using the peak position of the source in galactic coordinates: SH\_Glll.llll  $\pm$  bb.bbbb. An additional digit with respect to the BGPS catalog was required to account for the better resolution and smaller pixel size in the SHARC-II maps. Table 2.3 presents the properties recovered for the extracted sources. The positions of the recovered sources in the SHARC-II maps are shown in Figure B.1 in the Appendix.

Figure 2.9 shows the distribution of recovered flux for these sources using three methods from our catalog: photometry in  $20''$  and  $40''$  apertures, and the integrated flux. For the  $20''$  aperture, the average and median value of the flux density are  $23.15 \pm 1.59$  Jy and 8.95 Jy, respectively. For the  $40''$  aperture, the average and median values are  $45.11 \pm 2.82$  Jy and 16.63 Jy, resp. For the integrated flux density, the average and median values are  $59.59 \pm 5.19$  Jy and 12.06 Jy, resp.

Figure 2.10 shows the deconvolved radii and the aspect ratio distribution. The deconvolved radii distribution extends to  $46''$ , and the catalog has 257 sources ( $\sim 19\%$  of the total) with radii not resolved. These small sources are usually faint, with an average value of their peak signal-to-noise ratio of 4.4. The average and median of the radii distribution are  $15.0''$  and  $14.0''$ , respectively. The aspect ratio is defined as  $\sigma_{maj}/\sigma_{min}$ , and its average and median values are 1.53 and 1.45, respectively.

A similar median aspect ratio is found in the BGPS V2.1 catalog, and this could be a common feature of millimeter and submillimeter sources, or an artifact of the extraction algorithm.

#### 2.4.5 Correlation with BGPS sources

We performed a spatial position matching analysis to get a correlation between sources found in the  $350\ \mu\text{m}$  maps and the BGPS V2.1 sources contained in them. A simple criterion to match sources from catalogs at different resolutions is to take the position of maximum intensity for sources of one catalog, and find which sources in the second catalog are 1 beam distant from that position. For example, Contreras et al. (2013) performed this kind of matching between sources of the ATLASGAL survey ( $870\ \mu\text{m}$ ,  $19.2''$  FWHM beam size) and BGPS V1.0 sources, considering that sources between these catalogs will be associated if their peak positions are less than  $40''$  in angular distance, finding around  $\sim 3000$  likely matches. One of the issues with this approach is that it does not yield a one-to-one association, and additional conditions are required for that. This has special importance in catalogs based on sources extracted from maps at different resolutions. Even more, Ginsburg et al. (2013) found that for the same  $1.1\ \text{mm}$  data at  $33''$  FWHM beam resolution, re-processed V2.1 maps with better spatial filtering recover in some cases more than the one source that previous V1.0 maps found, and then they required more than simple matching at beam distance to compare different versions of the catalog.

Considering the different beam size of the  $350\ \mu\text{m}$  maps ( $8.5''$ ) and  $1.1\ \text{mm}$  maps ( $33''$ ), we expect to resolve extended millimeter sources in some cases in multiple

smaller components, and we put the constraint that compact sources identified in the 350  $\mu\text{m}$  maps are associated to a single 1.1 mm source. For the following analysis, we will consider as a “parental clump” a 1.1 mm source from the BGPS catalog, harboring one or more associated matched structures on the 350  $\mu\text{m}$  maps, which we will refer to as “high-resolution sources” or just simply as “substructures”.

We made use of one of the sub-products of the *Boloccat* algorithm, the mask produced for each map in the identification of individual significant emission. These *labelmask* maps give information on which particular position in a map contains emission, and if it does, it associates that position to a single source from the catalog produced for that map. Our approach was taking the position of maximum intensity from the 350  $\mu\text{m}$  sources and associating it with a single BGPS source in the V2.1 *labelmask* maps.

For the 104 SHARC-II maps that contain a BGPS source, there are 1374 high-resolution sources. Only 24 (2%) of those sources have their peak position not associated to a BGPS V2.1 source from the *labelmask* maps. The association between 350  $\mu\text{m}$  high resolution sources and 1.1 mm sources suffers from the algorithm uncertainties in determination of both the peak flux density position and the area in the *labelmask* assigned to a specific source. We improved the matching of sources considering also the *labelmask* maps of the 350  $\mu\text{m}$  emission, overlapping both masks and estimating how much of the substructure mask area is associated with the parental source in the BGPS *labelmask* area. Two of the 24 sources have most of their mask area associated to a parental source and therefore are re-considered as matched sources. For the sample 350  $\mu\text{m}$  sources with a match, there are 17 sources

with their mask area shared between two parent sources, and for them we made a visual inspection to see the most likely correct parental association. Figure 2.11 shows a couple of examples for association between 350  $\mu\text{m}$  and 1.1 mm *labelmask* regions.

We obtained a total of 1352 high-resolution sources associated with 349 different parental sources. The results of the previously described spatial matching of 350  $\mu\text{m}$  SHARC-II and 1.1 mm BGPS sources are shown in Figure 2.12. Half of the parental clumps have only one or two associated high-resolution sources, but toward several of the parental clumps we found a large multiplicity of sources, indicating possible fragmentation. The clumps with the largest multiplicity are:

- BGPSv2\_G213.705-12.603 (34 substructures)
- BGPSv2\_G034.256+00.154 (27)
- BGPSv2\_G133.716+01.220 (25)
- BGPSv2\_G000.014-00.017 (23)
- BGPSv2\_G029.916-00.045 (22)
- BGPSv2\_G081.477+00.020 (20)
- BGPSv2\_G029.958-00.017 (19)

There are 22 parental millimeter sources with more than 10 substructures, concentrating a total of 350 high-resolution sources (26% of the total).

These parental sources show some clear strong compact sources in them, but also some elongated, filamentary structures are present. We explored whether the large number of substructures in parental sources is due to spurious low brightness sources, and/or algorithm fragmentation of large sources on the de-blending process. We consider the peak signal-to-noise ratio identified for each source by *Bolocat*, and compare different ranges. Table 2.4 presents the number of substructures with amplitude  $P_{amp}$  (described in section 2.4.2) above  $6\sigma_{rms}$ ,  $10\sigma_{rms}$  and  $20\sigma_{rms}$  for the 22 BGPS sources with large multiplicity. For these, 66% of 350  $\mu\text{m}$  sources have  $P_{amp}$  of  $6\sigma_{rms}$ , 42% of  $10\sigma_{rms}$ , and 19% of  $20\sigma_{rms}$ . Figure 2.11 shows two examples of the distribution at different peak signal-to-noise levels for two of these parental sources. While compact, strong sources have  $P_{amp}$  above  $10\sigma_{rms}$ , detections below this limit recover not only isolated low emission objects, but also filament-like features in chains of sources, and weak detections produced in the de-blending process of the algorithm. We conclude then that sources with  $P_{amp}$  above  $10\sigma_{rms}$  (“compact substructure”) are more related with possible dense core-like structures in the interior of millimeter clumps, and sources below this limit (“faint substructure”) trace a more diffuse medium in addition to weak sources. For the total number of high-resolution sources recovered from the SHARC-II maps, only 437 ( $\sim 32\%$ ) are considered compact substructures. Column 14 in Table 2.3 indicates if a source recovered in the 350  $\mu\text{m}$  maps is “compact” or “faint”.

#### 2.4.6 Flux densities of BGPS sources at 350 $\mu\text{m}$

We determined the flux densities at 350  $\mu\text{m}$  of BGPS V2.1 sources by measuring the flux density in an aperture of  $40''$  on our sample of SHARC-II maps. To match the  $33''$  FWHM effective BGPS beam at 1.1 mm, the 350  $\mu\text{m}$  images, ( $1.618''$  per pixel) were convolved with gaussian kernels (using IRAF task GAUSS) having  $\sigma = 13.5''$  (8.33 pixels).

From the total of 619 V2.1 sources in the 350  $\mu\text{m}$  maps, there are 82 sources that appear in more than one map; we preferred the flux determination on the maps where those sources suffer fewer sampling artifacts, such as high noise due to map edge proximity, or negative bowls around the source. In case that there are not evident problems in the source flux estimation, we just considered the averaged result of the flux density. In addition, there are 45 sources with negative integrated fluxes due to proximity to noisy edges or negative bowls surrounding areas of strong emission, and therefore these sources are not considered as reliable measurements.

Results of the estimated values of 350  $\mu\text{m}$  continuum emission from BGPS sources are presented in Table 2.5. Column 1 gives the name of the source in the V2.1 catalog. Column 2 gives the flux density integrated in an aperture of  $40''$  centered on the peak position of the 1.1 mm source. The values of the flux density are corrected by the factor 1.46 suggested by Aguirre et al. (2011) for the  $40''$  aperture flux obtained in BGPS catalog. Column 3 gives the integrated flux density for aperture photometry in the same previous position, but this time in the 350  $\mu\text{m}$  convolved maps.

### 2.4.7 Comparison between SHARC-II and *Herschel* images

From Molinari et al. (2010), we used the Hi-GAL  $2^\circ \times 2^\circ$  images at  $350 \mu\text{m}$  obtained during science verification phase centered toward  $l = 30^\circ$ ,  $b = 0^\circ$  and compared the results of flux recovery between the *Herschel*/SPIRE image and the 10 SHARC-II maps contained in that area. The *Herschel* image has a FWHM beam resolution of  $24.9''$ , and details in the reduction process are found in detail in Traficante et al. (2011). Figure C.1 in the Appendix shows 1.1 mm BGPS images, and their corresponding Hi-GAL images at  $350 \mu\text{m}$  toward  $l = 30^\circ$ ,  $b = 0^\circ$ , for regions mapped with SHARC-II. While the 1.1 mm images in this figure show the position of the sources from the BGPS V2.1 catalog, the  $350 \mu\text{m}$  images show in blue ( $< 10\sigma$ ) or red ( $> 10\sigma$ ) the objects identified in our high-resolution sources catalog. There are 213 of these substructures found, with only one left out of the following analysis due to noisy edge effects. First, we compared the flux obtained on the sources recovered directly by *Bolocatt* in this set of SHARC-II images, and emission measured in the *Herschel* map. Figure 2.13 shows the ratio between the density flux at  $40''$  aperture  $F_{SHARC}$  and the recovered flux at the same aperture, centered on the peak position of the high-resolution sources, obtained from the *Herschel* image,  $F_{Herschel}$ . For faint substructures, the flux ratio is in general below 0.3, with a cut around  $F_{Herschel} \sim 100 \text{ Jy}$ , which suggests that the *Herschel* image is recovering additional flux from diffuse, large scale emission that SHARC-II maps do not recover. Uniform background emission ranging between  $2700 - 3300 \text{ MJy ster}^{-1}$  in the *Herschel* image would give a flux density into a  $40''$  aperture of  $80 - 100 \text{ Jy}$ . Figure 2.14 shows one of the SHARC-II maps toward  $l = 30^\circ$ , L029.95-0.05, and the *Herschel* emission



in the same region. This figure also presents the SHARC-II map convolved to a resolution of  $24.9''$ , to match the beam size of Hi-GAL data at the same wavelength. The emission level at  $17\sigma$  in the *Herschel* corresponds to  $\sim 2790$  MJy  $\text{ster}^{-1}$ , and it would set then the limit for the  $3\sigma$  detection level in the SHARC-II images. A “background emission” level for the SHARC-II maps would lie at about 2460 MJy  $\text{ster}^{-1}$ , corresponding to the  $15\sigma$  level (white contour in Fig. 2.14), and a  $40''$  aperture integrated flux density of  $\sim 73$  Jy. The beam-matched SHARC-II image shows that the  $1\sigma$  emission level has a good resemblance with that background emission level.

Inspecting Figure C.1, most of the faint substructures do not look like well-defined entities at a  $10\sigma$  contour, but instead they seem to be immersed in background extended emission. For the compact substructures recovered in the SHARC-II maps, the average and median values for the flux ratio are  $0.56 \pm 0.03$  and  $0.53$ , respectively. For those high-emission compact sources with peak signal-to-noise above 50, represented by green points in Figure 2.13, flux recovery in the SHARC-II maps and the *Herschel* map are nearly the same (average flux ratio of  $1.00 \pm 0.11$ ).

We performed a similar analysis for the 102 BGPS sources found in this region. We first convolved the  $350 \mu\text{m}$  *Herschel* image to match the  $33''$  resolution of Bolocam, and compare later the  $40''$  aperture flux emission obtained toward the peak position of BGPS sources. Results are shown in Figure 2.15. Errors in the flux ratio consider conservative uncertainties of 20% in the flux from the *Herschel* image, and 30% in fluxes from SHARC-II data. Sources without any substructure associated have low mm emission and flux ratio  $F_{SHARC}/F_{Herschel}$  on average lower than 0.1. For those 1.1 mm parental clumps associated with compact substructures (shown in

red in the figure), the average and median values of the flux ratio are  $0.76 \pm 0.08$  and 0.69, respectively.

## 2.5 Analysis

### 2.5.1 Temperature determination

The data at 350  $\mu\text{m}$  and 1.1 mm can be used to define a color temperature. We will refer to this quantity through this analysis as the “dust temperature”, although variations in temperature across and along the line of sight make this color temperature only a rough guide to the actual dust temperatures.

The observed intensity of continuum emission is given by  $S_\nu = \Omega_{beam}[1 - e^{-\tau_{\nu d}}]B_\nu(T_d)$ , where  $\Omega_{beam}$  is the beam solid angle (33'' beam) for both the 1.1 mm data and the convolved, beam matched, 350  $\mu\text{m}$  observations,  $\tau_{\nu d}$  is the optical depth of the emitting dust at each frequency and  $B_\nu(T_d)$  is the Planck function at the dust temperature  $T_d$ . The optical depth in the submm to mm regime is considered proportional to  $\nu^\beta$ . In the optically thin limit, the temperature can be estimated according to:

$$R = \frac{S_{350\mu\text{m}}}{S_{1.1\text{mm}}} = \frac{\nu_{350\mu\text{m}}^{3+\beta} [\exp(h\nu_{1.1\text{mm}}/kT_d) - 1]}{\nu_{1.1\text{mm}}^{3+\beta} [\exp(h\nu_{350\mu\text{m}}/kT_d) - 1]} . \quad (2.1)$$

$S_{350\mu\text{m}}$  and  $S_{1.1\text{mm}}$  are the integrated flux densities obtained in 40'' apertures in the convolved SHARC-II maps and in the BGPS maps, respectively. The distribution of the ratio  $S_{350\mu\text{m}}/S_{1.1\text{mm}}$  for the 574 V2.1 sources with reliable flux values is shown in Figure 2.16. The ratio distribution has a maximum of 181.0, with a median value

of 19.7.

Equation 2.1 cannot be solved analytically for  $T_d$ . The adjustment of the pair of parameters  $T_d$  and  $\beta$  has been a recurrent issue in the study of the interstellar medium and star formation. Frequently, a value of  $\beta \sim 2$  in the millimeter to submillimeter regime is assumed, referring to studies of dust grains composed by graphite and silicate (Draine & Lee, 1984), but models with variations of ice mantles due to coagulation give lower values (e.g., Ossenkopf & Henning, 1994, estimated  $\beta = 1.75$  for their OH5 model). Values near  $\beta \sim 1$  may be appropriate for circumstellar disks (e.g., Beckwith & Sargent, 1991). Shirley et al. (2005) summarize different opacity models in the submillimeter-millimeter regime for low-mass pre-protostellar cores, with values of  $\beta$  between 1.3 and 2.3. For the present analysis, we obtained dust temperatures considering three different values of  $\beta$ : 1.0, 1.7, and 2.0. Nevertheless, considering that most BGPS sources properties are related with dust clumps of dense material,  $\beta = 1.7$  should be the closest model of the true nature of these structures. Figure 2.17 shows the fitted values for temperatures as a function of the ratio  $S_{350\mu m} / S_{1.1mm}$  for the three models previously described. For  $\beta = 1.7$ , uncertainties in the determination of temperatures are shown in the figure, considering an error of the flux ratio of 10%.

The large uncertainty for high temperatures is unavoidable with these data. At high temperatures, both 1.1 mm and 350  $\mu$ m flux densities approach the Rayleigh-Jeans limit, and therefore the ratio becomes nearly constant, increasing significantly the uncertainty in the determination of  $T_d$ .

The computed temperatures using three different values of  $\beta$  are presented

in Table 2.5. Columns 4 and 5 gives the source color temperature determined from equation 2.1, using a emissivity index  $\beta = 1.0$ , and the upper and lower limit for that temperature. Values of temperatures and upper and lower limits for a spectral index of  $\beta = 1.7$  and  $\beta = 2.0$  are given in Columns 6-7 and 8-9, respectively.

From equation 2.1, sources with flux ratio  $S_{350\mu m} / S_{1.1 mm}$  below 70.2 have temperatures lower than 1000 K for  $\beta = 1.7$ . Only 32 V2.1 sources ( $\sim 6\%$  of sample) have estimated temperatures above 1000 K, most of them (24) found toward the Galactic Center region. In only one source, the large flux ratio is the consequence of low emission at 1.1 mm and comparable noise level, and almost half of the rest have  $S_{1.1 mm} > 1$  Jy, which included well-known regions such as G034.256+00.154, G029.958-00.017, G030.702-00.067, and the ‘‘Brick’’ IRDC (Longmore et al., 2012). These very high temperatures reflect flux density ratios near those expected in the Rayleigh-Jeans limit, and the temperatures are not constrained by our data. A centrally heated region will produce strong 350  $\mu m$  emission; using a ratio with the 1.1 mm emission, which traces a larger region of cold dust, can produce an artificially high color temperature.

At a limiting temperature of 50 K, the corresponding flux ratio is 52.7 for  $\beta = 1.7$ , and a variation of 10% of this ratio will give an increase of 40% in the estimated temperature. Therefore, to avoid large uncertainties we consider as a ‘‘good fit’’ a determined temperature less or equal than 50 K, and a similar limiting temperature value is found for  $\beta = 1.0$  and  $\beta = 2.0$ . There are 512 sources in our sample below this limit for  $\beta = 1.7$ , and 30 sources with temperatures between 50 and 290 K with quite large uncertainties.

Figure 2.18 shows the temperature distribution for the 512 sources, assuming  $\beta = 1.7$ , with good fits for temperature. The median value is 13.3 K, with an average of  $16.3 \pm 0.4$  K. The difference between the median and the average is explained by the positive skewness of the distribution. The figure also shows the distribution of sources with different models for the spectral index. Considering a value of  $\beta = 1.0$ , the sample of V2.1 sources tends to have larger values of temperature, and then the number of these sources with  $T_d \leq 50$  K is 322, with a median value of 17.3 K and an average of  $19.6 \pm 0.5$  K. For  $\beta = 2.0$ , the distribution of fitted temperatures has lower values, with 535 sources below 50 K, and with median and average temperatures of 11.2 K and  $13.3 \pm 0.3$  K, respectively.

Figure 2.19 plots temperature versus flux density at 1.1 mm for a fixed value  $\beta = 1.7$ . For faint mm sources, uncertainties in the flux dominate the uncertainties in the temperature. In contrast, temperatures above 30-40 K are uncertain because of the weak constraints as the Rayleigh-Jeans limit is approached. The figure also shows the presence of 28 sources with high flux density ( $> 1$  Jy at 1 mm) and low estimated temperatures ( $< 15$  K). These sources could be dense, prestellar clumps, but further observations and analysis, particularly in molecular line observations of high-density tracers, are necessary to test their nature.

### 2.5.2 Comparison of temperatures with other surveys

In this section we compare our results on temperature estimation with other surveys of high-mass star forming regions. Faúndez et al. (2004) performed an analysis of physical properties of 146 continuum emission structures detected at 1.2 mm

with SIMBA toward IRAS sources associated with CS(2–1) detections. The temperature and spectral index of these sources were obtained from SED fitting using additional IRAS four band fluxes, obtaining values for  $\beta$  ranging between 1.5 and 2.5, with average temperature for their sample of  $\sim 32$  K. Although temperatures found for their millimeter structures are larger than ours, their selection of sources is biased toward strong emission at 1.2 mm, with all their sources (except one) above 1 Jy and with an average flux density of  $16.3 \pm 3.2$  Jy. Considering the emission at 1.1 mm from our sources that are, within uncertainties and corrections, comparable with their sample, the average temperature for the 124 V2.1 sources with  $40''$  aperture flux at 1.1 mm above 1 Jy is  $\sim 38$  K for  $\beta = 1.7$ . Similarly, Mueller et al. (2002) modeled SEDs of a group of 51 massive star forming clumps, originally selected by having water masers, and found that a temperature of  $29 \pm 9$  K best characterized the sources. Cross-matching their sample with BGPS sources inside SHARC-II maps, considering one beam ( $33''$ ) in distance associations between samples, we found 13 BGPS clumps with good determination of dust temperature associated with the sources in Mueller et al. (2002). These sources have average and median values for their  $40''$  aperture integrated flux of 8.5 Jy and 7 Jy, respectively, with only one source with integrated flux below 1 Jy. The fitted dust temperatures of these sources have an average of 30 K, and a median of 31 K. Thus, the parameters that we found in sources with strong ( $>1$  Jy) integrated emission at 1.1 mm are similar to those found with SED fitting, giving some confidence to our values based on only two wavelengths. In addition, BGPS clumps associated with massive star forming regions generally have strong emission at mm and submm wavelengths, with warm temperatures  $\sim 30$  K, lying

above 89% of the distribution of fitted temperatures of BGPS sources with  $T \leq 50$  K.

Battersby et al. (2011) used Hi-GAL 70 to 500  $\mu\text{m}$  data to identify significant dust continuum emission in two  $2^\circ \times 2^\circ$  regions centered at  $l = 30^\circ$  and  $l = 59^\circ$ , and obtaining temperature and column density maps for them by fitting spectral energy distributions for each pixel. While the temperature is a free parameter for their fitting model, the spectral index is fitted to 1.75 following Ossenkopf & Henning (1994). From our sample, we have 92 BGPS V2.1 sources with determined temperatures in the  $l = 30^\circ$  map, and none in the  $l = 59^\circ$  map. Considering  $T_{SHARC}$  the fitted temperature obtained from equation 2.1, the median and average temperature for those sources from our analysis is 18 K and  $34 \pm 4$  K for  $\beta = 1.7$ . We estimated a value of the temperature of these sources from the maps presented by Battersby et al.,  $T_{Herschel}$ , averaging the temperature values of each pixel on an aperture of  $40''$  centered on the peak position of each source. Figure 2.20 shows the ratio  $T_{SHARC} / T_{Herschel}$  as a function of the flux density at 1.1 mm for the sample of BGPS sources. The average ratio from this figure, without considering those sources with  $T_{SHARC} > 50$  K for which the uncertainties are much larger, is  $0.83 \pm 0.05$ , while the weighted mean is  $0.50 \pm 0.01$ .

### 2.5.3 Comparison between gas temperature from $\text{NH}_3$ and color temperature

Figure 2.21 shows the ratio of gas to dust temperatures. The gas temperatures were determined from  $\text{NH}_3$  observations (Dunham et al., 2010; Wienen et al., 2012, and BGPS team in prep.). For those observations not centered on peak positions of

BGPS sources, we associated the  $\text{NH}_3$  detections to their closest BGPS source within one beam distance. Only the 49 clumps with dust temperatures below 50 K and gas temperatures below 30 K are plotted. The ratio  $T_{gas}/T_{dust}$  has a weighted average of 0.88 and a median of 0.76. There are few sources with equal temperatures, but instead a group with lower  $T_{gas}$  and a group with higher  $T_{gas}$ .

#### 2.5.4 Comparison with tracers of dense gas

Schlingman et al. (2011) presented spectroscopic observations of  $\text{HCO}^+$  and  $\text{N}_2\text{H}^+$  (3-2) for 1882 sources from BGPS. The selection of sources was made between galactic longitudes  $10^\circ \leq l \leq 100^\circ$ , considering all sources with integrated flux in a  $40''$  aperture greater than  $S_{1.1mm} \sim 0.4$  Jy, and from bins of logarithmically spaced flux of 0.1 for sources with  $S_{1.1mm} = 0.1 - 0.4$  Jy. A new, complete version of this catalog by Shirley et al. (2013) includes all 6194 sources in the BGPS V1.0 catalog between  $7.5^\circ \leq l \leq 194^\circ$  of this pair of molecular transitions. After considering a one-to-one match between sources from V1.0 and V2.1 catalogs, with a spatial matching of one beam of distance ( $33''$ ), we checked which of those sources are present in our sample of SHARC-II maps. There are 300 V2.1 sources with spectroscopy data, 250 of them with  $\text{HCO}^+$  detections and estimated dust temperatures from our analysis, and 199 with  $\text{N}_2\text{H}^+$  detections with dust temperatures. Figure 2.22 shows the peak main beam temperature versus our fitted temperature for that group of sources. The points scatter widely about the plot. Considering only the sources with dust temperatures less than 50 K (169 for  $\text{N}_2\text{H}^+$  and 223 for  $\text{HCO}^+$ ), the Spearman's rank correlation coefficient of the distributions of  $\log(T_{mb}^{pk})$



and  $\log(T_{dust})$  are 0.51 for sources with  $N_2H^+$  detections, and 0.33 for sources with  $HCO^+$  detections. We tested the null hypothesis of no significant correlation between  $\log(T_{mb}^{pk})$  and  $\log(T_{dust})$  for these distributions. For a sample size  $n$ , the Student's  $t$  value for the Pearson correlation coefficient  $r(n)$  is estimated from  $t = r/s_r$ , with  $s_r = \sqrt{(1 - r^2)/(n - 2)}$ . For a two-tailed probability value  $p = 0.05$ , our sample requires  $t = 2$ , corresponding to  $r(169) = 0.151$  and  $r(223) = 0.131$ . The estimated values for the correlation coefficients of our sample are  $r = 0.508$  and  $r = 0.332$  for  $N_2H^+$  and  $HCO^+$ , respectively, rejecting the null hypothesis at a 95% confidence. Therefore, although the correlation is weak, in both cases it is statistically significant for the detected peak main beam temperature and the fitted dust temperature. In the case of  $N_2H^+$ , the correlation can be fitted as  $\log(T_{mb}^{pk}) = B \times \log(T_d) + A$ , with fitted values  $A = -1.55$  and  $B = 1.04 \pm 0.13$ . For  $HCO^+$ , the fitted parameters are  $A = -0.59$  and  $B = 0.52 \pm 0.08$ .

Shirley et al. suggested that BGPS sources with a higher  $N_2H^+/HCO^+$  ratio could be clumps with dense core-like structures in them, as a consequence of cold, CO-depleted gas within those cores. Nevertheless, we did not find a clear correlation between the ratio of high density tracers  $N_2H^+/HCO^+$ , and number of substructures or estimated dust temperature in our source sample. Parental clumps with large multiplicity of substructures and high  $N_2H^+/HCO^+$  ratios do represent good candidates for future interferometric observations to study core properties in regions of clustered massive-star formation.

### 2.5.5 Mass and surface density of substructures

We use the following equation to calculate the mass:

$$M_d = \frac{S_\nu D^2}{k_\nu B_\nu(T_d)}, \quad (2.2)$$

where  $S_\nu$  is the flux density,  $D$  is the distance to the source, and  $k_\nu$  is the dust mass opacity coefficient.

We use a dust opacity of  $1.14 \text{ cm}^2 \text{ g}^{-1}$  of dust at 1.1 mm (Ossenkopf & Henning, 1994) for a model with thin ice mantles (OH5). Assuming a dust-to-gas mass ratio of  $R = M_d/M_g = 0.01$ , the mass of gas and dust will be given by:

$$\begin{aligned} M_{1.1mm} &= 14.26 \left( \frac{S_\nu}{Jy} \right) \left( \frac{1.14 \text{ cm}^2 \text{ g}^{-1}}{\kappa_{1.1mm}} \right) \left( \frac{D}{\text{kpc}} \right)^2 \\ &\times \left\{ \exp \left( \frac{13.01}{T_d} \right) - 1 \right\} M_\odot. \end{aligned} \quad (2.3)$$

From our sample of 512 BGPS sources with temperatures  $\leq 50$  K, we can give some estimations of how the values of masses will change when a fixed temperature is used. The average ratio between the clump mass  $M(T_d)$ , with  $T_d$  the fitted dust temperature from continuum observations between 350  $\mu\text{m}$  and 1.1 mm, and the mass estimated at a fixed temperature,  $M(T_{fix})$ , is obtained from:

$$\left\langle \frac{M(T_d)}{M(T_{fix})} \right\rangle = \left\langle \frac{\exp(13.01/T_d) - 1}{\exp(13.01/T_{fix}) - 1} \right\rangle. \quad (2.4)$$

Figure 2.23 shows the results of the above equation for different values of  $T_{fix}$ . It is common to use for simplicity a fixed value of 20 K in determination of masses from millimeter surveys of Galactic star forming regions (e.g. Motte et al., 2007; Schlingman et al., 2011; Urquhart et al., 2013). Using  $T_{fix} = 20$  K, the average value of the ratio is  $2.43 \pm 0.11$ , with a median value of 1.83. Therefore, assuming a fiducial value for the temperature of 20 K for our sample of clumps, the estimation of masses would be underestimated on average, with respect to the mass obtained from our analysis of color temperatures.

Until distances are known, we cannot calculate masses for the entire sample, but we can estimate the contribution of masses from substructures detected at 350  $\mu\text{m}$  with respect to the parental clump, because both substructures and clump are located at the same distance. We use the flux density at 350  $\mu\text{m}$  to compute masses of the substructures. Similarly to equation 2.3, but with appropriate change in the exponential and with a dust opacity of  $11 \text{ cm}^2 \text{ g}^{-1}$  (OH5), the mass measured at 350  $\mu\text{m}$  is as follows:

$$M_{350\mu\text{m}} = 0.053 \left( \frac{S_\nu}{Jy} \right) \left( \frac{11 \text{ cm}^2 \text{ g}^{-1}}{\kappa_{350\mu\text{m}}} \right) \left( \frac{D}{\text{kpc}} \right)^2 \times \left\{ \exp \left( \frac{41.14}{T_d} \right) - 1 \right\} M_\odot \quad (2.5)$$

From our sample of 349 BGPS parental clumps associated with 1352 high-resolution sources, the fraction of the total mass estimated for structures at 350  $\mu\text{m}$

with respect to the mass of the parental 1.1 mm clump is determined by:

$$\frac{\Sigma(M_{substructures})}{M_{clump}} = 3.75 \times 10^{-3} \left( \frac{S_{350\mu m}^*}{S_{1.1mm}^*} \right) \times \left( \frac{\exp(41.14/T_d) - 1}{\exp(13.01/T_d) - 1} \right), \quad (2.6)$$

where  $S_{1.1mm}^*$  is the emission of the parental BGPS clump,  $S_{350\mu m}^*$  represent the total emission of substructures inside that clump, and  $T_d$  is the dust temperature fitted from equation 2.1. Here we consider the integrated emission recovered by *Bolocat* for each clump, which estimates the total flux for the area delimited by the *labelmask* region (see Section 2.4.5). In that way, the contribution of each substructure will be associated with a single parental clump, with both considered at the same dust temperature.

Figure 2.24 shows the ratio between masses obtained for high-resolution sources at 350  $\mu m$  and their parental BGPS clump, as a function of the dust temperature and as a function of the integrated flux at 1.1 mm. Black points represent the mass ratio considering the flux contribution of all high-resolution sources, and red points only consider emission from strong, compact sources. The average and median values for the mass ratio  $\Sigma(M_{substructures})/M_{clump}$  when all substructures are considered, are 0.48 and 0.40, respectively, with a weighted mean of  $0.22 \pm 0.01$ . When only compact substructures (see §4.5) are considered, the average and median of the distribution are 0.39 and 0.37, respectively, with a weighted mean of  $0.19 \pm 0.01$ . These results for the mass fraction are larger than the results from Ragan et al. (2013), who fit SEDs and obtained a value of  $\sim 14\%$  for the mass contribution of core-like features observed at a resolution of  $7.8''$  compared to the total mass of their harboring IRDCs.

Possible explanations of this difference are our larger sample of sources (Ragan et al. consider 11 IRDCs, harboring a total of 83 substructures), and also that our sample of clumps has a broader range of evolutionary stages, not necessarily limited to the coldest, initial stages of massive star formation, represented by the IRDC phase.

Considering a uniform temperature will also introduce errors in the mass determination. The parental molecular clump will be affected by both embedded stars and the external radiation field, and it is likely that substructures will have a different temperature from their surrounding medium. In addition, SHARC-II and Bolocam are sensitive to different spatial scale emission (see Section 2.4.3), and therefore the recovered flux at 1.1 mm could include faint, extended background emission not detected in 350  $\mu\text{m}$  continuum emission. A better analysis of the mass ratio between parental clumps and their internal structures (compact, core-type sources, and faint, filamentary emission) will require modeling these sources using radiative transfer codes.

Figure 2.25 shows the surface density  $\Sigma_{350\mu\text{m}}$  estimated for the substructures found in the 350  $\mu\text{m}$  maps, as a function of the surface density of their parental clump,  $\Sigma_{1.1\text{mm}}$ . We considered the deconvolved radius of resolved substructures at 8.5'', and resolved clumps at 33''. Identified substructures have in general larger surface densities than their parental BGPS source. For the sample of spatially resolved sources, there are 418 compact substructures, with 286 of them with estimated temperatures  $T_d \leq 50$  K. These are represented by red circles in the figure. A linear fit of the compact sources indicate that they have  $\Sigma_{350\mu\text{m}} \sim 2.2 \times \Sigma_{1.1\text{mm}}$ . Eighteen of them (6%) have  $\Sigma_{350\mu\text{m}} \geq 1.0 \text{ g cm}^{-2}$ , a theoretically predicted threshold for the

formation of massive stars Krumholz & McKee (2008). More recently a lower value of  $0.2 \text{ g cm}^{-2}$  was proposed by Butler & Tan (2012) as the initial condition of massive star formation in the Galaxy; 88 (31%) of our sources meet that criterion.

Thus, for our sample of high-resolution structures observed at  $350 \mu\text{m}$ , there are probably many dense cores, whose physical parameters suggest on-going or imminent formation of massive stars.

## 2.6 Summary and Conclusions

We presented a set of 107 SHARC-II  $350 \mu\text{m}$  maps toward star forming clumps from the BGPS V2.1 catalog. The maps have a resolution of  $8.5''$ , improving upon the resolution of the BGPS maps at  $1.1 \text{ mm}$  ( $33''$ ) and revealing a population of substructures.

We used *Bolocatt* to identify significant emission on the SHARC-II maps, and we obtained a catalog of 1386 high-resolution sources, with average fluxes of  $23.15 \pm 1.59 \text{ Jy}$  and average size of  $15''$ . We found that  $\sim 32\%$  of these features have peak emission above  $10\sigma_{rms}$ , and we consider these “compact substructures” as core-like sources immersed in parental clumps. Below this limit, recovered sources are called “faint substructures”, and they are related with fragmentation of filamentary features, isolated low intensity sources, and residuals from the source extraction algorithm.

We found 619 BGPS V2.1 sources in our set of  $350 \mu\text{m}$  maps, for which only 56% of those are associated to 1352 high-resolution substructures. While most of the

parental clumps have only one or two associated substructures, we found significant multiplicity in some of them, with 22 clumps having more than 10 substructures in them.

We compared the 350  $\mu\text{m}$  continuum emission from SHARC-II maps with *Herschel* images from the Hi-GAL survey toward the  $l = 30^\circ$  region at same wavelengths. Strong emission detected in SHARC-II maps is in general in good agreement with the *Herschel* fluxes, but faint sources from the SHARC-II maps are immersed in background emission.

We estimated temperatures for different models of the spectral index. For the 512 sources with “good fits” in the determination of temperatures ( $T_d \leq 50$  K), the median and average values of their temperatures are 13.3 K and  $16.3 \pm 0.4$  K, respectively, in reasonable agreement with other temperature determination methods based on SED analysis.

Comparison to gas temperatures derived from  $\text{NH}_3$  observations reveals sources with ratios of  $T_{gas}/T_{dust}$  both larger and smaller than unity, but with mean value of 0.88.

Sources with  $\text{N}_2\text{H}^+$  and  $\text{HCO}^+$  detections present weak correlations between their observed peak main beam temperature and their fitted dust temperature. There is no clear correlation between the ratio  $T_{mb}^{pk}(\text{N}_2\text{H}^+)/T_{mb}^{pk}(\text{HCO}^+)$  and the number of substructures found on parental clumps.

The fraction of the mass contained in substructures compared with the total parental clump mass has an average of 0.48, but this value decreases to 0.22 when

weighted by uncertainties. Considering only the compact structures, likely to be core sources, the mass fraction between substructures and parental clumps is 0.19, higher than other studies of high angular resolution at  $350 \mu\text{m}$ .

Small, but significant fractions of substructures satisfy theoretical thresholds for massive star formation of 0.2 (31%) or  $1.0 \text{ g cm}^{-2}$  (6%).



Table 2.1. Average calibration factors of SHARC-II maps

Date	$C_{beam}$ (Jy beam <sup>-1</sup> $\mu V^{-1}$ )	$C_{20}$ (Jy $\mu V^{-1}$ )	$C_{40}$ (Jy $\mu V^{-1}$ )	$C_{40}^{33''}$ (Jy $\mu V^{-1}$ )
2006 Jun	9.84±0.68	0.35±0.03	0.28±0.02	0.42±0.03
2007 Jul	7.01±0.21	0.23±0.01	0.20±0.01	0.29±0.01
2007 Oct	8.08±0.32	0.27±0.01	0.23±0.01	0.34±0.01
2009 Sep	6.05±0.25	0.21±0.02	0.17±0.01	0.26±0.02
2009 Dec	5.89±0.11	0.22±0.01	0.17±0.01	0.25±0.01
2010 Jul <sup>a</sup>	7.31±0.25	0.24±0.01	0.20±0.01	0.30±0.01
2010 Jul 24	17.83±2.50	0.67±0.06	0.51±0.06	0.77±0.09
2010 Dec	6.69±0.16	0.23±0.01	0.19±0.01	0.28±0.01
2011 Dec	10.82±0.39	0.38±0.01	0.31±0.01	0.46±0.02
2012 Sep	15.59±0.85	0.52±0.03	0.43±0.02	0.65±0.04

<sup>a</sup>Does not include calibration from July 24, 2010.

Table 2.2. Observing information of 350  $\mu\text{m}$  continuum maps

Map	Config. <sup>a</sup>	Size	Map Center		Obs. Date	1 $\sigma$ Noise (mJy beam <sup>-1</sup> )
			R.A. (J2000)	Dec. (J2000)		
L359.85+0.00	A	10' $\times$ 10'	17:45:15.356	-29:03:48.64	2006Jun	994
L000.00+0.00	A	10' $\times$ 10'	17:45:38.222	-28:56:15.83	2006Jun	1453
L000.15+0.00	A	10' $\times$ 10'	17:45:59.055	-28:48:38.10	2006Jun	1438
L000.30+0.00	A	10' $\times$ 10'	17:46:20.056	-28:40:51.99	2006Jun	1086
L029.95-0.05	A	10' $\times$ 10'	18:46:10.078	-02:40:45.19	2006Jun	514
L030.00+0.00	A	10' $\times$ 10'	18:46:05.764	-02:36:40.25	2006Jun	462
L030.15+0.00	A	10' $\times$ 10'	18:46:21.926	-02:28:41.39	2006Jun	426
L030.30+0.00	A	10' $\times$ 10'	18:46:38.373	-02:20:39.29	2006Jun	496
L030.45+0.00	A	10' $\times$ 10'	18:46:54.711	-02:12:38.81	2006Jun	603
L030.60+0.00	A	10' $\times$ 10'	18:47:11.158	-02:04:35.09	2006Jun	888
L030.70-0.07	A	10' $\times$ 10'	18:47:36.576	-02:01:32.42	2006Jun	510
L030.80-0.05	A	10' $\times$ 10'	18:47:43.784	-01:55:09.17	2006Jun	529
L030.88+0.13	A	10' $\times$ 10'	18:47:13.872	-01:45:57.32	2006Jun	367
L034.26+0.15	A	10' $\times$ 10'	18:53:19.759	+01:14:36.57	2006Jun	395
L076.16+0.09	A	10' $\times$ 10'	20:23:52.185	+37:36:41.20	2006Jun	249
L077.93+0.02	A	10' $\times$ 10'	20:29:23.675	+39:00:58.88	2006Jun	389
L078.14-0.32	A	10' $\times$ 10'	20:31:26.817	+38:58:53.21	2006Jun	408
L078.96+0.37	A	10' $\times$ 10'	20:31:03.924	+40:02:54.24	2006Jun	445
L079.28+0.30	A	10' $\times$ 10'	20:32:20.042	+40:15:45.21	2006Jun	558
L080.92-0.11	A	10' $\times$ 10'	20:39:16.364	+41:19:41.83	2006Jun	724
L081.45+0.04	A	10' $\times$ 10'	20:40:23.200	+41:50:33.25	2006Jun	274
L081.68+0.54	A	10' $\times$ 10'	20:39:01.659	+42:19:37.11	2006Jun	802
L082.55+0.14	A	10' $\times$ 10'	20:43:35.922	+42:46:07.20	2006Jun	255
L075.76+0.41	A	10' $\times$ 10'	20:21:24.076	+37:27:55.95	2007Jul	652
L076.12-0.24	B	6' $\times$ 6'	20:25:07.547	+37:23:14.34	2007Jul	388
L076.35-0.58	B	6' $\times$ 6'	20:27:10.982	+37:22:29.34	2007Jul	430
L078.92-0.19	A	10' $\times$ 10'	20:33:18.191	+39:41:24.34	2007Jul	689
L078.17-0.31	A	10' $\times$ 10'	20:31:29.785	+39:00:20.75	2007Jul	800
L079.62+0.49	A	10' $\times$ 10'	20:32:36.698	+40:39:16.34	2007Jul	1489
L079.11-0.35	A	10' $\times$ 10'	20:34:33.491	+39:44:46.95	2007Jul	1226
L080.86+0.38	A	10' $\times$ 10'	20:37:00.649	+41:34:35.34	2007Jul	1874
L110.11+0.05	C	4' $\times$ 4'	23:05:11.371	+60:14:41.67	2007Oct	288
L111.62+0.38	C	4' $\times$ 4'	23:15:32.196	+61:07:30.77	2007Oct	342
L134.28+0.86	C	4' $\times$ 4'	02:29:02.834	+61:33:28.83	2007Oct	275
L134.83+1.31	C	4' $\times$ 4'	02:34:45.364	+61:46:15.77	2007Oct	296
L136.38+2.27	C	4' $\times$ 4'	02:50:08.515	+61:59:54.27	2007Oct	257
L136.83+1.07	C	4' $\times$ 4'	02:49:04.352	+60:43:23.95	2007Oct	250
L111.28-0.66	A	10' $\times$ 10'	23:16:04.681	+60:02:06.00	2009Sep-2009Dec	286
L111.54+0.78	A	10' $\times$ 10'	23:13:44.302	+61:28:10.18	2009Sep	496
L133.71+1.21	A	10' $\times$ 10'	02:25:41.066	+62:05:42.68	2009Sep-2009Dec	338
L133.95+1.06	A	10' $\times$ 10'	02:27:03.912	+61:52:14.05	2009Sep-2009Dec	338
L111.26-0.77	A	10' $\times$ 10'	23:16:11.144	+59:55:27.74	2009Dec	538
L111.78+0.59	A	10' $\times$ 10'	23:16:13.500	+61:22:51.01	2009Dec	412
L111.79+0.71	D,A	10' $\times$ 10'	23:15:52.220	+61:30:02.26	2009Dec-2012Sep	307
L111.88+0.82	D,A	10' $\times$ 10'	23:16:15.419	+61:37:42.69	2009Dec	473
L136.52+1.24	D	10' $\times$ 10'	02:47:25.531	+61:00:34.20	2009Dec	260
L136.85+1.14	E	3' $\times$ 3'	02:49:28.155	+60:47:02.96	2009Dec	337
L136.95+1.09	D	10' $\times$ 10'	02:50:02.727	+60:41:52.32	2009Dec	475
L137.69+1.46	H	11' $\times$ 11'	02:56:47.527	+60:41:21.90	2009Dec	667

Table 2.2 (cont'd)

Map	Config. <sup>a</sup>	Size	Map Center		Obs. Date	1 $\sigma$ Noise (mJy beam <sup>-1</sup> )
			R.A. (J2000)	Dec. (J2000)		
L138.30+1.56	D,A	10' $\times$ 10'	03:01:34.013	+60:29:10.72	2009Dec-2011Dec -2012Sep	205
L138.48+1.63	D,A	10' $\times$ 10'	03:03:09.052	+60:27:39.61	2009Dec-2011Dec -2012Sep	266
L173.14+2.36	A	10' $\times$ 10'	05:37:57.556	+36:00:18.63	2009Dec	777
L173.17+2.35	G	4' $\times$ 4'	05:37:59.420	+35:58:27.54	2009Dec	320
L173.47+2.43	F	2.5' $\times$ 2.5'	05:39:07.589	+35:46:02.82	2009Dec	487
L173.57+2.44	F	2.5' $\times$ 2.5'	05:39:24.823	+35:40:55.71	2009Dec	421
L173.62+2.81	D	10' $\times$ 10'	05:41:07.430	+35:50:21.17	2009Dec	359
L173.72+2.70	G	4' $\times$ 4'	05:40:52.684	+35:41:45.31	2009Dec	387
L173.76+2.67	G	4' $\times$ 4'	05:40:51.995	+35:38:53.79	2009Dec	301
L188.79+1.03	A	10' $\times$ 10'	06:09:06.309	+21:50:45.79	2009Dec	259
L188.95+0.88	D,A	10' $\times$ 10'	06:08:52.987	+21:38:19.76	2009Dec	268
L189.03+0.78	D,A	10' $\times$ 10'	06:08:39.856	+21:31:11.38	2009Dec	290
L189.12+0.64	A	10' $\times$ 10'	06:08:20.114	+21:22:04.54	2009Dec	403
L189.68+0.19	D,A	10' $\times$ 10'	06:07:47.653	+20:39:28.06	2009Dec	155
L189.85+0.39	I	18' $\times$ 18'	06:08:53.475	+20:36:24.00	2009Dec	505
L190.17+0.74	A	10' $\times$ 10'	06:10:51.620	+20:29:49.63	2009Dec	184
L192.60-0.16	D	10' $\times$ 10'	06:12:28.348	+17:56:17.12	2009Dec	340
L192.60-0.05	D,A	10' $\times$ 10'	06:12:53.279	+17:59:28.55	2009Dec-2010Dec	271
L192.72+0.04	A	10' $\times$ 10'	06:13:28.147	+17:55:38.60	2009Dec	335
L192.81+0.11	D	10' $\times$ 10'	06:13:55.135	+17:53:09.02	2009Dec	328
L192.98+0.14	D	10' $\times$ 10'	06:14:21.502	+17:45:02.52	2009Dec	383
L196.42-1.66	A	10' $\times$ 10'	06:14:36.606	+13:52:04.40	2009Dec	470
L203.23+2.06	A	10' $\times$ 10'	06:41:00.779	+09:33:56.58	2009Dec	269
L203.35+2.03	A	10' $\times$ 10'	06:41:07.741	+09:26:52.53	2009Dec	314
L213.71-12.62	D	10' $\times$ 10'	06:07:42.663	-06:23:27.15	2009Dec	421
L217.37-0.07	A	10' $\times$ 10'	06:59:17.374	-03:59:14.04	2009Dec	704
L234.57+0.82	D	10' $\times$ 10'	07:35:28.482	-18:45:34.36	2009Dec	1051
L001.10-0.07	A	10' $\times$ 10'	17:48:28.655	-28:01:44.77	2010Jul	849
L023.31-0.26	A	10' $\times$ 10'	18:34:39.947	-08:40:36.21	2010Jul	379
L023.43-0.22	A	10' $\times$ 10'	18:34:45.046	-08:32:55.27	2010Jul	375
L024.50-0.08	A	10' $\times$ 10'	18:36:14.747	-07:31:49.77	2010Jul	306
L024.65-0.13	A	10' $\times$ 10'	18:36:44.447	-07:25:23.71	2010Jul	357
L024.78+0.12	A	10' $\times$ 10'	18:36:04.446	-07:11:28.75	2010Jul	363
L025.40-0.18	A	10' $\times$ 10'	18:38:16.246	-06:47:09.20	2010Jul	482
L030.61+0.16	A	10' $\times$ 10'	18:46:39.147	-01:59:36.24	2010Jul	349
L031.28+0.05	A	10' $\times$ 10'	18:48:14.651	-01:26:51.80	2010Jul	303
L081.11-0.16	A	10' $\times$ 10'	20:40:05.498	+41:26:56.24	2010Jul	341
L081.28+1.01	A	10' $\times$ 10'	20:35:39.600	+42:17:38.79	2010Jul	250
L081.39+0.73	A	10' $\times$ 10'	20:37:12.963	+42:12:38.77	2010Jul	341
L081.48+0.00	A	10' $\times$ 10'	20:40:37.896	+41:50:26.77	2010Jul	353
L081.76+0.60	A	10' $\times$ 10'	20:39:01.567	+42:25:36.73	2010Jul	329
L031.41+0.31	A	10' $\times$ 10'	18:47:34.152	-01:12:46.30	2010Jul24	791
L081.88+0.77	A	10' $\times$ 10'	20:38:39.559	+42:37:37.68	2010Jul24	717
L183.40-0.58	A	10' $\times$ 10'	05:51:16.720	+25:43:32.50	2010Dec	255
L189.78+0.33	A	10' $\times$ 10'	06:08:32.990	+20:38:33.34	2010Dec	294
L202.58+2.42	A	10' $\times$ 10'	06:41:06.051	+10:18:59.80	2010Dec	370
L142.01+1.77	A	10' $\times$ 10'	03:27:29.910	+58:43:55.31	2011Dec	305
L151.61-0.24	A	10' $\times$ 10'	04:11:07.205	+51:09:21.54	2011Dec	266

Table 2.2 (cont'd)

Map	Config. <sup>a</sup>	Size	Map Center		Obs. Date	1 $\sigma$ Noise (mJy beam <sup>-1</sup> )
			R.A. (J2000)	Dec. (J2000)		
L154.37+2.58	A	10' $\times$ 10'	04:36:18.153	+51:11:02.11	2011Dec	266
L169.18-0.89	A	10' $\times$ 10'	05:13:26.754	+37:27:38.75	2011Dec	232
L172.88+2.27	A	10' $\times$ 10'	05:36:53.085	+36:10:29.56	2011Dec	315
L211.53-19.27	A	10' $\times$ 10'	05:39:57.873	-07:27:48.36	2011Dec	254
L111.42+0.76	A	10' $\times$ 10'	23:12:52.873	+61:24:31.27	2012Sep	375
L111.88+0.99	A	10' $\times$ 10'	23:15:45.489	+61:47:37.40	2012Sep	226
L134.20+0.75	A	10' $\times$ 10'	02:28:05.671	+61:29:25.54	2012Sep	525
L189.85+0.50	A	10' $\times$ 10'	06:09:19.407	+20:39:39.18	2012Sep	506
L189.94+0.34	A	10' $\times$ 10'	06:08:53.761	+20:30:07.72	2012Sep	590
L206.60-16.37	A	10' $\times$ 10'	05:41:47.488	-01:57:59.97	2012Sep	563

<sup>a</sup>A: BOX SCAN 571.429 600 40.0 45. B: BOX SCAN 345.600 360 30.0 45. C: BOX SCAN 228.571 240 20.0 45. D: BOX SCAN 606.1 636.4 60.0 45. E: BOX SCAN 169.7 167.5 60.0 45. F: BOX SCAN 144.6 148.0 60.0 45. G: BOX SCAN 144.6 148.0 60.0 45. H: BOX SCAN 707.1 669.9 60.0 45. I: BOX SCAN 1060.7 1157.1 60.0 45. The configuration BOX SCAN X Y R A indicates that the map has a size of X(arcsec) $\times$ Y(arcsec), a scan rate R (arcsec/sec), and a scanning angle A (deg).

Table 2.3. Properties of sources recovered in the 350  $\mu\text{m}$  maps

No.	Name	$l_{max}$	$b_{max}$	$l$	$b$	$\sigma_{maj}$	$\sigma_{min}$	P.A.	$\Theta_R$	$S_{20}$	$S_{40}$	$S$	Type
(1)	(2)	( $^{\circ}$ )	( $^{\circ}$ )	( $^{\circ}$ )	( $^{\circ}$ )	( $''$ )	( $''$ )	( $^{\circ}$ )	( $''$ )	(Jy)	(Jy)	(Jy)	(14)
1	SH_G000.0002-00.0200	0.0002	-0.0200	359.9995	-0.0175	8	6	36	15	42.91 $\pm$ 4.51	118.56 $\pm$ 11.11	100.41 $\pm$ 6.94	F
2	SH_G000.0006-00.0246	0.0006	-0.0246	359.9994	-0.0253	7	6	64	13	55.84 $\pm$ 5.86	122.38 $\pm$ 11.47	96.41 $\pm$ 6.66	C
3	SH_G000.0008-00.0304	0.0008	-0.0304	0.0002	-0.0305	5	4	102	7	26.85 $\pm$ 2.82	55.23 $\pm$ 5.18	26.29 $\pm$ 1.82	F
4	SH_G000.0013-00.0784	0.0013	-0.0784	0.0008	-0.0780	5	4	142	7	13.62 $\pm$ 1.43	23.03 $\pm$ 2.17	12.71 $\pm$ 0.89	F
5	SH_G000.0065-00.0557	0.0065	-0.0557	0.0058	-0.0575	13	8	153	22	49.25 $\pm$ 5.17	104.71 $\pm$ 9.81	146.57 $\pm$ 10.13	C
6	SH_G000.0067-00.0146	0.0067	-0.0146	0.0052	-0.0139	6	5	104	9	30.57 $\pm$ 3.21	89.52 $\pm$ 8.39	37.29 $\pm$ 2.58	F
7	SH_G000.0075-00.0199	0.0075	-0.0199	0.0058	-0.0208	11	6	67	17	68.11 $\pm$ 7.15	162.68 $\pm$ 15.24	163.46 $\pm$ 11.30	C
8	SH_G000.0089+00.0034	0.0089	0.0034	0.0092	0.0035	5	3	17	...	7.53 $\pm$ 0.80	13.34 $\pm$ 1.26	5.00 $\pm$ 0.35	F
9	SH_G000.0120-00.0201	0.0120	-0.0201	0.0129	-0.0182	12	8	47	21	80.66 $\pm$ 8.47	188.93 $\pm$ 17.70	237.90 $\pm$ 16.44	C
10	SH_G000.0121-00.0513	0.0121	-0.0513	0.0113	-0.0511	9	7	34	17	60.03 $\pm$ 6.30	121.66 $\pm$ 11.40	122.43 $\pm$ 8.46	C
11	SH_G000.0130+00.0064	0.0130	0.0064	0.0127	0.0065	9	4	164	10	15.16 $\pm$ 1.60	34.25 $\pm$ 3.21	21.75 $\pm$ 1.51	F
12	SH_G000.0135-00.0217	0.0135	-0.0217	0.0156	-0.0233	7	5	165	10	78.04 $\pm$ 8.19	161.42 $\pm$ 15.12	102.54 $\pm$ 7.09	C
13	SH_G000.0142+00.0364	0.0142	0.0364	0.0148	0.0359	10	8	111	19	26.86 $\pm$ 2.82	48.54 $\pm$ 4.55	55.72 $\pm$ 3.86	F
14	SH_G000.0145+00.0127	0.0145	0.0127	0.0150	0.0125	3	3	169	...	5.00 $\pm$ 0.54	7.71 $\pm$ 0.74	3.05 $\pm$ 0.22	F
15	SH_G000.0188+00.0040	0.0188	0.0040	0.0186	0.0072	7	5	20	11	26.13 $\pm$ 2.75	59.59 $\pm$ 5.58	39.78 $\pm$ 2.75	F
16	SH_G000.0195-00.0067	0.0195	-0.0067	0.0184	-0.0077	12	6	62	19	32.01 $\pm$ 3.36	56.13 $\pm$ 5.26	63.15 $\pm$ 4.37	F
17	SH_G000.0196-00.0501	0.0196	-0.0501	0.0199	-0.0511	12	10	30	24	73.00 $\pm$ 7.66	143.62 $\pm$ 13.46	208.13 $\pm$ 14.38	C
18	SH_G000.0197+00.0017	0.0197	0.0017	0.0197	0.0016	6	5	165	10	27.63 $\pm$ 2.90	58.82 $\pm$ 5.51	34.29 $\pm$ 2.37	F
19	SH_G000.0238+00.0359	0.0238	0.0359	0.0237	0.0357	11	6	78	16	15.41 $\pm$ 1.62	33.58 $\pm$ 3.15	33.12 $\pm$ 2.30	F
20	SH_G000.0247+00.0032	0.0247	0.0032	0.0252	0.0024	7	5	166	11	19.90 $\pm$ 2.09	39.84 $\pm$ 3.74	26.18 $\pm$ 1.81	F
21	SH_G000.0279-00.0533	0.0279	-0.0533	0.0279	-0.0538	7	6	14	13	29.31 $\pm$ 3.08	79.58 $\pm$ 7.46	55.47 $\pm$ 3.84	F
22	SH_G000.0281-00.0576	0.0281	-0.0576	0.0278	-0.0587	8	4	87	10	23.22 $\pm$ 2.44	55.01 $\pm$ 5.16	32.71 $\pm$ 2.26	F
23	SH_G000.0308+00.0211	0.0308	0.0211	0.0303	0.0218	11	7	18	18	35.87 $\pm$ 3.77	65.86 $\pm$ 6.17	71.75 $\pm$ 4.96	F
24	SH_G000.0315-00.0512	0.0315	-0.0512	0.0304	-0.0507	5	4	35	7	26.45 $\pm$ 2.78	65.31 $\pm$ 6.12	26.94 $\pm$ 1.86	F
25	SH_G000.0331+00.0054	0.0331	0.0054	0.0337	0.0061	8	4	90	8	15.37 $\pm$ 1.62	15.11 $\pm$ 1.43	16.67 $\pm$ 1.16	F

Note. — **Notes.** (1) Running source number. (2) Name derived from Galactic coordinates of the maximum intensity in the object. (3)(4) Galactic coordinates of maximum intensity in the catalog object. (5)(6) Galactic coordinates of emission centroid. (7)(9) Major and minor axis 1/e widths and position angle of source. (10) Deconvolved angular size of source. (11)(12) Flux densities derived for 20 and 40 apertures. (13) Integrated flux density in the object. (14) Type of substructure: “C”=compact or “F”=faint.

(This table is available in its entirety in a machine-readable form in the online journal. A portion is shown here for guidance regarding its form and content.)

Table 2.4. Sources from BGPS catalog with large number of high-resolution associated substructures.

BGPS V2.1 name	Peak emission of 350 $\mu\text{m}$ substructures			
	Total	$> 6\sigma_{rms}$	$> 10\sigma_{rms}$	$> 20\sigma_{rms}$
BGPSv2_G213.705-12.603	34	24	15	12
BGPSv2_G034.256+00.154	27	18	15	8
BGPSv2_G133.716+01.220	25	15	9	4
BGPSv2_G000.014-00.017	23	9	5	1
BGPSv2_G029.916-00.045	22	18	8	3
BGPSv2_G029.958-00.017	19	13	6	4
BGPSv2_G359.867-00.083	16	12	8	4
BGPSv2_G081.477+00.020	16	11	6	0
BGPSv2_G359.982-00.069	14	12	7	1
BGPSv2_G359.946-00.045	14	5	1	0
BGPSv2_G030.751-00.051	14	8	7	5
BGPSv2_G081.753+00.593	13	9	7	5
BGPSv2_G076.359-00.600	13	11	7	1
BGPSv2_G030.786-00.025	13	12	11	3
BGPSv2_G203.223+02.076	12	8	1	0
BGPSv2_G192.598-00.049	12	7	5	1
BGPSv2_G203.320+02.058	11	7	6	4
BGPSv2_G023.437-00.183	11	5	2	1
BGPSv2_G023.273-00.211	11	7	1	0
BGPSv2_G081.721+00.573	10	9	8	7
BGPSv2_G030.690-00.043	10	4	3	0
BGPSv2_G024.493-00.039	10	7	6	3

Table 2.5. Fluxes and estimated temperatures of BGPS sources

BGPS source	1.1 mm	Convolved 350 $\mu\text{m}$	Temperature					
	Flux 40''	Flux 40''	$\beta = 1.0$		$\beta = 1.7$		$\beta = 2.0$	
	(Jy)	(Jy)	(K)		(K)		(K)	
BGPSv2_G024.743+00.179	0.51±0.11	17.82±0.64	>1000.0	$\frac{>1000.0}{103.1}$	23.5	$\frac{31.1}{18.3}$	16.7	$\frac{19.9}{14.1}$
BGPSv2_G024.745+00.161	0.60±0.12	18.42±0.66	351.7	$\frac{>1000.0}{58.2}$	20.2	$\frac{24.8}{16.6}$	15.1	$\frac{17.3}{13.1}$
BGPSv2_G024.757+00.091	1.36±0.12	61.75±2.19	>1000.0	$\frac{>1000.0}{>1000.0}$	34.9	$\frac{42.9}{29.2}$	21.2	$\frac{23.6}{19.1}$
BGPSv2_G024.759+00.065	0.43±0.09	8.47±0.38	33.3	$\frac{52.7}{23.4}$	14.2	$\frac{16.2}{12.3}$	11.6	$\frac{12.9}{10.4}$
BGPSv2_G024.760+00.163	0.34±0.13	4.80±0.18	20.8	$\frac{31.9}{14.2}$	11.7	$\frac{14.0}{9.5}$	10.0	$\frac{11.5}{8.4}$
BGPSv2_G024.773+00.125	0.22±0.09	1.67±0.07	12.9	$\frac{16.2}{9.9}$	8.9	$\frac{10.3}{7.5}$	8.0	$\frac{8.9}{6.8}$
BGPSv2_G024.791+00.083	10.07±0.64	556.65±19.73	>1000.0	$\frac{>1000.0}{>1000.0}$	58.6	$\frac{78.9}{46.3}$	27.1	$\frac{30.2}{24.4}$
BGPSv2_G024.795+00.101	3.14±0.22	142.57±4.87	>1000.0	$\frac{>1000.0}{>1000.0}$	34.8	$\frac{41.0}{30.1}$	21.2	$\frac{23.0}{19.5}$
BGPSv2_G024.807+00.039	0.32±0.09	5.84±0.23	29.1	$\frac{49.6}{19.4}$	13.5	$\frac{16.0}{11.3}$	11.2	$\frac{12.7}{9.7}$
BGPSv2_G024.815+00.189	0.10±0.09	-0.75±0.05	...	--	...	--	...	--

Table 2.5 (cont'd)

BGPS source	1.1 mm	Convolved 350 $\mu\text{m}$	Temperature					
	Flux 40''	Flux 40''	$\beta = 1.0$		$\beta = 1.7$		$\beta = 2.0$	
	(Jy)	(Jy)	(K)		(K)		(K)	
BGPSv2_G024.817+00.129	0.48 $\pm$ 0.09	6.69 $\pm$ 0.27	20.7	$\frac{25.5}{17.0}$	11.6	$\frac{12.8}{10.5}$	9.9	$\frac{10.7}{9.1}$
BGPSv2_G024.824+00.181	0.17 $\pm$ 0.09	1.89 $\pm$ 0.07	16.5	$\frac{25.0}{10.7}$	10.3	$\frac{12.7}{7.9}$	9.0	$\frac{10.7}{7.2}$
BGPSv2_G024.850+00.085	0.90 $\pm$ 0.11	36.60 $\pm$ 1.32	>1000.0	$\frac{>1000.0}{>1000.0}$	28.9	$\frac{35.9}{23.7}$	19.0	$\frac{21.5}{16.8}$
BGPSv2_G024.863+00.145	0.16 $\pm$ 0.09	1.08 $\pm$ 0.04	12.2	$\frac{16.4}{8.4}$	8.6	$\frac{10.3}{6.7}$	7.7	$\frac{9.0}{6.1}$
BGPSv2_G025.329-00.196	0.56 $\pm$ 0.12	3.95 $\pm$ 0.16	12.4	$\frac{13.9}{10.9}$	8.7	$\frac{9.4}{8.0}$	7.8	$\frac{8.3}{7.2}$
BGPSv2_G025.339-00.170	0.19 $\pm$ 0.12	0.76 $\pm$ 0.04	9.5	$\frac{11.7}{7.0}$	7.3	$\frac{8.4}{5.8}$	6.6	$\frac{7.5}{5.4}$
BGPSv2_G025.355-00.156	0.19 $\pm$ 0.13	1.49 $\pm$ 0.08	13.2	$\frac{19.5}{8.0}$	9.1	$\frac{11.3}{6.4}$	8.1	$\frac{9.7}{5.9}$
BGPSv2_G025.355-00.190	1.46 $\pm$ 0.15	40.94 $\pm$ 1.53	116.1	$\frac{738.0}{61.5}$	18.6	$\frac{20.6}{16.8}$	14.2	$\frac{15.3}{13.2}$



Table 2.5 (cont'd)

BGPS source	1.1 mm	Convolved 350 $\mu\text{m}$	Temperature					
	Flux 40''	Flux 40''	$\beta = 1.0$		$\beta = 1.7$		$\beta = 2.0$	
	(Jy)	(Jy)	(K)		(K)		(K)	
BGPSv2_G025.382-00.182	3.23±0.24	115.44±4.01	>1000.0	$\frac{>1000.0}{>1000.0}$	24.0	$\frac{26.7}{21.8}$	17.0	$\frac{18.1}{15.9}$
BGPSv2_G025.399-00.140	4.56±0.31	152.14±5.34	>1000.0	$\frac{>1000.0}{405.7}$	22.1	$\frac{24.1}{20.3}$	16.1	$\frac{17.0}{15.1}$
BGPSv2_G025.405-00.256	0.31±0.15	3.14±0.11	15.8	$\frac{23.1}{10.6}$	10.1	$\frac{12.3}{7.9}$	8.8	$\frac{10.4}{7.1}$
BGPSv2_G025.413-00.176	0.65±0.12	17.80±0.64	98.2	$\frac{>1000.0}{43.3}$	18.2	$\frac{21.6}{15.4}$	14.0	$\frac{15.8}{12.4}$
BGPSv2_G025.455-00.210	1.64±0.17	75.41±2.61	>1000.0	$\frac{>1000.0}{>1000.0}$	35.9	$\frac{46.0}{29.1}$	21.5	$\frac{24.4}{19.1}$
BGPSv2_G025.467-00.126	0.12±0.12	0.33±0.06	8.4	$\frac{11.2}{--}$	6.7	$\frac{8.2}{--}$	6.1	$\frac{7.4}{--}$
BGPSv2_G025.477-00.136	0.10±0.12	1.73±0.06	27.0	$\frac{>1000.0}{--}$	13.1	$\frac{25.9}{--}$	10.9	$\frac{17.8}{--}$

Note. — (This table is available in its entirety in a machine-readable form in the online journal. A portion is shown here for guidance regarding its form and content.)

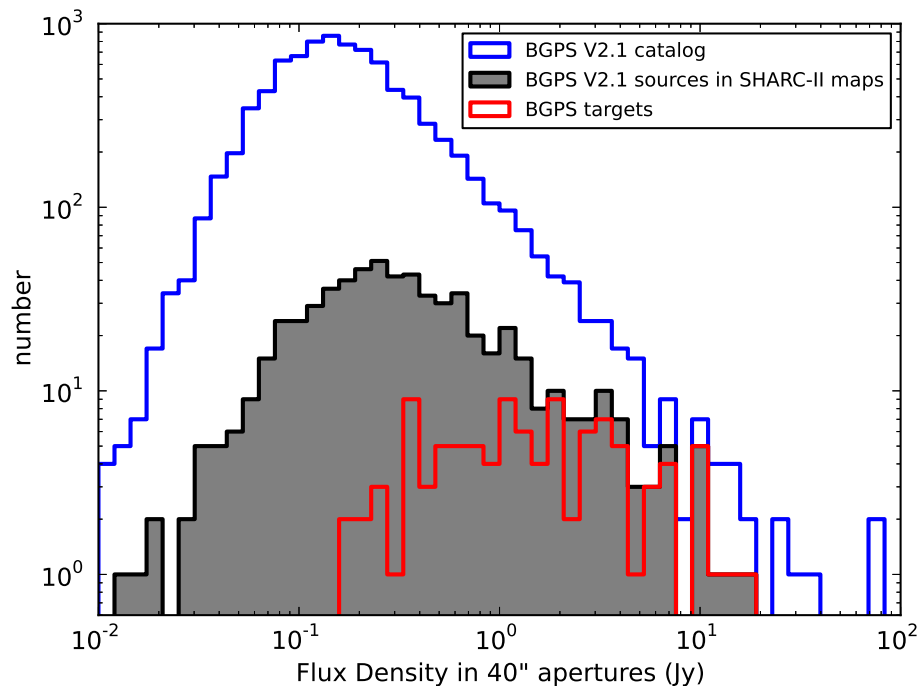


Figure 2.1 Distribution of 40'' aperture flux density of the complete sample of 8594 sources from the BGPS V2.1 catalog (blue line), along with those 619 sources contained in the SHARC-II maps (shaded black line). The distribution of the 104 sources considered as representative targets is also shown (red line).

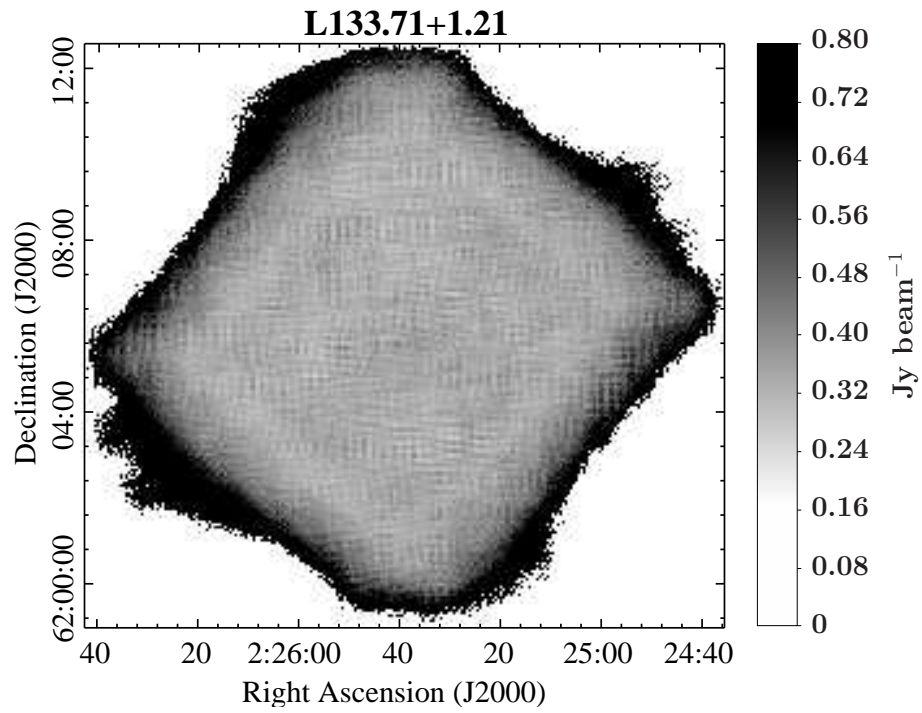


Figure 2.2 Error map obtained from CRUSH reduction for L133.71+1.21. The image unit is  $\text{Jy beam}^{-1}$ . The measured average noise for the L133.71+1.21 map is  $0.338 \text{ Jy beam}^{-1}$ .

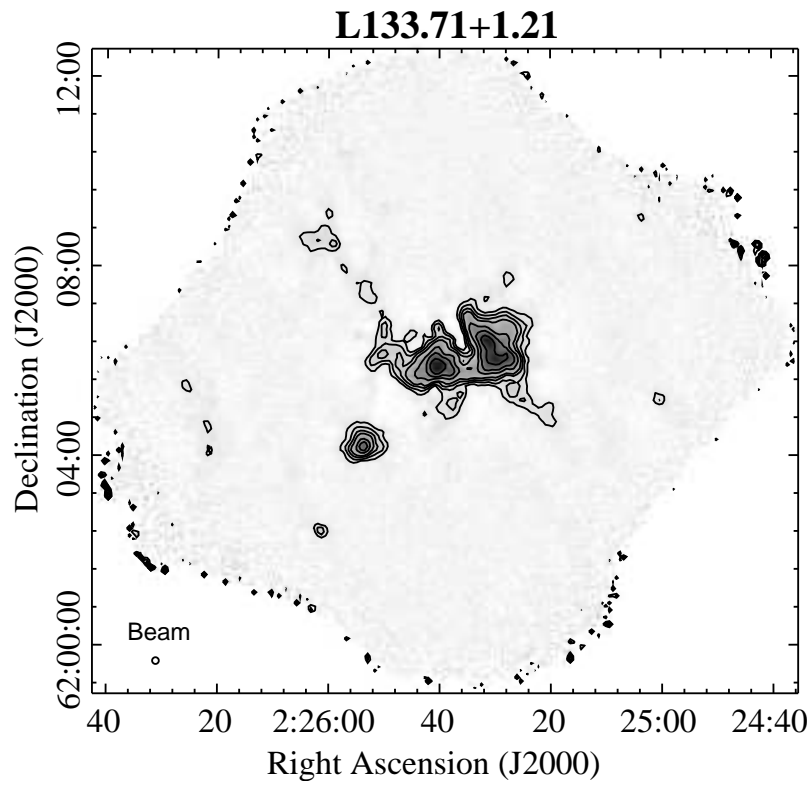


Figure 2.3 Map at  $350 \mu\text{m}$  obtained with SHARC-II toward the region L133.71+1.21. Beam size of image is shown in the bottom left corner. Contour levels represent  $3\sigma$ ,  $6\sigma$ ,  $10\sigma$ ,  $15\sigma$ ,  $30\sigma$ ,  $50\sigma$  and  $100\sigma$ , with a rms noise  $\sigma = 338 \text{ mJy beam}^{-1}$ .

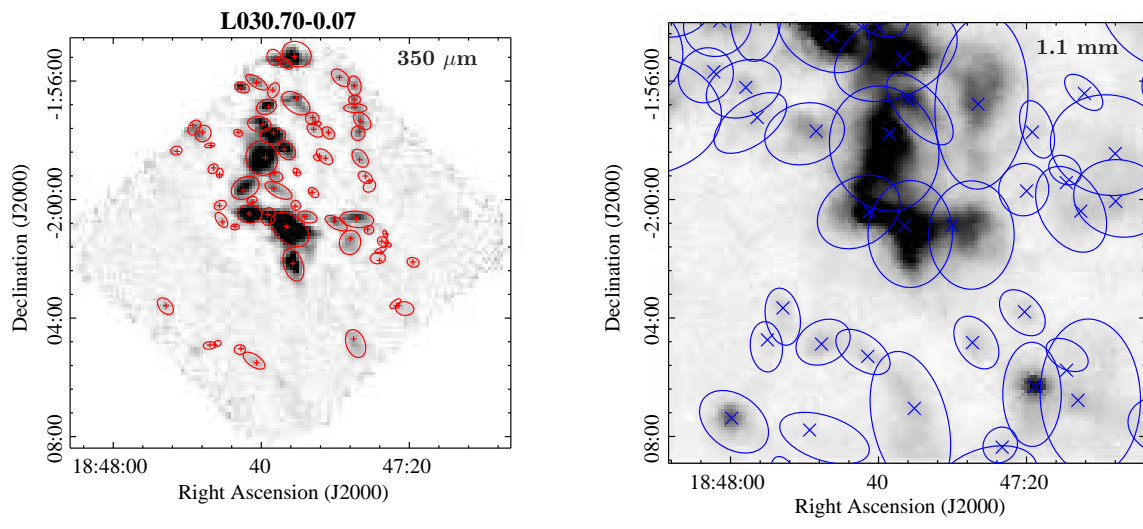


Figure 2.4 Example of the extraction of sources with *Bolocam*. Left: Map of L030.70-0.07 with SHARC-II at 350 μm (FWHM beam of 8.5"). Right: The same region mapped with Bolocam at 1.1 mm (FWHM beam of 33"). Some structures of Bolocam have several substructures mapped at the better resolution of SHARC-II. Also, the figure shows BGPS sources with no counterpart in the 350 μm map.

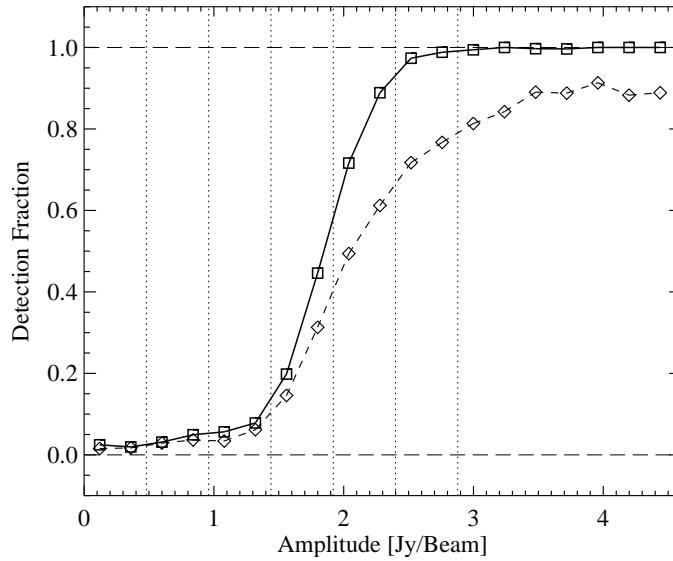


Figure 2.5 Completeness fraction derived from fake source tests. The tests were performed in nine SHARC-II maps with different noise levels. The plot shows the results of those detections, scaled to the mean noise of the catalog maps ( $0.48 \text{ Jy beam}^{-1}$ ). The fraction of sources recovered is plotted as a function of input source intensity. The vertical dotted lines indicate  $\{1, 2, 3, 4, 5, 6\}\sigma$ . The dashed line with diamonds corresponds to fake sources across the whole map, while the continuous line with squares corresponds to sources at a distance  $<3.5'$  from the center of the map. The completeness tests indicates that the catalog is complete at the  $>99\%$  limit for sources with flux densities  $>6\sigma$ .

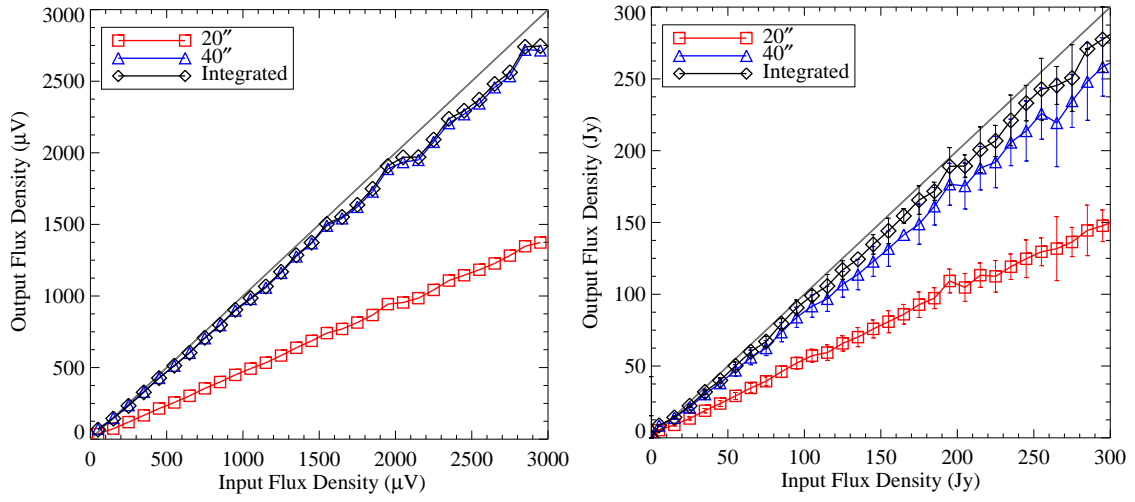


Figure 2.6 Recovery of source flux density for simulated resolved sources ( $\text{FWHM} = 2.7\theta_{\text{beam}} = 23''$ ) in SHARC-II maps. The left panel shows the flux recovery in instrument units ( $\mu\text{V}$ ). Right panel shows the results of the calibrated flux recovery in units of Jy. Small differences are found between the  $40''$  aperture and the integrated flux, with an under estimation of the integrated flux of  $\sim 10\%$ .

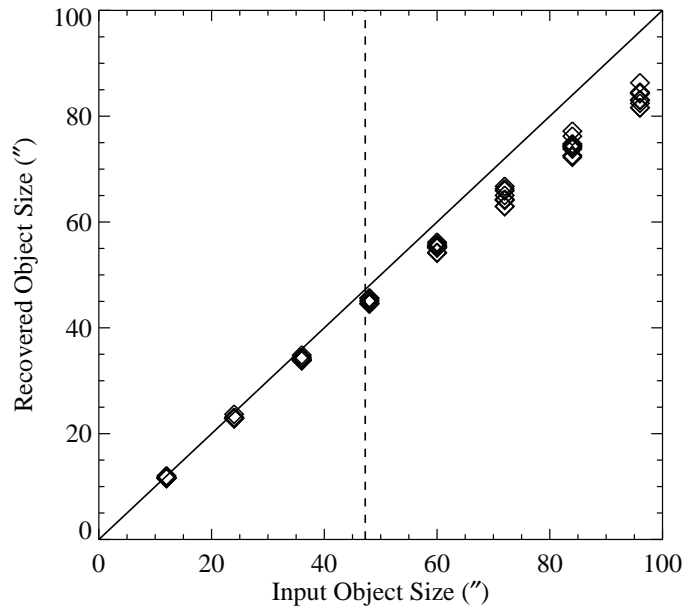


Figure 2.7 Recovery of source size for simulated observations in SHARC-II maps. The vertical line at  $48''$  indicates the largest size recovered for an object in our sample by *Boloccat*. The largest major-axis recovered is  $65''$ , and therefore the plot suggests that source sizes are typically well recovered.



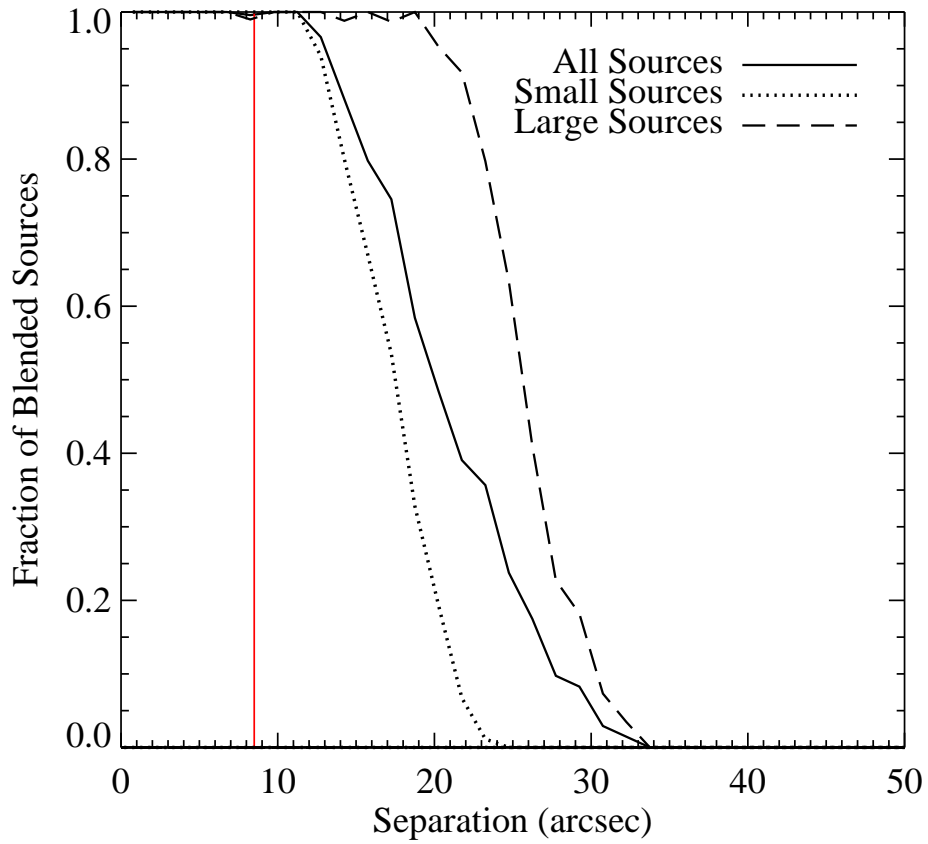


Figure 2.8 Fraction of blended objects as a function of source pair separation (solid line). The vertical red line shows the FWHM beam size of the  $350 \mu\text{m}$  maps. Smaller sources ( $15''$ – $24''$  in size) are represented by the dotted line, and large sources ( $24''$ – $34''$  in size) are represented by segmented line.

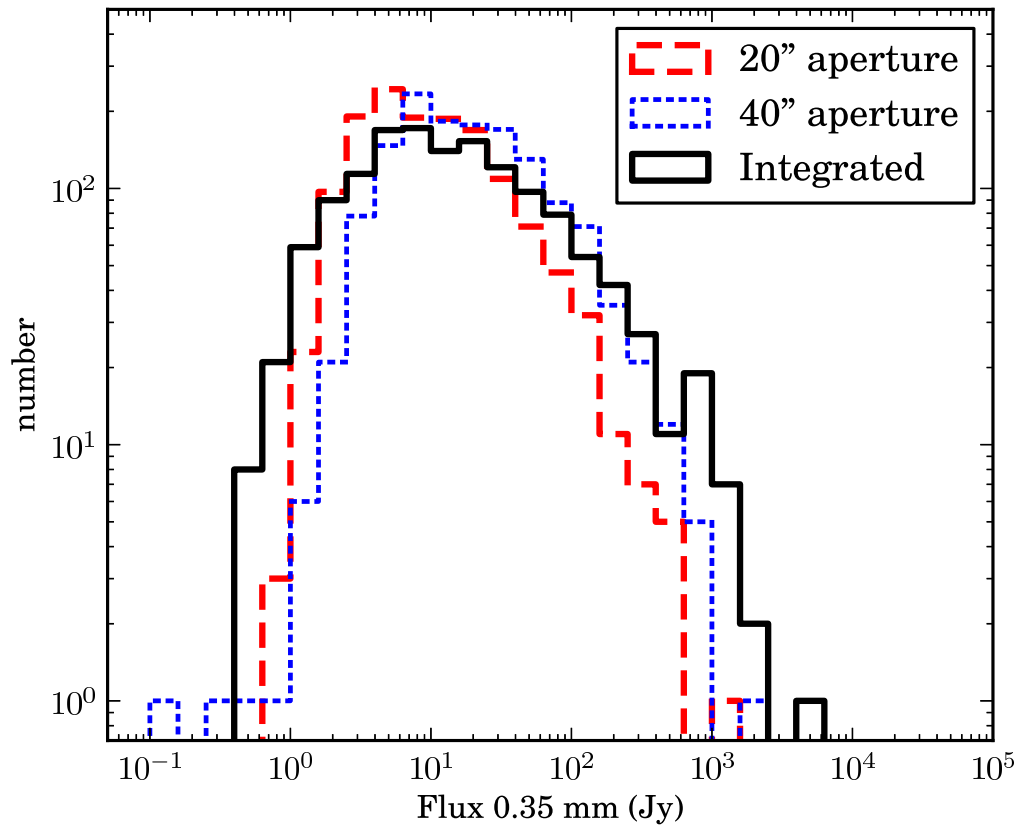


Figure 2.9 Flux distribution for objects identified in the 107 SHARC-II maps. Three methods of flux recovery are represented in the image: aperture photometry at 20" (red long dash) and 40" (blue short dash) toward the peak, and integrated emission of the source (solid black line).

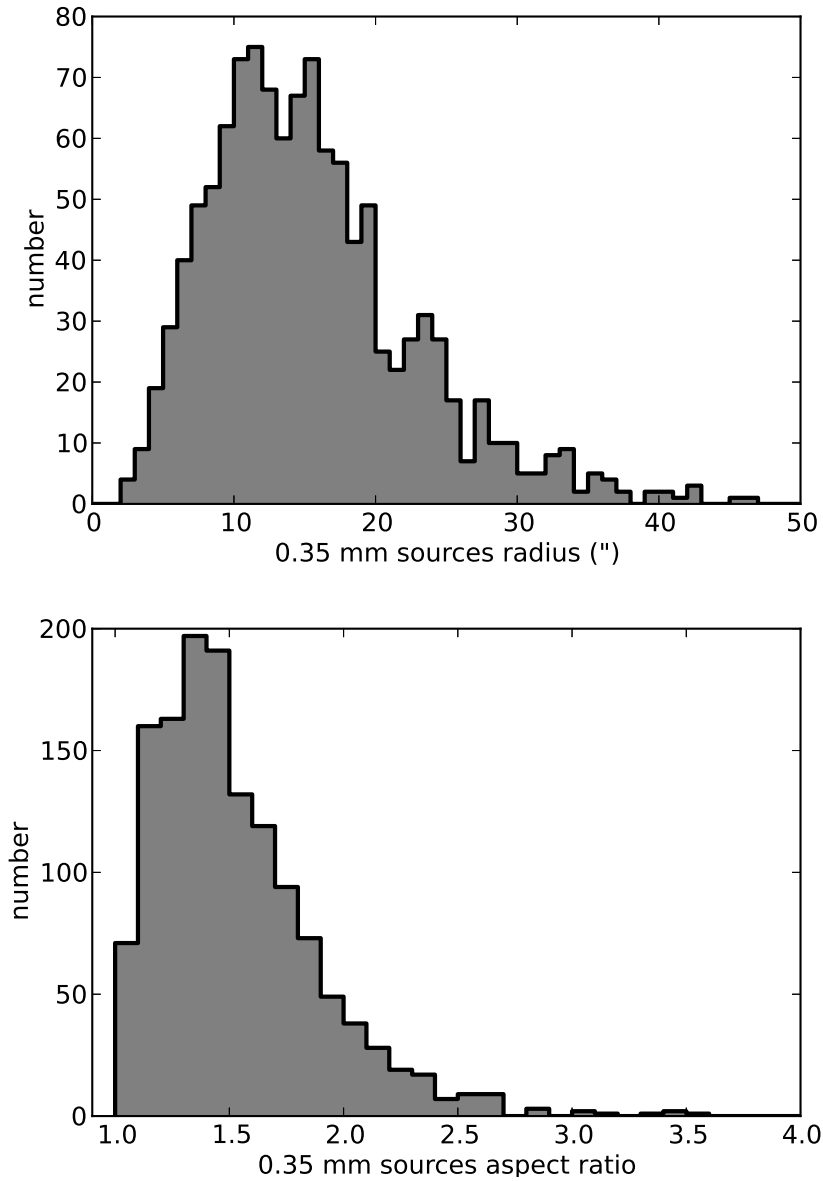


Figure 2.10 Distribution of the deconvolved radii and aspect ratio of sources in the SHARC-II maps. The average and median values of the radii distribution are 15'' and 14'', respectively. The average and median values of the aspect ratios are 1.53 and 1.45.

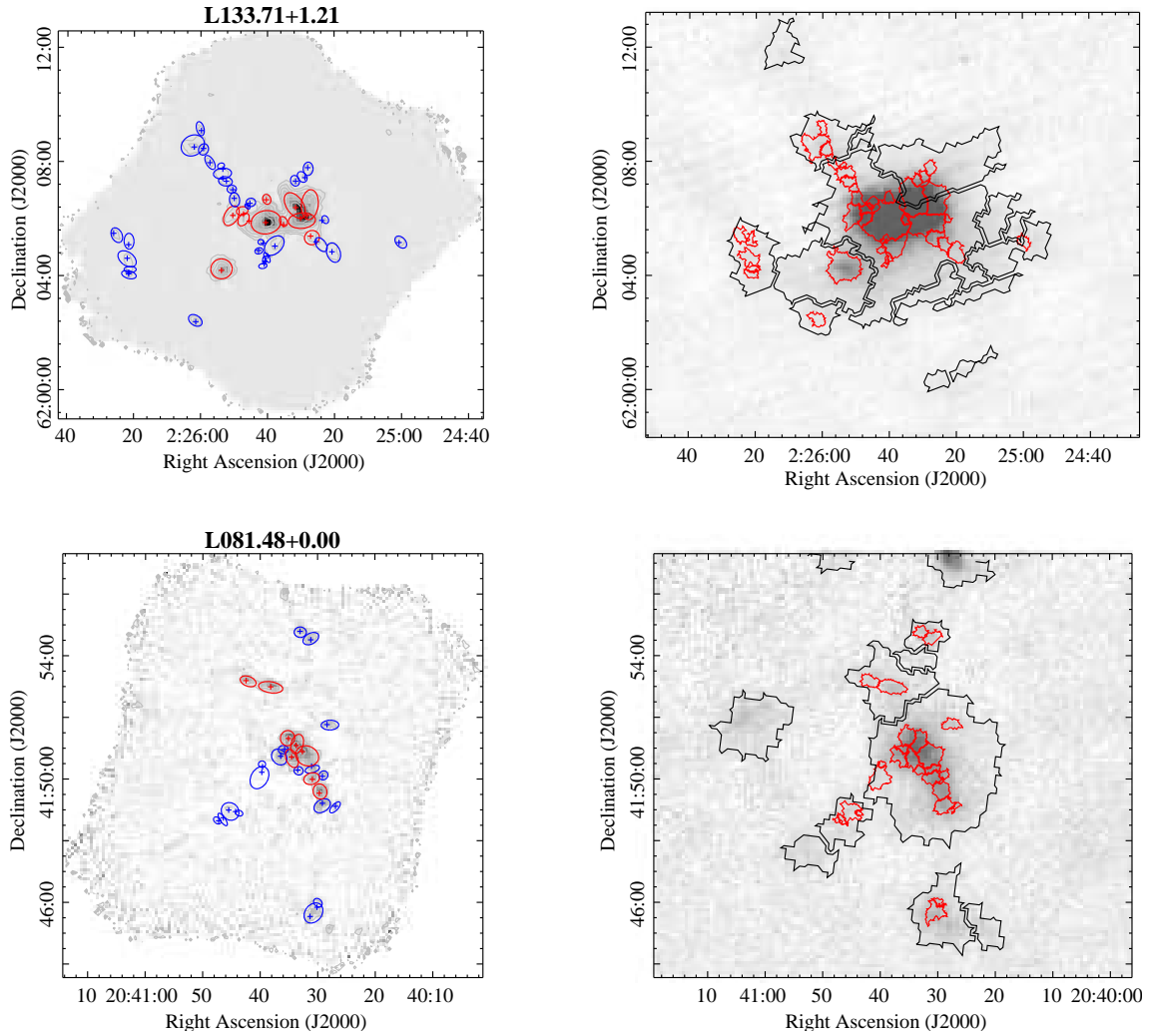


Figure 2.11 Upper left: Results of Bolocat on the  $350 \mu\text{m}$  map of L133.71+1.21, corresponding to the W3 main region. The different colors indicate the peak signal-to-noise of each source (above  $10\sigma$  in red, below that limit in blue). Sources in red are associated with compact and dense core-type structures, the blue sources are related to low emission, field material or possible filamentary structure. Upper right: Grey color scale of the 1.1 mm toward the same region. Black regions show the result of *Boloccat* on the 1.1 mm map, and red regions the results of *Boloccat* on the  $350 \mu\text{m}$  map. The central V2.1 source mask shows large number of substructures (both strong and faint). Lower panels are similar to the upper panels for L081.48 + 0.00, in the Cygnus X region. The comparison of source masks reveal a large population of BGPS V2.1 sources located inside the  $350 \mu\text{m}$  maps, but not associated with any source at high-resolution.

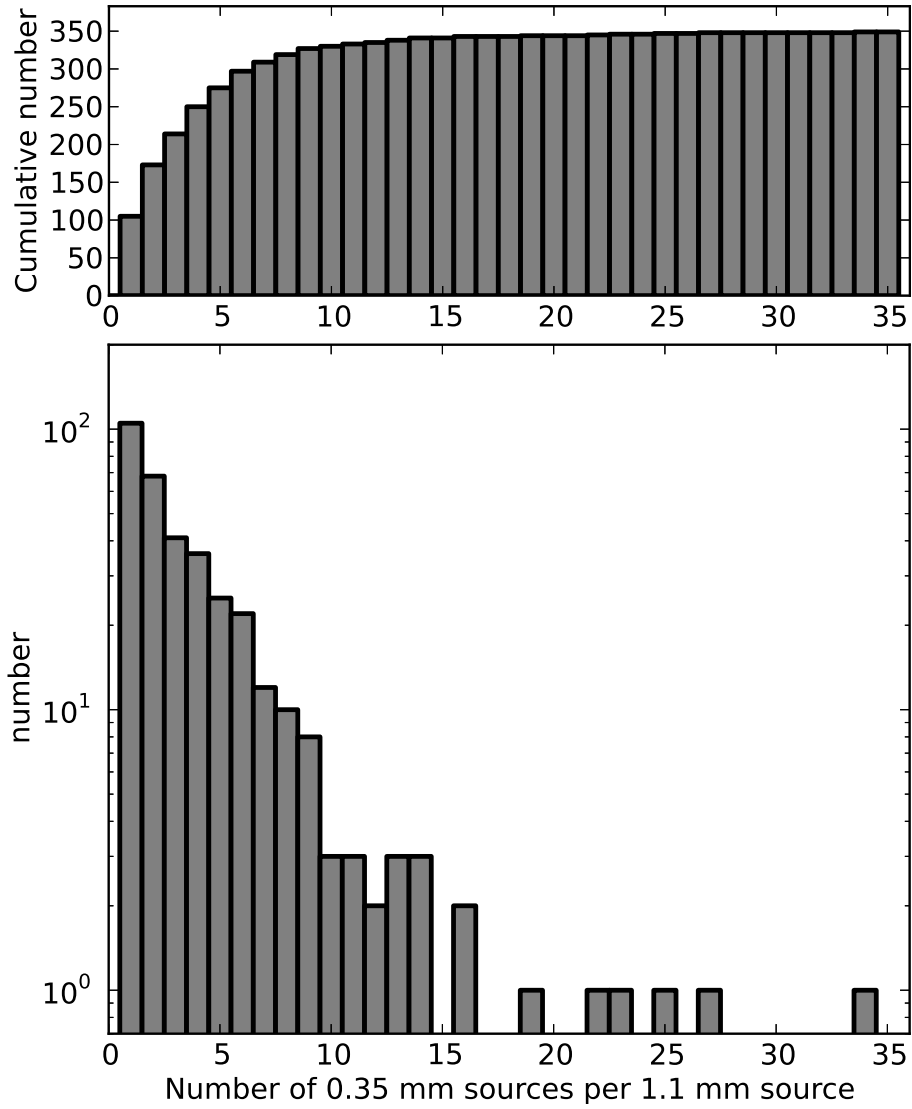


Figure 2.12 Distribution of 350  $\mu\text{m}$  sources per 1.1 mm source from BGPS. The top panel shows the cumulative number. Half of the 1.1 mm parental clumps are associated with one-or-two substructures identified at high-resolution.

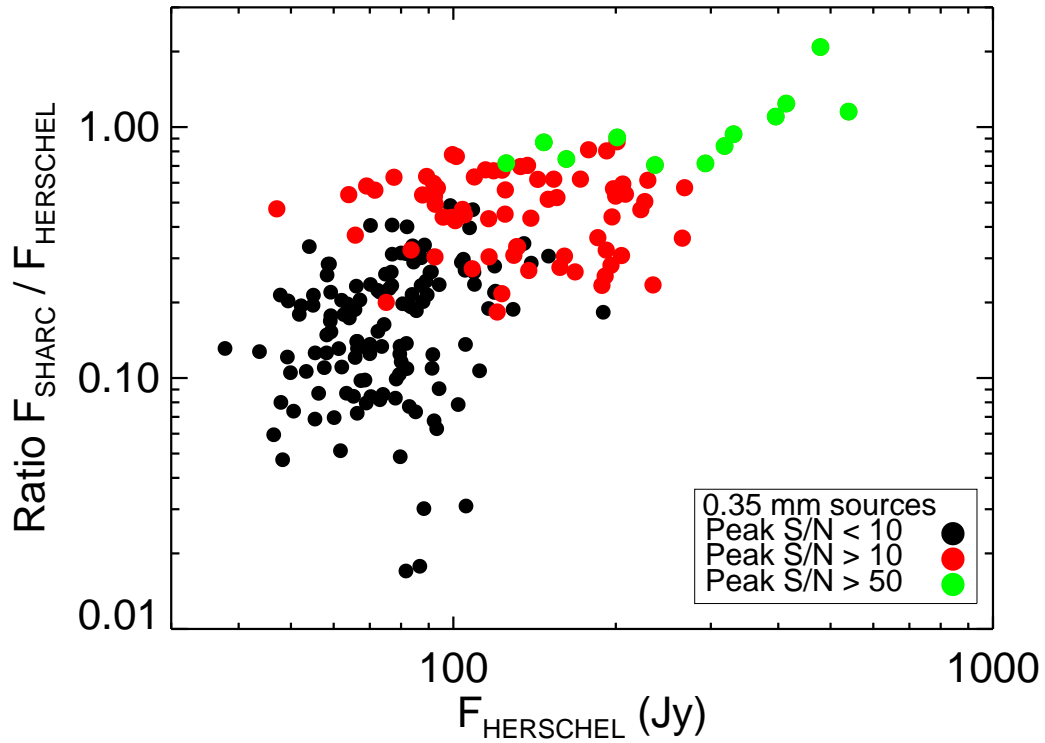


Figure 2.13 Comparison between integrated flux in  $40''$  apertures obtained at  $350 \mu\text{m}$  on SHARC-II and *Herschel* images toward  $l = 30^\circ$ . The points represent the 213 high-resolution sources recovered by *Boloccat* in SHARC-II maps, and the colors show different limits of peak signal-to-noise on those sources.

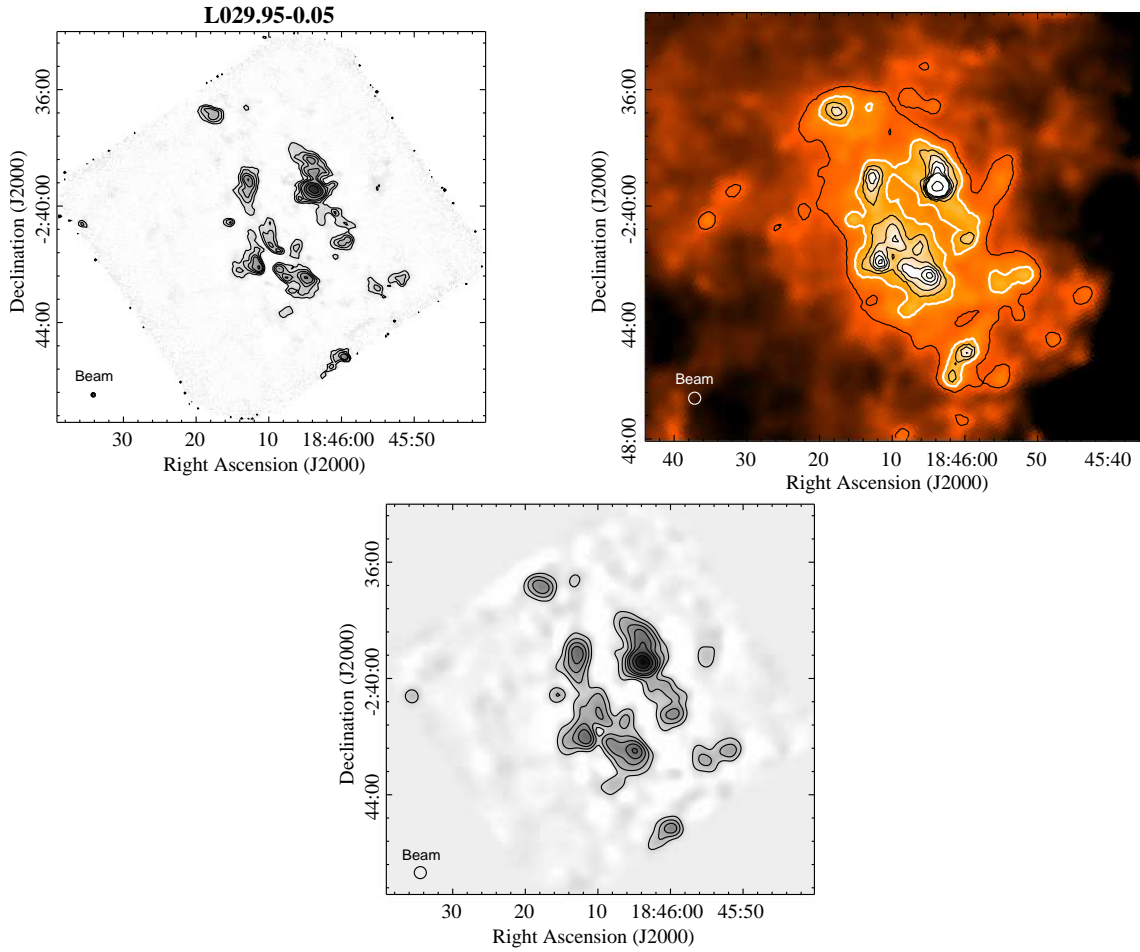


Figure 2.14 Example of the  $350\ \mu\text{m}$  continuum emission from SHARC-II (upper left) and *Herschel*/SPIRE (upper right) toward the region  $l = 28.95^\circ$ ,  $b = -0.05^\circ$ . Beam sizes are shown in the bottom left corner of each map. The contours of the SHARC-II image correspond to  $3\sigma$ ,  $6\sigma$ ,  $10\sigma$ ,  $15\sigma$ ,  $30\sigma$ ,  $50\sigma$  and  $100\sigma$ , with an rms noise  $\sigma = 514\ \text{mJy beam}^{-1}$ . Contours of the *Herschel* image start from  $10\sigma$ , with increasing steps of  $5\sigma$  ( $\sigma = 164\ \text{MJy ster}^{-1}$ ). The smaller beam size of SHARC-II images allow us to recover structures not identified by *Herschel* with lower resolution. Bottom: Convolved SHARC-II image with gaussian kernel of  $\sigma = 9.9''$  (6.14 pixels), to match the  $24.9''$  FWHM beam size of *Herschel* image. Contours represent 1, 3, 6, 10, 15, 30 and 50 times the rms noise of the image. The  $1\sigma$  contour level resembles the emission observed at the  $15\sigma$  white contour level of the *Herschel* image. The  $15\sigma$  level in the *Herschel* map sets then a limit of the diffuse emission filtered out in the SHARC-II maps.

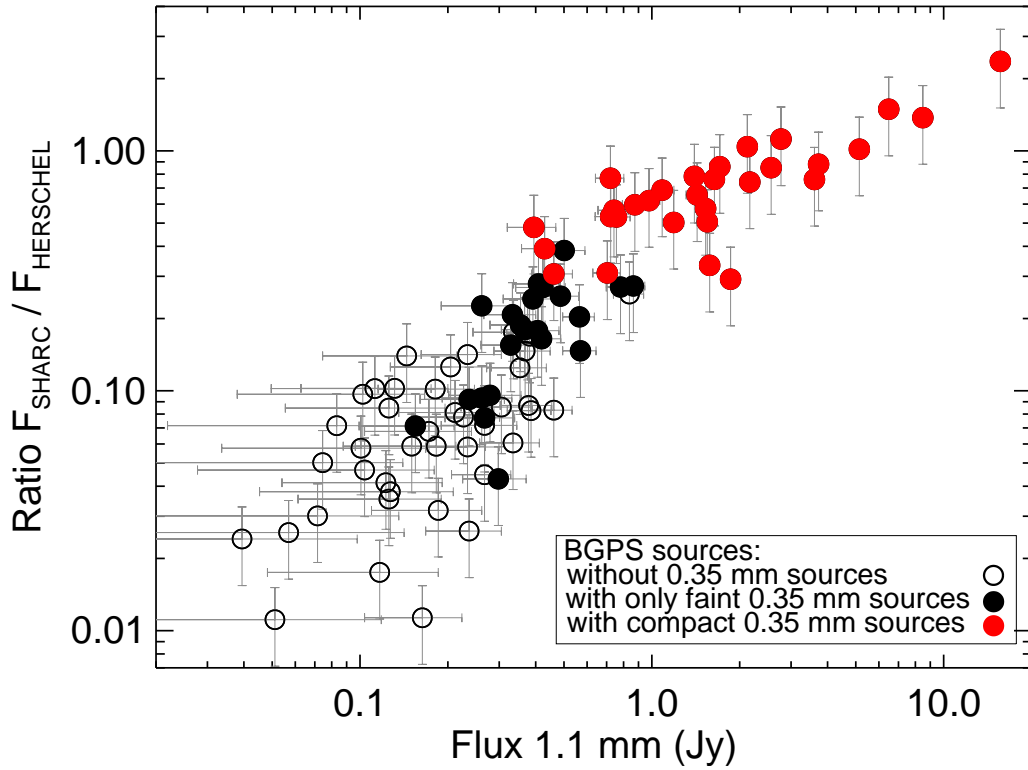


Figure 2.15 Comparison between integrated flux in  $40''$  apertures for  $350 \mu\text{m}$  images from SHARC-II and *Herschel* image on a sample of 102 BGPS sources located toward  $l = 30^\circ$ . Both SHARC-II and *Herschel* were convolved to match the resolution of the Bolocam maps ( $33''$ ). Unfilled circles represent BGPS sources with no associated source detected at  $350 \mu\text{m}$ , and filled circles show the 1.1 mm parental clumps with only faint objects (black) and with compact substructures (red). The error bars in the flux ratio considered 20% uncertainties in  $F_{\text{Herschel}}$ , and 30% in  $F_{\text{SHARC}}$ .



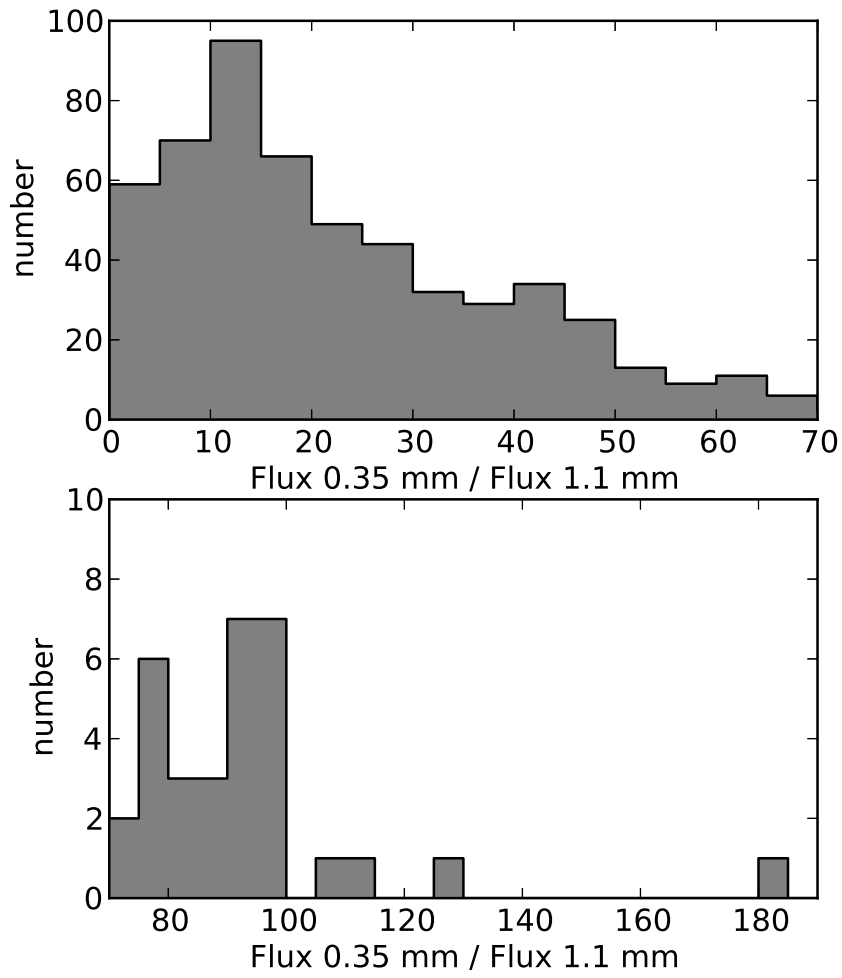


Figure 2.16 Distribution of the flux ratio between the emission at 0.35 mm and 1.1 mm for our sample of 574 BGPS V2.1 sources with reliable flux values. Nearly 94% of the sources have a flux ratio lower than 70.2

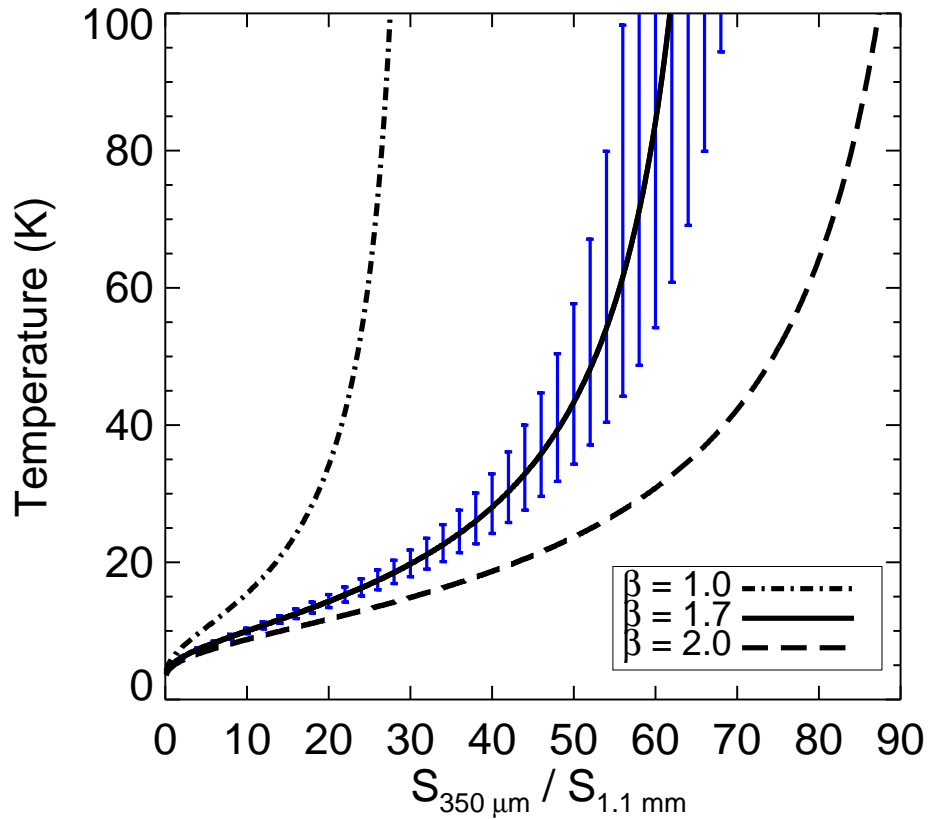


Figure 2.17 Models of dust temperature as a function of the flux ratio between continuum emission at  $350 \mu m$  and  $1.1 mm$ , in the optically thin limit. The three models correspond to different opacity laws,  $\beta = 1.0$ ,  $\beta = 1.7$  and  $\beta = 2.0$ . The error bars for the  $\beta = 1.7$  model show the expected uncertainty in temperature determination when the flux ratio has an error of 10%.

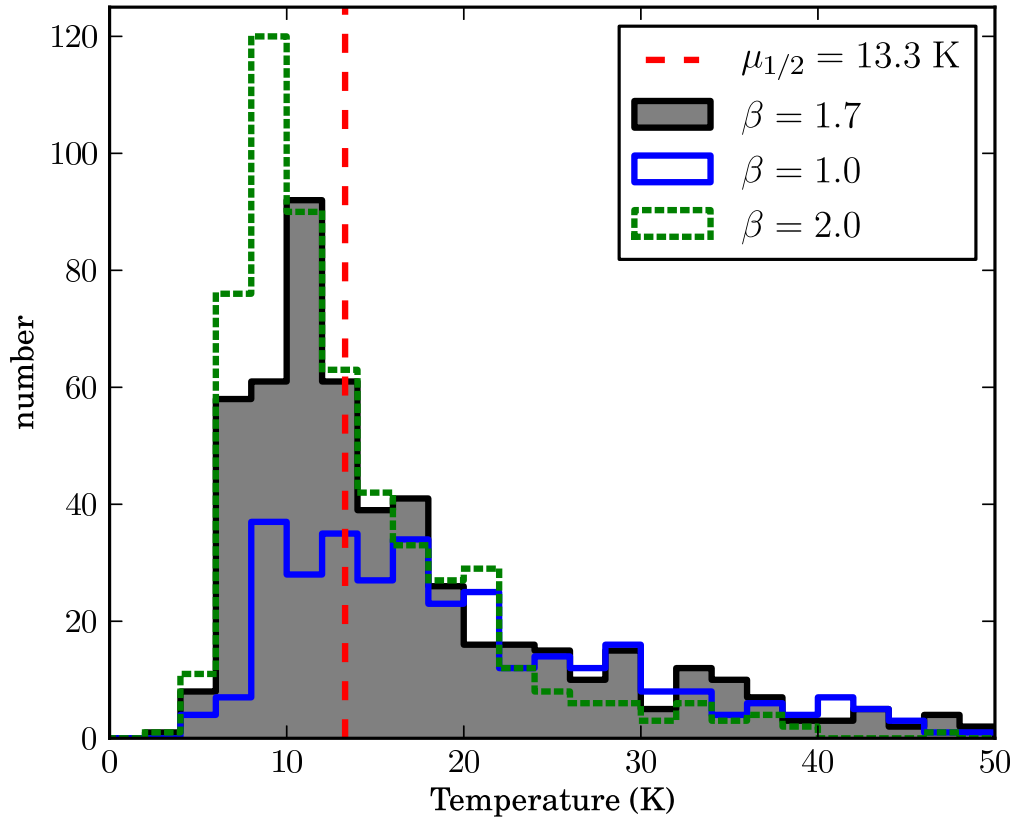


Figure 2.18 Distribution of temperatures of the BGPS sources with good fit in the determination of temperature, using the three different opacity models: spectral index  $\beta=1.0$  (blue line),  $\beta=2.0$  (green dashed line), and  $\beta=1.7$  (shaded black line). The vertical red dashed line at  $T=13.3$  K, represents the median value for the distribution with  $\beta=1.7$ .

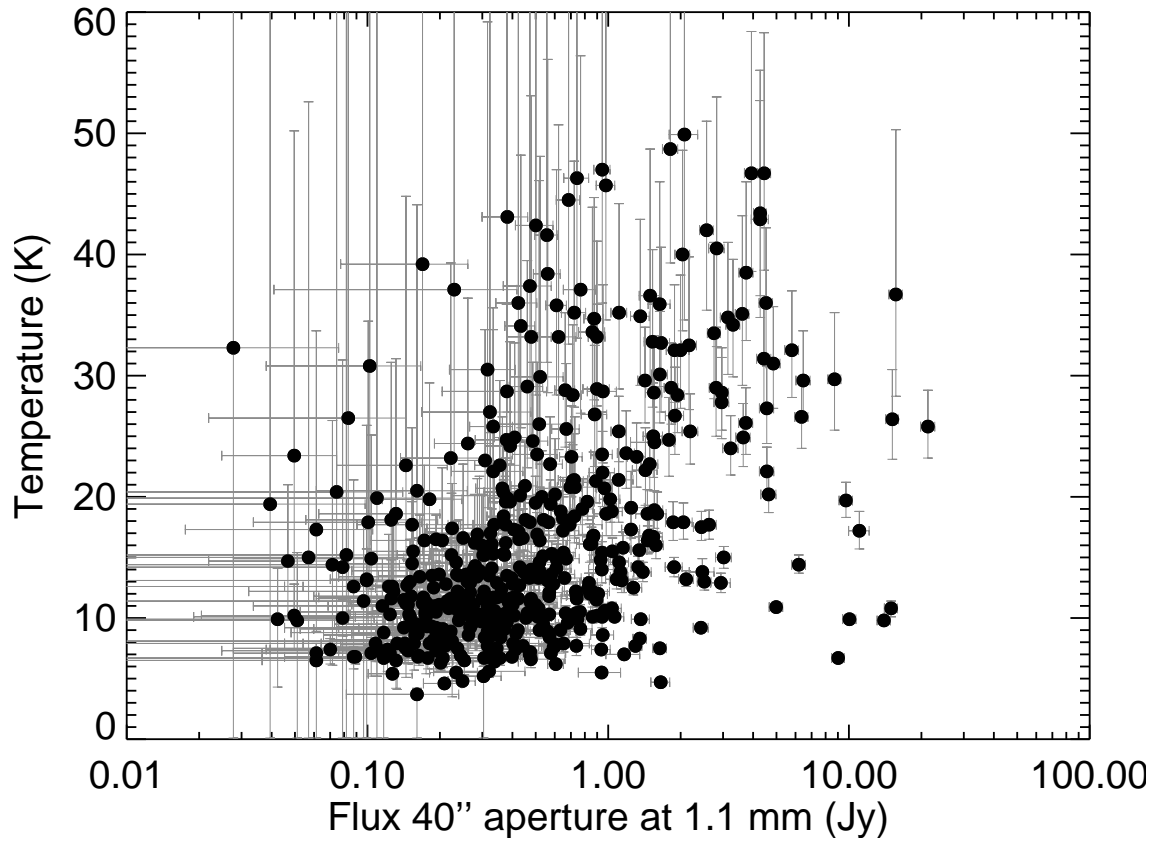


Figure 2.19 Temperature determined for the BGPS sample of sources as a function of their 40'' aperture flux, for a spectral index  $\beta = 1.7$ . Only sources with good fits in the determination of temperature ( $T \leq 50$  K) are shown in this figure.

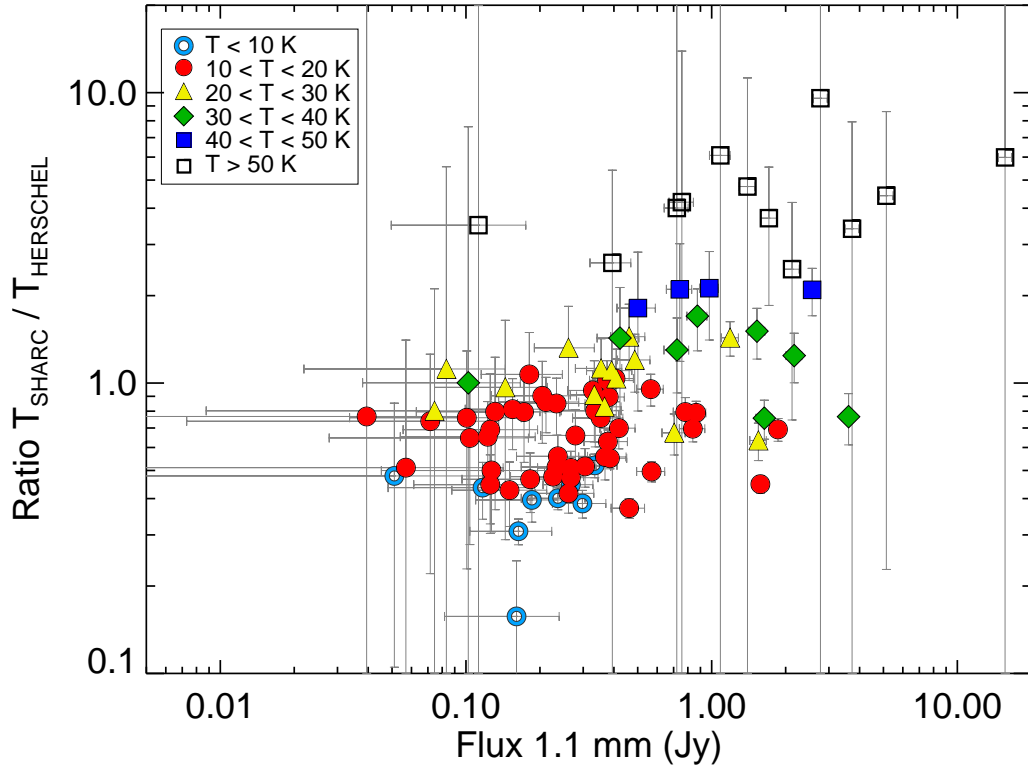


Figure 2.20 Comparison between estimated temperatures with  $350 \mu\text{m}$  and  $1.1 \text{ mm}$  continuum maps,  $T_{SHARC}$ , and temperatures obtained from SED fitting by Battersby et al. (2011),  $T_{Herschel}$ , as a function of  $40''$  aperture flux density at  $1.1 \text{ mm}$  for a sample of 91 BGPS sources toward  $l = 30^\circ$ . The colors shown in the legend represent different ranges for  $T_{SHARC}$ . The weighted mean value of the ratio is  $0.50 \pm 0.01$  for sources with  $T_{SHARC} \leq 50 \text{ K}$ .

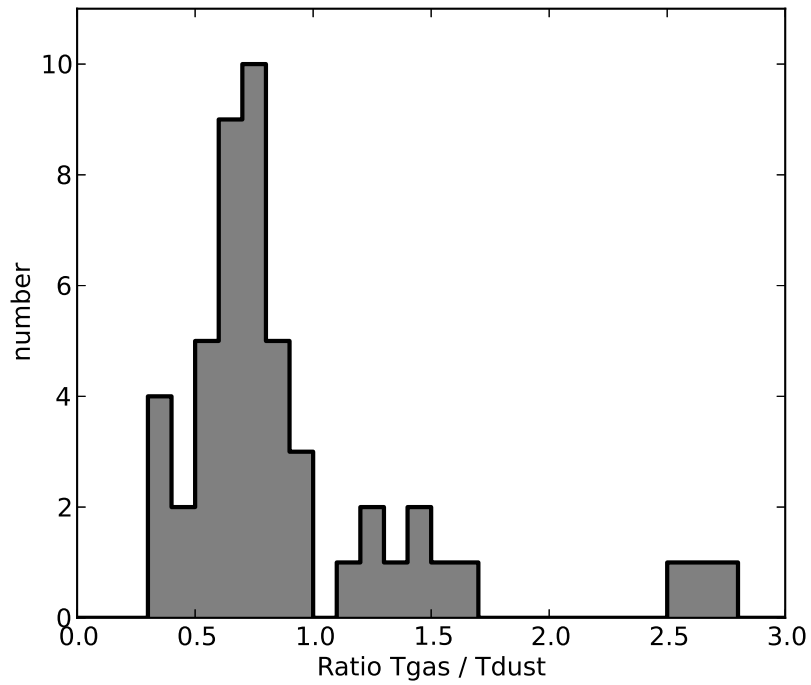


Figure 2.21 Distribution of the ratio of gas temperature determined from  $\text{NH}_3$  observations  $T_{gas}$ , and fitted dust temperatures  $T_{dust}$ , for the sample of 49 BGPS sources with  $T_{gas} < 30$  K and  $T_{dust} < 50$  K, ranges in which both values are relatively well determined. The average and median values of this distribution are 0.88 and 0.76, respectively.

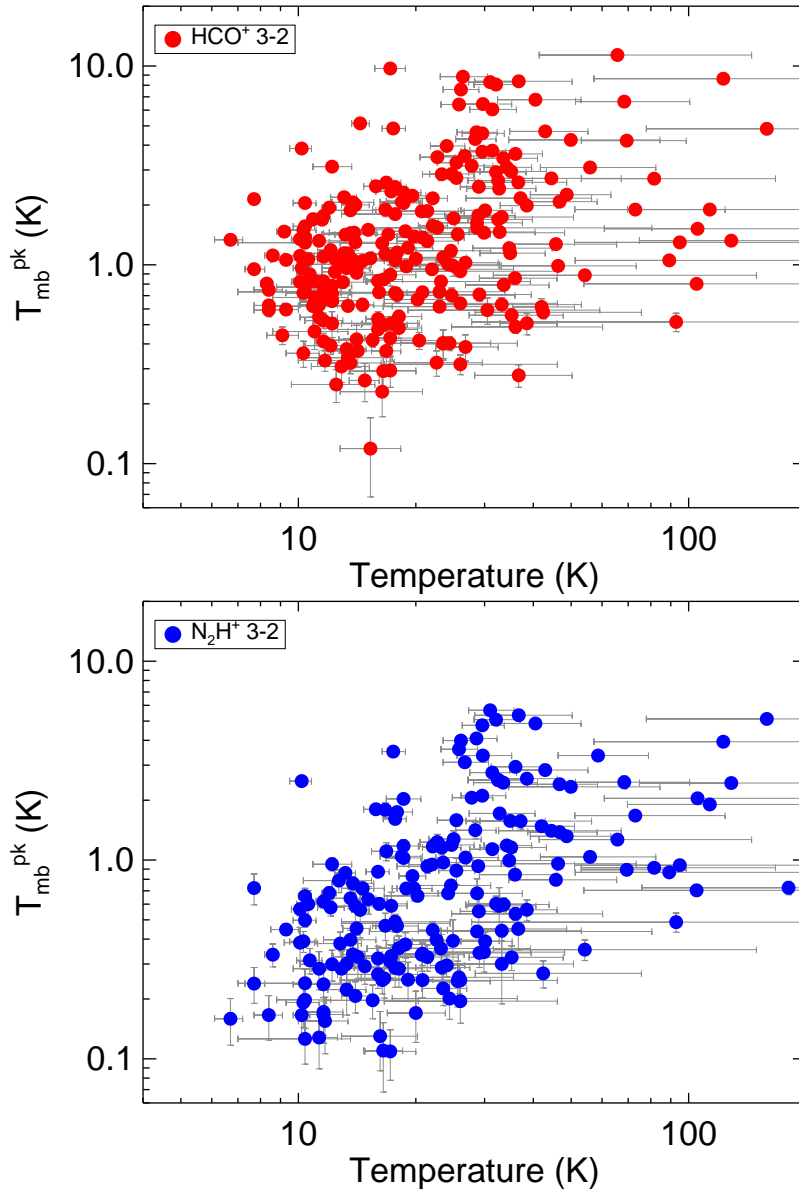


Figure 2.22 Peak main-beam temperature, as a function of dust temperature, for the sample of BGPS sources from the spectroscopy catalog by Shirley et al. (2013) that are contained in the SHARC-II maps. The number of sources with  $\text{HCO}^+$  emission is 250, and the number of sources with  $\text{N}_2\text{H}^+$  emission is 199.

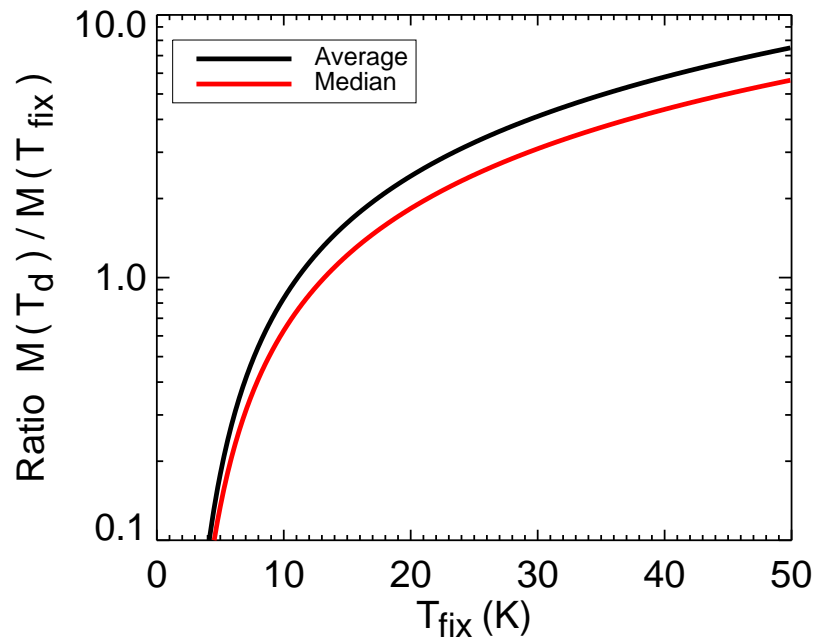


Figure 2.23 Ratio between the mass estimated using color temperatures determined from  $350 \mu\text{m}$  and  $1.1 \text{ mm}$  images ( $T_{clump}$ ), and the mass estimated using a single fiducial temperature ( $T_{fix}$ ). For the sample of 514 V2.1 BGPS sources with good fits in the determination of temperature, using  $T_{fix} = 20 \text{ K}$ , the average value of the source masses will be underestimated by a factor of  $\sim 2.4$ .



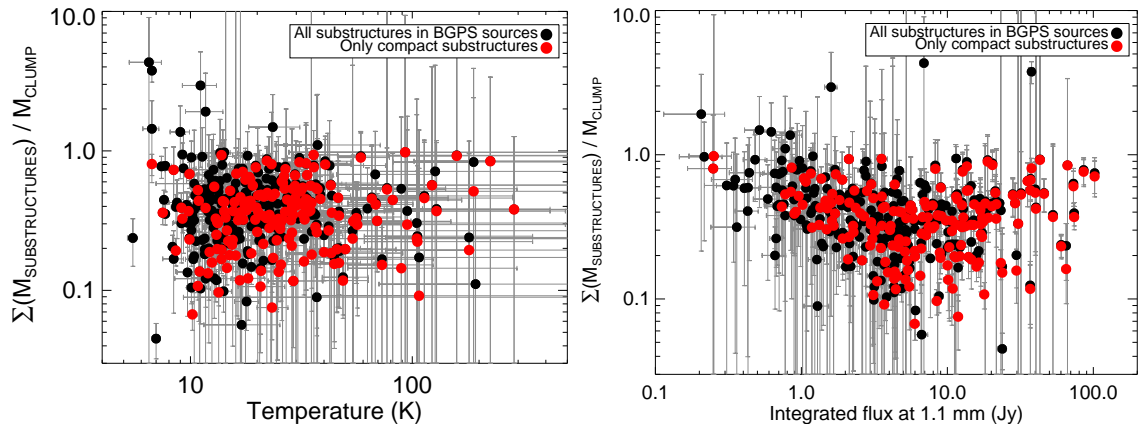


Figure 2.24 Comparison between the total estimated mass from  $350 \mu\text{m}$  substructures on each clump, and the mass estimated at  $1.1 \text{ mm}$  for that parental BGPS clump, as a function of dust temperature (left) and the integrated flux of the BGPS sources (right). Black points consider for  $M_{\text{substructures}}$  the flux contribution from all high-resolution sources in the parental clumps, and have a weighted averaged mass fraction  $\Sigma(M_{\text{substructures}})/M_{\text{clump}}$  of  $0.22 \pm 0.01$ . Red points only consider the flux contribution from strong, compact substructures, and the weighted averaged mass fraction of this distribution is  $0.19 \pm 0.01$ .

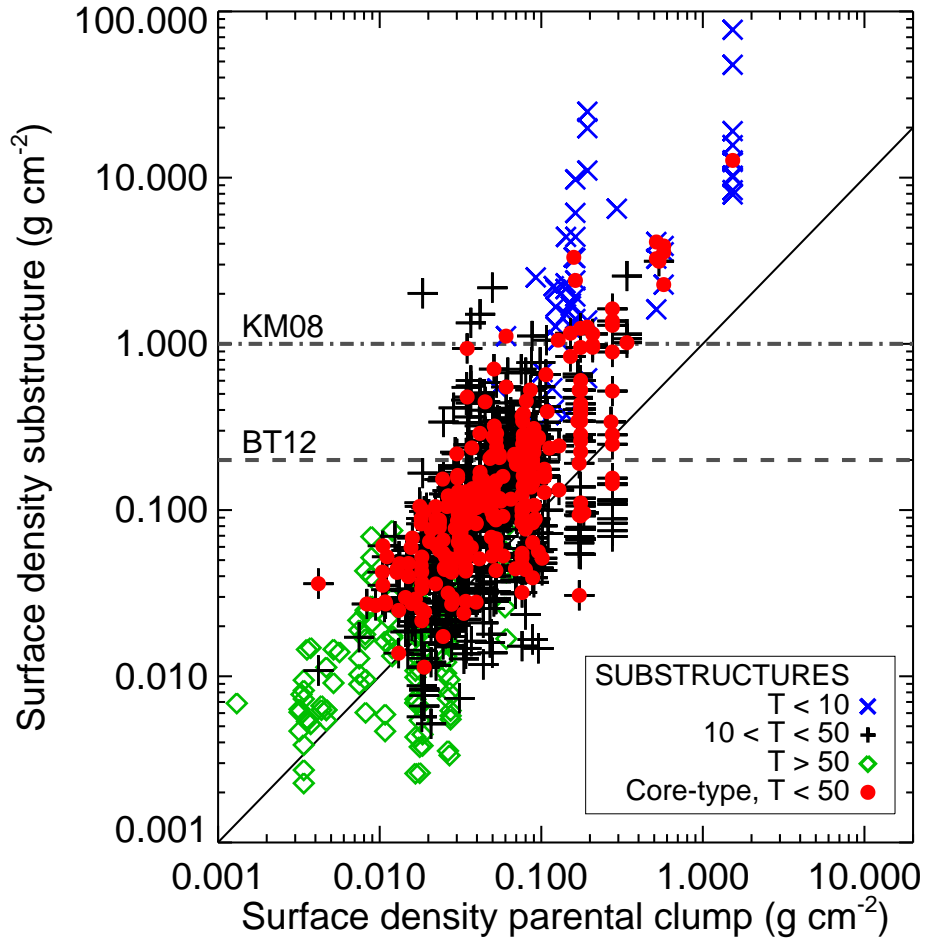


Figure 2.25 Estimation of surface density between substructures and parental clumps. Solid line represent the locus of equality between the structures. Black crosses show the bulk of the sources, with temperatures between 10–50 K. Blue marks show sources with low temperature ( $T < 10$  K), likely to overestimating the surface density. Grey marks show sources with high temperature ( $T > 50$  K). Red points show only those compact, core-type substructures found in the parental clumps, with detections above  $10\sigma$ . Most of these compact sources have higher surface 2-3 times larger than their parental clump. Several of these compact sources have surface densities above theoretical thresholds of  $0.2 \text{ g cm}^{-2}$  (Butler & Tan, 2012) or  $1.0 \text{ g cm}^{-2}$  (Krumholz & McKee, 2008) for massive star formation.

## Chapter 3

# Physical characteristics of G331.5-0.1: The luminous central region of a Giant Molecular Cloud

### 3.1 Introduction

Massive stars play a key role in the evolution of the Galaxy; hence they are important objects of study in astrophysics. Although their number is much smaller than the low mass stars, they are the principal source of heavy elements and UV radiation, affecting the process of formation of stars and planets (Bally et al., 2005) and the physical, chemical and morphological structure of galaxies (e.g. Kennicutt , 1998, 2005).

Diverse studies show that massive stars are formed in the denser regions of giant molecular clouds (GMC) (Churchwell et al., 1990; Cesaroni et al., 1991; Plume et al., 1992; Bronfman et al., 1996). The formation process of high-mass stars is, however, still under debate (Garay & Lizano, 1999). Observationally, recently formed massive stars cannot be detected at optical wavelengths because they are embedded within regions with high dust extinction. Another problem arises from theoretical considerations: a star with a mass larger than eight solar masses starts burning hydrogen during the accretion phase and the radiation pressure may halt or even reverse the infall process (e.g. Larson & Starrfield, 1971; Kahn, 1974; Yorke

& Kruegel, 1977; Wolfire & Cassinelli, 1987; Edgar & Clarke, 2004; Kuiper et al., 2010). Due to these difficulties, a paradigm that explains the formation of massive stars does not exist (Zinnecker & Yorke, 2007; McKee & Ostriker, 2007), contrary to the successful model accepted for low mass stars. Understanding the physical process that dominates during the early stages of the formation of massive stars and its influence back on its harboring molecular gas requires a study of the physical conditions of the environment previous to the star formation or at very early stages.

The object of our study is one of the most massive GMCs in the Southern Galaxy, at  $l = 331.5^\circ$  and  $b = -0.1$ , in the tangent region of the Norma spiral arm (Bronfman et al., 1985, 1989). Several observations have shown that the central region of this GMC harbors one of the most extended and luminous regions of massive star formation in the Galactic disk. Single dish radio continuum observations show the presence of an extended region of ionized gas (G331.5-0.1), with an angular size of  $\sim 3' - 4'$  (projected size 6.5-8.7 pc at a distance of 7.5 kpc), close to the peak CO position of the GMC (Shaver & Goss, 1970; Caswell & Haynes, 1987). From observations of the H109 $\alpha$  and H110 $\alpha$  hydrogen recombination lines, Caswell & Haynes (1987) determined that the line central velocity of the ionized gas is  $\sim -89 \text{ km s}^{-1}$ , similar to the peak velocity of the GMC. The dynamical timescale of the region of ionized gas is  $\sim 8.5 \times 10^5$  years, and the rate of ionizing photons required to excite the H II region is  $1.1 \times 10^{50} \text{ s}^{-1}$ . In addition, IRAS observations show the presence of an extended source, with an angular size similar to that of the ionized region and a FIR luminosity of  $3.6 \times 10^6 L_\odot$ .

While both the ionizing photon rate and the FIR luminosity could be provided

by a single O4 ZAMS star, it is most likely that the ionization and the heating of the region is provided by a cluster of massive OB stars. This explanation is supported by *Midcourse Space Experiment* and *Spitzer Space Telescope*-GLIMPSE survey data, which show that there are several sites of massive star formation spread over a region of  $\sim 6'$  in diameter. Bronfman et al. (2000) showed that toward the  $l = 331^\circ$  galactic longitude, there is a peak in the number density of IRAS sources with colors of ultracompact H II (UCHII) regions and associated with CS(2  $\rightarrow$ 1) emission, which are thought to correspond to massive star forming regions.

Evidence of active star formation in the G331.5–0.1 GMC is further provided by the detection of OH and methanol maser emission (Goss et al., 1970; Caswell et al., 1980; Caswell, 1997, 1998; Pestalozzi et al., 2005), as well as H<sub>2</sub>O maser emission (Caswell, private communication). Hydroxyl masers are known to be excellent indicators of UCHII regions, whereas methanol maser emission is a common phenomenon in regions of massive star formation (Menten et al., 1986) and H<sub>2</sub>O maser emission is thought to be a probe of the earliest stages of massive star formation (Furuya, 2003). Also, within a radius of 4.5' centered on the peak position of G331.5–0.1 there are three objects from the Red MSX Source (RMS) catalog of Massive Young Stellar Objects (MYSOs) candidates (Urquhart et al., 2008), further indicating that the G331.5–0.1 central region is an active region of massive star formation. In addition, Bronfman et al. (2008) showed the presence of a compact, extremely high velocity molecular outflow in the G331.5–0.1 region, suggesting that it is driven by one of the most luminous and massive objects presently known. The G331.5–0.1 region is thus an ideal region to study extremely active massive star formation in GMCs.

Here we present observations and a thorough analysis of the G331.5–0.1 region with dust continuum and molecular line emission data. Section 2 describes the telescopes used and methods of data acquisition. Section 3 describes the results of our study at several scales, starting from GMCs ( $\sim 100$  pc), to molecular clump sizes ( $\sim 1$  pc) and reaching sub-parsec scales in our interferometric data. This analysis considers dust emission and different molecular line tracers, along with mid-infrared and far-infrared data from SPITZER, MSX and IRAS telescopes, and free-free emission at cm wavelengths. Section 4 describes the physical parameters derived from our observations, including mass, density and bolometric luminosity estimates. We also include a rotational temperature analysis for a massive and energetic molecular outflow in the G331.5–0.1 GMC central region. Our results are summarized in section 5.

### 3.2 Observations

We observed emission in several molecular lines and continuum bands using several telescopes located in northern Chile: the NANTEN telescope of Nagoya University at the Las Campanas observatory, the 15-m Swedish-ESO Submillimetre Telescope (SEST) at La Silla, the 10-m Atacama Submillimeter Telescope Experiment (ASTE) at Pampa la Bola, and the 12-m Atacama Pathfinder Experiment (APEX) located in Llano Chajnantor. We also made observations using the Australia Telescope Compact Array (ATCA) located at Narrabri, Australia. The basic parameters of the molecular line observations are summarized in Table 4.1. Column 1 gives the telescope used, Col. 2 and 3, the observed transition and line frequency,

respectively. Col. 4 and 5 the half-power beam width and the main beam efficiency. Col. 6 to 10 give, respectively, the number of positions observed, the angular spacing, the integration time on source per position, the channel width and the resulting rms noise in antenna temperature, for each of the observed transitions. The observing parameters for the continuum observations are summarized in Table 3.2.

### 3.2.1 NANTEN Telescope

The NANTEN telescope is a 4-m diameter millimeter telescope designed for a large-scale survey of molecular clouds. With this telescope we observed the emission in the CO( $J = 1 \rightarrow 0$ ) ( $\nu = 115271.202$  MHz) and C<sup>18</sup>O( $J = 1 \rightarrow 0$ ) ( $\nu = 109782.173$  MHz) lines during several epochs between 1999 and 2003. The half-power beam width of the telescope at 115 GHz is 2.6', providing a spatial resolution of 5.7 pc at the assumed distance of the source of 7.5 kpc. The observed maps consisted in grids of 585 positions for the CO emission and 440 positions for the C<sup>18</sup>O emission, with spacing between observed positions of 2.5' (nearly the beam size of the instrument at the observed frequencies). The front-end was a superconductor-isolator-superconductor (SIS) receiver cooled down to 4 K with a closed-cycle helium gas refrigerator, and the backend was an acousto-optical spectrometer (AOS) with 2048 channels. The total bandwidth was 250 MHz and the frequency resolution was 250 kHz, corresponding to a velocity resolution of  $\sim 0.15$  km s<sup>-1</sup>. The typical system noise temperature was  $\sim 250$  K (SSB) at 115 GHz and  $\sim 160$  K (SSB) at 110 GHz. The main beam efficiency of the telescope is 0.89. A detailed description of the telescope and its instruments are given by Ogawa et al. (1990), Fukui et al. (1991) and Fukui & Sakakibara (1992).

Data reduction were made using the NANTEN Data Reduction Software (NDRS).

### **3.2.2 Swedish-ESO Submillimetre Telescope (SEST)**

#### **3.2.2.1 Millimeter continuum**

The 1.2 mm continuum observations were carried out using the 37-channel hexagonal Sest IMaging Bolometer Array (SIMBA) during 2001. The passband of the bolometer has an equivalent width of 90 GHz and is centered at 250 GHz (1200  $\mu\text{m}$ ). At the frequency band of SIMBA, the telescope has an effective beamwidth of 24'' (FWHM), that provides a spatial resolution of 0.87 pc at a distance of 7.5 kpc. The rms noise achieved is  $\sim 50$  mJy/beam. Data reduction was made using the package MOPSI (Mapping On-Off Pointing Skydip Infrared). The maps were calibrated from observations of Mars and Uranus and the calibration uncertainties are estimated to be lower than 20%.

#### **3.2.2.2 Molecular lines**

With SEST we observed the emission in the CS( $J = 5 \rightarrow 4$ ) ( $\nu = 244935.644$  MHz) and CS( $J = 2 \rightarrow 1$ ) ( $\nu = 97980.968$  MHz) lines during May 2001. The half-power beam width and the main beam efficiency of the telescope were 22'' and 0.48 at 245 GHz, and 52'' and 0.73 at 98 GHz, respectively. The total bandwidth was 43 MHz and the frequency resolution was 43 kHz, corresponding to a velocity resolution of  $\sim 0.05$  km s $^{-1}$  for the CS(5  $\rightarrow$ 4) observations, and a velocity resolution of  $\sim 0.13$  km s $^{-1}$  for the CS(2  $\rightarrow$ 1) observations. The typical system noise temperature was 350 K for CS(5  $\rightarrow$ 4) observations and 250 K for CS(2  $\rightarrow$ 1) observations. The CLASS



(Continuum and Line Analysis Single-dish Software) software, part of the GILDAS package, was used for data reduction.

Figures 3.17 and 3.18 present maps of the observed spectra toward the G331.5–0.1 central region in the CS(2 →1) and CS(5 →4) line emission over 81 positions with a spacing of 45". The CS(2 →1) map then is well sampled, while the CS(5 →4) map is undersampled at this spacing, considering the smaller beam size at that frequency.

### 3.2.3 Atacama Submillimeter Telescope Experiment

With ASTE we observed the emission in the CS( $J = 7 \rightarrow 6$ ) ( $\nu = 342882.950$  MHz) and  $^{13}\text{CO}(J = 3 \rightarrow 2)$  ( $\nu = 330587.957$  MHz) lines during 2005 July and 2006 July. ASTE has a beam size at 350 GHz of 22" (FWHM). For both transitions 167 positions were sampled, within a  $\sim 360'' \times 360''$  region with 22.5" spacing in position-switched mode, with the OFF position located at  $\alpha_{2000} = 16^h 14^m 08.4^s$  and  $\delta_{2000} = -51^\circ 37' 23''$ . The system temperatures ranged between 179 and 233 K, resulting in a rms noise antenna temperature of typically 0.1 K for an integration time of 4 minutes.

Main-beam temperatures,  $T_{MB} = T_A^*/\eta_{MB}$ , obtained by dividing the antenna temperature  $T_A^*$  by the main-beam efficiency,  $\eta_{MB}$ , are used throughout the analysis. During the first part of the observations, we mapped a grid of 88 positions, with  $\eta_{MB} = 0.65$ . On July, 2006. we completed the map observing 79 new positions, with  $\eta_{MB} = 0.77$ . The 1024 channels of the 350 GHz band receiver provided a bandwidth of 128 MHz, and a channel width of 0.125 MHz. The data reduction was carried out by use of the AIPS-based software package NEWSTAR developed at NRO.

Figures 3.19 and 3.20 present maps of the observed spectra toward the G331.5–0.1

central region in the CS( $7 \rightarrow 6$ ) and  $^{13}\text{CO}(3 \rightarrow 2)$  line emission over 167 positions with a spacing of  $22.5''$  (similar to the beam size of the instrument at this frequency).

### 3.2.4 Atacama Pathfinder Experiment

#### 3.2.4.1 Millimeter continuum: the ATLASGAL survey

The millimeter observations of the region were made as part of the APEX Telescope Large Area Survey of the Galaxy (ATLASGAL) project, which is a collaboration between the Max Planck Gesellschaft (MPG: Max Planck Institute für Radioastronomie, MPIfR Bonn, and Max Planck Institute für Astronomie, MPIA Heidelberg), the European Southern Observatory (ESO) and the Universidad de Chile. ATLASGAL is an unbiased survey of the inner region of the Galactic disk at 0.87 mm, made using the 295-channel hexagonal array Large Apex BOLometer CAmera (LABOCA), that operates in the 345 GHz atmospheric window, with a bandwidth of about 60 GHz. The angular resolution is  $18.6''$  (HPBW) (corresponding to a resolution of 0.68 pc at a distance of 7.5 kpc) and the total field of view is  $11.4'$ . The survey covers an area of  $\pm 1.5^\circ$  in galactic latitude, and  $\pm 60^\circ$  in longitude, with a sensitivity of 50 mJy/beam (Schuller et al., 2009).

#### 3.2.4.2 Molecular lines

Using the APEX-2a heterodyne receiver, we observed the emission in the SiO( $J = 7 \rightarrow 6$ ) ( $\nu = 303926.809$  MHz), SiO( $J = 8 \rightarrow 7$ ) ( $\nu = 347330.635$  MHz), SO( $8_7 \rightarrow 7_6$ ) ( $\nu = 304077.844$  MHz) and SO( $8_8 \rightarrow 7_7$ ) ( $\nu = 344310.612$  MHz) lines during May 2007. The telescope has a beam size of  $17.5''$  at 345 GHz, corresponding

to a spatial resolution of 0.63 pc at a distance of 7.5 kpc. The main beam efficiency of the telescope is  $\eta_{MB} = 0.73$  and the system temperature was  $\sim 170$  K. The observations were made toward the peak position of the CO(7  $\rightarrow$ 6) outflow emission ( $\alpha_{2000} = 16^h 12^m 10.09^s$  and  $\delta_{2000} = -51^\circ 28' 38.4''$ ) reported by Bronfman et al. (2008). The data were reduced using the CLASS software of the GILDAS package.

### 3.2.5 Australia Telescope Compact Array

The ATCA radio continuum observations were made in two epochs: 2002 November using the 6A configuration and 2005 November using the 1.5C configuration. These configurations utilize all six antennas and cover east-west baselines from 0.5 to 6 km. Observations were made at the frequencies of 4.80 and 8.64 GHz (6 and 3.6 cm), with a bandwidth of 128 MHz. The FWHM primary beam of ATCA at 4.8 GHz and 8.6 GHz are, respectively, 10' and 6'. The total integration time in each frequency was 2.5 hr.

The calibrator PKS 1600-48 was observed before and after every on-source scan in order to correct the amplitude and phase of the interferometer data due to atmospheric and instrumental effects. The flux density was calibrated by observing PKS 1934-638 (3C84) for which values of 5.83 Jy at 4.8 GHz and 2.84 Jy at 8.6 GHz were adopted. Standard calibration and data reduction were performed using MIRIAD (Sault et al., 1995). Maps were made by Fourier transformation of the uniformly weighted interferometer data using the AIPS task IMAGR. The noise level in the 4.8 and 8.6 GHz images are, respectively, 0.41 and 0.37 mJy beam<sup>-1</sup>. The resulting synthesized (FWHM) beams are  $2.7'' \times 1.8''$  at 4.8 GHz and  $1.5'' \times 1.0''$

at 8.6 GHz.

### 3.3 Results

#### 3.3.1 The G331.5–0.1 Giant Molecular Cloud

Figure 3.1 shows grey scale maps and contours of the velocity integrated CO and C<sup>18</sup>O emission between  $330.9^\circ < l < 332.3^\circ$  and  $-0.42^\circ < b < 0.14^\circ$ . The range of the velocity integration is from  $-117.7$  to  $-73.2$  km s<sup>-1</sup>, chosen from the average spectrum of the region (shown in Fig. 3.2). The contours represent 20% to 90%, in steps of 10%, of the peak intensity of each map (297.6 K km s<sup>-1</sup> for CO, 19.6 K km s<sup>-1</sup> for C<sup>18</sup>O). The rms noise of the CO and C<sup>18</sup>O maps are 19.8 K km s<sup>-1</sup> and 0.98 K km s<sup>-1</sup>, respectively. The emission at 50% of the peak is shown with a thicker contour in each map. The CO emission arises from an extended cloud elongated along the galactic longitude, with major and minor axes of 81.7' and 18.9' (full width at half-power), which imply linear sizes of 178 by 41 pc at the assumed distance of 7.5 kpc. The peak position on the CO map is located at  $l = 331.5^\circ$ ,  $b = -0.125^\circ$ , with an intensity of 297.6 K km s<sup>-1</sup>.

To estimate the kinematic distance of the G331.5–0.1 cloud, we locate it in the subcentral point at the source longitude, for the following reasons. Using the Galactic rotation curve derived by Alvarez et al. (1990), with  $R_0 = 8.5$  kpc and  $V_0 = 220$  km s<sup>-1</sup>, and a mean average velocity of  $-92.8$  km s<sup>-1</sup> for the integrated GMC spectrum, the near kinematic distance would be 5.7 kpc and the far kinematic distance 9.2 kpc. While the near distance has been preferred by Goss et al. (1972), the far distance has been considered by Kerr & Knapp (1970). However, the GMC has two velocity

components, at  $-100 \text{ km s}^{-1}$  and  $-90 \text{ km s}^{-1}$  (see section 3.3.2.2), the lowest one almost reaching the terminal velocity due to pure rotation of  $-110 \text{ km s}^{-1}$ . Caswell & Haynes (1987) reported hydrogen recombination line absorption at  $l = 331.515^\circ$ ,  $b = -0.069$ , with a  $V_{LSR}$  of  $-89 \text{ km s}^{-1}$ , as well as  $\text{H}_2\text{CO}$  absorption lines at  $-99.8$  and  $-89.3 \text{ km s}^{-1}$ , favoring the far distance, even when they adopted the near distance following Goss et al. (1972). Nevertheless, Bronfman et al. (1996) reported emission in  $\text{CS}(2 \rightarrow 1)$  from the IRAS point source 16086-5119, at  $l = 331.552$ ,  $b = -0.115$ , with a  $V_{LSR}$  of  $-100.7$ , corresponding to the higher velocity component, so the continuum source for the  $\text{H}_2\text{CO}$  absorption lines at both velocities is most probably the IRAS point source at  $-100 \text{ km s}^{-1}$ , setting them both at the near distance.

Given the large spread in velocity of the integrated spectrum; the presence of two velocity components for the GMC, the lowest one almost reaching the terminal velocity; and the conflicting evidence for locating the GMC at the far or near distance, we will consider in the estimation of its physical parameters that the G331.5–0.1 cloud is located in the tangent of the Norma spiral arm, at a distance of  $\sim 7.5 \text{ kpc}$ , corresponding to the subcentral point. With this assumption, the distance of the GMC will have an estimated uncertainty of  $\sim 30\%$ , given by the near and far kinematic positions, leading to an uncertainty in the estimation of masses and luminosities of a factor of  $\sim 2$ . A recent study of kinematic distances using HI absorption done by Jones & Dickey (2012) puts the region G331.552-0.078, located toward the peak position of our CO emission maps, at the Norma spiral arm tangent point distance, at  $7.47 \text{ kpc}$ , a similar value to the one used in the present work.

The emission in the  $\text{C}^{18}\text{O}(1 \rightarrow 0)$  line has a position angle of approximately

$\sim 30^\circ$  with respect to the galactic longitude, with observed major and minor axes of  $18.2'$  and  $11.6'$ , respectively ( $39.7 \times 25.3$  pc at a distance of 7.5 kpc). The size of the  $\text{C}^{18}\text{O}$  structure is four times smaller than the CO cloud. It is necessary to keep in mind that the appearance and dimension of a molecular cloud depend strongly on the tracer used to observe it (Myers, 1995). The CO observations most likely trace all the gas within the GMC, including low and high column density gas, while  $\text{C}^{18}\text{O}$  is tracing only the high column density gas. The  $\text{C}^{18}\text{O}$  peak position coincides with the peak emission in the CO(1  $\rightarrow$ 0) line. Fitting gaussian profiles to the spectra observed at  $l=331.5^\circ$ ,  $b=-0.125^\circ$ , we determine  $V_{lsr} = -89.7$  km s $^{-1}$  and  $\Delta V$  (FWHM) = 3.8 km s $^{-1}$  for CO, and  $V_{lsr} = -89$  km s $^{-1}$  and  $\Delta V$  (FWHM) = 2.9 km s $^{-1}$  for the  $\text{C}^{18}\text{O}$  emission.

Using the  $\text{C}^{18}\text{O}(1 \rightarrow 0)$  integrated map, we define the central region of the G331.5–0.1 GMC as the region that emits more than seventy percent of the peak integrated emission (red dashed box in Figure 3.1). This area is  $7'$  in size ( $\sim 15$  pc at the source distance) and it is centered at  $l = 331.523^\circ$ ,  $b = -0.099^\circ$  ( $\alpha_{2000} = 16^h 12^m 12^s$  and  $\delta_{2000} = -51^\circ 28' 00''$ ). The central region is a single structure coherent in velocity, as it can be seen on the position-velocity maps for CO and  $\text{C}^{18}\text{O}$  (Fig. 3.3). Further observations with better angular resolution have shown that this region has two velocity components, with a difference of  $\sim 12$  km s $^{-1}$  (see section 3.3.2.2).

Figure 3.4 shows a map of the emission observed at  $870 \mu\text{m}$  by ATLASGAL between  $331^\circ < l < 332^\circ$  and  $-0.4^\circ < b < 0.15^\circ$ . Overlaid is a velocity integrated  $\text{C}^{18}\text{O}$  emission map. The range of velocity integration and the emission contours are the same as for Figure 3.1. The 0.87 mm map also shows the position of 13

sources (two of them are double sources) from the RMS catalog in the proximity of the tangent area of the Norma spiral arm. Clearly there is a concentration of dust continuum emission sources towards the defined central region of the cloud (red dashed box in Figure 3.4). Six millimeter-wave compact sources were identified inside the defined G331.5–0.1 GMC central region, and three of them are associated to RMS sources. This suggests an active formation of massive stars within the central region of G331.5–0.1 GMC.

### 3.3.2 The G331.5–0.1 GMC central region

In this section we present a detailed study of millimeter continuum and molecular line observation toward the  $7' \times 7'$  area defined in the previous section as the G331.5–0.1 GMC central region. The beam sizes of the observations ( $\sim 30''$ ) are approximately five times better than the observations of CO(1  $\rightarrow$ 0) and C<sup>18</sup>O(1  $\rightarrow$ 0), and they give information in the  $\sim 1$  pc at a distance of 7.5 kpc. The maps of G331.5–0.1 GMC have been presented so far in galactic coordinates, mainly to show the extension of this region in galactic longitude. Nevertheless, we present our observations here and following sections in a more traditional style using equatorial coordinates.

#### 3.3.2.1 Dust emission: Millimeter continuum observations

Figure 3.5 presents maps of the 1.2 mm and 0.87 mm dust continuum emission observed with the SEST and APEX telescopes respectively. They reveal the presence of six dust continuum substructures with strong emission. We labeled these sources

as MM1, MM2, MM3, MM4, MM5 and MM6, according to increasing order in right ascension. The observed parameters of the millimeter sources are given in Table 3.3. Column 3 and 4 give their peak position. Column 5 and 6 give the peak flux density and the total flux density, respectively, the latter measured with the AIPS task IMEAN. Column 7 give the deconvolved major and minor FWHM angular sizes obtained from Gaussian fits to the observed spatial distribution. Column 8 gives the physical size of the sources, obtained from the geometric mean of the angular size obtained at 1.2 mm and 0.87 mm, and considering a distance to the sources of 7.5 kpc. The average size of the millimeter sources within the G331.5–0.1 central region is 1.6 pc. Following the description of Williams et al. (2000), we refer to these millimeter-wave structures as clumps.

### 3.3.2.2 Molecular line emission

The observed parameters of the line emission detected at the peak position of the millimeter clumps are given in Table 3.4. Also given are the parameters of an average spectrum of each clump for the CS(7 →6) and <sup>13</sup>CO(3 →2) lines, obtained from a three by three map centered at the peak position of each clump. For non-gaussian profiles, the velocity spread  $\Delta V$  is estimated from  $\Delta V = I(T_A^*) / T_A^*{}_{Peak}$ . The equations for  $I(T_A^*)$  and its associated error  $\sigma_{I(T_A^*)}^2$  are obtained from (e.g. Shirley et al., 2003)

$$\begin{aligned}
 I(T_A^*) &= \int_{v_1}^{v_2} T_A^* dv \\
 \sigma_{I(T_A^*)}^2 &= \langle \sqrt{\Delta v_{line} \delta v_{chan}} \sigma_{T_A^*} \rangle_{map}^2 + \sigma_{base}^2 ,
 \end{aligned}
 \tag{3.1}$$



with  $\Delta v_{line} = v_2 - v_1$  is the full velocity range of the line emission,  $\delta v_{chan}$  is the velocity resolution of the spectrometer, and  $\sigma_{T_A^*}$  is the uncertainty in the antenna temperature. The additional error contribution  $\sigma_{base}$ , from residual variation in the baseline due to linear baseline subtraction, was not considered. The error  $\sigma_{I(T_A^*)}$  was propagated into the uncertainty in  $\Delta V$ .

Figure 3.6 shows the spectra toward the peak intensity position of the clumps MM1 through MM6 in the molecular lines CS(2  $\rightarrow$  1), CS(5  $\rightarrow$  4), CS(7  $\rightarrow$  6) and  $^{13}\text{CO}$ (3  $\rightarrow$  2).

We discovered in the CS(7  $\rightarrow$  6) map the presence of a broad and strong wing emission toward the peak position of the brightest 1.2 mm clump (MM3), at  $\alpha_{2000} = 16^h 12^m 10.13^s$  and  $\delta_{2000} = -51^\circ 28' 37.5''$ . The characteristics of this spectrum, along with other CO emission lines, were previously reported by Bronfman et al. (2008). Their analysis indicates that it corresponds to an unresolved, energetic and massive molecular outflow (flow mass of  $\sim 55 M_\odot$ ; momentum of  $\sim 2.4 \times 10^3 M_\odot \text{ km s}^{-1}$ ; kinetic energy of  $\sim 1.4 \times 10^{48}$  ergs).

The molecular transitions SiO(7  $\rightarrow$  6), SiO(8  $\rightarrow$  7), SO(8<sub>7</sub>  $\rightarrow$  7<sub>6</sub>) and SO(8<sub>8</sub>  $\rightarrow$  7<sub>7</sub>) were observed toward the position of the molecular outflow. SO and SiO trace shocked gas towards dense cores (see Gottlieb et al. 1978; Rydbeck et al. 1980; Swade 1989; Miettinen et al. 2006) where the density is high enough to excite it. High-velocity SiO and SO has been observed in some of the most powerful molecular outflows (e.g. Welch et al. 1981; Plambeck et al. 1982; Martin-Pintado et al. 1992), and our current understanding is that SiO and SO are evaporated from the dust grains when the shock velocity is greater than about 20 km s<sup>-1</sup>, depending on

the composition of the grain-mantle in the preshock gas (e.g. Schilke et al. 1997). Figure 3.7 shows the spectra of the SO and SiO lines.

Line profiles of the CS and CO emission show the presence of two distinct velocity components centered at  $\sim -88.9$  and  $\sim -100.8$  km s<sup>-1</sup> (see Fig. 3.6). Maps of the velocity integrated emission in the ranges of -93.9 to -84.4 km s<sup>-1</sup> and -105.4 to -95 km s<sup>-1</sup> are presented in Figures 3.8 and 3.9. Clumps MM1 and MM6 are associated with the lowest velocity component ( $\sim -100.8$  km s<sup>-1</sup>), while clumps MM2, MM3, MM4 and MM5 are associated with the high velocity component ( $\sim -88.9$  km s<sup>-1</sup>). There is a good correspondence between CS(7 → 6) map and the dust continuum emissions (see Fig. 3.10), indicating that these two tracers are probes of regions with similar physical conditions. We will refer to the region including the four high-velocity clumps as the “**complex of clumps**” in the G331.5–0.1 GMC central region.

The angular sizes of the structures defined by the integration of the CS(7 → 6) line and associated to the clumps, and the nominal radii resulting from the deconvolution of the telescope beam size, are summarized in Table 3.5. For MM3, the CS(7 → 6) peak position and average spectra are well fitted with two gaussian components. The first component corresponds to the broad wind emission, associated with the high-velocity molecular outflow, while the second gaussian component corresponds to the ambient gas emission. For the peak position spectrum, the gaussian fit of the wing emission has  $T_A^* = 0.92 \pm 0.12$  K and  $\Delta v = 31.1 \pm 2.8$  km s<sup>-1</sup> (FWHM), and the ambient gas gaussian fitting has  $T_A^* = 1.40 \pm 0.12$  K and  $\Delta v = 6.1 \pm 0.1$  km s<sup>-1</sup> (FWHM).

### 3.3.2.3 Mid-infrared and far-infrared emission

Infrared observations are a useful tool to study the process of massive star formation. At these wavelengths, radiation is less affected by extinction than at visible wavelengths; therefore infrared observations can give us information of the nearby environment of newly formed massive stars that are surrounded and obscured by cool dust. The mid-infrared (range 5 - 25  $\mu\text{m}$ ) and far-infrared (range 25 - 400  $\mu\text{m}$ ) observations are dominated by the thermal emission from dust, that re-radiates the absorbed UV radiation from newly born OB stars and reprocessed photons from the ionized nebula. In the mid-infrared range the contribution from polycyclic aromatic hydrocarbons, from which emission is strong in photo-dissociation regions, is also significant.

Figure 3.11 shows a three color infrared image made using data from the IRAC bands at 3.6  $\mu\text{m}$  (blue), 4.5  $\mu\text{m}$  (green) and 8.0  $\mu\text{m}$  (red), overlaid with contours of the emission at 0.87 mm. While the infrared emission agrees with the millimeter emission in the global sense, the 8.0  $\mu\text{m}$  emission seems to trace the envelope of a ionized region, with the millimeter emission of the complex of clumps, surrounding this structure. Also, we find strong and compact emission associated with the MM3 clump in the three IRAC bands, with an angular size of  $\sim 14''$ .

For each millimeter clump, we measured the integrated flux densities in the four Spitzer IRAC bands (8.0  $\mu\text{m}$ , 5.8  $\mu\text{m}$ , 4.5  $\mu\text{m}$  and 3.6  $\mu\text{m}$ , Fazio et al. 2004), on the MSX bands (21.3  $\mu\text{m}$ , 14.7  $\mu\text{m}$ , 12.1  $\mu\text{m}$  and 8.3  $\mu\text{m}$ , Mill et al. 1994) and IRAC bands (100  $\mu\text{m}$ , 60  $\mu\text{m}$ , 25  $\mu\text{m}$  and 12  $\mu\text{m}$ , Neugebauer et al. 1984). The results are tabulated in Table 3.6.

### 3.3.3 High angular resolution observations of the G331.5–0.1 GMC central region.

We present in this section interferometric observations of radio continuum emission toward the G331.5–0.1 GMC central region. The beam size of the observations ( $\sim 2''$ ) allow us to study compact structures at sub-parsec scales. The analysis also considered association between the radio continuum components found in recent OH and methanol maser catalogs at high resolution.

#### 3.3.3.1 Radio continuum emission

Figure 3.12 shows contour maps of the radio continuum emission at 6 and 3.6 cm towards the central region of G331.5–0.1 GMC. Our observations reveal the presence of four distinct compact radio sources within the mapped field of  $10'$ , labeled as components A,B,C and D, and associated with the clumps MM1, MM4, MM3 and MM6, respectively (see Fig. 3.11). The positions, flux densities and beam deconvolved sizes (FWHM) of the sources, obtained with the AIPS task IMFIT, are given in Table 3.7.

Components A, B and D are also associated, respectively, with the G331.4904-00.1173, G331.5414-00.0675, and G331.5582-00.1206 RMS sources candidates to MYSOs (Urquhart et al., 2008). The detection of radio emission indicate that these three candidates are UCHII regions and therefore related with a more evolved state than a genuine MYSOs. The brightest radio source (component C) is associated with the very energetic outflow detected towards the G331.5–0.1 central region (Bronfman et al., 2008). Figure 3.13 shows the radio spectra of all four components. Components B

and C exhibit an increasing flux density with frequency, thus they could be optically thick ultracompact regions or stellar wind sources. The dotted line corresponds to the best fit of the spectral energy distribution (SED) assuming that they correspond to regions of ionized gas with uniform density, and that the emission can be modeled as a modified blackbody, with  $I_\nu = B_\nu(T_e)[1 - \exp(-\tau_\nu)]$  and the opacity  $\tau$  estimated from (Wilson et al., 2009):

$$\tau_\nu = 8.235 \times 10^{-2} \left( \frac{T_e}{\text{K}} \right)^{-1.35} \left( \frac{\nu}{\text{GHz}} \right)^{-2.1} \left( \frac{EM}{\text{pc cm}^{-6}} \right), \quad (3.2)$$

with  $T_e$  the electron temperature and  $EM$  the emission measure. We considered  $T_e = 10^4$  K. The derived spectral indexes of component B and C are given in Column 9 of Table 3.7. Component B has a spectral index of the radio emission between 4.8 and 8.6 GHz of  $0.8 \pm 0.2$ , similar the value expected for a spherical, isothermal, constant-velocity model of stellar wind (Reynolds, 1986). The error in the determination of spectral indexes include the 5% uncertainty in the absolute flux density scale. Component C spectral index has a value of  $1.2 \pm 0.2$  already reported by Bronfman et al. (2008). This index suggests that source C corresponds to an ionized jet which is likely to drive the associated energetic molecular outflow.

Components A and D are more extended than B and C, and they present a decrease in the integrated flux density from 4.8 to 8.6 GHz. We attribute this particular behavior to an observational artifact, that could be related with a less complete uv-coverage at higher frequency. An estimation of the flux density inside an area comparable with the beam size ( $\sim 2.5''$ ) gives an almost flat spectrum for

component A, and even though the flux still decreases with frequency for component D, the flux difference was reduced from 47% to 30%. We expected for both sources, A and D, a flat spectral energy distribution in the radio continuum, consistent with the free-free emission from a thermal source.

### 3.3.3.2 Maser emission

Earlier studies of masers across our Galaxy have shown that regions of high-mass star formation can be associated with OH, H<sub>2</sub>O and Class II methanol masers (Caswell et al., 1995; Szymczak et al., 2002). In particular, OH masers are usually considered signposts of UCHII regions, while methanol masers are found associated to hot molecular cores, UCHII regions and near-IR sources (Garay & Lizano, 1999; Bartkiewicz & van Langevelde, 2012). Therefore, OH and methanol masers often coincide, and they are found in regions with active star formation. With this in mind, we searched in methanol and OH surveys toward the Norma spiral arm region. We found three sources from the 6-GHz methanol multibeam maser catalog from Caswell et al. (2011). Two of them, 331.542-0.066 and 331.543-0.066, are toward the MM4 millimeter clump and they are coincident, within the errors, with the radio component B. The velocity of the peak reported for these maser sources are  $-86 \text{ km s}^{-1}$  and  $-84 \text{ km s}^{-1}$  respectively, within  $5 \text{ km s}^{-1}$  difference from the molecular line velocities of MM4 shown in Table 3.4, and therefore consistent with the ambient velocity of the complex of clumps. The third 6668 MHz methanol maser spot, 331.556-0.121 ( $\alpha_{2000} = 16^{\text{h}}12^{\text{m}}27.21^{\text{s}}$  and  $\delta_{2000} = -51^{\circ}27'38.2''$ ), is associated with the MM6 millimeter clump, it has a velocity at peak emission of  $-97 \text{ km s}^{-1}$ , similar to values

found with molecular lines for MM6, and it is located  $5.8''$  ( $\sim 3$  times the beamsize in the maser catalog) away from the peak position of radio component D. Each of these three maser spots has a counterpart OH maser (Caswell, 2009, 1998). The peak position of radio component C ( $\alpha_{2000} = 16^h 12^m 10.04^s$ ,  $\delta_{2000} = -51^\circ 28' 37.7''$ ) is coincident, within the errors, with the interferometrically derived position of an 1665 MHz OH maser spot (G331.512-0.103; Caswell, 1998). No methanol class II emission was reported towards the outflow up to a detection limit of 0.6 Jy (Caswell et al., 2011). The position of masers in the G331.5–0.1 GMC central region is shown in Fig. 3.12, along their association with the radio continuum sources.

No methanol or OH emission is associated with the MM1, MM2 and MM5 clumps. While MM1 is associated with the radio component A and with a RMS source, no other signposts of star formation activity are found in MM2 and MM5, suggesting that these clumps are in a state prior to the formation of an UCHII region.

## 3.4 Discussion

### 3.4.1 Physical properties of the GMC

The mass of the G331.5–0.1 GMC can be derived from the CO NANTEN observations considering two approaches: a) from the relation of the integrated intensity of CO line emission with  $H_2$  mass, and b) using the local thermodynamic equilibrium (LTE) formalism.

In the first method, the column density  $N(H_2)$  of the GMC is considered proportional to the CO emission integrated in velocity [ $I(\text{CO}) = \int T_{\text{mb}}(^{12}\text{CO}) dv$  (K km s $^{-1}$ )],

$$N(\text{H}_2) = X(\text{CO})I(\text{CO}), \quad (3.3)$$

where  $X(\text{CO})$  corresponds to the Galactic average  $I(\text{CO})$ -to- $N(\text{H}_2)$  conversion factor. With this approach, the luminosity of CO,  $L_{\text{CO}} = D^2 \iint T_{\text{mb}}(^{12}\text{CO}) dv d\Omega$ , is proportional to the total mass of the cloud,  $M_{\text{CO}} = \alpha_{\text{CO}} L_{\text{CO}}$ . Here we assumed that  $X(\text{CO}) = 2.3 \times 10^{20} \text{ cm}^{-2} (\text{K km s}^{-1})^{-1}$  (Kennicutt & Evans, 2012), which implies  $\alpha_{\text{CO}} = 4.6 M_{\odot} (\text{K km s}^{-1} \text{pc}^2)^{-1}$  with correction for helium.

From the CO emission integrated in the velocity range between -117.7 and -73.3  $\text{km s}^{-1}$ , we measured a CO luminosity of  $1.9 \times 10^6 (\text{K km s}^{-1} \text{pc}^2)$ , giving a total mass of  $8.7 \times 10^6 M_{\odot}$  and an average column density of  $3.2 \times 10^{22} \text{ cm}^{-2}$ .

We also estimate the column density and mass from the  $\text{C}^{18}\text{O}$  observation following the derivation of physical parameters presented by Bourke et al. (1997). Assuming that the emission is optically thin,

$$\begin{aligned} N(\text{C}^{18}\text{O}) &= 2.42 \times 10^{14} \frac{T_{\text{ex}} + 0.88}{1 - \exp(-5.27/T_{\text{ex}})} \\ &\times \frac{1}{J(T_{\text{ex}}) - J(T_{\text{bg}})} \int T_{\text{mb}}(\text{C}^{18}\text{O}) dv, \end{aligned} \quad (3.4)$$

and

$$\begin{aligned} \left( \frac{M_{\text{LTE}}}{M_{\odot}} \right) &= 1.44 \left( \frac{\mu_m}{2.72 m_{\text{H}}} \right) \left( \frac{[\text{H}_2/\text{C}^{18}\text{O}]}{3.3 \times 10^6} \right) \left( \frac{D}{\text{kpc}} \right)^2 \\ &\times \frac{T_{\text{ex}} + 0.88}{1 - \exp(-5.27/T_{\text{ex}})} \frac{1}{J(T_{\text{ex}}) - J(T_{\text{bg}})} \\ &\times \iint T_{\text{mb}}(\text{C}^{18}\text{O}) dv d\Omega, \end{aligned} \quad (3.5)$$



where  $T_{\text{ex}}$  is the excitation temperature of the transition,  $T_{\text{bg}}$  is the background temperature,  $v$  is in  $\text{km s}^{-1}$ ,  $\Omega$  is in  $\text{arcmin}^2$ , and

$$J(T) = \frac{h\nu}{k} \frac{1}{\exp(h\nu/kT) - 1} .$$

We assumed an abundance ratio  $[\text{CO}/\text{C}^{18}\text{O}] = 330$ , which is the suggested value for GMCs inside the 4 kpc Galactic molecular ring (Wilson & Rood, 1994). Considering an average temperature of 15 K, the total mass value for this region is then  $3.5 \times 10^6 M_{\odot}$ , with an average column density  $N(\text{C}^{18}\text{O}) = 4.0 \times 10^{15} \text{ cm}^{-2}$ . The mass estimated is less than half that the mass obtained from CO, but the denser material traced by  $\text{C}^{18}\text{O}$  is emitting in a smaller area. Since the continuum millimeter sources are seen in the  $\text{C}^{18}\text{O}$  map concentrated within the area defined for the G331.5–0.1 central region, we estimated the column density towards the position of the peak emission on this map, considering a higher temperature than the average value used for the GMC. For  $T = 20$  K, we obtained  $N(\text{C}^{18}\text{O}) = 2.6 \times 10^{16} \text{ cm}^{-2}$ .

### 3.4.2 Physical properties of the G331.5–0.1 central region.

#### 3.4.2.1 Spectral energy distributions

To determine the dust temperature and bolometric luminosity of the GMC central region and each clump, we fit the spectral energy distribution (SED) using a modified blackbody model,

$$S_{\nu} = \Omega B_{\nu}(T_d) \{1 - \exp(-\tau_{\nu})\}, \quad (3.6)$$

where  $S_\nu$  is the flux density of the source,  $B_\nu$  is the Planck function,  $\Omega$  is the solid angle subtended by the emitting region, and  $T_d$  is the dust temperature. The optical depth,  $\tau_\nu$ , is assumed to depend on frequencies,  $\tau_\nu = (\nu/\nu_0)^\beta$ , with  $\beta$  the power law spectral index and  $\nu_0$  the frequency at which the optical depth is unity.

SEDs were fit for each clump and for the region harboring the complex of clumps at high velocity. The flux densities were measured in the areas shown in dashed boxes in figure 3.5, using the data observed at 1.2 mm and 0.87 mm, and at four IRAS, MSX and SPITZER bands (see Table 3.6). A good fit to the emission from the complex of clumps required three dust components at different temperatures (see Fig. 3.14). For the individual clumps, we only considered a two component model, without considering the SPITZER data (Fig. 3.15). In the case of MM1 clump, the source is only marginally detected at short wavelengths, and therefore we only considered a cold component for the model. The parameters obtained (see Table 3.8) are typical of regions associated with high-mass star formation (Faúndez et al., 2004). For the six clumps in the G331.5–0.1 central region, the average temperature of the cold fit component is 32 K, and for the region containing the complex of clumps, the cold component has a fitted temperature of 30 K. The average value of the spectral indexes of the cold component for the six clumps is 1.8, which is consistent with the OH5 model from Ossenkopf & Henning (1994). The steeper value of the spectral index found for the region containing the complex of clumps at high velocity could be due to low recovery of some extended flux in the 1.2 mm image. The bolometric luminosities were obtained according to:

$$L_{bol} = F_{int} 4\pi d^2, \quad (3.7)$$

with  $d$  the distance of the source. The results are tabulated in Table 3.9. The clumps have an average bolometric luminosity of  $L_{bol} = 5.7 \times 10^5 L_{\odot}$ , above the average value derived by Faúndez et al. (2004) of  $2.3 \times 10^5 L_{\odot}$ . If the source of energy of each clump is due to a single object, then it will correspond to a star with spectral type of O6 ZAMS or earlier (Panagia, 1973). However, an inspection of Figure 3.11 shows that the clumps are unlikely to be associated with just one star. Most likely the G331.5–0.1 central region has several early type stars, considering, for example, that a dozen of O9 ZAMS stars will produce the luminosity of a single O6 ZAMS star.

#### 3.4.2.2 Masses and densities

Using the mm continuum observations we determined the mass of each clump from the expression:

$$M_d = \frac{S_{\nu} D^2}{k_{\nu} B_{\nu}(T_d)}, \quad (3.8)$$

where  $S_{\nu}$  is the flux density,  $D$  is the distance to the source,  $k_{\nu}$  is the dust mass coefficient,  $B_{\nu}$  is the Planck function, and  $T_d$  is the dust temperature.

We use a dust opacity of  $1 \text{ cm}^2 \text{ g}^{-1}$  at 1.2 mm and  $1.89 \text{ cm}^2 \text{ g}^{-1}$  at 0.87 mm, which are values computed for typical conditions of dense protostellar objects (Ossenkopf & Henning, 1994). The opacity at 0.87 mm is obtained from a linear interpolation in the OH5 model of grains with thin ice mantles. Assuming a dust-to-gas mass ratio of  $R = M_d/M_g = 0.01$ , the total mass of each clump is given

by:

$$\begin{aligned} \left(\frac{M_{1.2mm}}{M_{\odot}}\right) &= 20.82 \left(\frac{S}{\text{Jy}}\right) \left(\frac{1 \text{ cm}^2 \text{ g}^{-1}}{\kappa_{1.2mm}}\right) \left(\frac{D}{\text{kpc}}\right)^2 \\ &\times \left\{ \exp\left(\frac{11.990}{T_d}\right) - 1 \right\} \end{aligned} \quad (3.9)$$

$$\begin{aligned} \left(\frac{M_{0.87mm}}{M_{\odot}}\right) &= 4.29 \left(\frac{S}{\text{Jy}}\right) \left(\frac{1.89 \text{ cm}^2 \text{ g}^{-1}}{\kappa_{0.87mm}}\right) \left(\frac{D}{\text{kpc}}\right)^2 \\ &\times \left\{ \exp\left(\frac{16.538}{T_d}\right) - 1 \right\} . \end{aligned} \quad (3.10)$$

The mass of the clumps is estimated using the temperature obtained from the SED fitting. The masses estimated from the emission at 0.87 mm and 1.2 mm are given in Table 3.10. If we instead considered a fiducial temperature  $T = 20$ , for example, the masses will be in general larger by a factor of two with respect to the masses estimated using the temperature from SED fitting. We note that the masses obtained from 1.2 mm are lower than the masses obtained from the 0.87 mm observations typically by a factor of two. Uncertainties in the dust opacities or in the dust temperatures could give other possible explanations. A better determination of the power law index  $\beta$  of the dust optical depth could improve this value. Considering the results from the 1.2 mm observations, the average mass of the millimeter clumps in the central region is  $3.2 \times 10^3 M_{\odot}$ . The total mass and size of the complex of clumps are  $\sim 2.1 \times 10^4 M_{\odot}$  and  $\sim 15$  pc. These values are bigger than the average masses and sizes of dust compact sources associated with high-mass star forming regions ( $\sim 5 \times 10^3 M_{\odot}$  and  $\sim 1$  pc, Faúndez et al., 2004). However, each clump is by itself like one of these sources.

Columns 4 and 5 in Table 3.10 give the number density and surface density

estimated from the emission at 1.2 mm for each clump. The density and the average surface density were computed using the expressions

$$n = \frac{M}{(4/3)\pi R^3 \mu m_H}; \quad \Sigma = \frac{M}{\pi R^2} \quad , \quad (3.11)$$

assuming spherical morphologies and a mean mass per particle of  $\mu = 2.29$  (corrected for helium). The clumps have an average gas surface density of  $0.4 \text{ g cm}^{-2}$  ( $\sim 1900 \text{ M}_\odot \text{ pc}^{-2}$ ). The values of the surface densities are similar to those of the densest clumps reported in a study of massive star-forming regions by Dunham et al. (2011), and they are above the surface density threshold of  $\Sigma_{th} = 129 \pm 14 \text{ M}_\odot \text{ pc}^{-2}$  found by Heiderman et al. (2010) for “efficient” star formation. In an independent study Lada et al. (2010) found a threshold of  $\Sigma_{th} = 116 \text{ M}_\odot \text{ pc}^{-2}$ . Only one of the millimeter clumps in the G331.5–0.1 central region have gas surface densities above  $1 \text{ g cm}^{-2}$ , which is the theoretical lower limit determined by Krumholz & McKee (2008) to avoid excessive fragmentation and form massive stars. Nevertheless the inner and densest parts of each clump, mapped with a high-density gas tracer such as CS(7 → 6), will exceed this requirement.

### 3.4.2.3 Virial and LTE masses

For a spherical, nonrotating cloud of radius  $R$ , and a gaussian velocity profile  $\Delta v$  (FWHM), the virial mass is given by

$$\left(\frac{M_{virial}}{M_\odot}\right) = 210 \left(\frac{\Delta v}{\text{km s}^{-1}}\right)^2 \left(\frac{R}{\text{pc}}\right), \quad (3.12)$$

assuming that the broadening due to optical depth is negligible. Column 6 in Table 3.10 shows the virial mass obtained for each clump, determined from the

CS(7 → 6) molecular line. The radius of the clumps was computed from the deconvolved angular size measured from the maps, and  $\Delta v$  from the spatially average CS line emission (see Table 3.5). In the case of MM3, the outflow clump, we considered only the gaussian component corresponding to the ambient gas emission. The total mass obtained for the complex of clumps is  $1.4 \times 10^4 M_\odot$ .

We also estimate the mass of the complex of clumps from the  $^{13}\text{CO}(3 \rightarrow 2)$  observations using the LTE formalism, assuming that this transition is optically thin. Using eq. [A4] from Bourke et al. (1997), the mass is estimated from the  $^{13}\text{CO}$  line in a similar way than the  $\text{C}^{18}\text{O}$  mass presented in section 4.1:

$$\begin{aligned} \left( \frac{M_{\text{LTE}}}{M_\odot} \right) &= 0.082 \left( \frac{\mu_m}{2.72 m_{\text{H}}} \right) \left( \frac{[\text{H}_2/^{13}\text{CO}]}{5.3 \times 10^5} \right) \left( \frac{D}{\text{kpc}} \right)^2 \\ &\times \frac{T_{\text{ex}} + 0.88}{1 - \exp(-15.87/T_{\text{ex}})} \frac{\exp(15.87/T_{\text{ex}})}{J(T_{\text{ex}}) - J(T_{\text{bg}})} \\ &\times \iint T_{\text{mb}}(^{13}\text{CO}) \, dv d\Omega, \end{aligned} \quad (3.13)$$

where  $v$  is in  $\text{km s}^{-1}$  and  $\Omega$  is in  $\text{arcmin}^2$ . We considered an excitation temperature of 30 K and a  $[\text{CO}/^{13}\text{CO}]$  abundance ratio of 53 (Wilson & Rood, 1994). The mass obtained for the complex of clumps is  $2.9 \times 10^4 M_\odot$ , which agrees within a factor of two with the mass estimates from millimeter continuum emission and virial mass from CS.

Once the mass of the complex and of the individual clumps were obtained, we are able to investigate whether the clumps at low velocity (MM1 and MM6) and the complex of clumps at high velocity are bounded. Considering that the velocity

difference  $v_{dif}$  of the two systems is  $11.9 \text{ km s}^{-1}$ , and that the projected distance  $r_p$  from their respective center of mass is  $\sim 5 \text{ pc}$ , a gravitationally bounded system will require a mass of  $\sim 2 \times 10^5 M_\odot$ , exceeding the total mass of the clumps by a factor of ten. Then, we discarded that the low velocity clumps are gravitationally bounded to the complex. We cannot rule out for the moment other kind of interaction between these two systems.

#### 3.4.2.4 Rotational temperatures of the G331.512-0.103 outflow

When observations of several transitions in a particular molecule are available, it is possible to estimate the rotational temperature,  $T_{rot}$  and the total column density,  $N_T$  from a rotational diagram analysis, assuming that the lines are optically thin and that excitation temperatures follow  $T_{ex} \gg T_{bg}$  (e.g. Linke et al., 1979; Blake et al., 1987; Garay et al., 2002). We considered the equation

$$\frac{N_k}{g_k} = \frac{3k \int T_{mb} dv}{8\pi^3 \mu^2 \nu S}, \quad (3.14)$$

with  $S$  the intrinsic line strength,  $\mu$  the permanent dipole moment,  $N_k$  and  $g_k$  the column density and degeneracy of the upper transition state. If we assume that a single rotational temperature is responsible for the thermalization of the population distribution, then

$$\frac{N_k}{g_k} = \frac{N_T}{Q(T_{rot})} \exp(-E_u/k T_{rot}), \quad (3.15)$$

with  $N_T$  is the total molecular column density summed over all the levels,  $E_u$  is the

energy of the upper transition state, and  $Q(T_{rot})$  is the rotational partition function at temperature  $T_{rot}$ .

The previous analysis was made on the redshifted and blueshifted wing emission of the G331.512-0.103 outflow, using the SiO transitions  $J = 7 \rightarrow 6$  and  $J = 8 \rightarrow 7$ , and the SO transitions  $J_K = 8_8 \rightarrow 7_7$  and  $J_K = 8_7 \rightarrow 7_6$ . We consider two ranges of velocity for integration: -144.1 to -95.6, and -79.9 to -16.3. The values computed for  $T_{rot}$ ,  $Q(T_{rot})$  and  $N_T$  from the diagrams are tabulated in Table 3.11. The uncertainty in the estimates of rotational temperatures are obtained using the error in the estimate of  $I(T_{MB}) = I(T_A^*)/\eta_{MB}$  (see equation 3.1), and propagating them through equations 3.14 and 3.15

For SiO transitions, the rotational temperatures of the blue and red wing are  $123 \pm 15$  K and  $138 \pm 29$  K respectively, with column densities ranging between  $2.6 \times 10^{13}$  and  $3.3 \times 10^{13}$   $\text{cm}^{-2}$ . For the SO lines, the rotational temperatures of the blue wing ( $94 \pm 5$  K) is higher than the temperature of the red wing, ( $77 \pm 4$  K), with column densities varying between  $3.8 \times 10^{14}$  and  $4.6 \times 10^{14}$   $\text{cm}^{-2}$ . We note that since our estimation of temperatures has been done with only two transitions for each molecule, these values should be considered as a rough estimation and more transitions should be considered for a more robust estimation of the temperature in the wings of the molecular outflow. ALMA observations recently obtained toward this source (Merello et al., in prep.) shows several transitions of  $\text{SO}_2$  that will give better determination of rotation temperatures.



### 3.4.2.5 Comparison with other massive star-forming regions

In this section we compare the characteristics of the clumps in G331.5–0.1 with those of the sample of 42 massive star forming regions presented by Molinari et al. (2008). In that study, a 8-1200  $\mu\text{m}$  SED for each YSO is presented, using MSX, IRAS and sub-mm/mm data, aiming to relate their envelope mass with the bolometric luminosity. Those sources that were fitted with an embedded ZAMS envelope were named as “IR”, and those fitted only with a modified blackbody peaking at large wavelengths were named “MM”. A further classification, as “P” or “S” source, was made according if they were the primary (most massive) object in the field or not. The parameters fitted for MM sources gave temperatures with a median value of  $\sim 20$  K, and spectral indexes  $\beta$  with median value  $\sim 1.5$ . Our sample of millimeter clumps in the G331.5–0.1 GMC central region seems to correspond to the MM sources in their sample.

Figure 3.16 shows a  $L_{bol} - M_{env}$  diagram for the sample of 42 sources from Molinari et al. (2008), including the values derived for our six millimeter clumps (filled circles). Clearly our sources are more massive and luminous than most of the objects in that sample, with bolometric luminosities in general an order of magnitude larger than their MM sources. It is worth noticing that the six clumps in the G331.5–0.1 GMC central region fall in the  $L_{bol} - M_{env}$  diagram toward the prolongation of the isochrone of  $\sim 10^5$  yrs shown in Fig. 9 of Molinari et al. (2008). This trend is associated with the end of the accelerated accretion phase, and therefore our sample of millimeter clumps MM1-MM6 may be in the phase of envelope clean-up, observationally identified with Hot Cores and UC H II regions by Molinari et al.

Similar conclusions can be obtained when compared with the study with *Herschel* of star-forming compact dust sources from Elia et al. (2010), where modified blackbody SED fitting was made for sources extracted in two  $2^\circ \times 2^\circ$  Galactic plane fields centered at  $l=30^\circ$ ,  $b=0^\circ$ , and  $l=59^\circ$ ,  $b=0^\circ$  using the five Hi-GAL bands (70, 160, 250, 350 and 500  $\mu\text{m}$ ). Our sample of millimeter clumps remains in the extreme of most luminous and massive millimeter sources.

### 3.5 Summary

Observations at several wavelengths show that the G331.5–0.1 GMC central region is one of the largest, most massive and most luminous regions of massive star formation in the Galactic disk. We have obtained a multi-tracer view of this source using radio, (sub)millimeter and infrared images, starting from an analysis of the global parameters of the parent GMC of this region at a scale of  $1^\circ$ , and continuing to smaller scales until identifying and resolving features at a scale inside G331.5–0.1 of one arcsecond.

Millimeter maps reveal that the G331.5–0.1 GMC central region harbors six massive clumps within a region of 15 pc in diameter. The average size, mass and molecular hydrogen density of these clumps are 1.6 pc,  $3.2 \times 10^3 M_\odot$  and  $3.7 \times 10^4 \text{ cm}^{-3}$ , respectively. From the SED analysis of the clumps, we estimated an average dust temperature and bolometric luminosity of 32 K and  $5.7 \times 10^5 L_\odot$ , respectively. These values are similar to those of massive and dense clumps typically found in high-mass star forming regions. The high number of massive and dense clumps within G331.5-0.1 makes it one of the most densely populated GMC central regions in the

Milky Way. At the center of the brightest, most massive and densest molecular clump within G331.5-0.1 central region, we discovered one of the most luminous and massive protostellar objects presently known, which drives a powerful molecular outflow and a thermal jet. The outflow is not resolved at a resolution of  $\sim 7''$ , so it could be directed along the line of sight. Further high resolution observations with ALMA are underway and will be reported elsewhere.

We found four compact radio sources along the G331.5–0.1 central region. Two of them have a spectral index consistent with ionized stellar winds, which originated from young luminous objects. In particular, one of these radio sources is located at the center of the molecular outflow clump, which suggests that is associated with its driving source.

Table 3.1. Parameters of the molecular line observations of the G331.5 region

Telescope	Line	Frequency (MHz)	Beam (FWHM)	$\eta_{mb}$	Pos. obs.	Spacing	$t_{in}$ (sec)	$\Delta v$ (km s <sup>-1</sup> )	Noise (K)
NANTEN	CO(1 → 0)	115271.202	2.6'	0.89	585	2.5'	≤60	0.15	0.35
	C <sup>18</sup> O(1 → 0)	109782.173	2.6'	0.89	440	2.5'	≤600	0.15	0.1
SEST	CS(2 → 1)	97980.968	52''	0.73	81	45''	180	0.130	0.06
	CS(5 → 4)	244935.644	22''	0.48	81	45''	180	0.052	0.08
ASTE	<sup>13</sup> CO(3 → 2)	330587.957	22''	0.61	167	22.5''	240	0.113	0.1
	CS(7 → 6)	342882.950	22''	0.61	167	22.5''	240	0.109	0.1
APEX	SiO(7 → 6)	303926.809	20''	0.7	1	...	670	0.48	0.04
	SiO(8 → 7)	347330.635	17.6''	0.7	1	...	670	0.42	0.04
	SO(8 <sub>7</sub> → 7 <sub>6</sub> )	304077.844	20''	0.7	1	...	680	0.48	0.04
	SO(8 <sub>8</sub> → 7 <sub>7</sub> )	344310.612	17.6''	0.7	1	...	680	0.48	0.05

Table 3.2. Parameters of continuum observations of the G331.5 region

Telescope	Frequency (GHz)	Bandwidth (GHz)	Beamwidth (FWHM)	Noise (mJy/beam)
SEST	250	90	24''	50
APEX	345	60	18.6''	50
ATCA	4.8	0.128	2.7'' × 1.8''	0.41
	8.6	0.128	1.5'' × 1.0''	0.37

Table 3.3. Observed parameters of dust continuum emission

Condensation	$\lambda$ ( $\mu\text{m}$ )	$\alpha$ (J2000)	$\delta$ (J2000)	Peak flux density (Jy/beam)	Flux density (Jy)	Angular size ('')	Diameter (pc)
MM1	1200	16 12 07.69	-51 30 07.1	1.2	3.1	36×32	1.3
	870	16 12 07.57	-51 30 03.5	5.0	27.4	44×31	
MM2	1200	16 12 08.43	-51 27 11.1	1.2	6.4	62×40	1.9
	870	16 12 06.90	-51 27 15.6	4.5	38.3	59×49	
MM3	1200	16 12 09.34	-51 28 39.0	2.9	11.6	50×34	1.2
	870	16 12 10.13	-51 28 39.5	13.8	66.7	36×30	
MM4	1200	16 12 10.08	-51 25 51.0	1.2	4.9	56×38	1.9
	870	16 12 10.73	-51 25 45.5	4.6	42.7	72×45	
MM5	1200	16 12 14.45	-51 27 42.6	1.2	7.6	76×34	1.9
	870	16 12 15.25	-51 27 39.41	5.5	52.5	69×38	
MM6	1200	16 12 27.28	-51 27 41.8	1.6	3.5	32×32	1.2
	870	16 12 27.45	-51 27 39.1	8.0	27.6	30×21	

Table 3.4. Molecular Lines: Observed Parameters

Line	Peak			Average		
	$T_A^*$ (K)	$V$ (km s <sup>-1</sup> )	$\Delta v$ (km s <sup>-1</sup> )	$T_A^*$ (K)	$V$ (km s <sup>-1</sup> )	$\Delta v$ (km s <sup>-1</sup> )
MM1						
CS(2 → 1)	0.896 ± 0.052	-102.39 ± 0.03	5.7 ± 0.1	...	...	...
	0.734 ± 0.052	-88.06 ± 0.05	5.7 ± 0.1	...	...	...
CS(5 → 4)	0.134 ± 0.073	-102.31 ± 0.20	5.2 ± 0.5	...	...	...
	0.181 ± 0.073	-88.43 ± 0.13	3.1 ± 0.4	...	...	...
CS(7 → 6)	0.634 ± 0.084	-102.42 ± 0.07	4.6 ± 0.2	0.148 ± 0.035	-102.21 ± 0.11	4.3 ± 0.3
<sup>13</sup> CO(3 → 2)	6.466 ± 0.110	-101.30 ± 0.03 <sup>a</sup>	5.2 ± 0.1 <sup>b</sup>	3.283 ± 0.046	-101.32 ± 0.03 <sup>a</sup>	5.1 ± 0.1 <sup>b</sup>
	2.442 ± 0.110	-87.78 ± 0.04	6.0 ± 0.1	3.246 ± 0.046	-87.94 ± 0.03 <sup>a</sup>	6.2 ± 0.1 <sup>b</sup>
MM2						
CS(2 → 1)	1.591 ± 0.053	-89.67 ± 0.02	4.3 ± 0.1	...	...	...
CS(5 → 4)	0.738 ± 0.083	-89.65 ± 0.03	3.6 ± 0.1	...	...	...
CS(7 → 6)	1.080 ± 0.120	-89.72 ± 0.05	4.5 ± 0.1	0.680 ± 0.049	-89.76 ± 0.04	4.4 ± 0.1
<sup>13</sup> CO(3 → 2)	10.753 ± 0.106	-88.93 ± 0.03 <sup>a</sup>	6.1 ± 0.1 <sup>b</sup>	9.386 ± 0.067	-89.40 ± 0.01	5.5 ± 0.1
MM3						
CS(2 → 1)	2.650 ± 0.067	-89.21 ± 0.01	5.3 ± 0.1	...	...	...
CS(5 → 4)	1.033 ± 0.086	-88.89 ± 0.03 <sup>a</sup>	5.0 ± 0.4 <sup>b</sup>	...	...	...
CS(7 → 6)	1.398 ± 0.120	-90.24 ± 0.05	6.1 ± 0.1 <sup>c</sup>	0.422 ± 0.048	-89.68 ± 0.06	6.0 ± 0.2 <sup>d</sup>
	0.916 ± 0.120	-91.79 ± 2.46	31.1 ± 2.8 <sup>c</sup>	0.146 ± 0.049	-91.91 ± 0.40	26.3 ± 0.9 <sup>d</sup>
<sup>13</sup> CO(3 → 2)	0.996 ± 0.110	-99.93 ± 0.07	6.3 ± 0.2	0.770 ± 0.051	-100.38 ± 0.01	4.1 ± 0.1
	15.915 ± 0.110	-89.44 ± 0.01	6.8 ± 0.1	11.869 ± 0.051	-88.98 ± 0.03 <sup>a</sup>	6.0 ± 0.1 <sup>b</sup>
SO(8 <sub>7</sub> → 7 <sub>6</sub> )	2.709 ± 0.042	-90.20 ± 0.03 <sup>a</sup>	29.8 ± 0.5 <sup>b</sup>	...	...	...
SO(8 <sub>8</sub> → 7 <sub>7</sub> )	2.024 ± 0.046	-90.31 ± 0.03 <sup>a</sup>	32.6 ± 0.6 <sup>b</sup>	...	...	...
SiO(7 → 6)	0.859 ± 0.035	-89.31 ± 0.03 <sup>a</sup>	43.3 ± 1.8 <sup>b</sup>	...	...	...
SiO(8 → 7)	0.899 ± 0.045	-89.64 ± 0.03 <sup>a</sup>	47.2 ± 2.4 <sup>b</sup>	...	...	...
MM4						
CS(2 → 1)	2.262 ± 0.055	-88.34 ± 0.01	4.7 ± 0.1	...	...	...
CS(5 → 4)	0.776 ± 0.064	-89.17 ± 0.03	4.6 ± 0.1	...	...	...
CS(7 → 6)	1.498 ± 0.120	-88.21 ± 0.04	3.9 ± 0.1	0.413 ± 0.046	-88.83 ± 0.06	4.6 ± 0.1
<sup>13</sup> CO(3 → 2)	15.320 ± 0.090	-87.79 ± 0.01	4.5 ± 0.1	8.616 ± 0.047	-88.33 ± 0.01	5.1 ± 0.1
MM5						
CS(2 → 1)	2.949 ± 0.056	-88.44 ± 0.01	5.1 ± 0.1	...	...	...
CS(5 → 4)	1.057 ± 0.085	-88.89 ± 0.03	4.7 ± 0.1	...	...	...
CS(7 → 6)	0.899 ± 0.130	-89.21 ± 0.07	4.5 ± 0.2	0.463 ± 0.048	-88.76 ± 0.05	4.9 ± 0.1
<sup>13</sup> CO(3 → 2)	0.701 ± 0.100	-100.32 ± 0.05	2.1 ± 0.1	0.714 ± 0.066	-100.54 ± 0.02	2.9 ± 0.05
	19.143 ± 0.100	-88.41 ± 0.03 <sup>a</sup>	5.4 ± 0.1 <sup>b</sup>	14.312 ± 0.066	-88.07 ± 0.01	5.2 ± 0.1
MM6						
CS(2 → 1)	1.039 ± 0.075	-100.48 ± 0.04	4.5 ± 0.1	...	...	...
CS(5 → 4)	0.205 ± 0.073	-100.35 ± 0.12	4.0 ± 0.3	...	...	...
CS(7 → 6)	1.837 ± 0.099	-100.05 ± 0.03	5.7 ± 0.1	0.423 ± 0.045	-100.00 ± 0.05	6.3 ± 0.1
<sup>13</sup> CO(3 → 2)	10.806 ± 0.110	-99.84 ± 0.02	6.2 ± 0.1	5.684 ± 0.042	-100.48 ± 0.03 <sup>a</sup>	5.6 ± 0.1 <sup>b</sup>

<sup>a</sup>The error in the estimation of the velocity is fixed to  $\sigma_V = 0.03$

<sup>b</sup>Non-gaussian profile.  $\Delta V = I(T_A^*) / T_A^* Peak$ .

<sup>c</sup>For this spectrum, we considered two gaussian fittings. The first is related with the broad emission related with outflowing gas, and the second gaussian fit is made to the spectrum after the subtraction of the broad emission and is related with the ambient gas.

<sup>d</sup>Same as previous note, but for the composited integrated spectrum.

Table 3.5. Sizes (FWHM) obtained with CS(7  $\rightarrow$ 6) line

Clump	$\Delta v$ (km s <sup>-1</sup> )	Maj axis ( $''$ )	Min axis ( $''$ )	Radius (pc)
MM1	4.3 $\pm$ 0.3	35 $\pm$ 3.6	23 $\pm$ 2.4	0.30 $\pm$ 0.03
MM2	4.4 $\pm$ 0.1	68 $\pm$ 7.6	47 $\pm$ 5.3	0.94 $\pm$ 0.04
MM3	6.0 $\pm$ 0.2	37 $\pm$ 1.4	21 $\pm$ 0.8	0.29 $\pm$ 0.01
MM4	4.6 $\pm$ 0.1	44 $\pm$ 3.7	24 $\pm$ 1.9	0.42 $\pm$ 0.02
MM5	4.9 $\pm$ 0.1	110 $\pm$ 17.3	44 $\pm$ 6.9	1.19 $\pm$ 0.07
MM6	6.3 $\pm$ 0.1	29 $\pm$ 0.7	25 $\pm$ 0.6	0.25 $\pm$ 0.01

Table 3.6. Fluxes from continuum observations

Region	Millimeter cont.		IRAS bands				MSX bands				Spitzer bands			
	1.2mm (Jy)	0.87mm (Jy)	100 $\mu$ m (Jy)	60 $\mu$ m (Jy)	25 $\mu$ m (Jy)	12 $\mu$ m (Jy)	21.3 $\mu$ m (Jy)	14.7 $\mu$ m (Jy)	12.1 $\mu$ m (Jy)	8.3 $\mu$ m (Jy)	8 $\mu$ m (Jy)	5.8 $\mu$ m (Jy)	4.5 $\mu$ m (Jy)	3.6 $\mu$ m (Jy)
Complex	37.0	227.9	36517.0	30998.2	3855.8	649.1	2680.8	1143.3	1005.1	373.0	712.2	262.2	36.3	34.1
MM1	3.1	27.3	2254.0	629.3	24.9	3.7	22.9	13.1	21.4	13.1	25.0	7.5	0.7	0.9
MM2	6.4	38.3	8548.7	7948.4	1177.2	232.5	855.4	387.9	305.7	86.4	136.7	48.8	6.9	5.7
MM3	11.6	66.7	7687.6	6682.3	496.3	72.3	731.5	309.9	269.5	99.2	171.8	73.6	10.7	9.6
MM4	4.9	42.7	5098.2	5243.1	707.9	122.2	500.8	222.7	169.7	54.3	84.3	29.9	4.4	3.9
MM5	7.6	52.5	8618.1	6530.5	923.5	147.2	482.0	187.7	173.7	71.5	102.8	38.7	4.6	4.2
MM6	3.5	27.6	2086.1	1710.6	192.1	33.9	115.0	47.5	51.4	24.6	40.63	14.1	2.3	2.0

Table 3.7. Observed parameters of radio sources detected towards G331.5–0.1

Component	Freq. (GHz)	$\alpha$ (J2000)	$\delta$ (J2000)	Flux Peak (Jy/beam)	Flux density (Jy)	Beam (")	Deconv. angular size (")	Spectral index
A	4.80	16 12 07.510	-51 30 02.23	0.155	0.255	2.7×1.8	1.97×1.54	...
	8.64	16 12 07.471	-51 30 02.39	0.101	0.217	1.5×1.0	1.49×1.34	
B	4.80	16 12 09.036	-51 25 47.83	0.125	0.141	2.7×1.8	0.81×0.60	0.8±0.2
	8.64	16 12 09.038	-51 25 47.79	0.166	0.222	1.5×1.0	0.84×0.36	
C	4.80	16 12 10.039	-51 28 37.72	0.085	0.095	2.7×1.8	0.86×0.37	1.2±0.2
	8.64	16 12 10.030	-51 28 37.66	0.158	0.194	1.5×1.0	0.61×0.40	
D	4.80	16 12 27.308	-51 27 32.54	0.066	0.135	2.7×1.8	2.30×2.06	...
	8.64	16 12 27.264	-51 27 32.81	0.022	0.092	1.5×1.0	2.15×1.87	



Table 3.8. Spectral Energy Distributions

Region	$T^c$ (K)	$\beta^c$	$\nu_0^c$ (THz)	$\theta^c$ (")	$T^w$ (K)	$\beta^w$	$\nu_0^w$ (THz)	$\theta^w$ (")	$T^h$ (K)	$\beta^h$	$\nu_0^h$ (THz)	$\theta^h$ (")
Complex	30	2.2	7.3	200	114	1.0	25	4.3	302	1.0	316	0.85
MM1	29	1.7	6.1	33	...	...	...	...	...	...	...	...
MM2	34	1.9	5.8	50	136	1.0	26	1.8	...	...	...	...
MM3	35	1.6	5.9	40	109	1.0	29	2.0	...	...	...	...
MM4	30	1.9	5.8	50	112	1.0	24	2.3	...	...	...	...
MM5	33	1.8	5.7	51	114	1.0	28	2.4	...	...	...	...
MM6	31	1.7	5.8	30	112	1.0	28	1.2	...	...	...	...

<sup>c</sup>Cold component

<sup>w</sup>Warm component

<sup>h</sup>Hot component

Table 3.9. Bolometric luminosities of complex and individual clumps

Region	Integrated flux $10^6$ (Jy GHz)	Bolometric luminosity $10^6 L_\odot$
Complex	252.2	4.4
MM1	7.2	0.1
MM2	57.6	1.0
MM3	40.9	0.7
MM4	35.5	0.6
MM5	48.2	0.8
MM6	12.3	0.2

Table 3.10. Masses and densities derived for the clumps

Clump	0.87 mm	1.2 mm			CS(7 $\rightarrow$ 6)
	Mass $10^3 M_\odot$	Mass $10^3 M_\odot$	Density $10^4$ ( $\text{cm}^{-3}$ )	Surface density ( $\text{g cm}^{-2}$ )	Virial mass $10^3 M_\odot$
MM1	5.1	1.9	2.9	0.30	$1.2 \pm 0.2$
MM2	5.8	3.2	1.6	0.24	$3.8 \pm 0.3$
MM3	9.7	5.6	10.9	1.03	$2.2 \pm 0.2$
MM4	7.6	2.8	1.4	0.21	$1.9 \pm 0.1$
MM5	8.2	3.9	1.9	0.29	$6.0 \pm 0.4$
MM6	4.7	1.9	3.7	0.35	$2.1 \pm 0.1$

Table 3.11. Outflow parameters obtained from rotational diagrams

Molecule	Velocity range	$T_{rot}$ (K)	$Q(T_{rot})$	$N_T$ $10^{13}$ ( $\text{cm}^{-2}$ )
SiO	-144.1 $\leftrightarrow$ -95.6	123.2 $\pm$ 15.2	118.3	3.26
	-79.9 $\leftrightarrow$ -16.3	138.0 $\pm$ 29.4	132.5	2.56
SO	-144.1 $\leftrightarrow$ -95.6	93.7 $\pm$ 4.8	254.3	45.93
	-79.9 $\leftrightarrow$ -16.3	77.3 $\pm$ 4.4	207.1	37.95

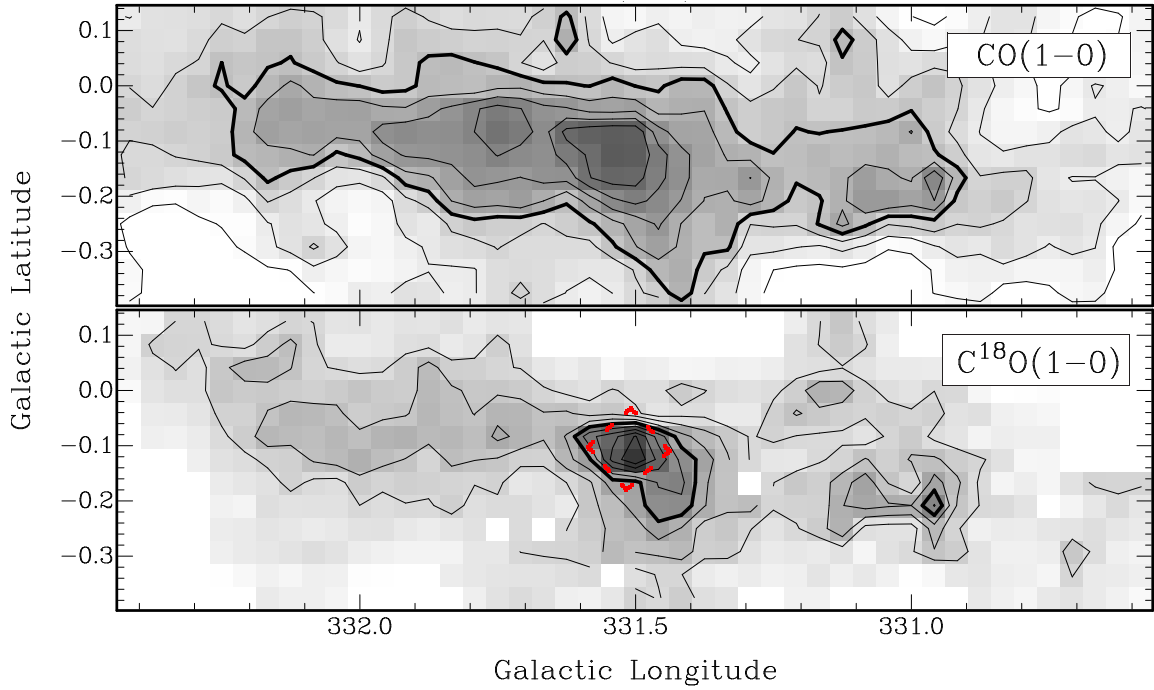


Figure 3.1 Maps of velocity integrated emission, in the range  $-117.7$  to  $-73.2$   $\text{km s}^{-1}$ , of the G331.5-0.1 GMC. *Top* :  $\text{CO}(1 \rightarrow 0)$ . Contour levels are drawn from 20% ( $3\sigma$ ) to 90%, in steps of 10%, of the peak intensity ( $297.6 \text{ K km s}^{-1}$ ). *Bottom* :  $\text{C}^{18}\text{O}(1 \rightarrow 0)$ . Contour levels are drawn from 20% ( $4\sigma$ ) to 90%, in steps of 10%, of the peak intensity ( $19.6 \text{ K km s}^{-1}$ ). The 50% emission in each map is drawn with a thicker contour. A  $7' \times 7'$  red dashed box, oriented in equatorial coordinates, is drawn toward the 70% emission contour in the  $\text{C}^{18}\text{O}(1 \rightarrow 0)$  map. This area is considered as the central region of this cloud.

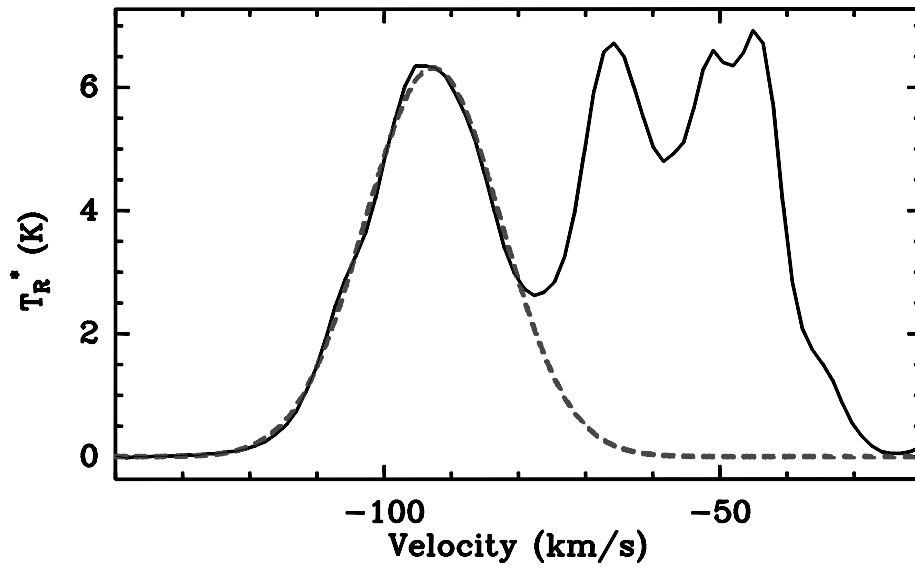


Figure 3.2 Average profile of the CO(1  $\rightarrow$  0) emission over the whole GMC. The dashed line corresponds to the gaussian fit of the spectrum on the velocity range of the G331.5-0.1 GMC. The parameters of the gaussian fit are  $v_0 = -92.8 \pm 0.006$  km s $^{-1}$ ,  $\Delta v = 23.8 \pm 0.017$  km s $^{-1}$  and  $T_{peak} = 6.31$  K.

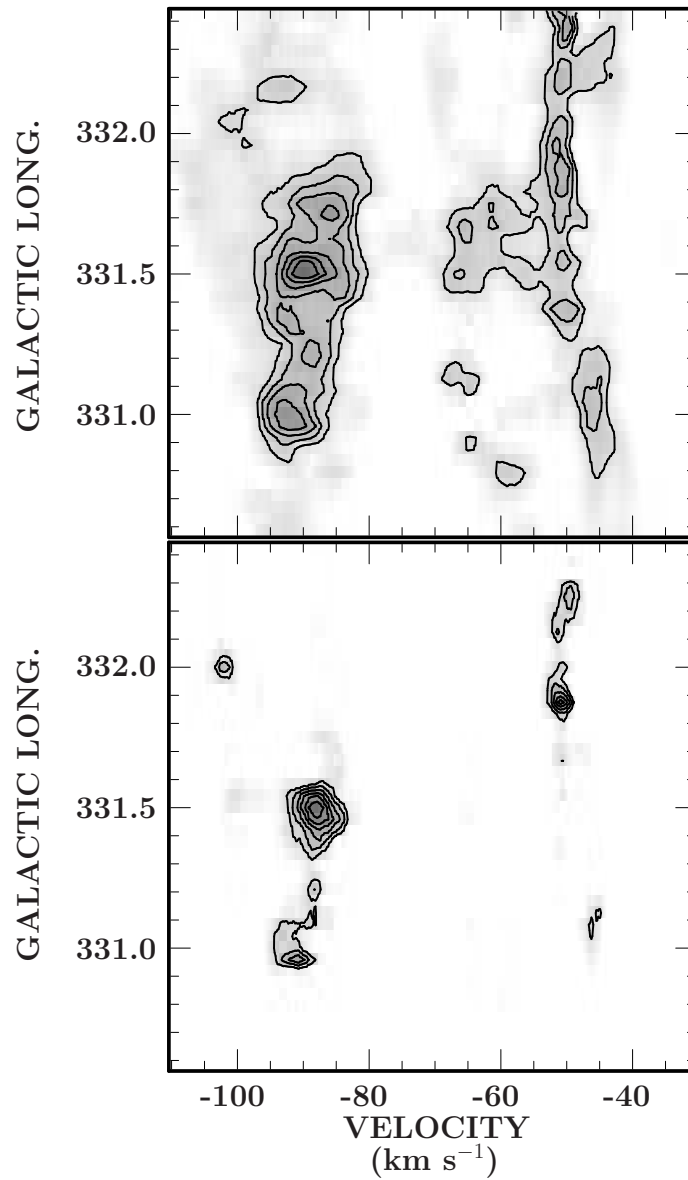


Figure 3.3 Position-velocity maps of the CO(1  $\rightarrow$ 0) (*top*) and C<sup>18</sup>O(1  $\rightarrow$ 0) emission (*bottom*) integrated between  $-0.21$  and  $-0.04$  in Galactic Latitude. Contour levels are drawn at 40% to 90%, in steps of 10%, of the peak intensity ( $11.5 \text{ K km s}^{-1}$  for CO and  $0.78 \text{ K km s}^{-1}$  for C<sup>18</sup>O). The C<sup>18</sup>O shows a clear component between  $l = 331.3^\circ$  and  $l = 331.6^\circ$  at  $\sim -90 \text{ km s}^{-1}$ .

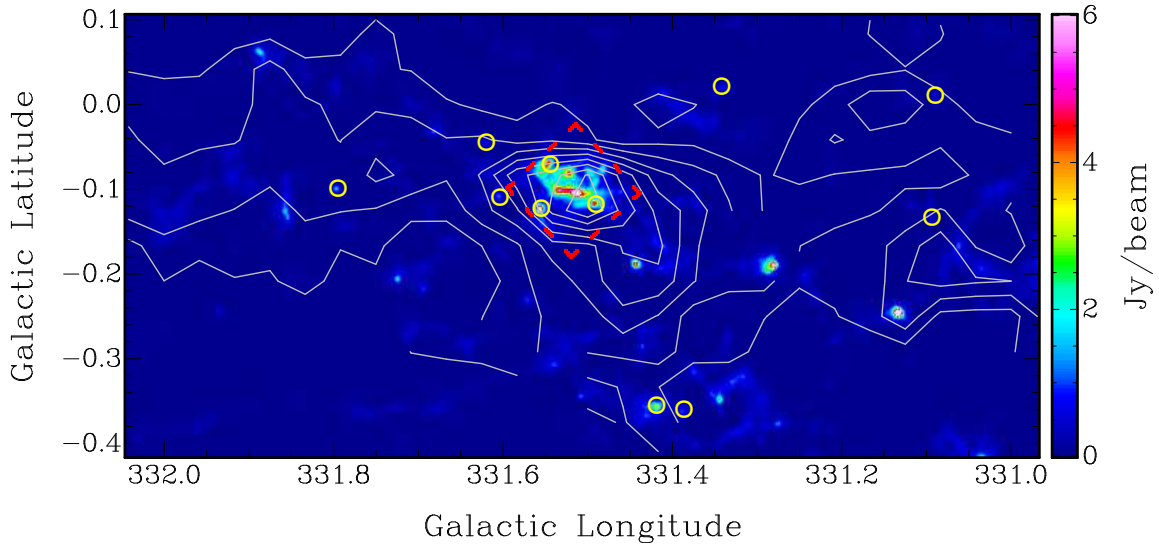


Figure 3.4 Map of dust continuum emission at 0.87 mm from ATLASGAL towards the Norma spiral arm tangent region. Overlaid in grey is the contour map of the  $\text{C}^{18}\text{O}(1 \rightarrow 0)$  emission integrated over the velocity range from  $-117.7$  to  $-73.2$   $\text{km s}^{-1}$ . Contour levels are from 20% to 90%, in intervals of 10%, of the peak intensity  $19.6$   $\text{K km s}^{-1}$ . The red dashed box,  $7' \times 7'$  in size ( $15 \times 15$   $\text{pc}^2$  at a distance of  $7.5$  kpc) and oriented in equatorial coordinates, shows the defined central region of the G331.5–0.1 GMC. The yellow circles show the position of the RMS sources in this region: G331.0890+00.0163A, G331.0890+00.0163B, G331.0931–00.1303, G331.3865–00.3598, G331.4117+00.0154, G331.4181–00.3546, G331.4904–00.1173, G331.5414–00.0675, G331.5582–00.1206, G331.6035–00.1081, G331.6191–00.0442A, G331.6191–00.0442B, and G331.7953–00.0979.

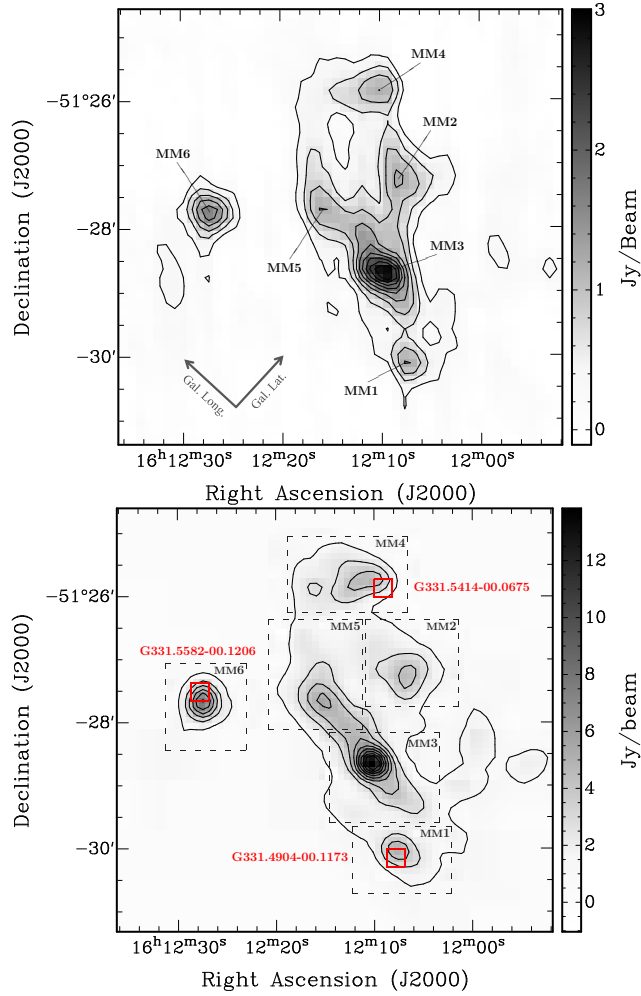


Figure 3.5 Maps of the dust continuum emission of the central region of the G331.5–0.1 GMC. *Top*: Map of the 1.2 mm emission observed with SIMBA. The angular resolution is  $24''$ . Contour levels are from 10% ( $3\sigma$ ) to 90%, in steps of 10%, of the peak intensity of  $2.9 \text{ Jy beam}^{-1}$ . The peak position of millimeter clumps MM1 through MM6, and the Galactic latitude and longitude directions are shown in this map. *Bottom*: Map of the 0.87 mm emission observed with LABOCA. The angular resolution is  $18.6''$ . Contours levels are from 10% ( $4\sigma$ ) to 90%, in steps of 10%, of the peak intensity of  $13.8 \text{ Jy beam}^{-1}$ . Dashed boxes in this map show the considered area of each millimeter clump for spectral energy distribution analysis. Red boxes mark the position of RMS sources in the region. The size of these red boxes is  $18'' \times 18''$  to account for the beam size of the RMS catalog.

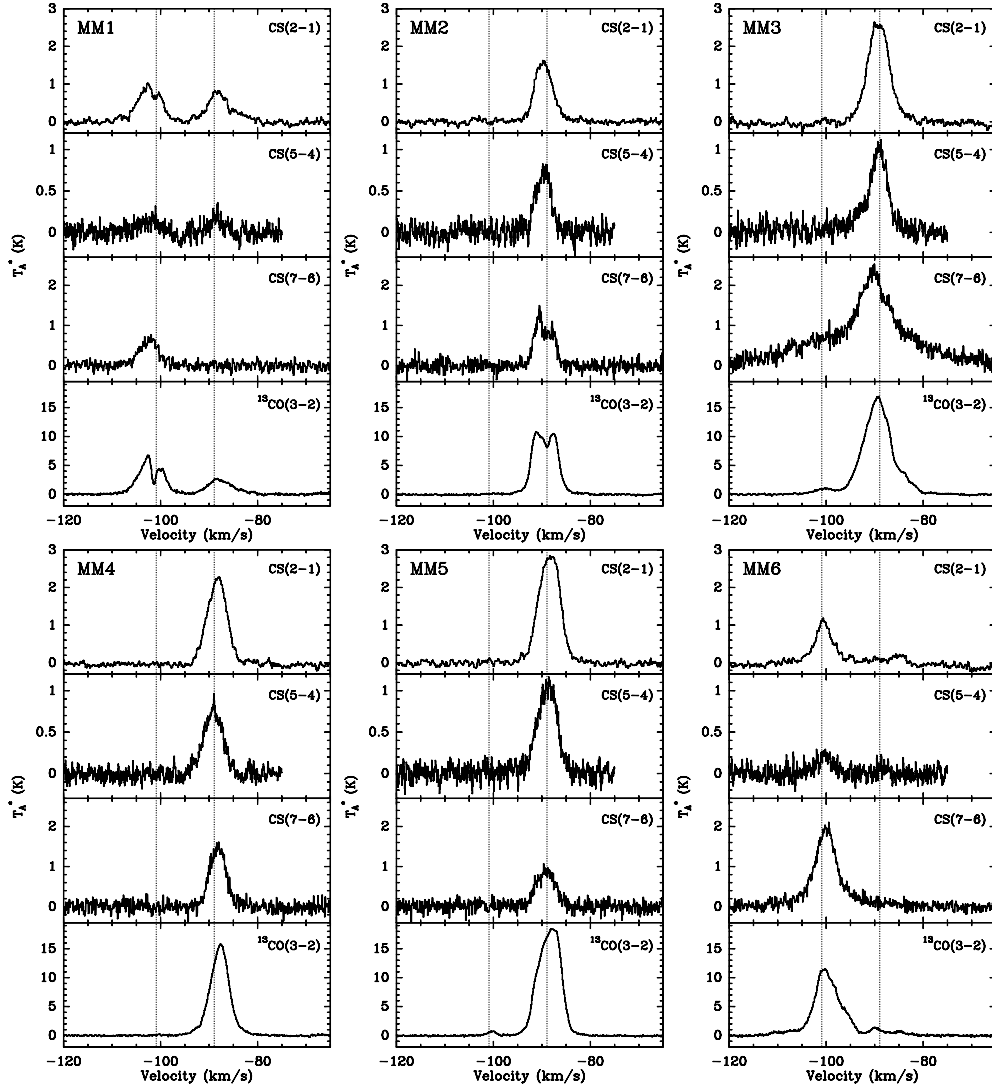


Figure 3.6 Spectra observed at the peak position of the millimeter clumps MM1 through MM6. The transition is given in the upper right corner. These spectra indicate that the emission arises from two different components: a high velocity component at  $v=-88.9 \text{ km s}^{-1}$ , and a low velocity component at  $v=-100.8 \text{ km s}^{-1}$ , indicated with vertical dotted lines. Molecular sources associated with millimeter clumps MM2, MM3, MM4 and MM5 are part of a single structure at high velocity that we defined as the complex of clumps.



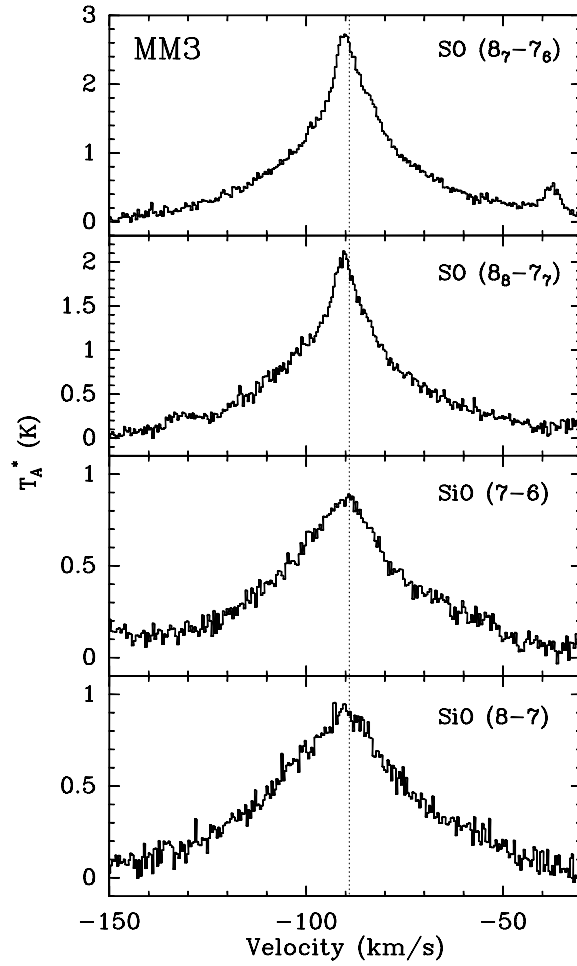


Figure 3.7 SiO and SO spectra observed toward the peak position of clump MM3, which is associated with the high-velocity molecular outflow G331.512-0.103. Transitions are given in the upper right corner. The vertical dotted line indicates the ambient gas velocity.

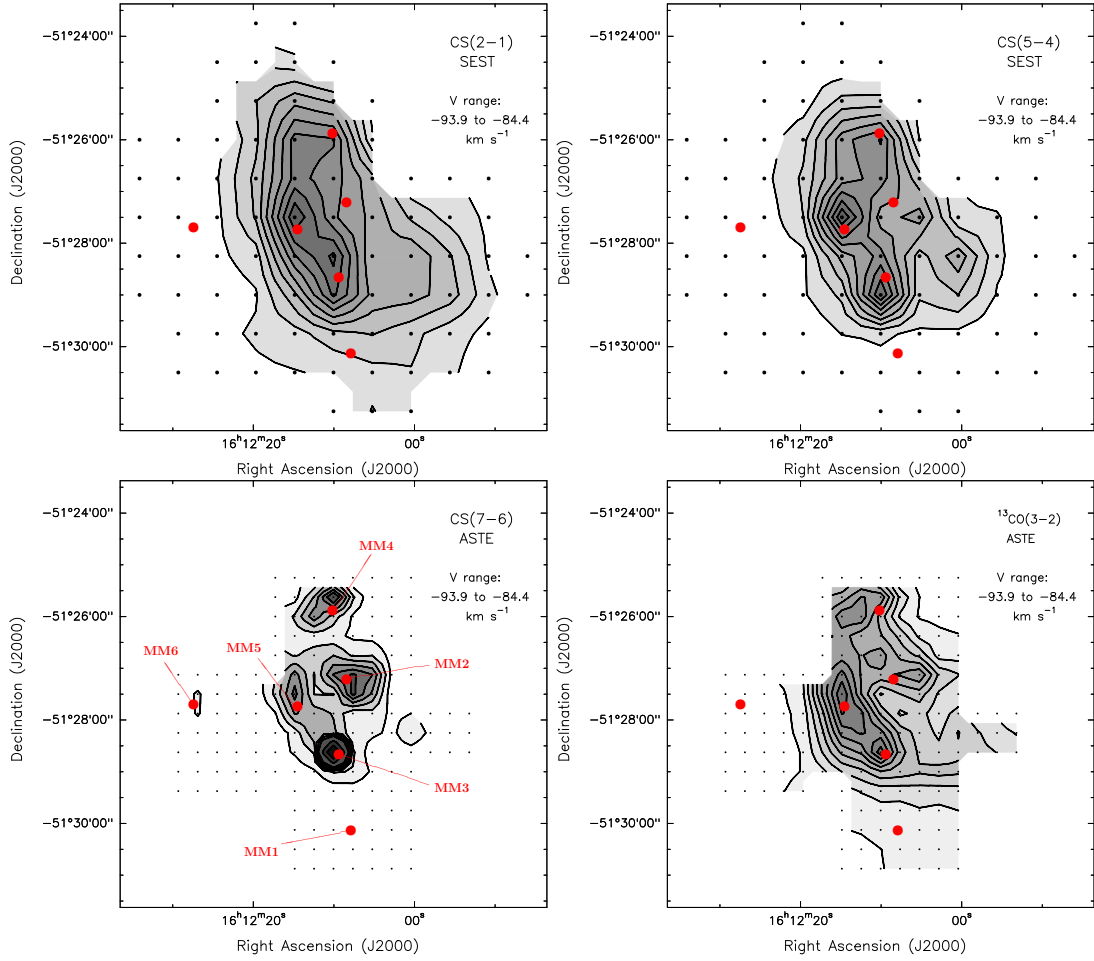


Figure 3.8 Contour maps of velocity-integrated emission, in the range from  $-93.9$  to  $-84.4$   $\text{km s}^{-1}$  from the central region of the G331.5–0.1 molecular cloud in four different transitions. For the CS(7  $\rightarrow$  6) map, the contour levels are drawn at 5%, 10%, 15%, 20%, 25%, 30%, 50% and 70% of the peak flux density  $25.6$   $\text{K km s}^{-1}$ . For CS(2  $\rightarrow$  1), CS(5  $\rightarrow$  4) and  $^{13}\text{CO}(3 \rightarrow 2)$  maps, the contours are drawn at 10% to 90%, with interval of 10%, of the peak intensity. For CS(2  $\rightarrow$  1), CS(5  $\rightarrow$  4) and  $^{13}\text{CO}(3 \rightarrow 2)$ , the peak intensities are  $15.3$ ,  $5.3$  and  $161.7$   $\text{K km s}^{-1}$ , respectively. The red points show the peak positions of the millimeter clumps MM1 through MM6, as is labeled in the CS(7  $\rightarrow$  6) contour map. Molecular sources associated with millimeter clumps MM2, MM3, MM4 and MM5 are part of a single structure at high velocity that we defined as the complex of clumps.

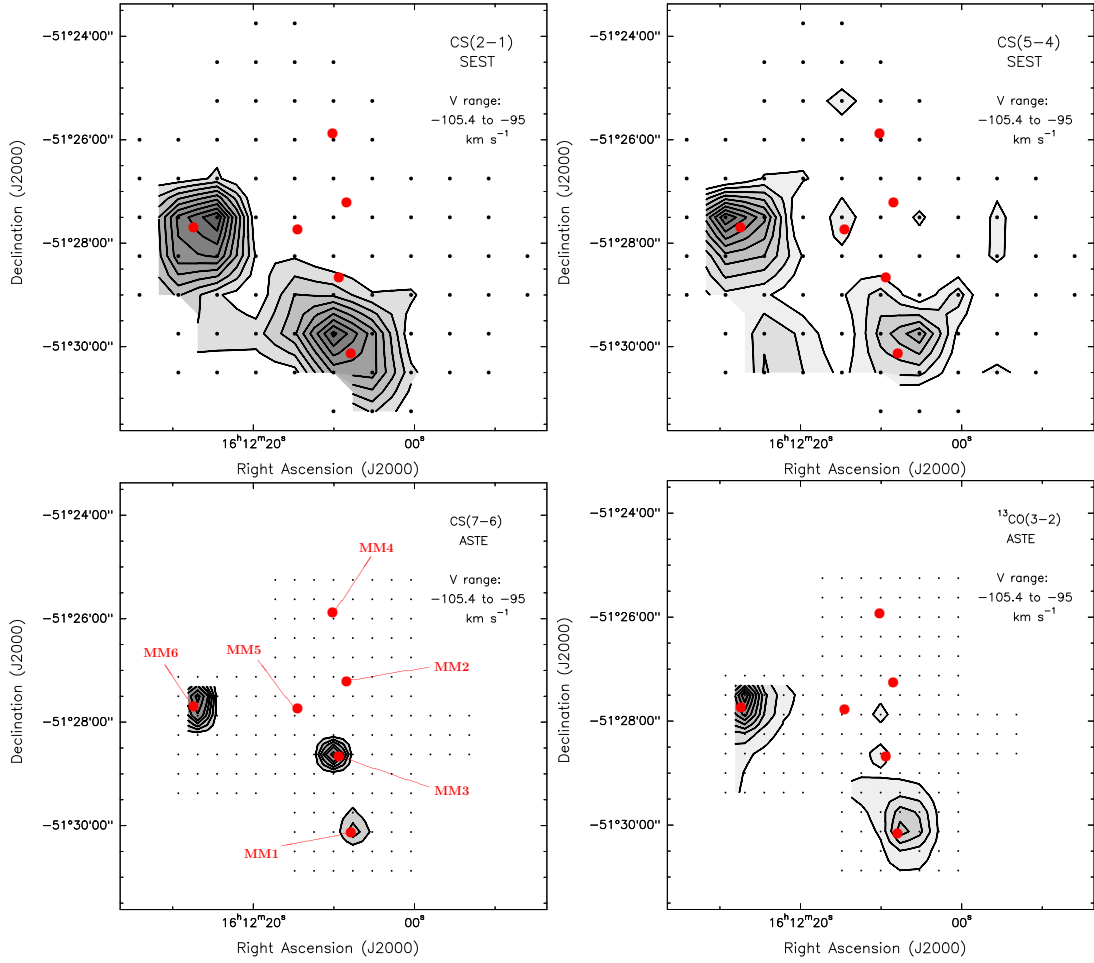


Figure 3.9 Contour maps of velocity-integrated emission, in the range between  $-105.4$  and  $-95 \text{ km s}^{-1}$ , from the central region of the G331.5–0.1 molecular cloud in four different transitions. For the CS(7  $\rightarrow$ 6) map, the contour levels are drawn at 10%, 20%, 30%, 40%, 50%, 70% and 90% of the peak flux density  $14.0 \text{ K km s}^{-1}$ . For CS(2  $\rightarrow$ 1), CS(5  $\rightarrow$ 4) and  $^{13}\text{CO}(3 \rightarrow 2)$  maps, the contours are drawn at 10% to 90%, with interval of 10%, of the peak intensity. For CS(2  $\rightarrow$ 1), the peak intensity is  $5.2 \text{ K km s}^{-1}$ . For CS(5  $\rightarrow$ 4), the peak intensity is  $1.4 \text{ K km s}^{-1}$ . For  $^{13}\text{CO}(3 \rightarrow 2)$ , the peak intensity is  $86.7 \text{ K km s}^{-1}$ . The red points show the peak positions of the millimeter clumps MM1 through MM6, as is labeled in the CS(7  $\rightarrow$ 6) contour map. The emission observed in the CS(7  $\rightarrow$ 6) map at  $\alpha_{2000} = 16^{\text{h}}12^{\text{m}}10.13^{\text{s}}$  and  $\delta_{2000} = -51^{\circ}28'37.5''$  (toward the MM3 point) is related with the emission integration on the blue wing of the G331.512-0.103 outflow.

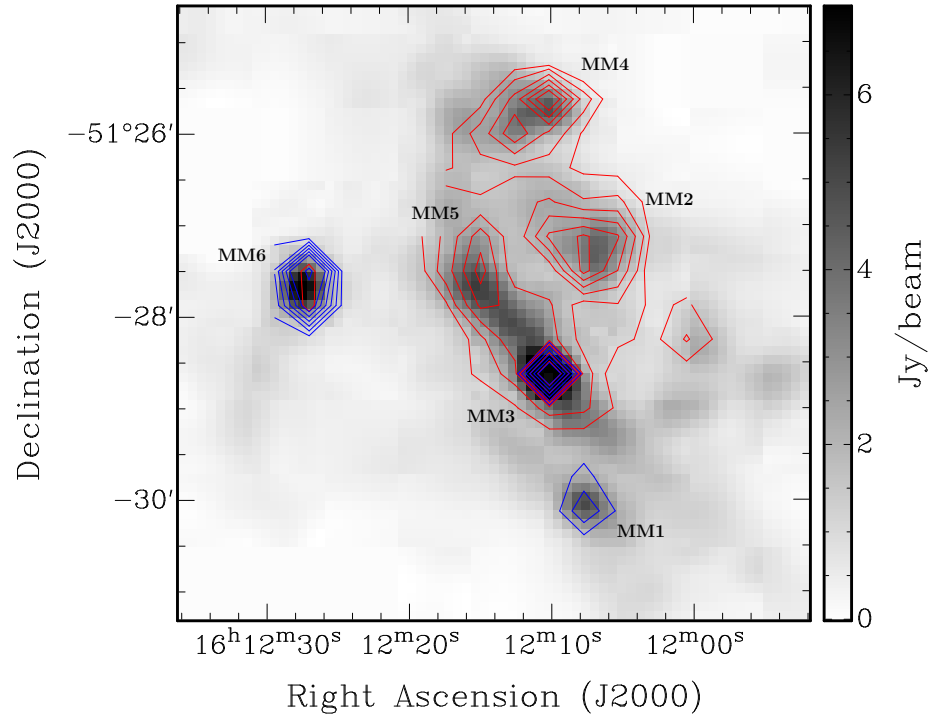


Figure 3.10 0.87 mm greyscale image of the central region of the G331.5–0.1 GMC, overlaid with CS velocity integrated contour map. The contour levels are drawn at 5%, 10%, 15%, 20%, 25%, 30%, 50% and 70% of the peak flux density  $25.6 \text{ K km s}^{-1}$ . The red contours show the integrated emission in the high velocity component of the spectra, integrated between  $-93.9$  and  $-84.4 \text{ km s}^{-1}$ . The blue contours show the low velocity component, integrated between  $-105.4$  and  $-95 \text{ km s}^{-1}$ . Labels MM1 through MM6 show the associated millimeter clump for each CS source. Molecular sources associated with millimeter clumps MM2, MM3, MM4 and MM5 are part of a single structure at high velocity that we defined as the complex of clumps.

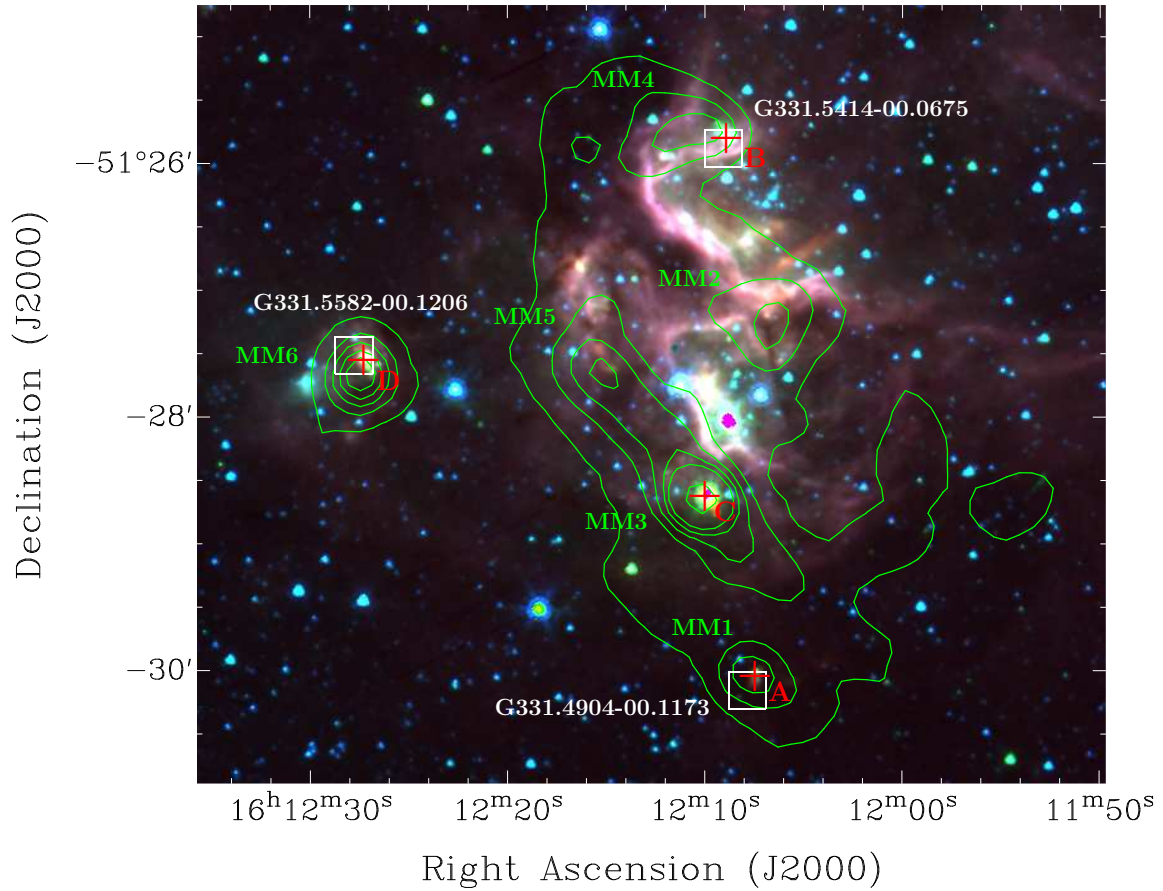


Figure 3.11 Contour map of the 0.87 mm continuum emission from the G331.5-0.1 region overlaid on a three color image of the mid infrared emission, made using the IRAC filters 1 ( $3.6 \mu\text{m}$ , blue), 2 ( $4.5 \mu\text{m}$ , green) and 4 ( $8 \mu\text{m}$ , red). Contour levels are drawn at 10%, 20%, 30%, 40%, 50% and 90% of the peak flux density  $13.8 \text{ Jy beam}^{-1}$ . Millimeter sources are labeled in the map with MM1, MM2, MM3, MM4, MM5 and MM6. Red crosses mark the positions of the four radio emission components in the central region of the G331.5-0.1 GMC (A, B, C and D). Component B and D are associated with methanol and OH masers. Component C is associated only with OH maser emission. White boxes mark the position of the three RMS sources in the region (G331.4904-00.1173, G331.5414-00.0675 and G331.5582-00.1206). The RMS box sizes are  $18''$  to account for the beam of MSX observation.

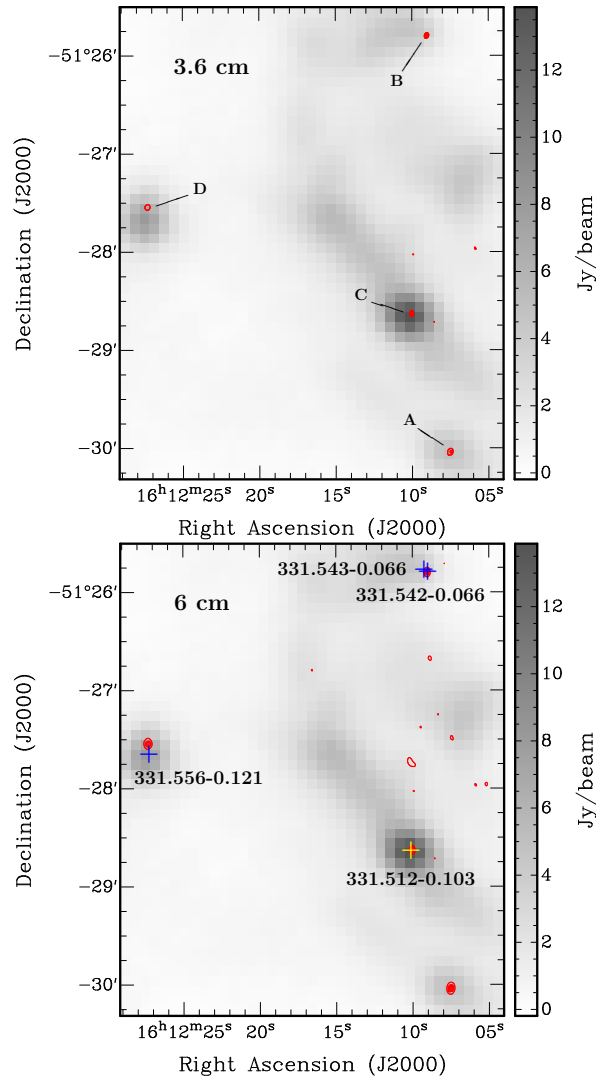


Figure 3.12 Contour maps of the radio emission from the G331.5–0.1GMC central region at 3.6 cm (*top*) and 6 cm (*bottom*), overlaid on 0.87 mm continuum emission. The contours are drawn at 10%, 30%, 60% and 90% of the peak flux. For the 6 cm map, the peak intensity is  $153.0 \text{ mJy beam}^{-1}$ , rms noise is  $1.04 \text{ mJy beam}^{-1}$ . For the 3.6 cm map, the peak intensity is  $159.5 \text{ mJy beam}^{-1}$ , rms noise is  $1.09 \text{ mJy beam}^{-1}$ . The blue crosses in the 6 cm map show the position of methanol masers in the central region of the G331.5–0.1 GMC. All methanol masers here are associated with OH masers. The yellow cross shows the position of the OH maser, without methanol counterpart, toward the G331.512-0.103 outflow.

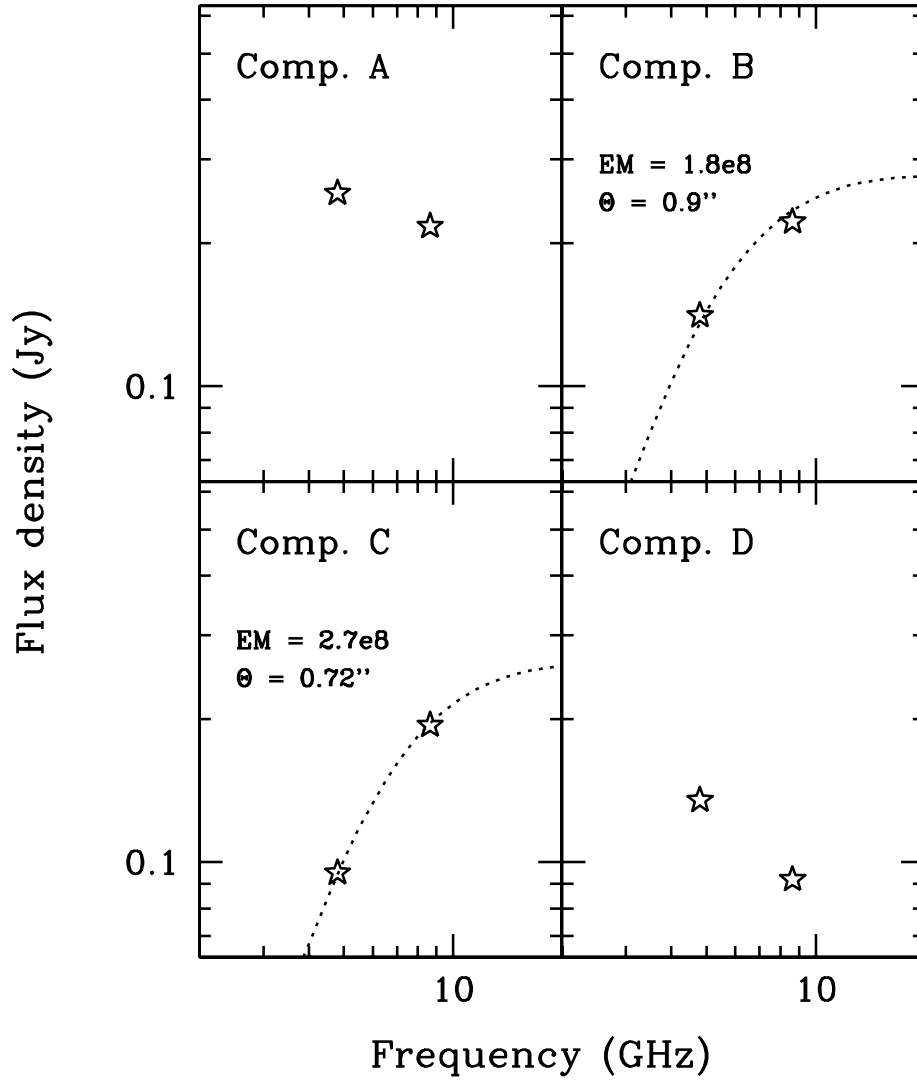


Figure 3.13 Spectral energy distributions at short frequency for each radio component found in the central region of the G331.5–0.1 GMC. For components B and C, the dotted line is a fit of the spectrum using modified blackbody function of the form  $B_\nu(T_e)[1 - \exp(-\tau_\nu)]$ , with  $\tau_\nu \propto T_e^{-1.35}\nu^{-2.1}EM$ . The emission measure  $EM$  is in units of  $[\text{pc cm}^{-6}]$ . The  $T_e$  considered is 10000 K. The spectral index of components B and C are  $0.8 \pm 0.2$  and  $1.2 \pm 0.2$ , respectively.

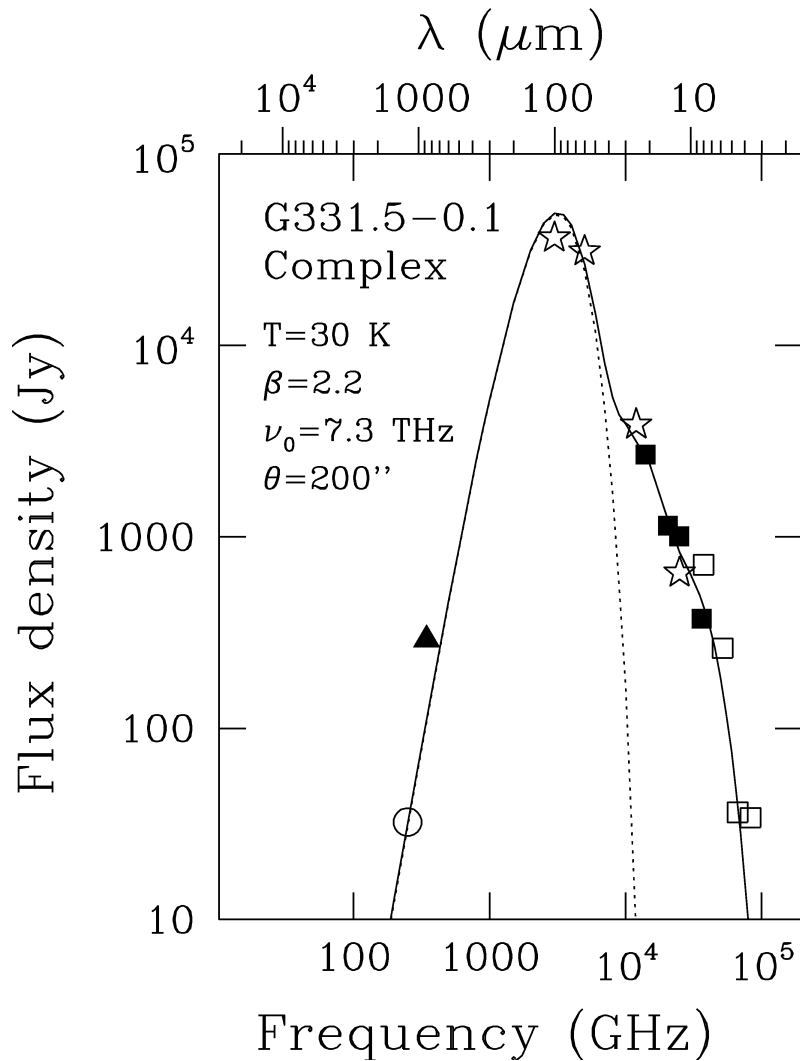


Figure 3.14 Spectral energy distribution of the region harboring the G331.5-0.1 complex of clumps. From left to right, the circle marks the SIMBA flux, the triangle the LABOCA, the stars mark IRAS fluxes, filled-squares MSX fluxes, and open-squares SPITZER fluxes. The solid curve is a fit to the spectrum using three modified black-body functions of the form  $B_\nu(T_e)[1 - \exp(-\nu/\nu_0)^\beta]$ , with different temperatures (cold, warm and hot components). The fitted parameters of the cold component (represented as the dotted line) are listed.



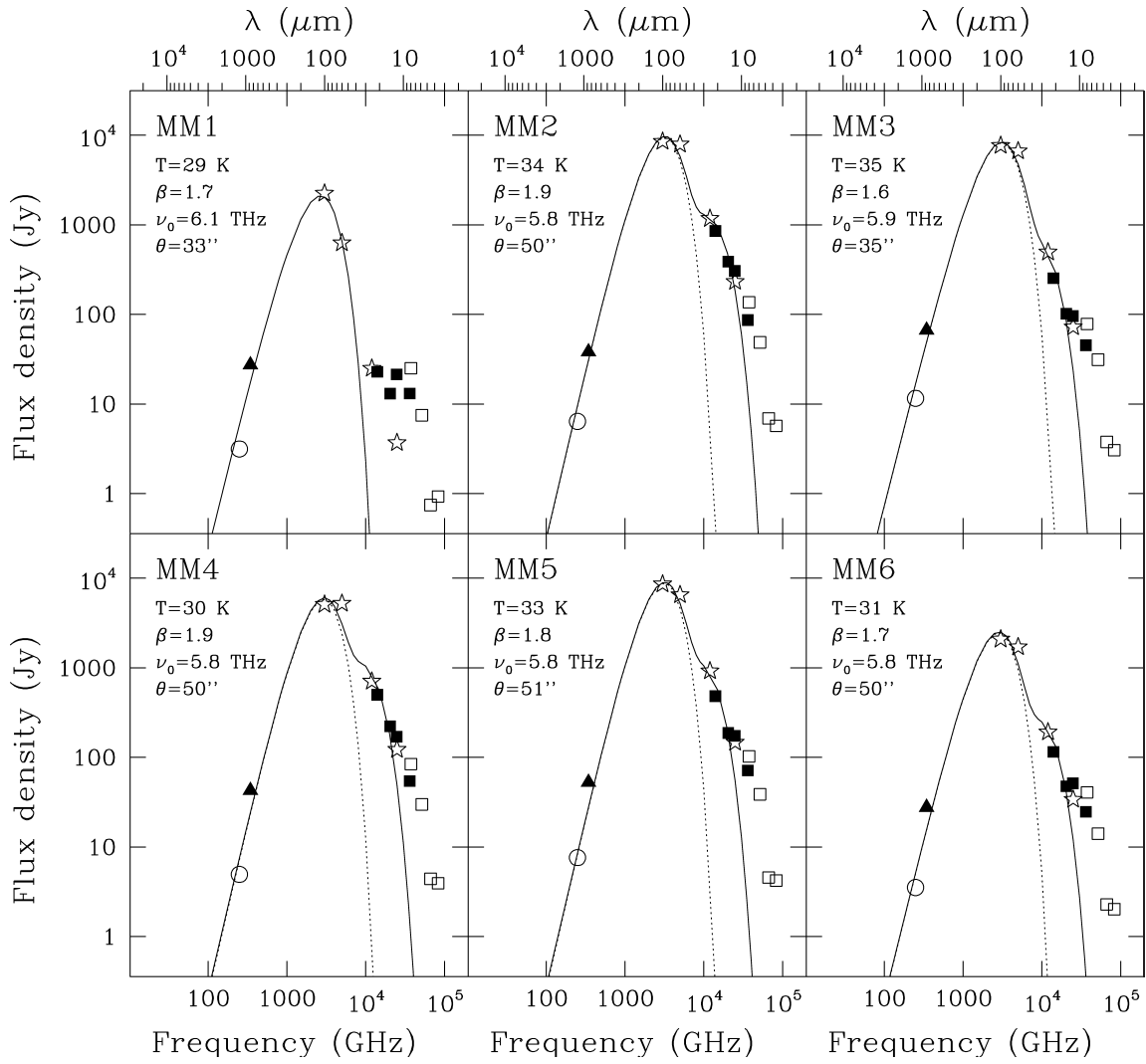


Figure 3.15 Spectral energy distributions of each millimeter clump in the G331.5–0.1 central region. The symbols are the same as in Fig. 3.14. The solid curve is a fit to the spectrum using two modified blackbody functions of the form  $B_\nu(T_e)[1 - \exp(-(\nu/\nu_0)^\beta)]$ , with different temperatures (cold and warm components). In the case of MM1, only one modified black function was considered. The fitted parameters of the cold component (represented as the dotted line) are listed on the upper left.

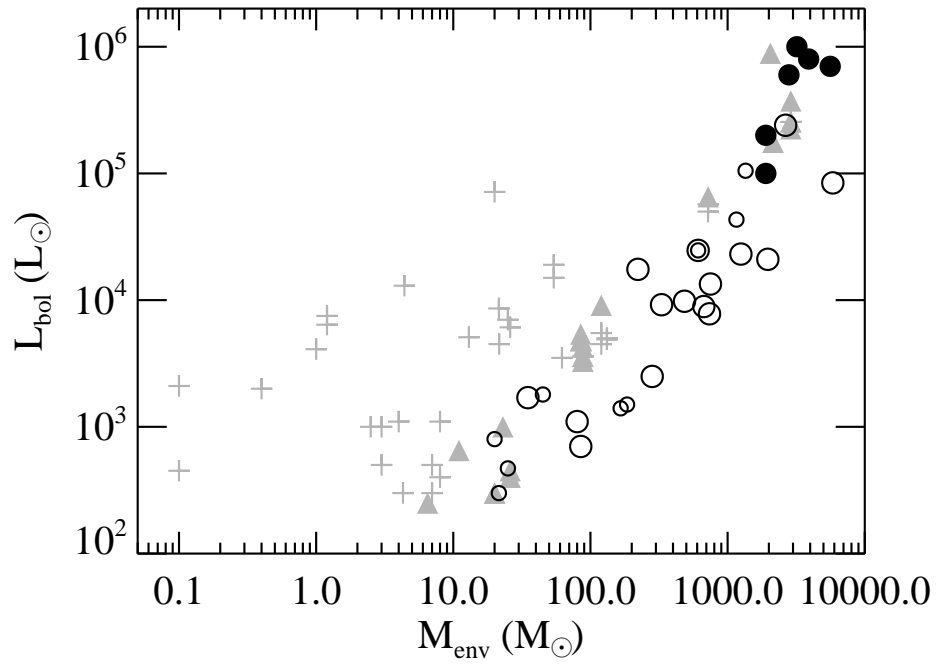


Figure 3.16  $L_{bol} - M_{env}$  diagram for the six millimeter clumps (MM1-MM6) in the G331.5–0.1 GMC central region (filled black circles), together with sources from Molinari et al. (2008). From Molinari et al. sample, MM sources are represented as open circles (small representing MM-S sources), IR-P sources are shown in grey filled triangles and IR-S are indicated in crosses.

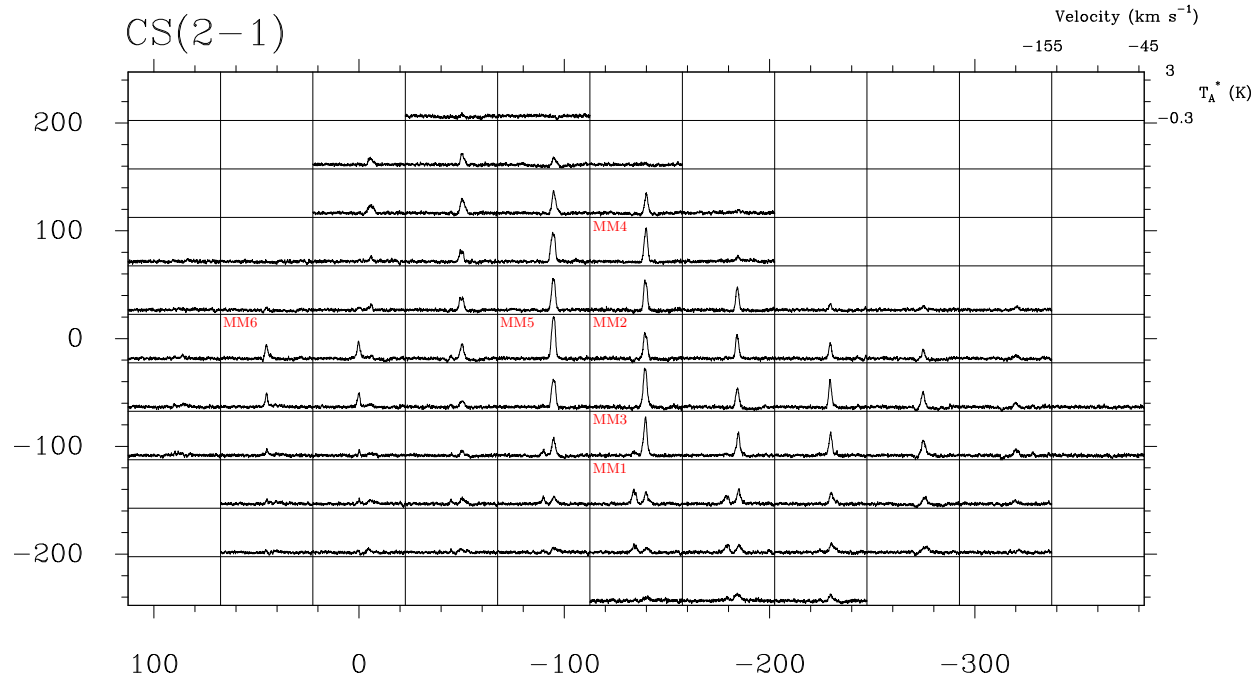


Figure 3.17 Observed spectra of the CS(2 → 1) line emissions toward the G331.5–0.1 GMC central region. The grid spacing is 45". Offsets are from the reference position at  $\alpha_{2000} = 16^h 12^m 24.5^s$  and  $\delta_{2000} = -51^\circ 27' 29.98''$ . In each box the velocity scale ranges from -155 to -45 km s<sup>-1</sup>. The antenna temperature scale is from -0.3 to 3 K. The labels MM1 to MM6 show the positions in the grid closer to the peak position of the millimeter clumps, defined in section 3.2.1.

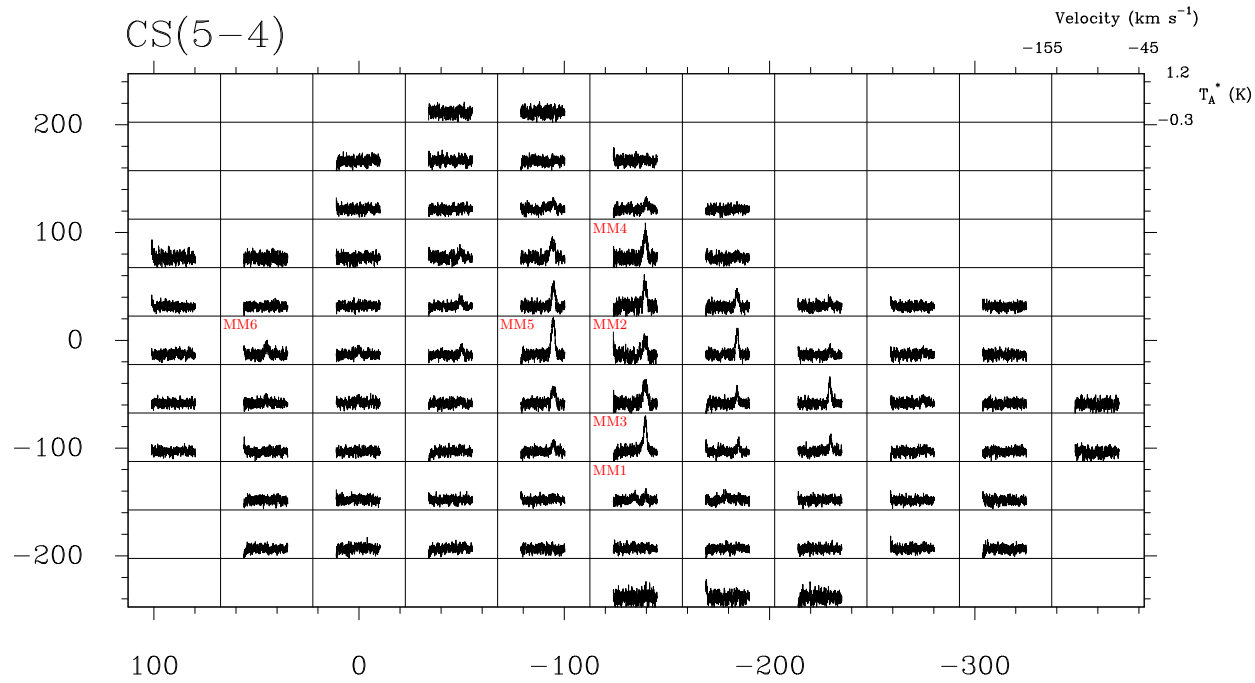


Figure 3.18 Observed spectra of the CS(5  $\rightarrow$ 4) line emissions toward the G331.5–0.1 GMC central region. The grid spacing is 45". Offsets are from the reference position at  $\alpha_{2000} = 16^h 12^m 24.5^s$  and  $\delta_{2000} = -51^\circ 27' 29.98''$ . In each box the velocity scale ranges from -155 to -45 km s $^{-1}$ . The antenna temperature scale is from -0.3 to 1.2 K. The labels MM1 to MM6 show the positions in the grid closer to the peak position of the millimeter clumps, defined in section 3.2.1.

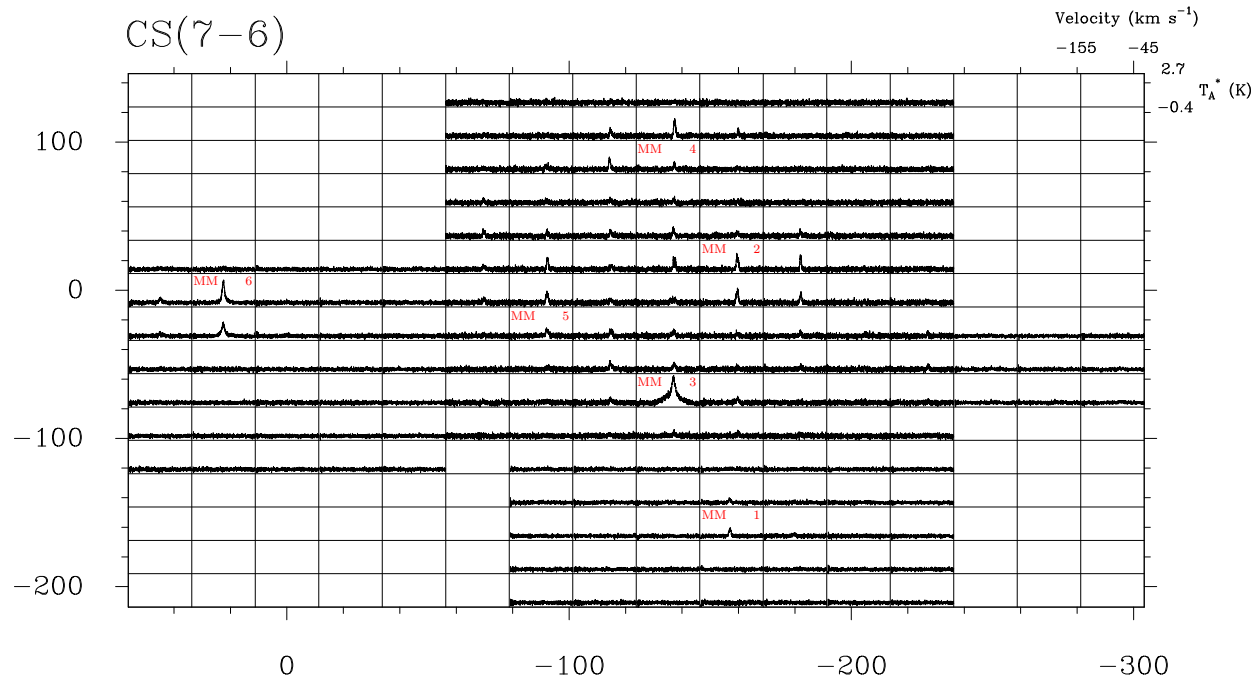


Figure 3.19 Observed spectra of the CS(7 → 6) line emissions toward the G331.5–0.1 central region. The grid spacing is 22.5". Offsets are from the reference position at  $\alpha_{2000} = 16^h 12^m 24.5^s$  and  $\delta_{2000} = -51^\circ 27' 29.9''$ . In each box the velocity scale ranges from -155 to -45 km s<sup>-1</sup>. The antenna temperature scale is from -0.4 to 2.7 K. The labels MM1 to MM6 show the positions in the grid closer to the peak position of the millimeter clumps, defined in section 3.2.1.

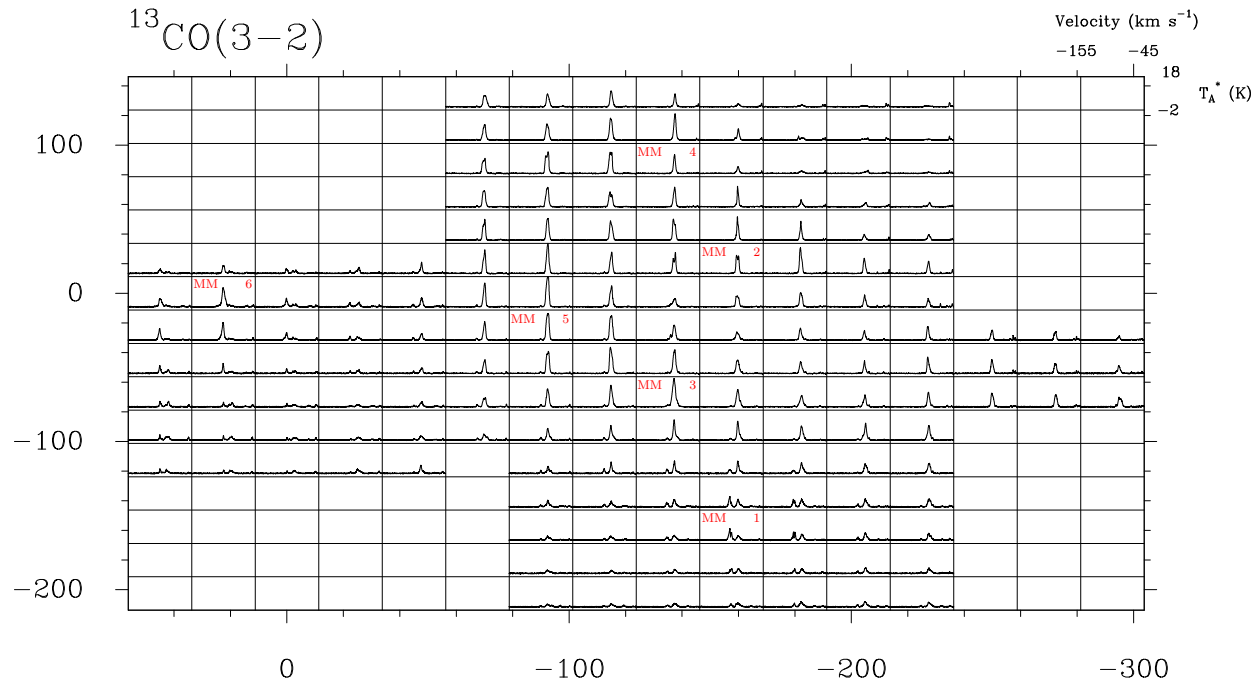


Figure 3.20 Observed spectra of the  $^{13}\text{CO}(3 \rightarrow 2)$  line emissions toward the G331.5–0.1 central region. The grid spacing is  $22.5''$ . Offsets are from the reference position at  $\alpha_{2000} = 16^{\text{h}}12^{\text{m}}24.5^{\text{s}}$  and  $\delta_{2000} = -51^{\circ}27'29.9''$ . In each box the velocity scale ranges from  $-155$  to  $-45 \text{ km s}^{-1}$ . The antenna temperature scale is from  $-2$  to  $18 \text{ K}$ . The labels MM1 to MM6 show the positions in the grid closer to the peak position of the millimeter clumps, defined in section 3.2.1.

## Chapter 4

# ALMA observations of the massive molecular outflow G331.512–0.103

### 4.1 Introduction

The formation of massive stars has a major impact on the surrounding interstellar medium, and regions of massive star formation dominate the star formation appearance of galaxies. While during the last couple of decades significant progress (both observational and theoretical) has been made in the study of massive stars and their parental molecular clouds, we are still far away from a complete picture of their formation process (for a recent discussion about this subject, see Kennicutt & Evans, 2012)

Massive stars rapidly affect their surroundings, so catching one early in the formation process can provide valuable insights. Since they form rarely compared with their low-mass counterpart, most are at large distances, making high resolution observations challenging. The Atacama Large Millimeter/submillimeter Array (ALMA) provides the capability to study distant objects in the Galaxy with good spatial resolution and sensitivity.

The G331.5-0.1 molecular cloud is a giant, elongated (178 by 41 pc) cloud in the Norma spiral arm, at a distance of 7.5 kpc, with a total CO mass of  $8.7 \times 10^6$

$M_{\odot}$  ( $M_{\text{LTE}} = 3.5 \times 10^6 M_{\odot}$  from  $\text{C}^{18}\text{O}$  emission) and a total infrared luminosity of  $3.6 \times 10^6 L_{\odot}$  (Bronfman et al. 2008; Merello et al. 2013), making it one of the most active and extreme high-mass star forming environments in our Galaxy. The central region hosts an extended H II region/infrared source and a number of ultracompact H II (UCHII) regions. Maps at submillimeter wavelengths show six continuum sources, with masses above  $10^3 M_{\odot}$  and average gas surface densities of  $0.4 \text{ g cm}^{-2}$ . Single dish spectral line observations with the Atacama Submillimeter Telescope Experiment and the Atacama Pathfinder EXperiment (APEX) of one of these sources, MM3, revealed extremely broad ( $\pm 80 \text{ km s}^{-1}$ ) wings on lines of CO, CS (Bronfman et al. 2008), SO, and SiO (Merello et al. 2013). This highly massive and energetic outflow, G331.512–0.103, is unresolved spatially in a  $7''$  beam.

Here we present observations with ALMA that resolve the G331.512–0.103 molecular outflow, allowing derivation of the outflow properties including age. In forthcoming papers we will describe the full set of molecular lines observed with ALMA Band 7.

## 4.2 Observations and results

The observations were performed on 2012 January 12 at frequencies around 350 GHz (0.86 mm) with ALMA Band 7 in Cycle 0 with 17 (12-m diameter) antennas in the compact configuration, with baselines ranging from 18.5 m to 269 m. We observed a single field of view centered at  $\alpha_{2000} = 16^{\text{h}}12^{\text{m}}10.09^{\text{s}}$ ,  $\delta_{2000} = -51^{\circ}28'38.4''$ . The primary beam was  $17.8''$  and the synthesized beam was  $1.38'' \times 0.68''$ , with a position angle (PA) of  $-37.6^{\circ}$ . The integration time was 34 minutes on source, with



an additional 24 minutes on calibrators. The nearby quasar J1604-446 was used for flux calibration, and J1427-421, located at  $27.7^\circ$  from the G331.512–0.103 source, was used for phase and bandpass calibrations. The data were processed using the Common Astronomy Software Application (CASA; McMullin et al., 2007), and the resulting maps have cells with sizes of  $0.14''$ , with 254 cells in each spatial dimension. Our images were obtained considering a “briggs” weighting mode on the data with  $\text{robust}=0.5$ . The four spectral windows have a bandwidth of 1875 MHz containing 3840 channels. The separation between each channel is 488.281 kHz ( $0.4215 \text{ km s}^{-1}$  at 357.3 GHz). The bands were centered at 345.79599 GHz, 347.2 GHz, 357.3 GHz and 358.60587 GHz.

While a rich spectrum of lines was observed, this Letter focuses on the lines of SiO(8-7) (347.33058 GHz),  $\text{H}^{13}\text{CO}^+(4-3)$  (346.99835 GHz),  $\text{HCO}^+(4-3)$  (356.73424 GHz), and CO(3-2) (345.79599 GHz), mostly diagnosing the outflow and its interaction with the surrounding cloud. Table 1 presents the four lines reported in the present work, the noise for each, the peak flux density, and the velocity at the peak. The rms noise was assessed over a region of  $35'' \times 35''$  centered on the source, avoiding a square area of  $11''$  in size centered on the emission. For line-free channels, the noise was  $\sim 0.014 \text{ Jy beam}^{-1}$ . However, for strong emission lines, the noise is larger, presumably because of incomplete  $uv$  coverage. On the channels of maximum intensity, toward the systemic velocity of the source, the noise increases substantially. To be conservative, we use the noise values at the line velocities in setting thresholds for contours, etc. Moment 0 maps were obtained for each emission line over its full velocity extension, and FWHM angular sizes and P.A.s of these maps were fitted using

the task IMFIT of CASA (Columns 6 and 7 of Table 1). Physical sizes, considering a source distance of 7.5 kpc, are presented in Column 8 of Table 1.

Figure 1 shows the integrated spectra for the lines described in Table 1. The integration is made over a box of  $10.5'' \times 10.5''$ , centered at  $\alpha_{2000} = 16^h 12^m 09.965^s$ ,  $\delta_{2000} = -51^\circ 28' 38.250''$ . Very wide wings (up to  $\pm 70 \text{ km s}^{-1}$ ) are seen on the SiO  $J = 8 \rightarrow 7$ , CO  $J = 3 \rightarrow 2$ , and HCO<sup>+</sup>  $J = 4 \rightarrow 3$  lines. The H<sup>13</sup>CO<sup>+</sup>  $J = 4 \rightarrow 3$  line is narrow toward the systemic velocity of the source ( $-88.9 \text{ km s}^{-1}$ ), but also shows traces of emission over the red wing of the outflow. The high velocity wings in the SiO profile match those in the APEX spectra presented in Merello et al. (2013), with differences between both profiles of less than 10%, indicating that the ALMA observations recover all the emission seen in the single-dish spectra. The CO spectrum presents several absorption features at different velocities. Besides the self-absorption component at the systemic velocity of the source, an absorption dip at  $\sim -100 \text{ km s}^{-1}$  is related to a second velocity component in the central region of the G331.5–0.1 giant molecular cloud, while the large feature between  $-70$  and  $-52 \text{ km s}^{-1}$  and the one at  $-40 \text{ km s}^{-1}$  are related to foreground galactic emission identified in Bronfman et al. (1989). The self-absorption dip at  $-88.9 \text{ km s}^{-1}$  is also present in the HCO<sup>+</sup> profile and weakly in the H<sup>13</sup>CO<sup>+</sup> profile.

The H<sup>13</sup>CO<sup>+</sup> profile resembles a typical blue-profile found in regions with infalling material (Myers et al., 2000), but observations of a more optically thin molecule, like HC<sup>18</sup>O<sup>+</sup>, will be needed to test this hypothesis. The H<sup>13</sup>CO<sup>+</sup> profile also shows a trace of emission in the red wing of the outflow, with a secondary peak of emission at  $\sim -50 \text{ km s}^{-1}$ .

Figure 2 shows the channel maps of the SiO line emission. The crosses indicate the peak positions at velocities about  $\pm 40 \text{ km s}^{-1}$  from the systemic velocity. These channels define a “bipolar axis” of symmetry of  $102.5 \pm 1.6^\circ$ . Experiments using other channels, different signal-to-noise levels, etc. resulted in variations around this value of only  $1.6^\circ$ , which we assign as the uncertainty. This angle differs slightly from the P.A. found in the deconvolved moment 0 map of SiO, (P.A. of  $105^\circ$ ; see Table 1).

The integrated intensity SiO map shows a ring-type feature toward the systemic velocity of the source ( $-90 \pm 15 \text{ km s}^{-1}$ ). We used the  $3\sigma$  contour level to estimate the outer edge of this emission, obtaining major and minor axes of  $5.12 \pm 0.16''$  and  $4.52 \pm 0.33''$ , respectively, with a P.A. of  $140.6^\circ$ . The deconvolved sizes are then  $4.79 \pm 0.19''$  and  $4.42 \pm 0.35''$  (0.17 pc at the source distance), with a P.A. of  $137^\circ$ .

The P.A. of the beam elongation is  $175^\circ$  from this angle, so some of the extension may be beam-related, but the extent is considerably larger than the beam, and the deconvolution should remove that effect. The inner cavity is centered at  $\alpha_{2000} = 16^h 12^m 10.00^s$ ,  $\delta_{2000} = -51^\circ 28' 37.45''$ , it has a size of  $0.99'' \times 0.66''$ , with a PA of  $160^\circ$ , and it is determined by the  $16\sigma$  emission contour. Therefore, the cavity in the SiO emission at the systemic velocity is not resolved with the present beam size. The SiO map also shows clumpy, irregular structure at the systemic velocity, with two peaks of emission of 5.0 and 3.9 Jy beam $^{-1}$ , located symmetrically at both sides of the inner cavity.

Figure 3 shows the intensity map of  $\text{H}^{13}\text{CO}^+$  in color, overlaid with SiO contours in black. The line maps are at  $\sim -91.9 \text{ km s}^{-1}$ , near the systemic velocity

of the source, where the  $\text{H}^{13}\text{CO}^+$  profile shows the peak of intensity. The  $\text{H}^{13}\text{CO}^+$  emission shows a ring shape similar to that seen in SiO, with a inner hole coincident with the cavity found in the SiO observations, but with most of this emission lying outside the SiO ring. The  $\text{H}^{13}\text{CO}^+$  inner hole has a size of  $1.82'' \times 1.12''$ , with a PA of  $112^\circ$ , and it is determined by the  $4\sigma$  emission contour. The  $\text{H}^{13}\text{CO}^+$  structure observed at this velocity channel has major and minor axes, considering the  $3\sigma$  contour as the outer edge of this emission, of  $8.10 \pm 0.32''$  and  $6.79 \pm 0.20''$ , respectively, with a PA of  $78^\circ$ . The deconvolved angular sizes are then  $8.03 \pm 0.32''$  and  $6.57 \pm 0.22''$ , with a PA of  $76^\circ$ , which correspond to a geometric mean size of 0.26 pc at the source distance.

The red ellipse in Figure 3 represents the 50% contour of the radio continuum source at 8.6 GHz (Merello et al. 2013). The emission at 8.6 GHz is located inside the inner cavity of the SiO emission and is unresolved within the beam ( $1.51'' \times 0.99''$ ).

### 4.3 Discussion

The SiO emission is an indicator of shocked gas, commonly seen around young stellar objects, with enhanced abundance attributed to Si being sputtered from dust grains for jet velocities exceeding  $25 \text{ km s}^{-1}$  (e.g., Arce et al., 2007; Garay et al., 1998, 2002). Because the wing velocities of the G331.512–0.103 outflow extend to  $\pm 70 \text{ km s}^{-1}$ , we expected to see SiO emission in the wings, likely with a bipolar pattern, and we do. However, the fact that a ring of SiO emission is also present at the systemic velocity, with a cavity of the size of the beam, indicates that a more isotropic high speed wind is producing shocked gas in a shell. We interpret then

that the G331.512–0.103 source corresponds to a jet almost in the line of sight with an expanding shocked shell surrounding its driving source, which in projection is observed as a ring at the systemic velocity.

To explore this hypothesis, we construct position-velocity (PV) diagrams of the SiO and H<sup>13</sup>CO<sup>+</sup> emission (Figure 4), for slices along the bipolar axis and perpendicular to it. The cavity is clearly present in all diagrams, centered near  $v = -90$  km s<sup>-1</sup>. The SiO PV diagram along the secondary axis shows two strong peaks nearly symmetric around the cavity. These two peaks extend around the cavity down to the 16  $\sigma$  emission contour (represented in red in Figure 4), extending in velocity between  $-111.9$  and  $-63.8$  km s<sup>-1</sup>. The PV diagram along the bipolar axis shows a strong peak at an angular offset of 1". The 3  $\sigma$  contour of the H<sup>13</sup>CO<sup>+</sup> traces the red wing of the outflow up to a velocity of  $\sim -25$  km s<sup>-1</sup>. An additional peak is observed at  $-45$  km s<sup>-1</sup> along the primary axis, but at  $-50$  km s<sup>-1</sup> along the secondary axis. This emission extends between  $-59 < v_{lsr} < -29$  km s<sup>-1</sup>, defined by the 6  $\sigma$  contour in the H<sup>13</sup>CO<sup>+</sup> PV diagram along the symmetry axis, and it has a size of  $2.5'' \times 1.4''$  ( $\sim 0.07$  pc). We consider this high-velocity emission likely to be a molecular “bullet”, feature sometimes observed in star formation regions (e.g. Masson & Chernin, 1993; Santiago-García et al., 2009; Kristensen et al., 2012).

The bipolar symmetry at the extreme velocities requires a jet-like outflow, but the ring structure at the systemic velocity indicates a nearly isotropic component. The latter surrounds a region of ionized material, whose expansion could produce the isotropic component. Considering the extension of the symmetric peaks in the PV diagram of SiO, we estimate that the expanding shell has a velocity of  $\sim 24$  km

$\text{s}^{-1}$ . A jet originating from the high-mass forming star, the likely source of the radio emission observed at 8.6 GHz, could drive the molecular outflow observed in the high-velocity wings of the SiO spectra. The  $\text{H}^{13}\text{CO}^+$  emission, being optically thin toward the wings of the outflow, is only tracing the red lobe of this outflow, and the line profile suggests that toward the systemic velocity, some gas is still infalling toward the central star. However, such a dip can also be created by resolving out ambient cloud emission, so further observations would be needed to test this interpretation.

An estimate for the crossing time is given by  $t_{cross} = \theta/(2v_{max})$ , with  $\theta$  the diameter of a projected shell, and  $v_{max}$  the maximum velocity relative to the ambient gas. Using  $v_{max} = 24 \text{ km s}^{-1}$ , we obtain  $t_{cross} < 600 \text{ yr}$  for the inner hole and  $\sim 2000 \text{ yr}$  for the SiO ring with diameter  $3''$  (or 0.11 pc, considered as the middle point between the inner and outer edges of the ring). These estimates would make this source one of the youngest examples of flows around massive forming stars. The momentum ( $2.4 \times 10^3 \text{ M}_\odot \text{ km s}^{-1}$ ) and kinetic energy ( $1.4 \times 10^{48} \text{ erg}$ ) of the outflow were measured by Bronfman et al. (2008) from CO(7-6) observations. Taking 2000 years as the relevant time, the resulting force is  $1.2 \text{ M}_\odot \text{ km s}^{-1} \text{ yr}^{-1}$  and the mechanical luminosity is  $6.4 \times 10^3 \text{ L}_\odot$ , both higher than any values found in the compilation of outflow properties by Wu et al. (2004).

The mass of the  $\text{H}^{13}\text{CO}^+$  emission toward the ambient gas and the bullet is estimated considering a local thermodynamic equilibrium (LTE) formalism and optically thin emission (see e.g. Garden et al., 1991). Considering an excitation temperature of 100 K, a mean molecular weight  $\mu = 2.72 m_{\text{H}}$ , and an abundance  $[\text{H}^{13}\text{CO}^+/\text{H}_2] = 3.3 \times 10^{-11}$  (Blake et al., 1987), the LTE mass of the ambient gas

and the bullet are  $36 M_{\odot}$  and  $1.8 M_{\odot}$ , respectively.

The continuum emission was determined from regions of the ALMA Band 7 spectrum that appeared to be line free, though we cannot rule out some level of contamination by line emission. The lower panel of Figure 4.3 shows the 0.86 mm continuum emission, overlaid on the  $\text{H}^{13}\text{CO}^+$  emission at  $-91.9 \text{ km s}^{-1}$ . A point-like source lies within the ring of SiO and  $\text{H}^{13}\text{CO}^+$  emission, and a more extended component agrees well with the  $\text{H}^{13}\text{CO}^+$  ring.

The continuum emission has a FWHM of  $2.94'' \times 2.18''$  and a total flux of 4.3 Jy. This emission could arise from either free–free emission from a very dense ionized wind or from dust emission, or a combination. As a test, we estimated the integrated flux of the continuum emission with a point source removed at the peak position of the 8.6 GHz continuum emission showed in Figure 3, obtaining a value of 3.9 Jy. This integrated flux of the continuum emission is much less than the 66.7 Jy measured at this wavelength in a  $33''$  region (Merello et al., 2013), but much more than would be expected from a uniformly distributed emission, therefore we associate this emission with an envelope around the central object. If we attribute this measured flux to dust emission, we can estimate mass and other properties of the source. At a radius of  $1''$ , or 0.036 pc at the source distance, and a luminosity of  $7 \times 10^5 L_{\odot}$  (Merello et al., 2013), the equilibrium dust temperature would be 400 – 1000 K, for a range of dust properties. Assuming 400 K, and using OH5 opacities, the mass estimated in a region of  $2.9''$  in size, or 0.11 pc, would be  $38 M_{\odot}$ , implying a mass surface density of  $5140 M_{\odot} \text{ pc}^{-2}$ , or  $1.07 \text{ g cm}^{-2}$ , and a mean volume density of  $1.3 \times 10^6 \text{ cm}^{-3}$ .

An interesting comparison can be made to the outflow from G5.89 (e.g., Har-

vey & Forveille 1988; Acord et al. 1997; Watson et al. 2007; Su et al. 2012), which also shows a shell morphology along with a bipolar flow. The expansion age for the UCHII region is 600 yr, measured from multi-epoch observations (Acord et al., 1998), while the bipolar outflow is older, with estimates ranging from 3000 to 7700 yr. Estimates of the outflow properties vary, but the values in the Wu et al. (2004) compilation are a mass of  $70 M_{\odot}$ , a momentum of  $1600 M_{\odot} \text{km s}^{-1}$ , and a mechanical luminosity of  $1600 L_{\odot}$ . In comparison with the G5.89 source, the G331.512–0.103 outflow has a shorter age and a higher mechanical luminosity and momentum.

#### 4.4 Summary and conclusions

We have performed a study with ALMA Band 7 of the massive and energetic molecular outflow G331.512–0.103. The high angular resolution observations allow us to resolve this source in a set of four molecular lines: SiO(8-7),  $\text{H}^{13}\text{CO}^+(4-3)$ ,  $\text{HCO}^+(4-3)$  and CO(3-2). The SiO emission is confined in a region of size less than  $5''$  (0.18 pc at a distance of 7.5 kpc), and reveal the presence of a ring-type structure toward the systemic velocity of the source. This feature is also observed in the  $\text{H}^{13}\text{CO}^+$  line, and the cavity is coincident with a strong and compact radio continuum source observed at 8.6 GHz. We interpret these observations as a young stellar object producing a compact H II region, with an expansion shock propagating into the medium and possibly with dense material still infalling around this shell. CO,  $\text{HCO}^+$  and SiO observations trace the full extension of the outflow wings, but the  $\text{H}^{13}\text{CO}^+$  only traces the red wing, also showing the possible presence of a bullet of dense material. We estimated an age of  $\sim 2000$  yrs for the expanding shell, making it



one of the youngest examples of massive molecular outflows observed toward massive young stars.

Table 4.1. Parameters of the molecular line observations of molecular outflow  
G331.512–0.103

Line	Frequency (GHz)	Noise (Jy beam <sup>-1</sup> )	Velocity at peak (km s <sup>-1</sup> )	Peak flux density (Jy)	Deconv. angular size <sup>a</sup> ( $''$ )	Position angle ( $^{\circ}$ )	Deconv. size <sup>a</sup> (pc)
SiO(8-7)	347.33058	0.139	-89.5311	40.4	2.6×2.3	105	0.09
H <sup>13</sup> CO <sup>+</sup> (4-3)	346.99835	0.045	-91.9158	30.1	3.5×2.4	93	0.11
HCO <sup>+</sup> (4-3)	356.73424	0.214	-85.0056	91.4	2.6×2.5	106	0.09
CO(3-2)	345.79599	0.365	-96.9012	238.5	2.8×2.5	110	0.10

<sup>a</sup>FWHM of moment 0 maps, integrated over full velocity extension of the line.

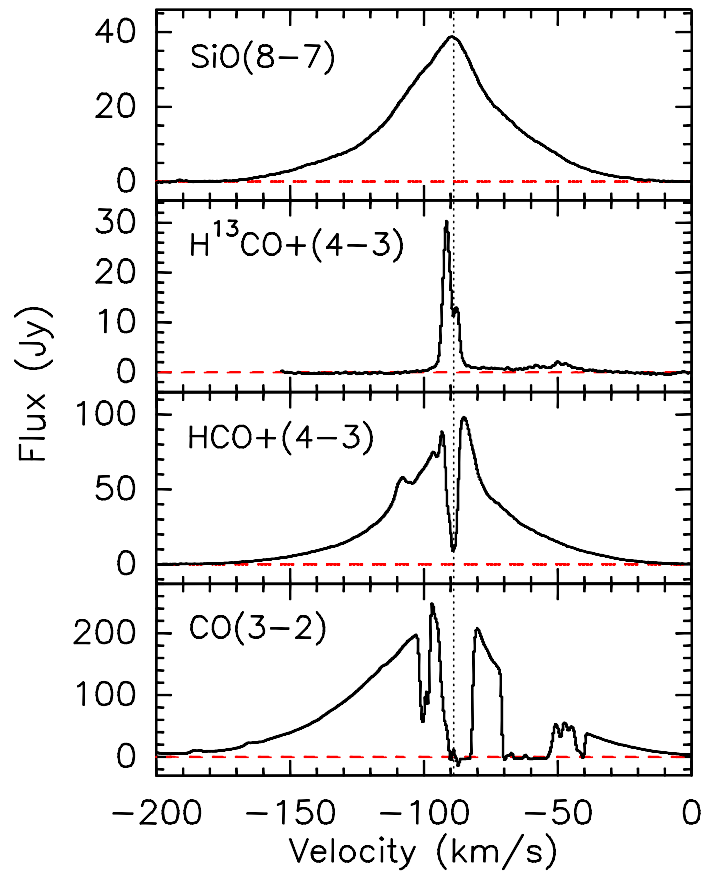


Figure 4.1 Integrated spectra observed with ALMA of the G331.512-0.103 molecular outflow. A dashed line is drawn in each spectrum representing the baseline. The dotted vertical line shows the systemic velocity of this source ( $-88.9 \text{ km s}^{-1}$ ).

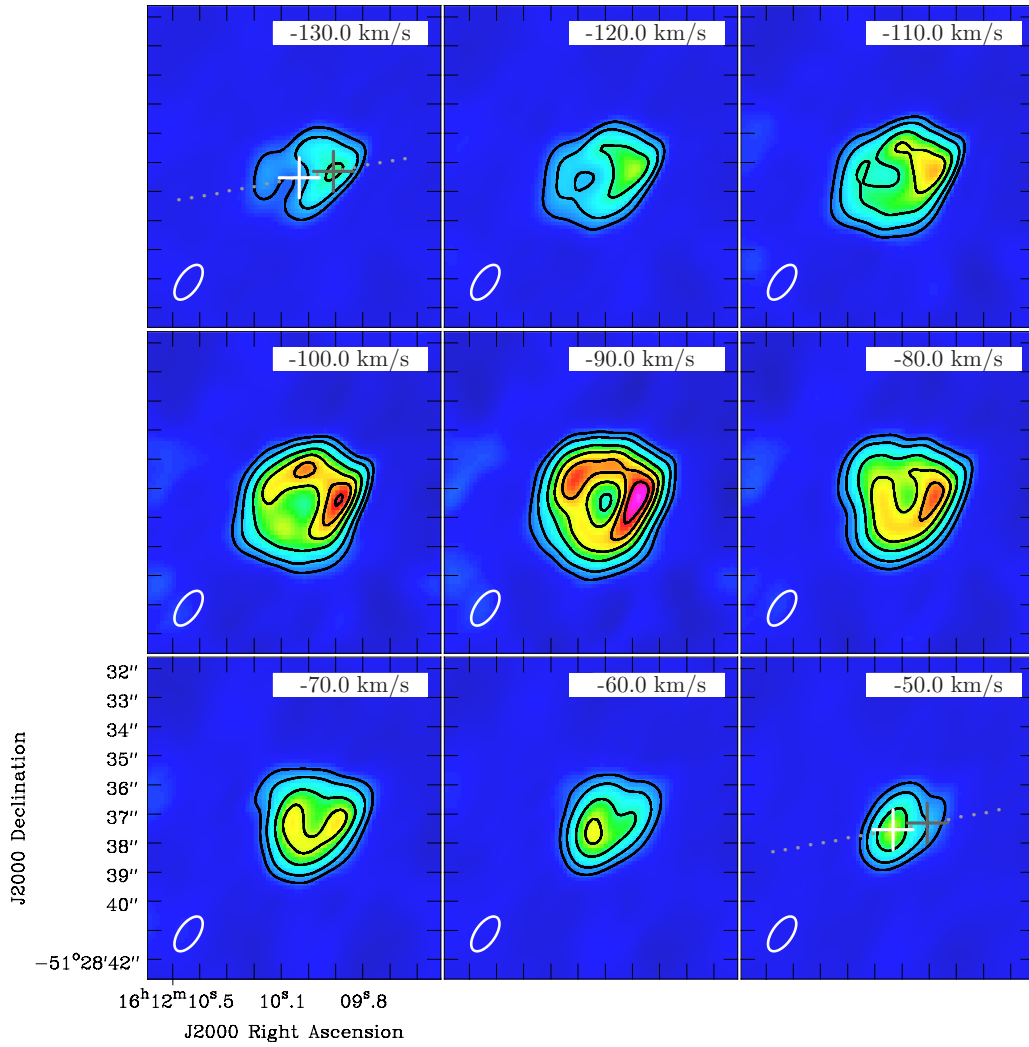


Figure 4.2 Channel maps of the SiO(8-7) line emission. The contours are at 3, 6, 12, 18, 24 and 30 times the rms defined for the SiO emission ( $0.14 \text{ Jy beam}^{-1}$ ). The velocity of each channel is indicated in the upper right corner of each box. The channels are separated by  $10 \text{ km s}^{-1}$ . In the central channel map, toward the systemic velocity of the source ( $-88.9 \text{ km s}^{-1}$ ), the emission shows a clear ring-type or projected shell structure, with the inner hole well determined at the  $18 \sigma$  contour. The ALMA synthesized beam is shown at the bottom left corner in each box. The gray and white crosses define the positions considered in the blue and red lobes to set the symmetry axis of the outflow, represented by the gray dotted line.

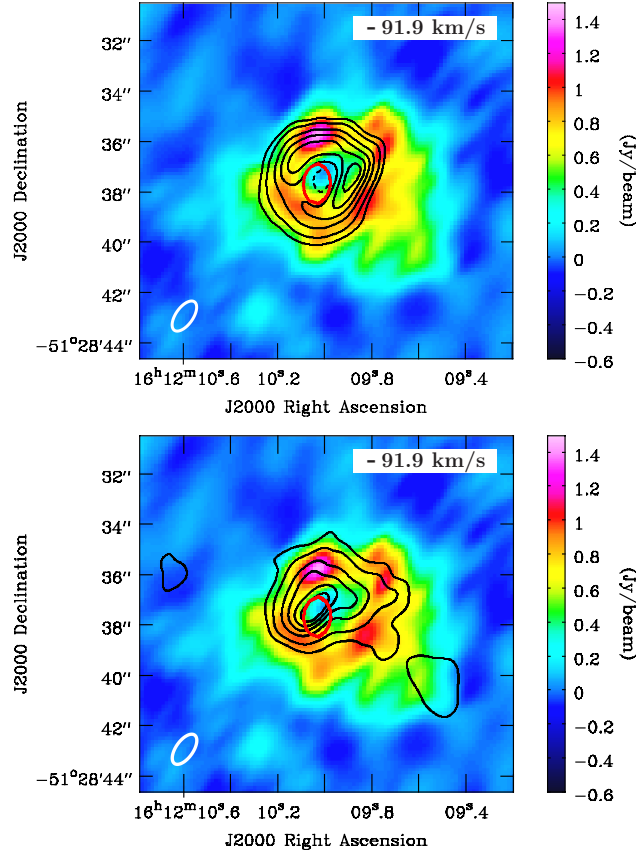


Figure 4.3 *Top* :  $\text{H}^{13}\text{CO}^+$  (4-3) emission (in colors) of the G331.512–0.103 source at a velocity of  $-91.9 \text{ km s}^{-1}$ , where the peak of flux density is found. The overlaid contours in black correspond to the SiO(8-7) emission at the same velocity, at 3, 6, 12, 18, 24 and  $30 \sigma$  (with  $\sigma=0.14 \text{ Jy beam}^{-1}$ ). The dashed contour represent the  $12 \sigma$  emission toward the cavity observed in SiO, which is coincident spatially with the ones observed with  $\text{H}^{13}\text{CO}^+$ . The red contour shows the 50% of emission (peak of  $158 \text{ mJy beam}^{-1}$ ) of the radio source detected at 8.6 GHz toward this source, presented by Merello et al. (2013). The peak position of the radio continuum observations is inside the cavity described by the SiO and  $\text{H}^{13}\text{CO}^+$  emissions. *Bottom* :  $\text{H}^{13}\text{CO}^+$  (4-3) emission (in colors), with overlaid black contours of the 0.86 mm continuum emission obtained with ALMA. The contours are at 3, 6, 12, 18, 24, 30  $\sigma$  (with  $\sigma=0.02 \text{ Jy beam}^{-1}$ ). The continuum emission peaks, within errors, in the center of the cavity shown in the  $\text{H}^{13}\text{CO}^+$  emission.

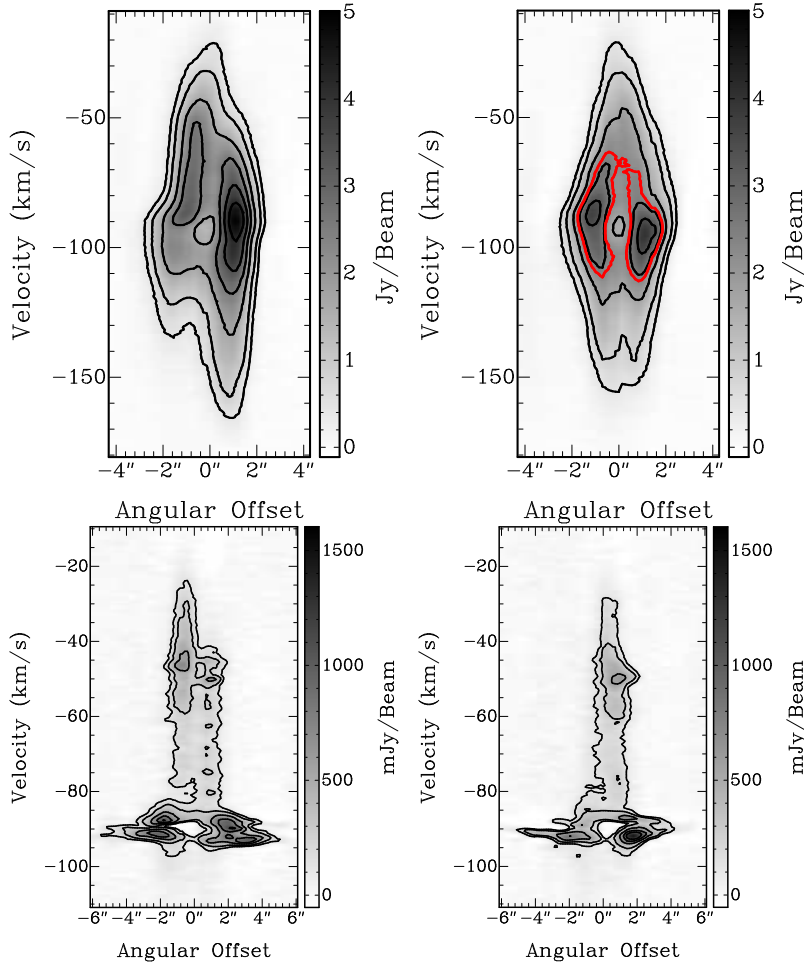


Figure 4.4 Position-velocity diagrams of the SiO(8-7) (*top*) and H<sup>13</sup>CO<sup>+</sup>(4-3) (*bottom*) emission of the G331.512–0.103 source. The slices are centered at the cavity observed in the SiO map ( $\alpha_{2000} = 16^h 12^m 09.985^s$ ,  $\delta_{2000} = -51^\circ 28' 37.42''$ ). Slices along the axis of symmetry of the outflow (primary axis), and perpendicular to this (secondary axis), are displayed in gray scale, with 3, 6, 12, 18, 24 and 30  $\sigma$  contours, with a slit of 4.5'' for the SiO emission, and 6'' for H<sup>13</sup>CO<sup>+</sup>. *Upper left* : Slice of the SiO emission, running along the axis of symmetry (position angle of 102.5°). *Upper right* : Slice of the SiO emission, running perpendicular to the axis of symmetry (position angle of 12.5°). An additional 16  $\sigma$  contour in red is shown, extending between -111.9 and -63.8 km s<sup>-1</sup>. *Bottom left* : Slice of the H<sup>13</sup>CO<sup>+</sup> emission, running along the axis of symmetry. *Bottom right* : Slice of the H<sup>13</sup>CO<sup>+</sup> emission, running perpendicular to the axis of symmetry.

# Chapter 5

## Summary and Future Work

### 5.1 Summary

This section presents a brief summary of some of the main results of this dissertation.

1. I presented a follow-up study of Galactic millimeter sources identified from the Bolocam Galactic Plane Survey, likely to be molecular clumps. For this, I observed a sample of 107 maps of continuum emission at  $350\ \mu\text{m}$ , obtained with the SHARC-II bolometer camera at the Caltech Submillimeter Observatory. The higher resolution of the SHARC-II images ( $8.5''$  beam) compared with the  $1.1\ \text{mm}$  images from BGPS ( $33''$  beam) allowed the identification of a large population of smaller substructures within the clumps. From the 619 clumps considered,  $\sim 50\%$  of them have more than two substructures and 22 clumps have more than 10. The fraction of the mass in dense substructures seen at  $350\ \mu\text{m}$  compared to the mass of their parental clump is  $\sim 0.19$ , and the surface densities of these substructures are, on average, 2.2 times those seen in the clumps identified at  $1.1\ \text{mm}$ .
2. The dust temperature of BGPS sources is determined using the  $350\ \mu\text{m}$  and  $1.1\ \text{mm}$  continuum maps. I found a large number of cold sources in the sample.

The distribution of temperatures of the clumps has a median of 13.3 K and mean of  $16.3 \pm 0.4$  K, assuming an opacity law index of 1.7. The single-color method for the estimation of temperatures is in reasonable agreement with values from studies using spectral energy distribution modeling. Comparison with gas temperatures derived from ammonia observations shows a mean value of the ratio  $T_{gas}/T_{dust}$  of  $\sim 0.8$  and a median of 0.76. I found a significant number of cold clumps, candidates to be prestellar sources.

3. A fraction of sources present properties characteristic of massive star forming regions. For a well-characterized sample of 286 substructures inside clumps, 88 (31%) of them exceed a surface density of  $0.2 \text{ g cm}^{-2}$ , and 18 (6%) exceed  $1.0 \text{ g cm}^{-2}$ , thresholds for massive star formation suggested by theorists. Comparison with surveys of continuum emission toward massive star forming regions shows that several clumps in the sample share similar characteristics. In general, these sources have temperatures  $\sim 30$  K, implying active star formation.
4. I presented molecular line and dust continuum observations toward the high-mass star forming region G331.5-0.1, one of the most active and extreme high-mass star forming environments in our Galaxy, located at the tangent region of the Norma spiral arm, at a distance of 7.5 kpc. Molecular line and millimeter continuum emission maps reveal the presence of six compact and luminous molecular clumps. These clumps have the following average properties: size of 1.6 pc, mass of  $3.2 \times 10^3 M_{\odot}$ , mean molecular hydrogen density of  $3.7 \times 10^4 \text{ cm}^{-3}$ , dust temperature of 32 K, and integrated luminosity of  $5.7 \times 10^5 L_{\odot}$ , consistent



with values found on clumps toward massive star-forming regions by Faúndez et al. (2004). While the rest of the clumps have surface density of  $0.2\text{--}0.3\text{ g cm}^{-2}$ , only the brightest clump has a surface density above the threshold of  $1.0\text{ g cm}^{-2}$  presented by Krumholz & McKee (2008) for the formation of a massive star.

5. At the center of the brightest clump in G331.5, molecular emission of CS, CO, SiO and SO reveal the presence of a high-velocity and energetic molecular outflow, with orientation most likely in the line of sight and gas rotational temperatures of  $>120\text{ K}$ . Radio continuum emission is found toward this position, with a spectral index consistent with models of high-velocity stellar winds, along with hydroxyl maser emission. Therefore, the G331.5 region harbors one of the most luminous and massive protostellar objects presently known.
6. Interferometric observations with ALMA of molecular line and continuum emission at  $350\text{ GHz}$  ( $0.86\text{ mm}$ ) show that the outflow is extremely compact, and unveils a ring-type structure toward the systematic velocity of the source, and emission of complex molecules usually found in “hot cores” sources. These observations are interpreted as a young stellar object producing a compact H II region, with an expansion shock propagating into the medium and possibly interacting with dense material infalling sound this shell. The expansion velocity of the shocked shell is  $\sim 24\text{ km s}^{-1}$ , implying a crossing time of about  $2000\text{ yr}$ . Along the symmetry axis of the outflow, there is a velocity feature, which could be a molecular “bullet” of high-velocity dense material, a feature sometimes found toward star forming region.

## 5.2 Future work

The next step will be to integrate the observations and results of this work into the “Via Lactea” collaboration, which aims to exploit the combination of state-of-the-art Galactic Plane surveys, from infrared to radio wavelengths, to obtain a complete panorama of the Milky Way as a star formation engine, and then to use our Galaxy as a paradigm for studies of nearby galaxies and star formation across time. Specifically, I will consider SHARC-II and BGPS data, along with several dust and gas surveys, both ground based and space missions, to complement the new results from the Hi-Gal survey (Molinari et al., 2010) on compact structures identified in *Herschel* maps. I will characterize those star forming structures from a physical and evolutionary point of view, using different evolutionary diagnostics provided by multi-wavelength studies, and estimate their star formation rates and efficiencies. The goals of this project work toward the definition a paradigm for the evolutionary classification of star-forming dense clumps and star forming regions.

A second research project involves selection of a sample of sources for mm interferometric observations. As a result of my dissertation, I obtained a large sample of sources at different stages of evolution, from cold sources ( $T < 15$  K) with high emission at millimeter wavelengths, to warm sources ( $T \sim 50$  K) with high surface densities, likely to harbor a massive protostellar object. A follow-up study would consist of high angular resolution interferometric observations of selected sources with intense continuum emission at 1.1 mm that present signposts of early stages of star formation. A high ratio of  $\text{N}_2\text{H}^+ / \text{HCO}^+$  indicates that these clumps could have core-type structures in them, with cold, CO–depleted gas within those cores. We

can refine our selection of targets using sources with estimated distances and masses, or target sources with low kinetic gas temperatures derived from  $\text{NH}_3$  observations. Results on selected clumps with a large multiplicity of cores and faint substructures will be compared with theories of clustered star formation, and kinematic information of the medium interior to these clumps will constrain the interaction between high-density cores.

The ALMA band 7 spectra (Figures 5.1 and 5.2) observed toward the high-velocity outflow G331.512-0.103 reveal many complex molecules, consistent with hot core chemistry. A future research project consists of the description and analysis of the complete set of molecular lines observed, and a posterior modeling of this source will be conducted with radiative transfer codes to characterize the interaction between extremely energetic outflows and their immediately surrounding medium. Further observations of radio continuum emission will constrain the properties of the emission of embedded ionized gas. I plan to study molecular line emission from highly excited transitions (frequency  $\sim 800$  GHz), which can trace very small scale structures identified for this outflow.

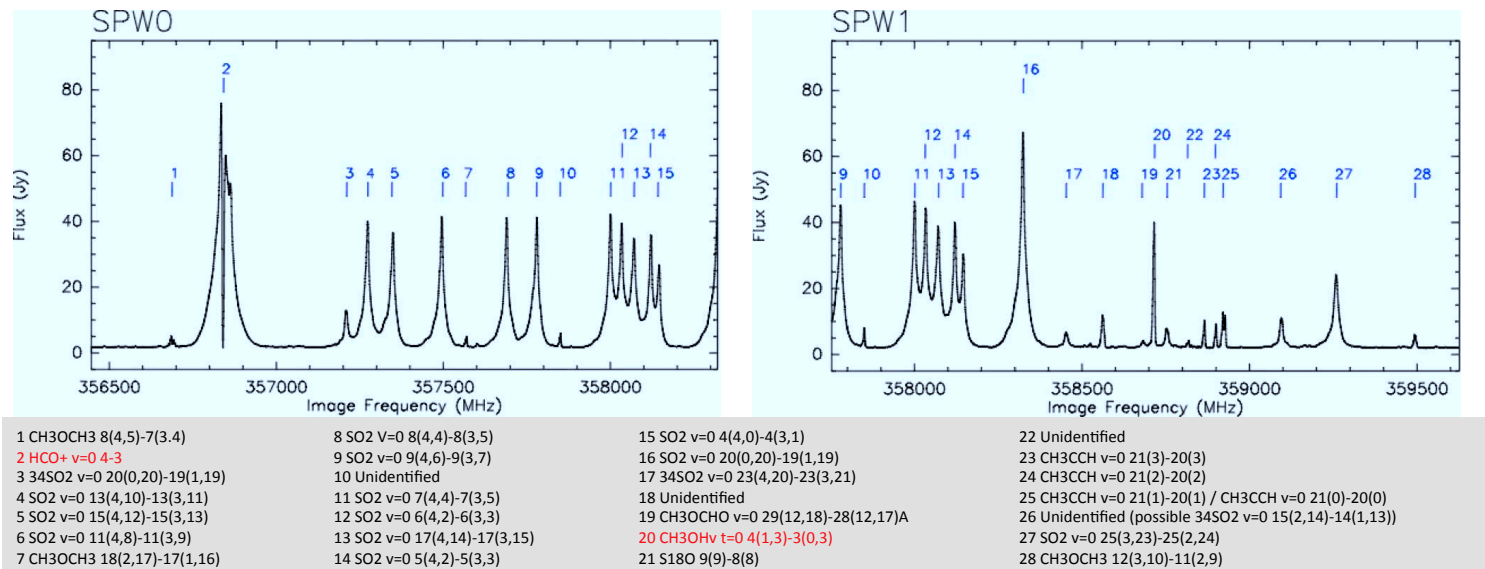


Figure 5.1 Spectral windows 0 and 1 observed with ALMA band 7 toward the molecular outflow G331.512-0.103. The numbers indicate the identified line transition.

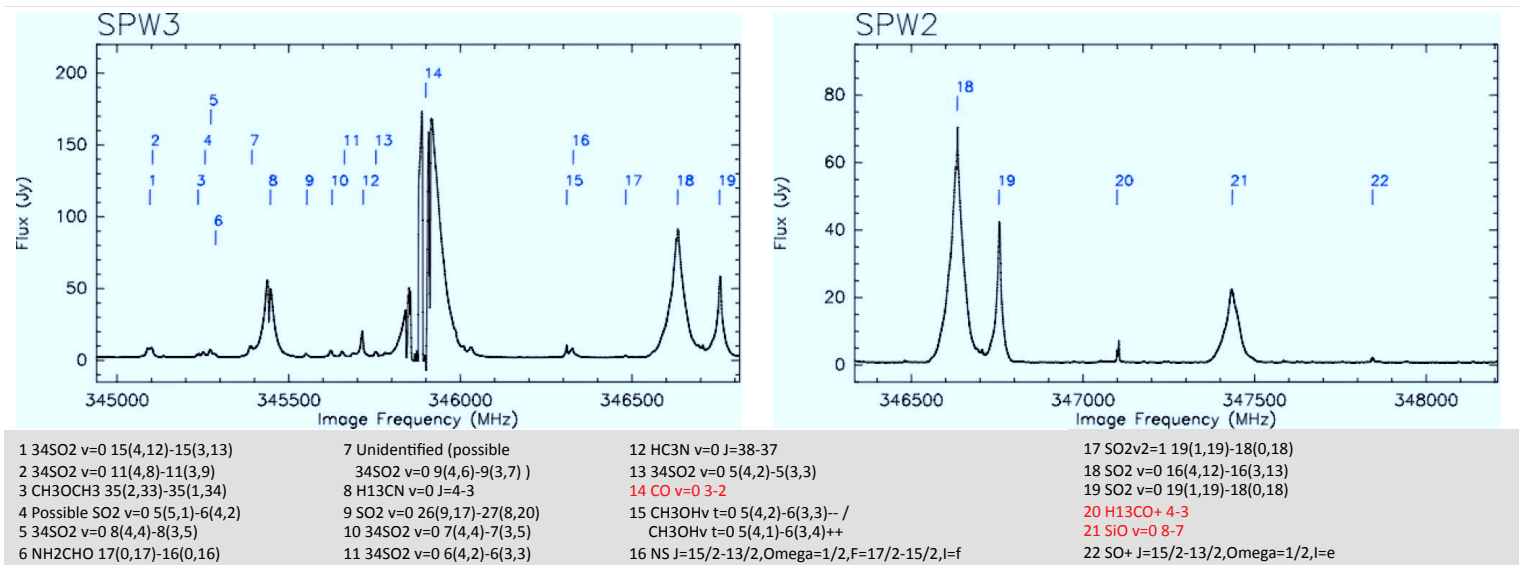


Figure 5.2 Spectral windows 2 and 3 observed with ALMA band 7 toward the molecular outflow G331.512-0.103. The numbers indicate the identified line transition

## Appendices

## Appendix A

### Calibrators of 350 $\mu\text{m}$ continuum maps of BGPS sources

Table A.1 presents in detail the flux calibration and the observed values of  $\tau$  at 225 GHz for each observation run. Flux conversion factors for one beam ( $C_{beam}$ ), 20'' and 40'' aperture conversion factors on SHARC-II maps ( $C_{20}$  and  $C_{40}$ ), and 40'' aperture conversion factors for SHARC-II maps convolved to a resolution of 33'' are shown in the table.

Table A.1. Calibrators of SHARC-II maps

Date	Calibrator	$\tau_{225\text{ GHz}}$	$C_{beam}$ (Jy beam $^{-1}$ $\mu V^{-1}$ )	$C_{20}$ (Jy $\mu V^{-1}$ )	$C_{40}$ (Jy $\mu V^{-1}$ )	$C_{40}^{33''}$ (Jy $\mu V^{-1}$ )
2006 Jun 11	Mars	0.071	10.86	0.39	0.31	0.46
	Mars	0.071	10.15	0.42	0.30	0.46
	Mars	0.071	11.63	0.40	0.33	0.49
2006 Jun 23	Uranus	0.061	8.55	0.28	0.24	0.36
	Uranus	0.062	8.02	0.28	0.23	0.34
2007 Jul 9	Mars	0.068	7.56	0.27	0.22	0.33
	Uranus	0.058	6.55	0.22	0.18	0.27
	Uranus	0.068	7.57	0.25	0.21	0.31
	Neptune	0.058	6.76	0.22	0.19	0.28
	Neptune	0.064	6.42	0.21	0.18	0.27
	Neptune	0.060	7.18	0.23	0.20	0.30
2007 Oct 24	Uranus	0.053	7.80	0.26	0.22	0.32
	Uranus	0.053	8.02	0.27	0.23	0.34
	Neptune	0.055	9.29	0.31	0.26	0.39
	Neptune	0.055	9.20	0.30	0.26	0.38
2007 Oct 27	Uranus	0.052	7.18	0.23	0.20	0.30
	Uranus	0.047	7.80	0.25	0.22	0.33
	Uranus	0.047	7.29	0.24	0.20	0.30
2009 Sep 10	Uranus	0.055	5.80	0.19	0.16	0.24
	Mars	0.062	6.31	0.23	0.18	0.27
2009 Dec 13	Uranus	0.050	6.34	0.22	0.18	0.26
	Uranus	0.050	6.13	0.23	0.18	0.26
	Mars	0.065	5.73	0.20	0.17	0.24
	Mars	0.065	5.67	0.20	0.16	0.24
2009 Dec 14	Uranus	0.068	6.01	0.22	0.17	0.25
	Mars	0.058	5.28	0.22	0.16	0.24
2009 Dec 29	Uranus	0.060	5.84	0.20	0.16	0.24
	Uranus	0.052	5.85	0.19	0.16	0.24
	Mars	0.062	5.72	0.22	0.17	0.26
	Mars	0.062	5.78	0.22	0.17	0.26
	Mars	0.056	5.80	0.22	0.17	0.26
2009 Dec 30	Uranus	0.050	7.06	0.24	0.19	0.28
	Uranus	0.051	7.08	0.24	0.19	0.28
	Mars	0.047	5.70	0.22	0.17	0.25
	Mars	0.052	5.68	0.22	0.17	0.25
	Mars	0.040	5.66	0.22	0.17	0.25
	Mars	0.040	5.81	0.24	0.18	0.26
2009 Dec 31	Uranus	0.051	6.43	0.22	0.18	0.27
	Uranus	0.049	6.32	0.22	0.18	0.26
	Uranus	0.050	6.26	0.22	0.18	0.27
	Mars	0.048	4.87	0.19	0.15	0.22
	Mars	0.048	4.79	0.20	0.15	0.22
2010 Jan 01	Mars	0.045	5.69	0.22	0.17	0.25
2010 Jul 24	Neptune	0.063	19.30	0.61	0.54	0.80
	Uranus	0.070	26.18	0.87	0.72	1.07
	Uranus	0.075	18.00	0.76	0.52	0.81
	Uranus	0.056	11.68	0.58	0.36	0.55
	Uranus	0.065	13.98	0.55	0.39	0.61



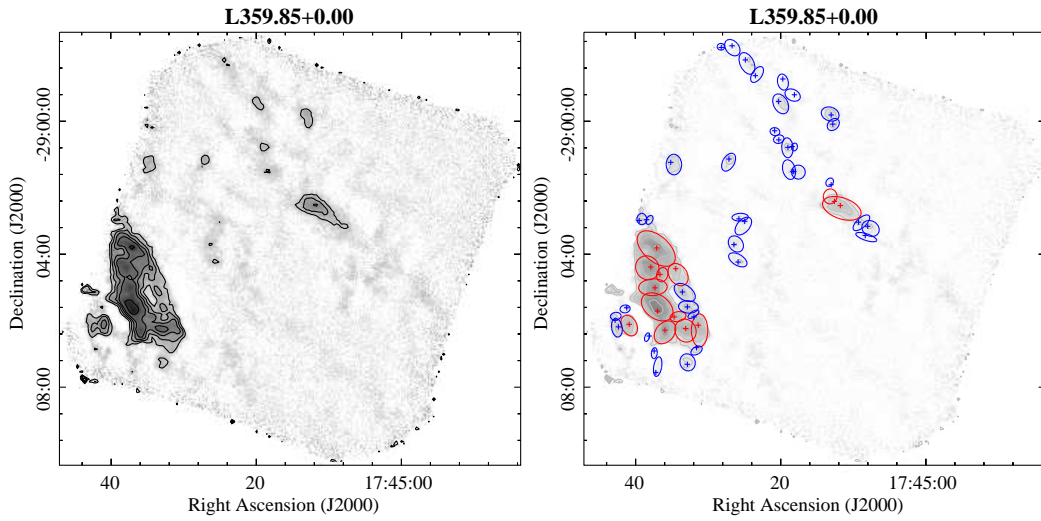
Table A.1 (cont'd)

Date	Calibrator	$\tau_{225\text{ GHz}}$	$C_{beam}$ (Jy beam $^{-1}$ $\mu V^{-1}$ )	$C_{20}$ (Jy $\mu V^{-1}$ )	$C_{40}$ (Jy $\mu V^{-1}$ )	$C_{40}^{33''}$ (Jy $\mu V^{-1}$ )
2010 Jul 25	Neptune	0.077	9.63	0.32	0.27	0.41
	Uranus	0.042	6.09	0.20	0.17	0.25
	Uranus	0.039	5.79	0.19	0.16	0.24
2010 Jul 28	Uranus	0.046	7.12	0.25	0.20	0.30
	Neptune	0.056	6.76	0.21	0.19	0.28
	Uranus	0.056	6.57	0.25	0.18	0.27
2010 Jul 31	Uranus	0.046	6.37	0.20	0.18	0.26
	Neptune	0.050	8.58	0.28	0.23	0.35
	Neptune	0.050	7.71	0.26	0.21	0.32
2010 Aug 01	Neptune	0.050	7.82	0.27	0.22	0.33
	Neptune	0.050	8.22	0.27	0.23	0.34
	Uranus	0.058	6.67	0.23	0.19	0.28
	Neptune	0.036	7.42	0.24	0.20	0.30
	Neptune	0.060	7.67	0.25	0.21	0.31
2010 Dec 05	Neptune	0.050	7.46	0.25	0.20	0.30
	Uranus	0.053	7.06	0.24	0.19	0.29
	Uranus	0.060	5.75	0.20	0.17	0.24
	Uranus	0.030	5.96	0.21	0.17	0.25
2010 Dec 06	Uranus	0.030	6.66	0.23	0.19	0.27
	Uranus	0.040	6.38	0.21	0.18	0.26
	Uranus	0.030	7.07	0.25	0.19	0.29
	Uranus	0.050	7.07	0.26	0.20	0.30
	Uranus	0.038	7.26	0.24	0.19	0.30
	Uranus	0.038	7.04	0.25	0.19	0.29
	Uranus	0.068	6.78	0.26	0.19	0.29
2011 Dec 23	Uranus	0.049	6.93	0.23	0.19	0.28
	Uranus	0.036	11.35	0.38	0.32	0.49
	Uranus	0.071	10.06	0.37	0.29	0.43
2012 Sep 14	Uranus	0.070	11.06	0.38	0.31	0.45
	Uranus	0.050	12.73	0.42	0.35	0.52
	Uranus	0.057	12.88	0.44	0.36	0.53
	Uranus	0.057	12.60	0.42	0.35	0.52
	Uranus	0.062	17.32	0.57	0.47	0.70
2012 Sep 21	Uranus	0.065	17.37	0.59	0.48	0.72
	Uranus	0.070	17.47	0.56	0.49	0.73
	Uranus	0.094	17.79	0.57	0.50	0.74
	Uranus	0.094	16.58	0.55	0.47	0.70

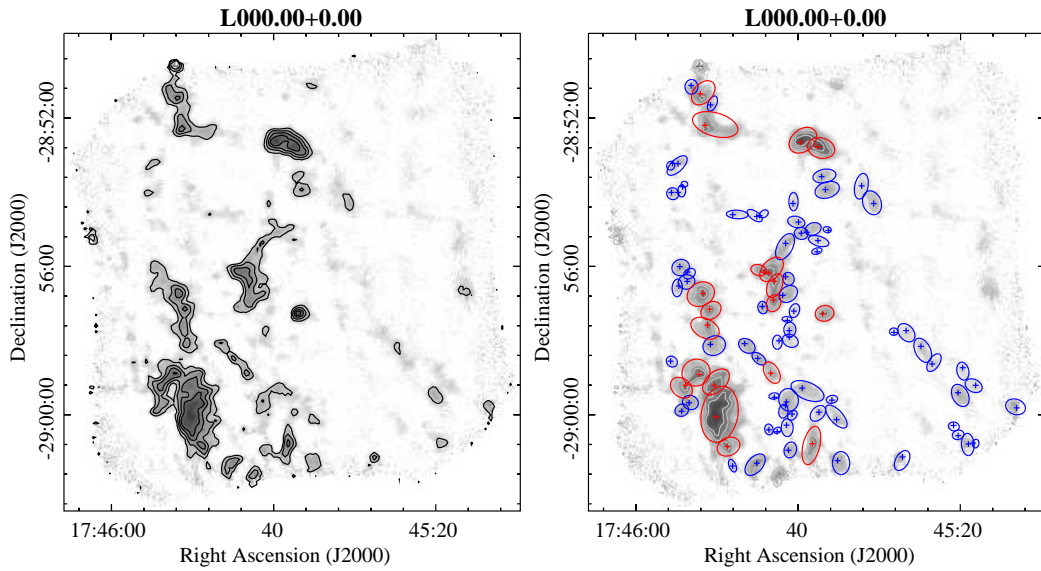
## Appendix B

### Complete sample of 350 $\mu\text{m}$ continuum maps

We present in Figure B.1 our complete sample of 107 regions mapped with SHARC-II. For each of them, the image shows grey scale maps with emission contours at  $3\sigma$ ,  $6\sigma$ ,  $10\sigma$ ,  $15\sigma$ ,  $30\sigma$ ,  $50\sigma$ , and  $100\sigma$ , with  $\sigma$  the rms noise. The value of  $\sigma$  in units of  $\text{mJy beam}^{-1}$  is stated below each map. The image also shows the high-resolution sources extracted with *Boloccat*. Red contours represent sources with signal-to-noise values above 10 (compact sources), and blue contours sources below this limit (faint sources).

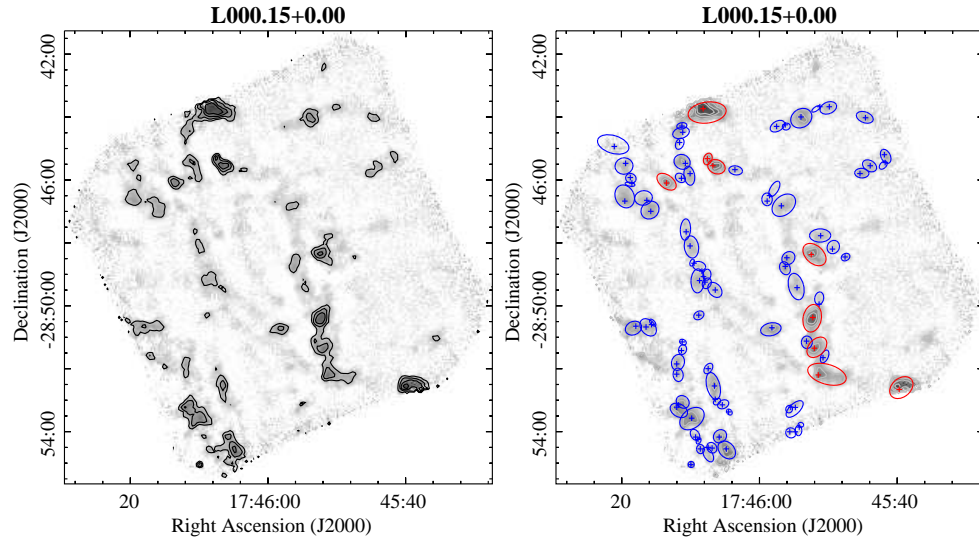


(B.1.1) L359.85+0.00 map,  $\sigma_{rms} = 994 \text{ mJy beam}^{-1}$ .

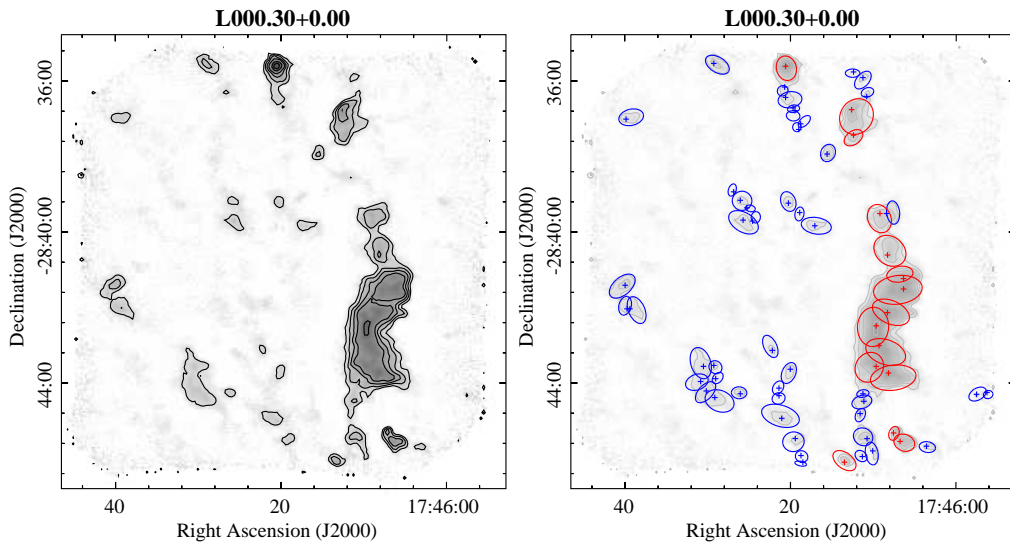


(B.1.2) L000.00+0.00 map,  $\sigma_{rms} = 1453 \text{ mJy beam}^{-1}$ .

Figure B.1 Continuum maps at  $350 \mu\text{m}$  of the 107 regions included in our catalog.. Left: Contours are drawn at  $3\sigma$ ,  $6\sigma$ ,  $10\sigma$ ,  $15\sigma$ ,  $30\sigma$ ,  $50\sigma$ , and  $100\sigma$ . Noise level  $\sigma_{rms}$  is indicated in the figure for each map. Right: Recovery of substructures with *Bolocat* algorithm. Red and blue regions represent the position of dense, compact cores-type sources and faint substructures, respectively. Figures 27.127.107 are available in the online version of the Journal.

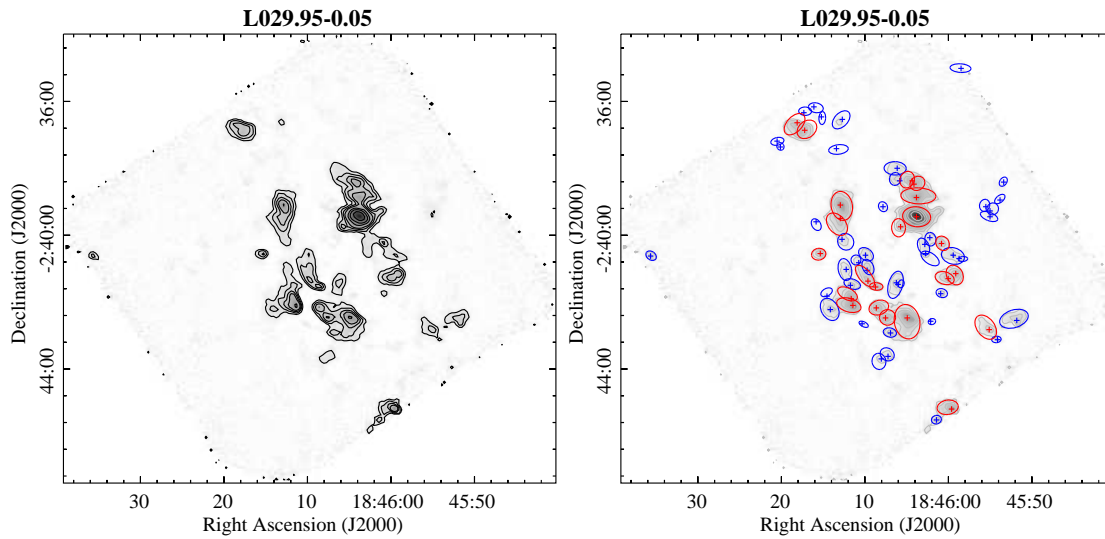


(B.1.3) L000.15+0.00 map,  $\sigma_{rms} = 1438 \text{ mJy beam}^{-1}$ .

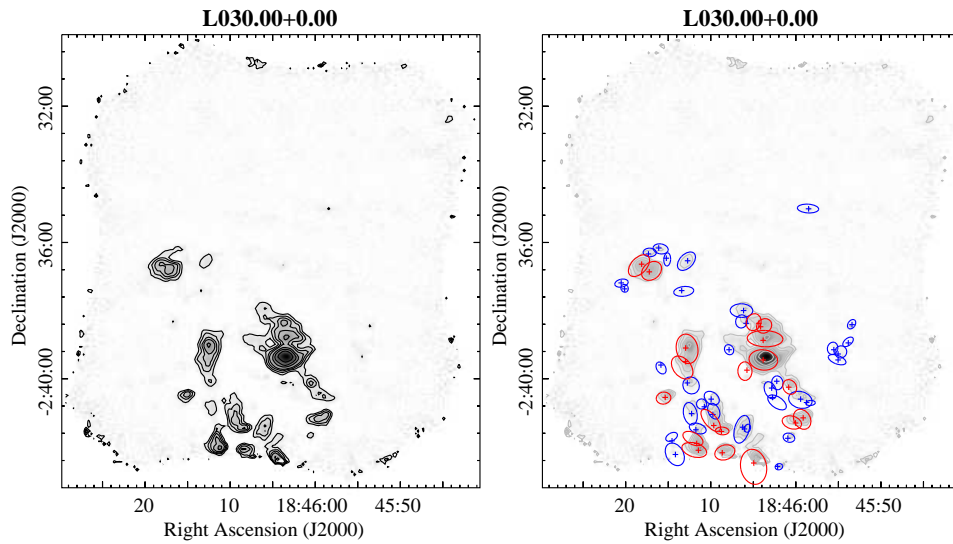


(B.1.4) L000.30+0.00 map,  $\sigma_{rms} = 1086 \text{ mJy beam}^{-1}$ .

Figure B.1 Continuation

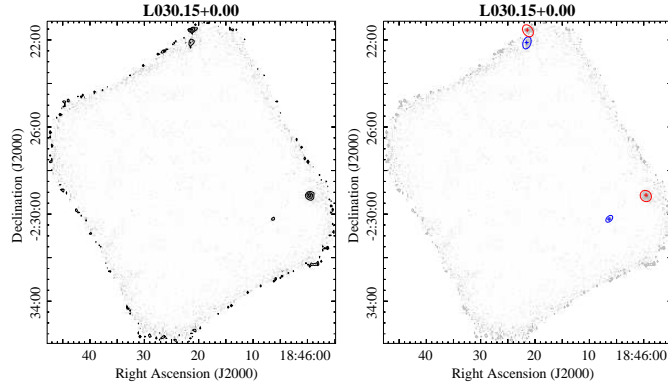


(B.1.5) L029.95-0.05 map,  $\sigma_{rms} = 514 \text{ mJy beam}^{-1}$ .

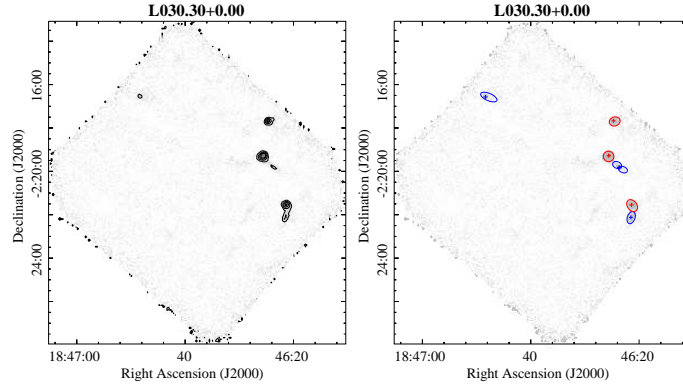


(B.1.6) L030.00+0.00 map,  $\sigma_{rms} = 462 \text{ mJy beam}^{-1}$ .

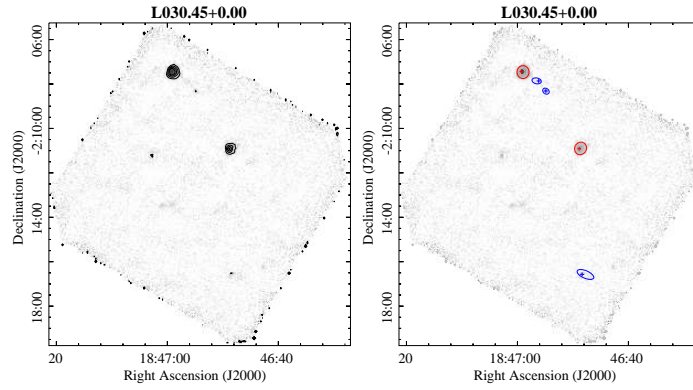
Figure B.1 Continuation



(B.1.7) L030.15+0.00 map,  $\sigma_{rms} = 426 \text{ mJy beam}^{-1}$ .

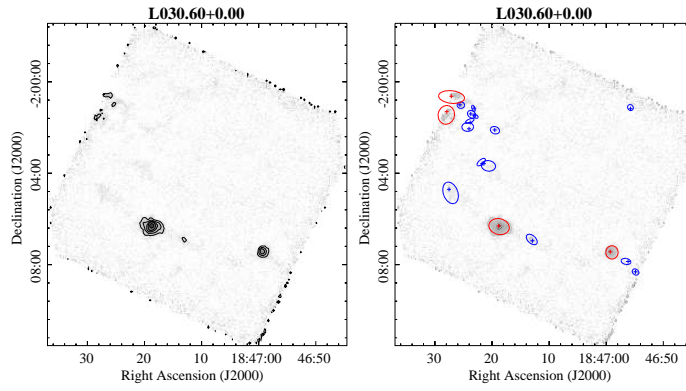


(B.1.8) L030.30+0.00 map,  $\sigma_{rms} = 496 \text{ mJy beam}^{-1}$ .

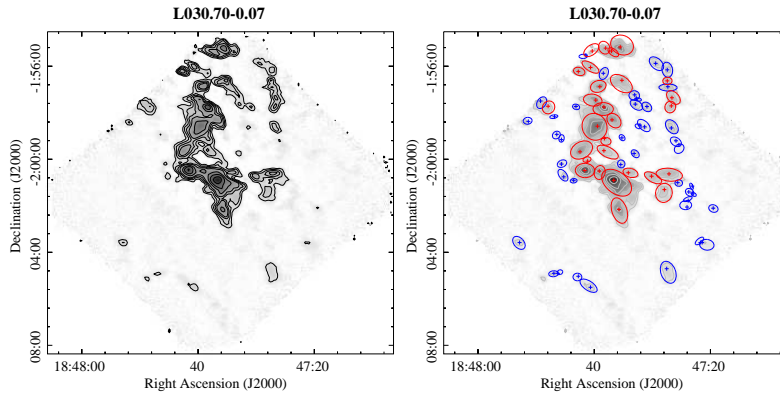


(B.1.9) L030.45+0.00 map,  $\sigma_{rms} = 603 \text{ mJy beam}^{-1}$ .

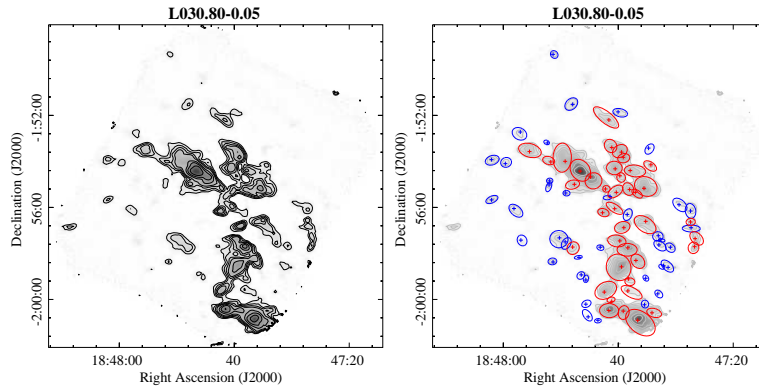
Figure B.1 Continuation



(B.1.10) L030.60+0.00 map,  $\sigma_{rms} = 888 \text{ mJy beam}^{-1}$ .

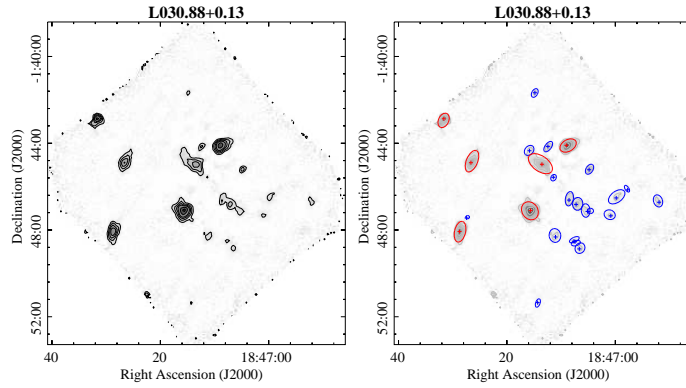


(B.1.11) L030.70-0.07 map,  $\sigma_{rms} = 510 \text{ mJy beam}^{-1}$ .

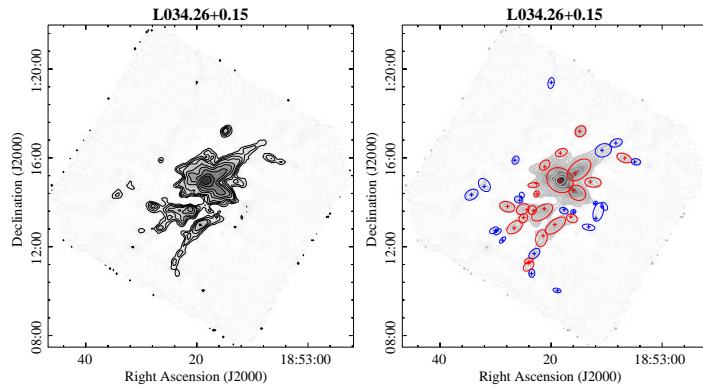


(B.1.12) L030.80-0.05 map,  $\sigma_{rms} = 529 \text{ mJy beam}^{-1}$ .

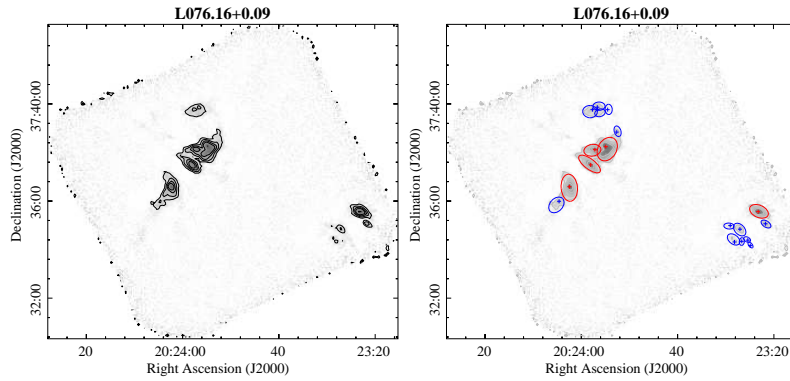
Figure B.1 Continuation



(B.1.13) L030.88+0.13 map,  $\sigma_{rms} = 367 \text{ mJy beam}^{-1}$ .



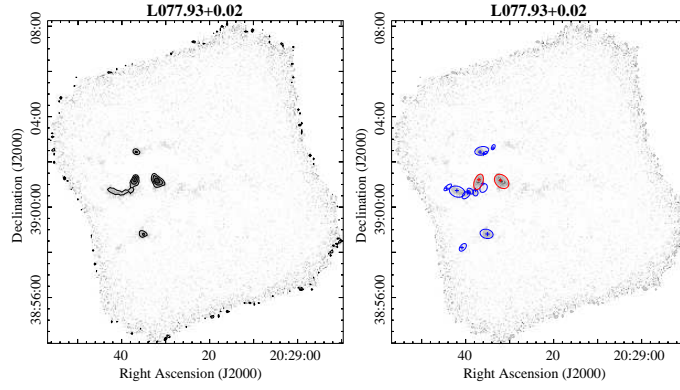
(B.1.14) L034.26+0.15 map,  $\sigma_{rms} = 395 \text{ mJy beam}^{-1}$ . Additional contour is drawn at  $200\sigma$  and  $400\sigma$ .



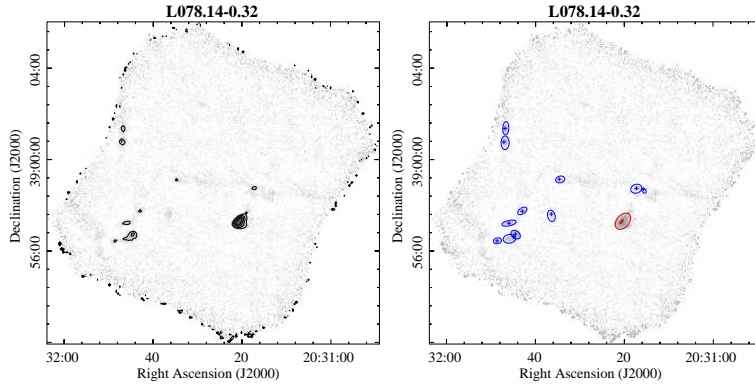
(B.1.15) L076.16+0.09 map,  $\sigma_{rms} = 249 \text{ mJy beam}^{-1}$ .

Figure B.1 Continuation

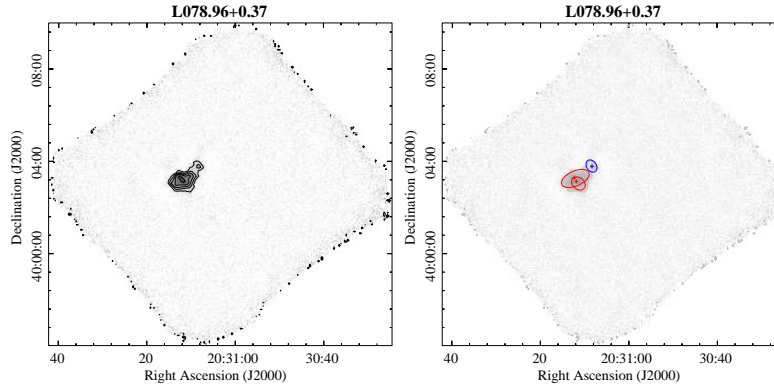




(B.1.16) L077.93+0.02 map,  $\sigma_{rms} = 389 \text{ mJy beam}^{-1}$ .

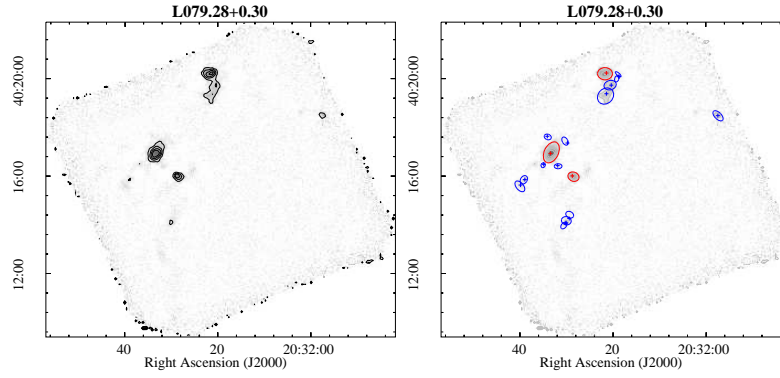


(B.1.17) L078.14-0.32 map,  $\sigma_{rms} = 408 \text{ mJy beam}^{-1}$ .

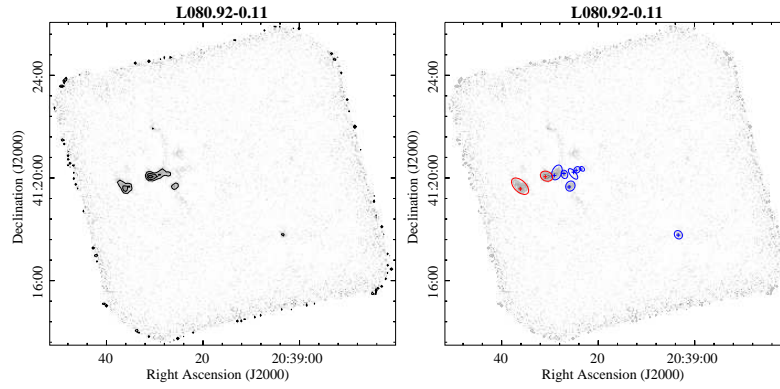


(B.1.18) L078.96+0.37 map,  $\sigma_{rms} = 445 \text{ mJy beam}^{-1}$ .

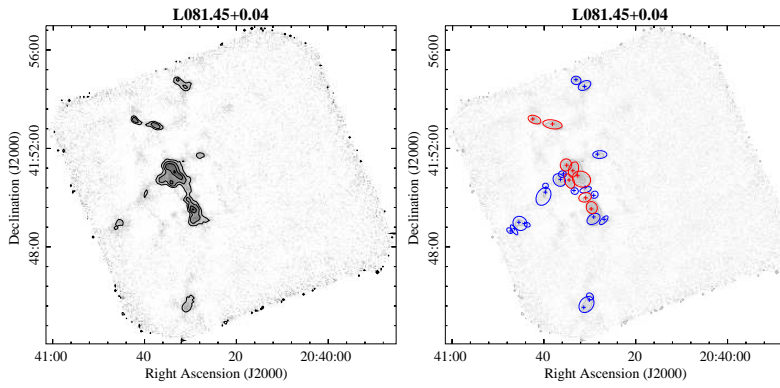
Figure B.1 Continuation



(B.1.19) L079.28+0.30 map,  $\sigma_{rms} = 558 \text{ mJy beam}^{-1}$ .

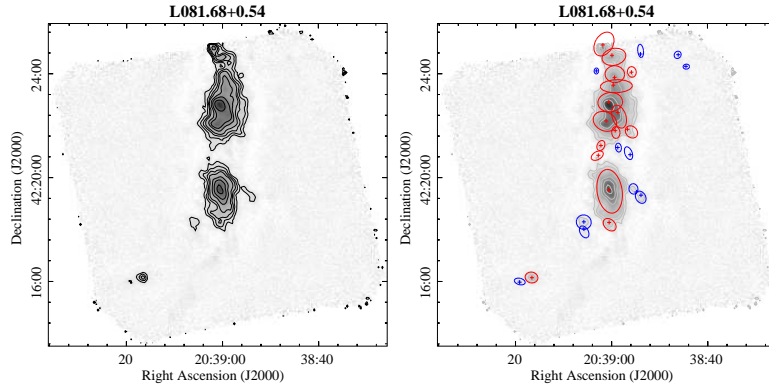


(B.1.20) L080.92-0.11 map,  $\sigma_{rms} = 724 \text{ mJy beam}^{-1}$ .

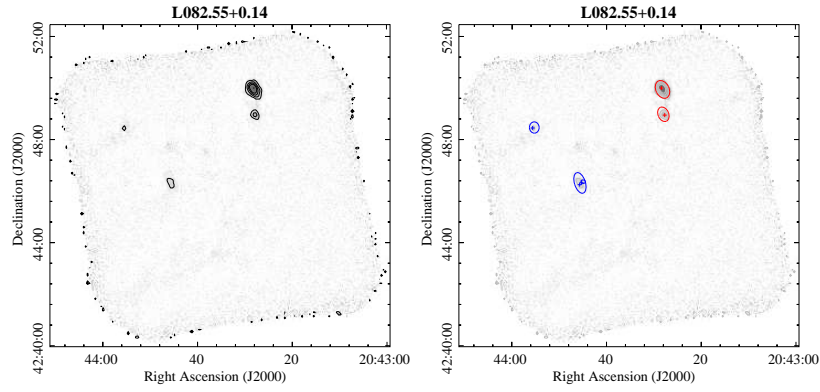


(B.1.21) L081.45+0.04 map,  $\sigma_{rms} = 274 \text{ mJy beam}^{-1}$ .

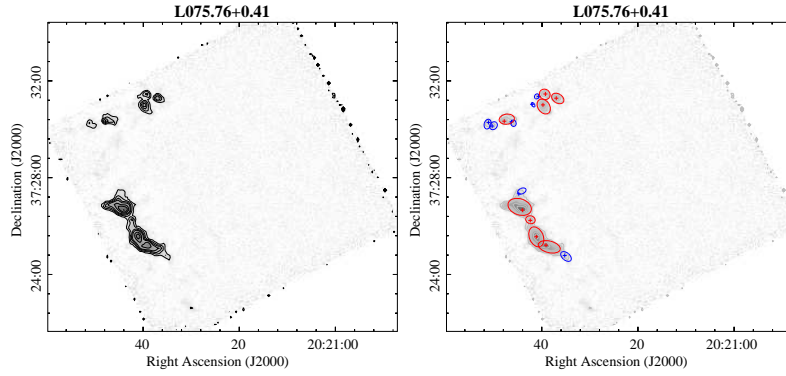
Figure B.1 Continuation



(B.1.22) L081.68+0.54 map,  $\sigma_{rms} = 802 \text{ mJy beam}^{-1}$ .

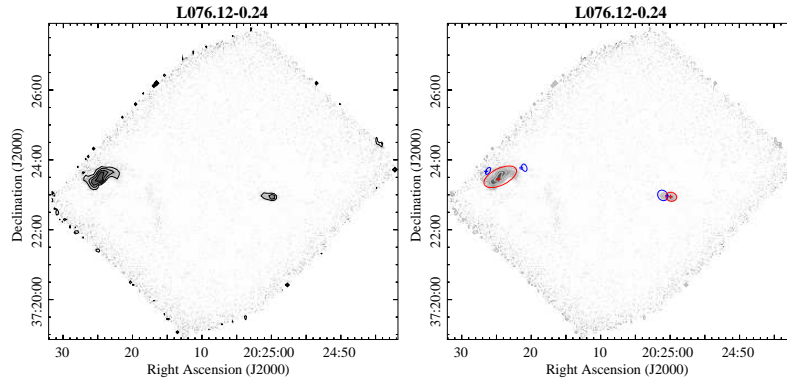


(B.1.23) L082.55+0.14 map,  $\sigma_{rms} = 255 \text{ mJy beam}^{-1}$ .

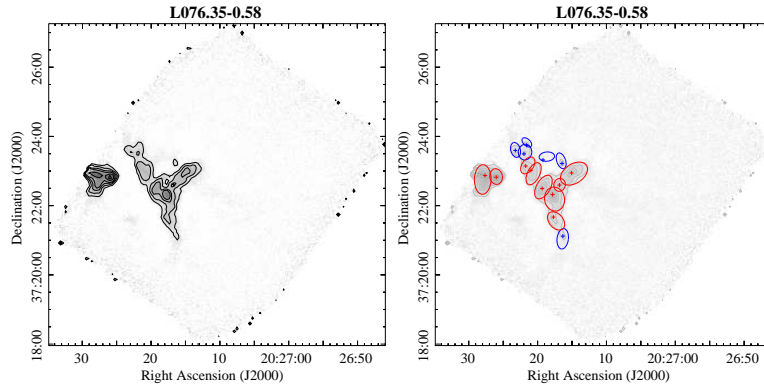


(B.1.24) L075.76+0.41 map,  $\sigma_{rms} = 652 \text{ mJy beam}^{-1}$ .

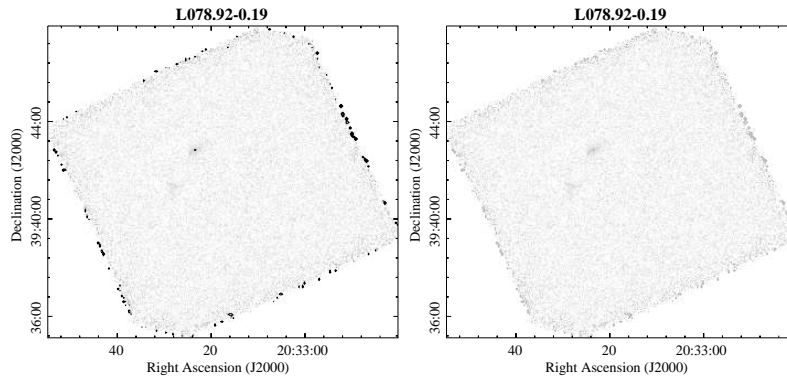
Figure B.1 Continuation



(B.1.25) L076.12-0.24 map,  $\sigma_{rms} = 388 \text{ mJy beam}^{-1}$ .

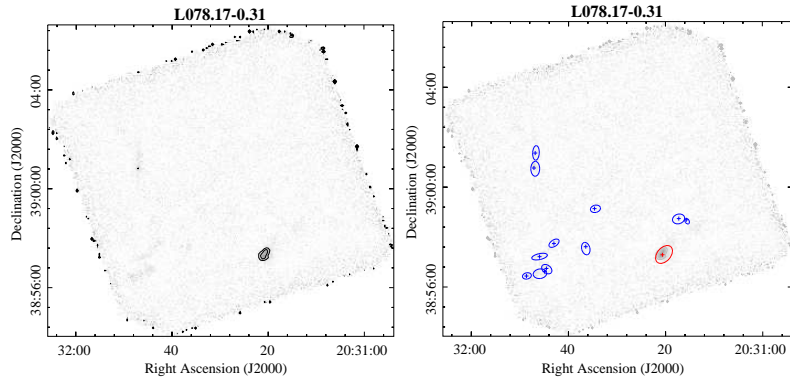


(B.1.26) L076.35-0.58 map,  $\sigma_{rms} = 430 \text{ mJy beam}^{-1}$ .

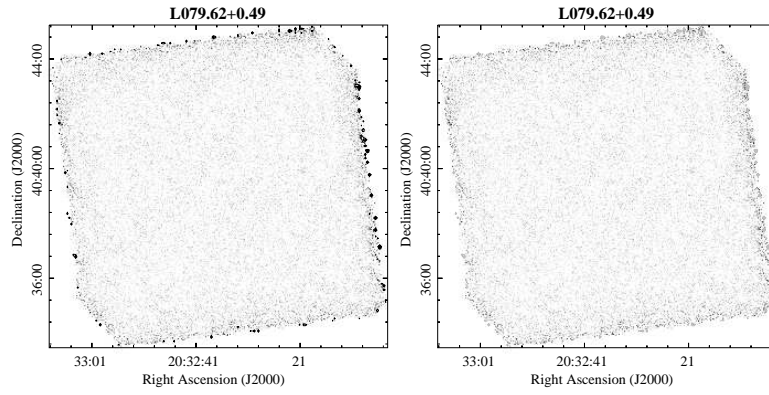


(B.1.27) L078.92-0.19 map,  $\sigma_{rms} = 689 \text{ mJy beam}^{-1}$ .

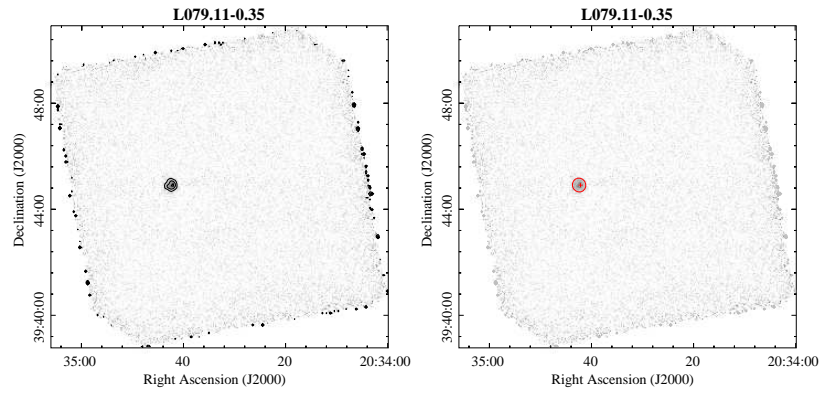
Figure B.1 Continuation



(B.1.28) L078.17-0.31 map,  $\sigma_{rms} = 800 \text{ mJy beam}^{-1}$ .

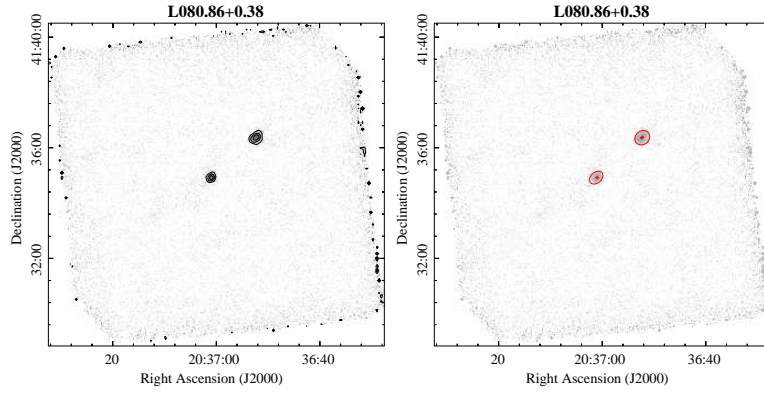


(B.1.29) L079.62+0.49 map,  $\sigma_{rms} = 1489 \text{ mJy beam}^{-1}$ .

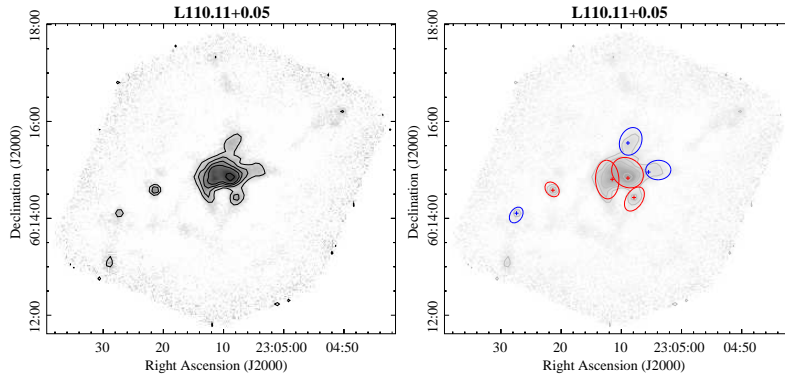


(B.1.30) L079.11-0.35 map,  $\sigma_{rms} = 1226 \text{ mJy beam}^{-1}$ .

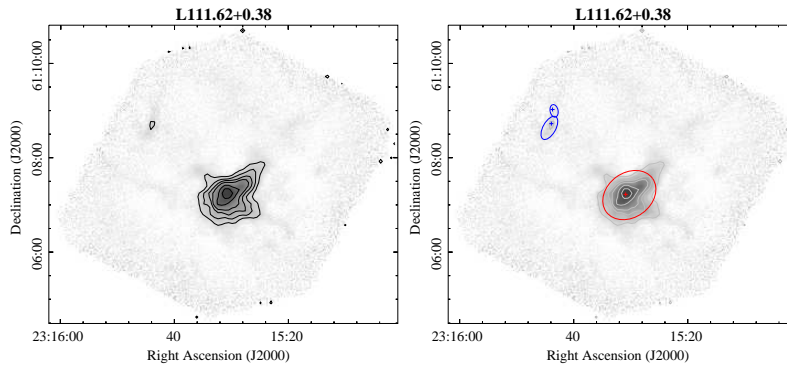
Figure B.1 Continuation



(B.1.31) L080.86+0.38 map,  $\sigma_{rms} = 1874 \text{ mJy beam}^{-1}$ .

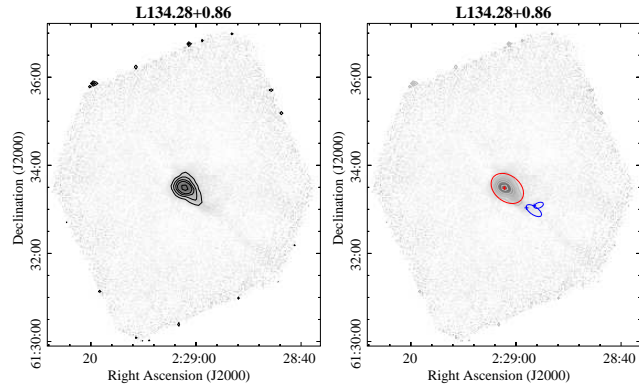


(B.1.32) L110.11+0.05 map,  $\sigma_{rms} = 288 \text{ mJy beam}^{-1}$ .

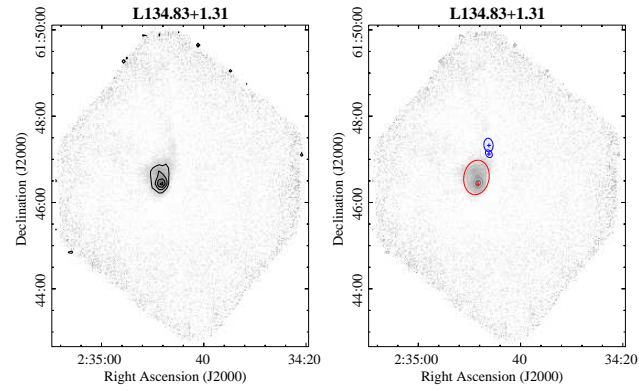


(B.1.33) L111.62+0.38 map,  $\sigma_{rms} = 342 \text{ mJy beam}^{-1}$ .

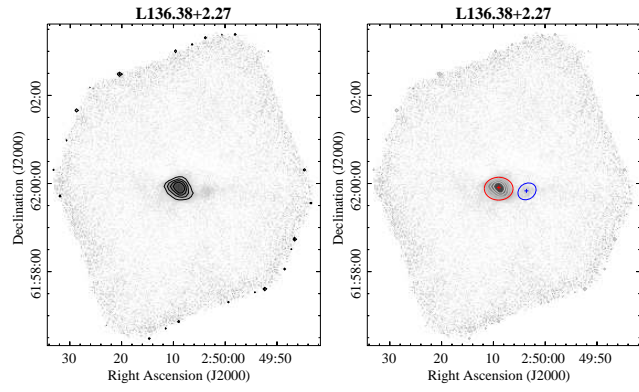
Figure B.1 Continuation



(B.1.34) L134.28+0.86 map,  $\sigma_{rms} = 275 \text{ mJy beam}^{-1}$ .

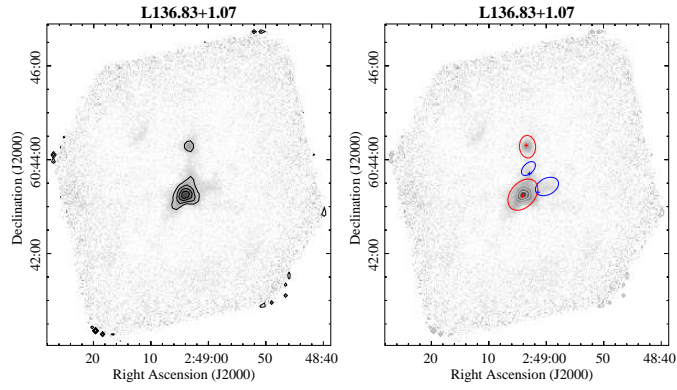


(B.1.35) L134.83+1.31 map,  $\sigma_{rms} = 296 \text{ mJy beam}^{-1}$ .

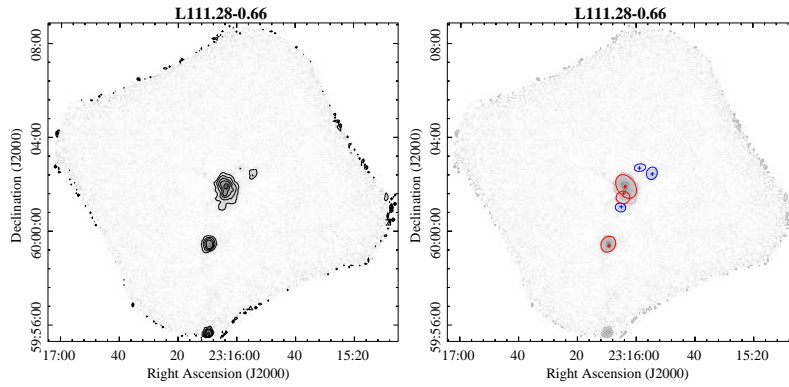


(B.1.36) L136.38+2.27 map,  $\sigma_{rms} = 257 \text{ mJy beam}^{-1}$ .

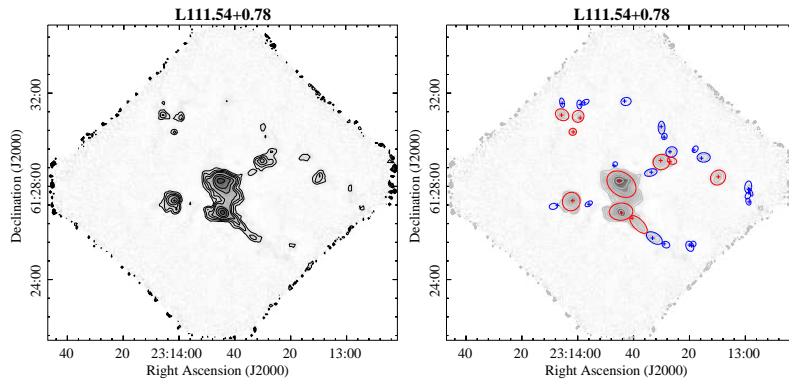
Figure B.1 Continuation



(B.1.37) L136.83+1.07 map,  $\sigma_{rms} = 250 \text{ mJy beam}^{-1}$ .



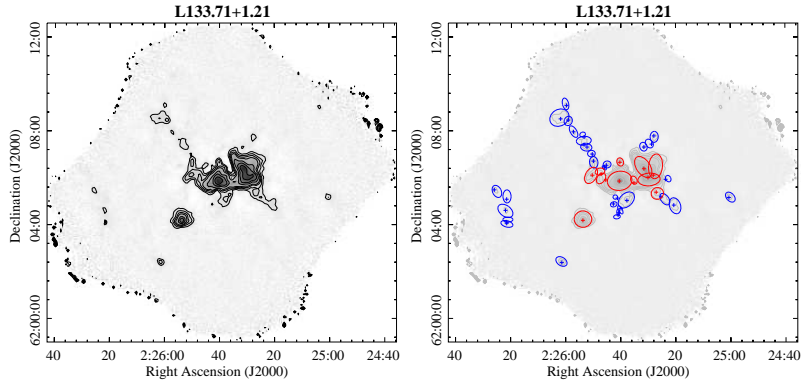
(B.1.38) L111.28-0.66 map,  $\sigma_{rms} = 286 \text{ mJy beam}^{-1}$ .



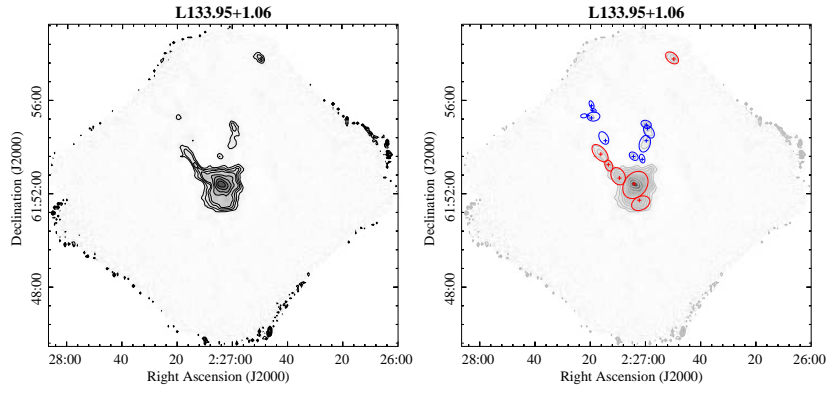
(B.1.39) L111.54+0.78 map,  $\sigma_{rms} = 496 \text{ mJy beam}^{-1}$ .

Figure B.1 Continuation

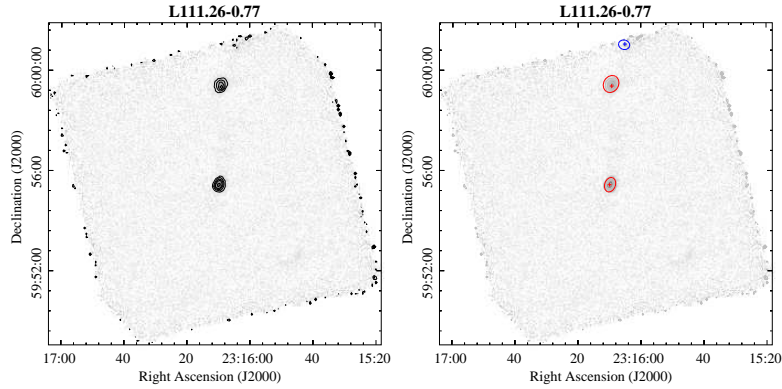




(B.1.40) L133.71+1.21 map,  $\sigma_{rms} = 338 \text{ mJy beam}^{-1}$ .

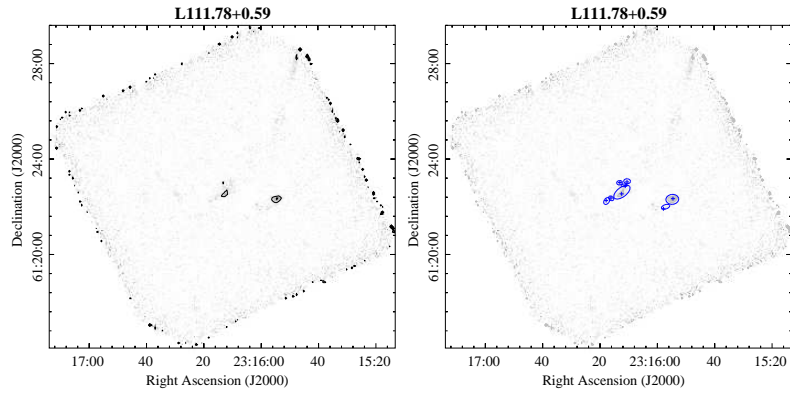


(B.1.41) L133.95+1.06 map,  $\sigma_{rms} = 338 \text{ mJy beam}^{-1}$ . Additional contour is drawn at  $200\sigma$ .

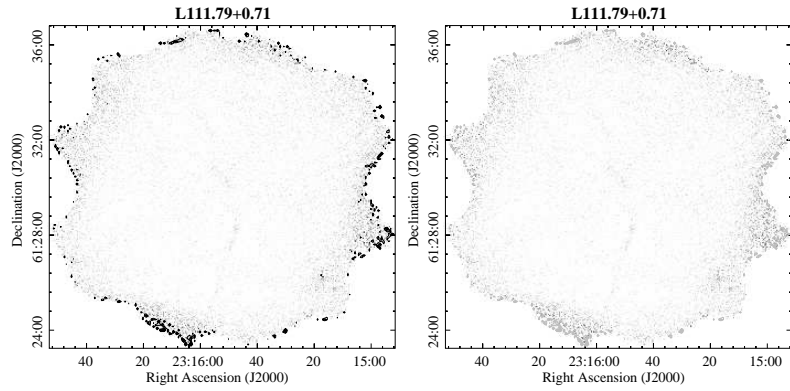


(B.1.42) L111.26-0.77 map,  $\sigma_{rms} = 538 \text{ mJy beam}^{-1}$ .

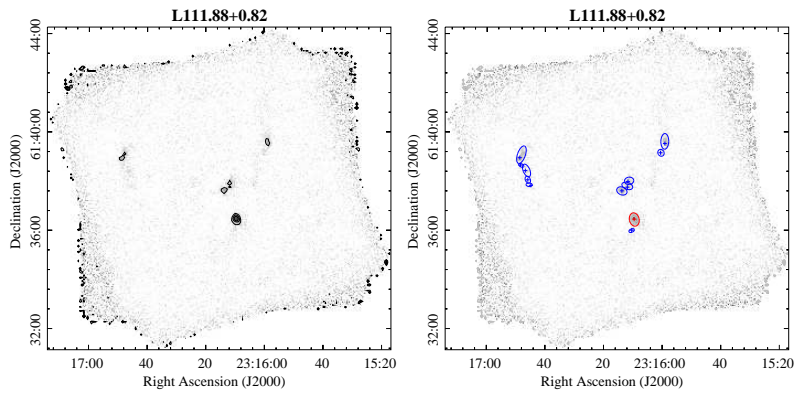
Figure B.1 Continuation



(B.1.43) L111.78+0.59 map,  $\sigma_{rms} = 412 \text{ mJy beam}^{-1}$ .

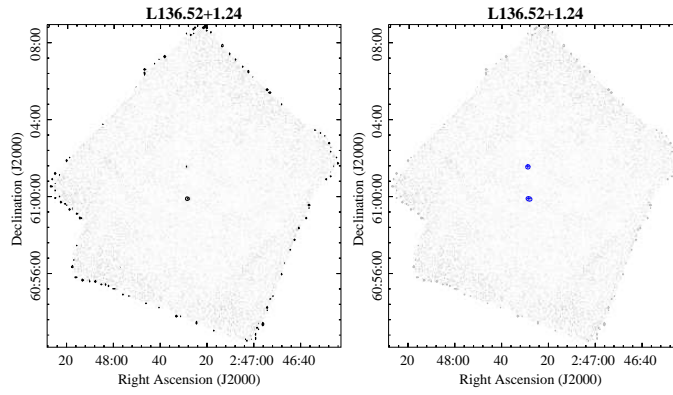


(B.1.44) L111.79+0.71 map,  $\sigma_{rms} = 307 \text{ mJy beam}^{-1}$ .

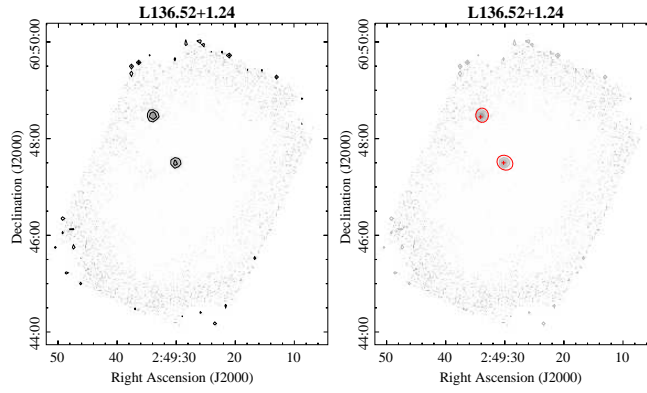


(B.1.45) L111.88+0.82 map,  $\sigma_{rms} = 473 \text{ mJy beam}^{-1}$ .

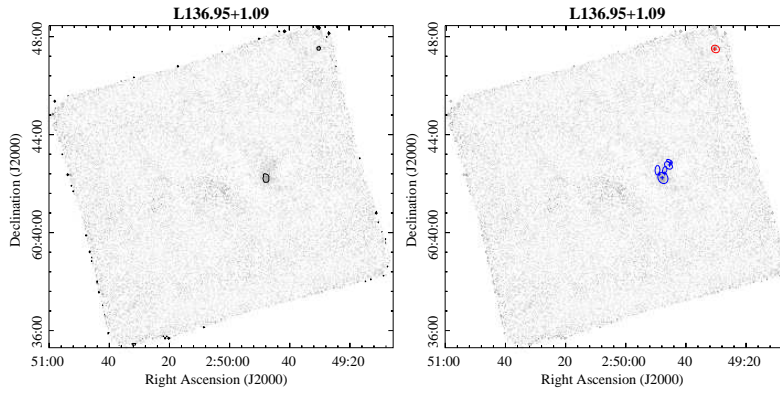
Figure B.1 Continuation



(B.1.46) L136.52+1.24 map,  $\sigma_{rms} = 260 \text{ mJy beam}^{-1}$ .

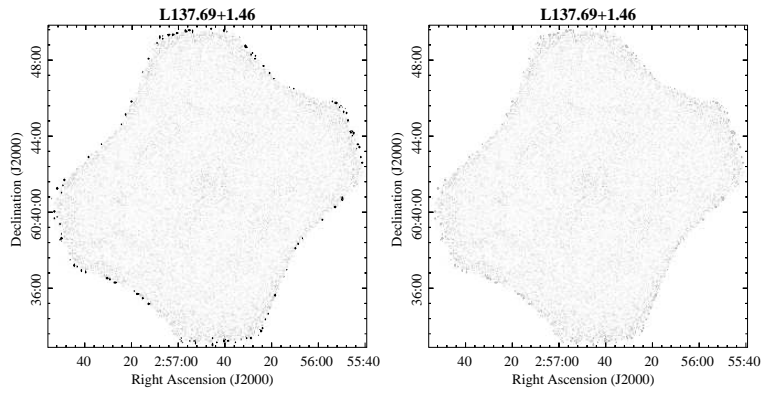


(B.1.47) L136.85+1.14 map,  $\sigma_{rms} = 337 \text{ mJy beam}^{-1}$ .

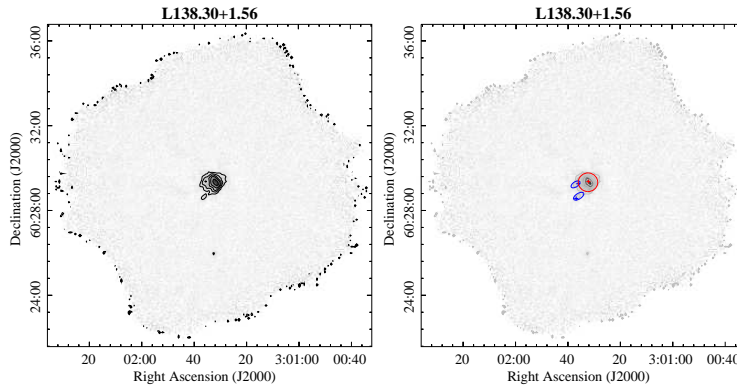


(B.1.48) L136.95+1.09 map,  $\sigma_{rms} = 475 \text{ mJy beam}^{-1}$ .

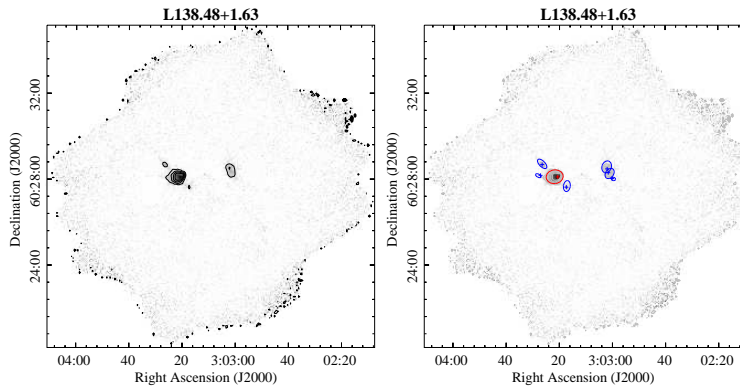
Figure B.1 Continuation



(B.1.49) L137.69+1.46 map,  $\sigma_{rms} = 667 \text{ mJy beam}^{-1}$ .

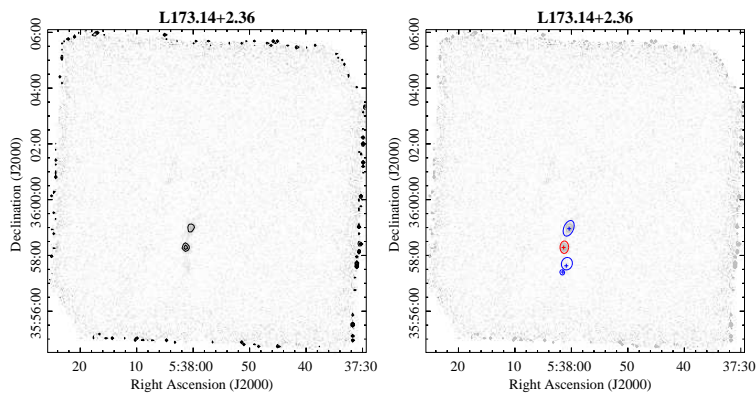


(B.1.50) L138.30+1.56 map,  $\sigma_{rms} = 205 \text{ mJy beam}^{-1}$ .

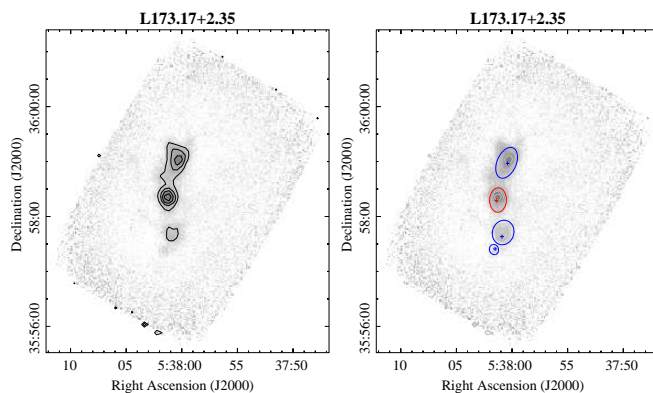


(B.1.51) L138.48+1.63 map,  $\sigma_{rms} = 266 \text{ mJy beam}^{-1}$ .

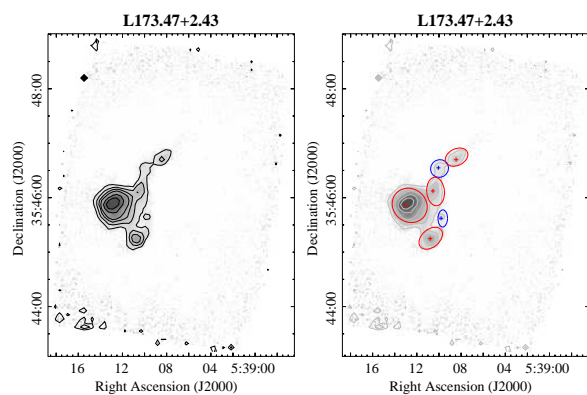
Figure B.1 Continuation



(B.1.52) L173.14+2.36 map,  $\sigma_{rms} = 777 \text{ mJy beam}^{-1}$ .

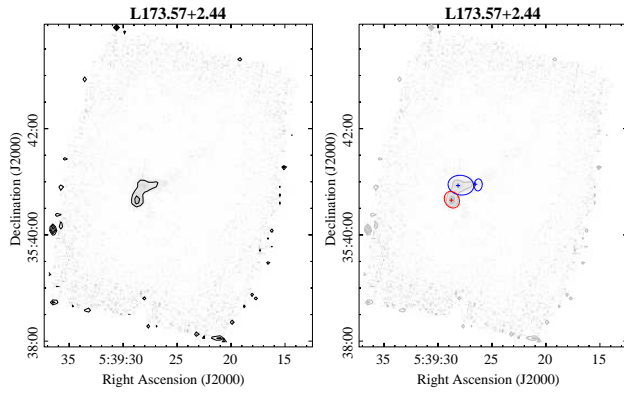


(B.1.53) L173.17+2.35 map,  $\sigma_{rms} = 320 \text{ mJy beam}^{-1}$ .

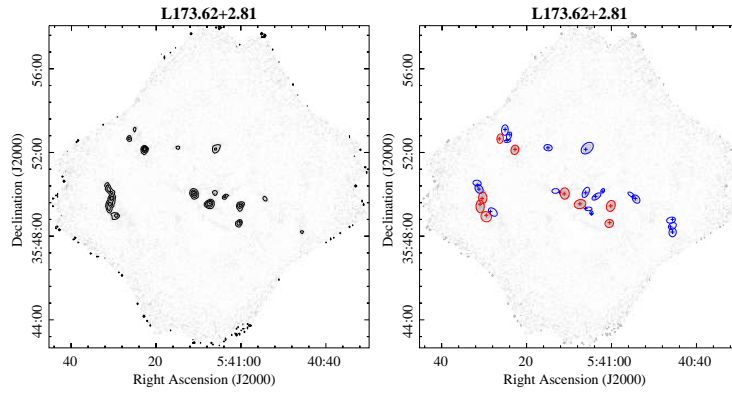


(B.1.54) L173.47+2.43 map,  $\sigma_{rms} = 487 \text{ mJy beam}^{-1}$ .

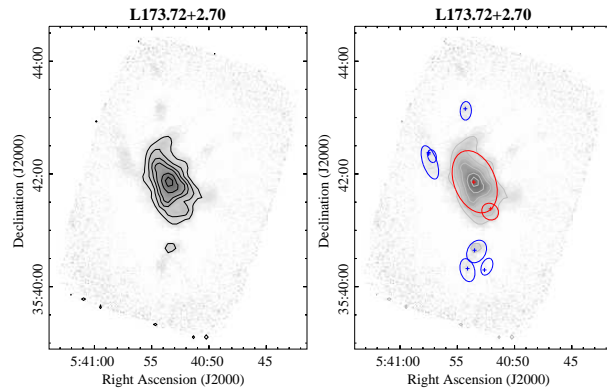
Figure B.1 Continuation



(B.1.55) L173.57+2.44 map,  $\sigma_{rms} = 421 \text{ mJy beam}^{-1}$ .

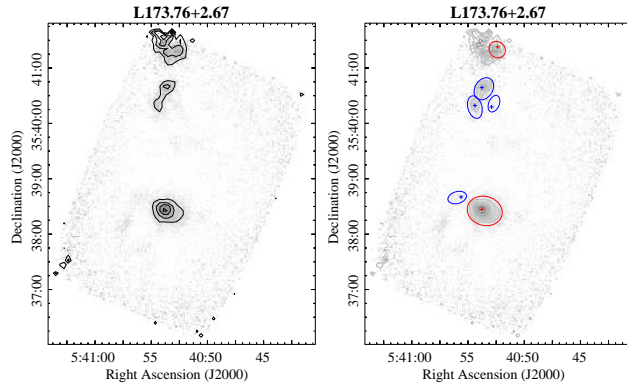


(B.1.56) L173.62+2.81 map,  $\sigma_{rms} = 359 \text{ mJy beam}^{-1}$ .

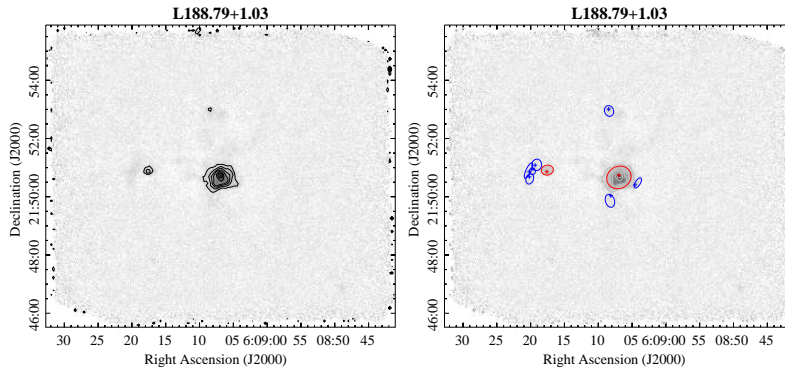


(B.1.57) L173.72+2.70 map,  $\sigma_{rms} = 387 \text{ mJy beam}^{-1}$ .

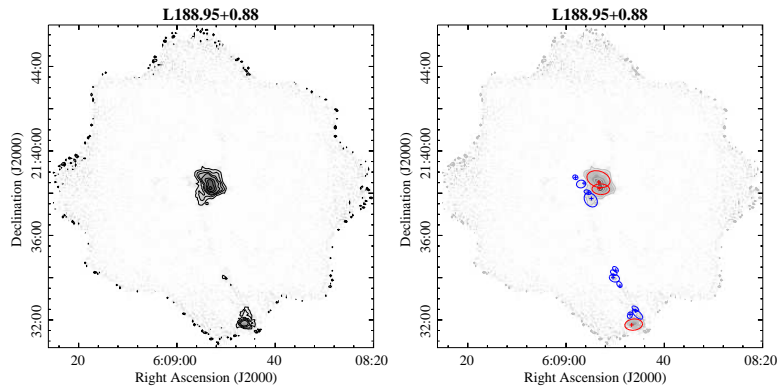
Figure B.1 Continuation



(B.1.58) L173.76+2.67 map,  $\sigma_{rms} = 301 \text{ mJy beam}^{-1}$ .

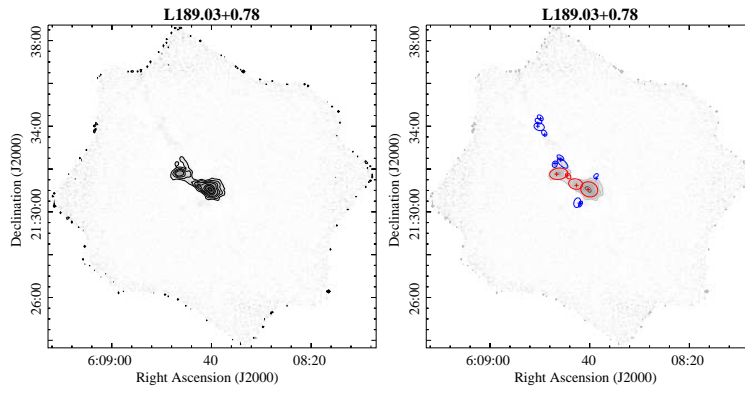


(B.1.59) L188.79+1.03 map,  $\sigma_{rms} = 259 \text{ mJy beam}^{-1}$ .

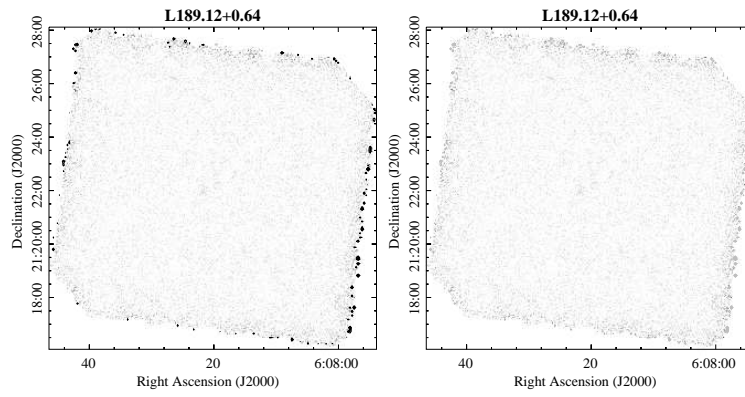


(B.1.60) L188.95+0.88 map,  $\sigma_{rms} = 268 \text{ mJy beam}^{-1}$ .

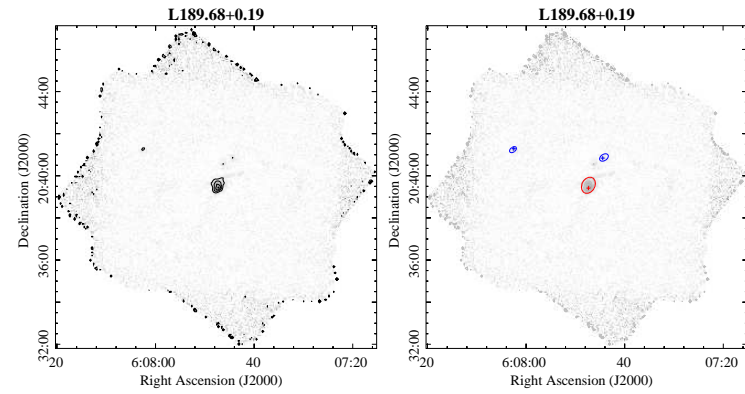
Figure B.1 Continuation



(B.1.61) L189.03+0.78 map,  $\sigma_{rms} = 290 \text{ mJy beam}^{-1}$ .



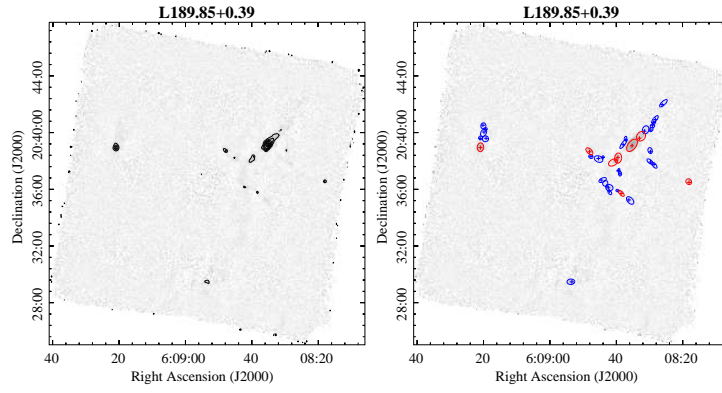
(B.1.62) L189.12+0.64 map,  $\sigma_{rms} = 403 \text{ mJy beam}^{-1}$ .



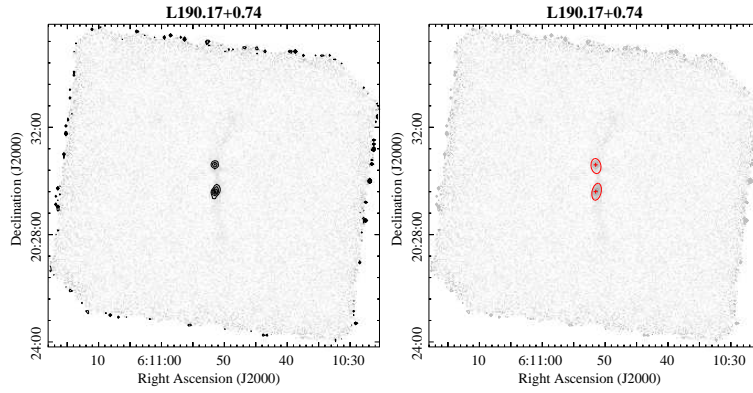
(B.1.63) L189.68+0.19 map,  $\sigma_{rms} = 155 \text{ mJy beam}^{-1}$ .

Figure B.1 Continuation

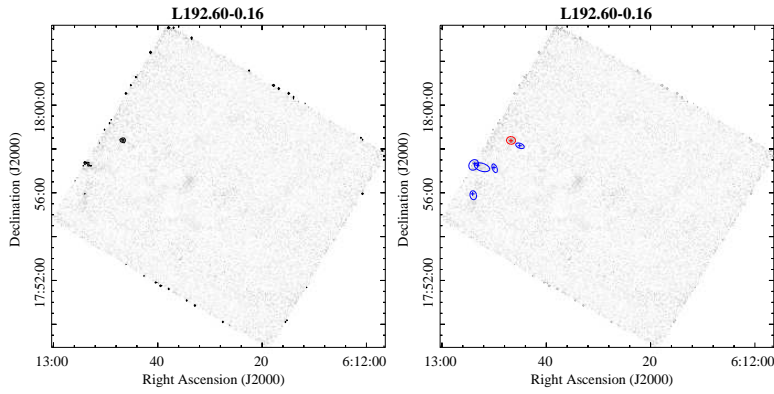




(B.1.64) L189.85+0.39 map,  $\sigma_{rms} = 505 \text{ mJy beam}^{-1}$ .

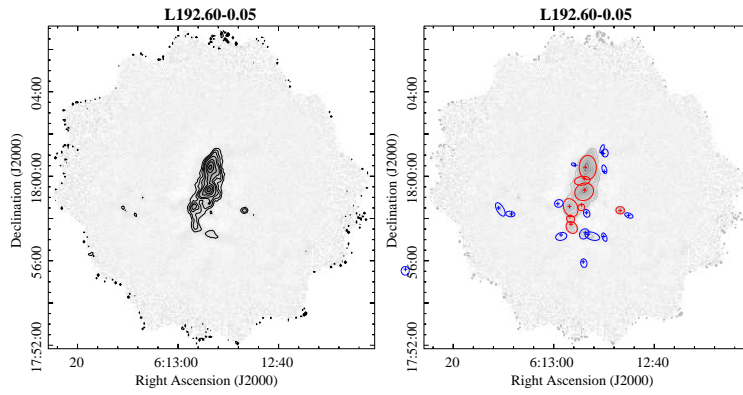


(B.1.65) L190.17+0.74 map,  $\sigma_{rms} = 184 \text{ mJy beam}^{-1}$ .

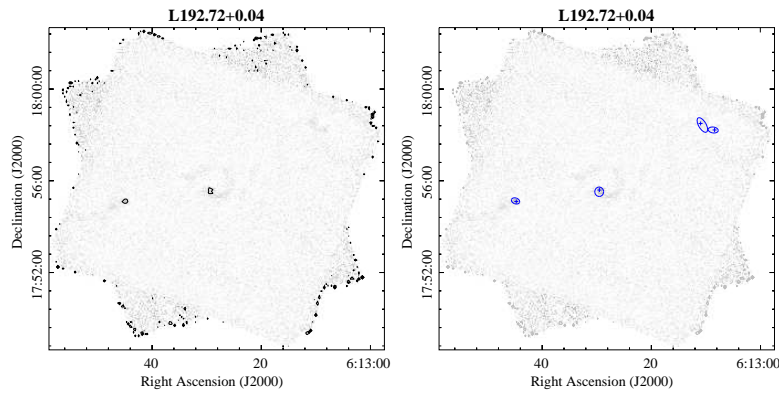


(B.1.66) L192.60-0.16 map,  $\sigma_{rms} = 340 \text{ mJy beam}^{-1}$ .

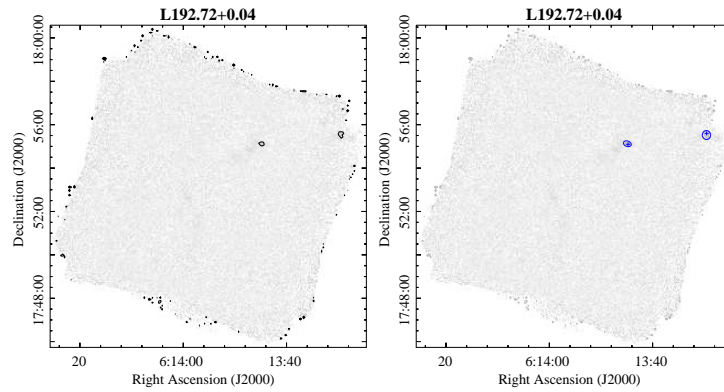
Figure B.1 Continuation



(B.1.67) L192.60-0.05 map,  $\sigma_{rms} = 271 \text{ mJy beam}^{-1}$ .

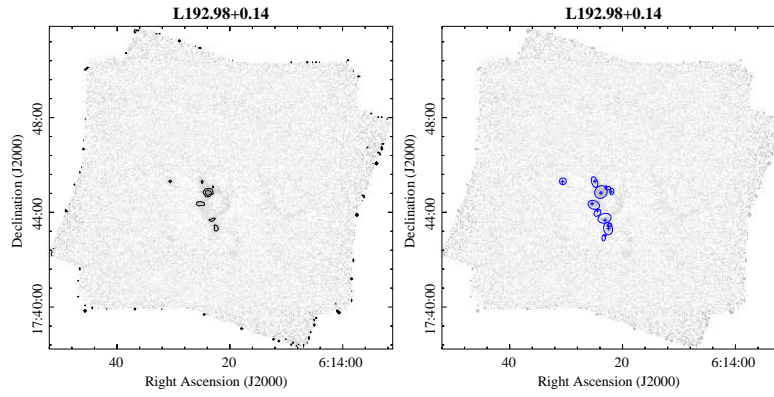


(B.1.68) L192.72+0.04 map,  $\sigma_{rms} = 335 \text{ mJy beam}^{-1}$ .

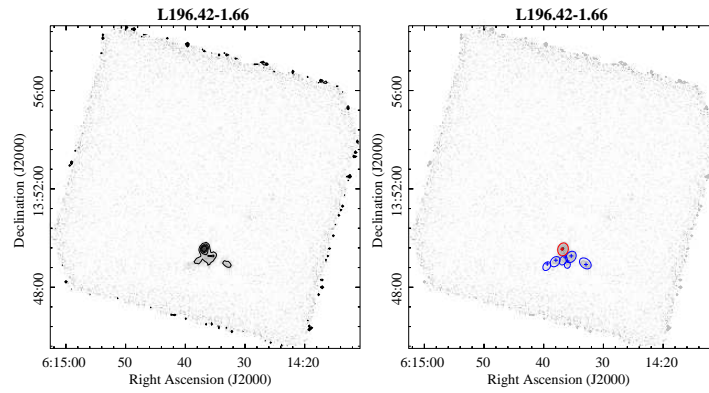


(B.1.69) L192.81+0.11 map,  $\sigma_{rms} = 328 \text{ mJy beam}^{-1}$ .

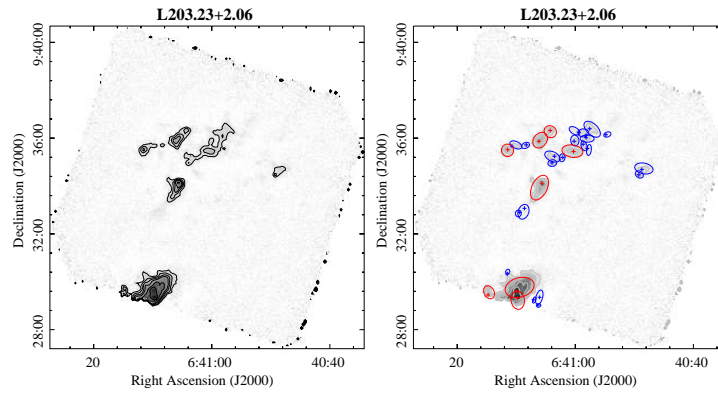
Figure B.1 Continuation



(B.1.70) L192.98+0.14 map,  $\sigma_{rms} = 383 \text{ mJy beam}^{-1}$ .

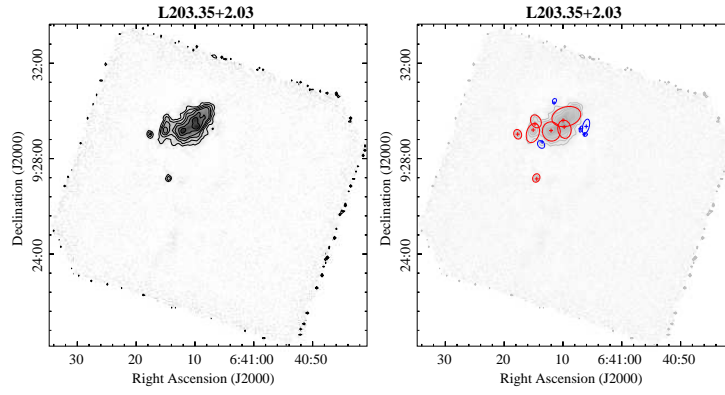


(B.1.71) L196.42-1.66 map,  $\sigma_{rms} = 470 \text{ mJy beam}^{-1}$ .

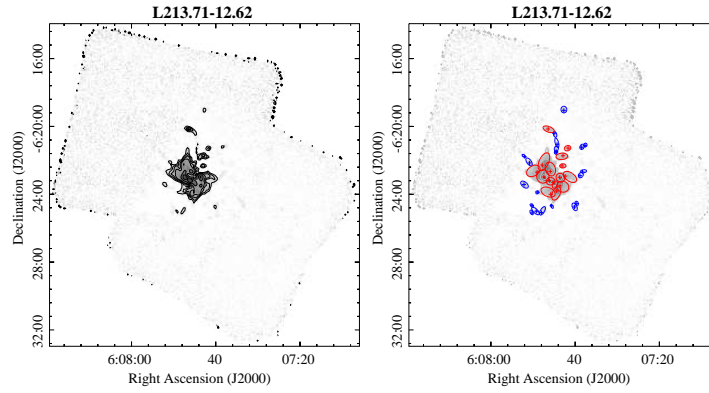


(B.1.72) L203.23+2.06 map,  $\sigma_{rms} = 269 \text{ mJy beam}^{-1}$ .

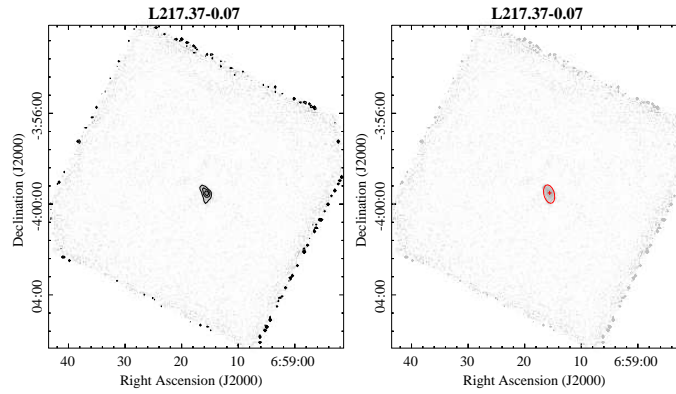
Figure B.1 Continuation



(B.1.73) L203.35+2.03 map,  $\sigma_{rms} = 314 \text{ mJy beam}^{-1}$ .

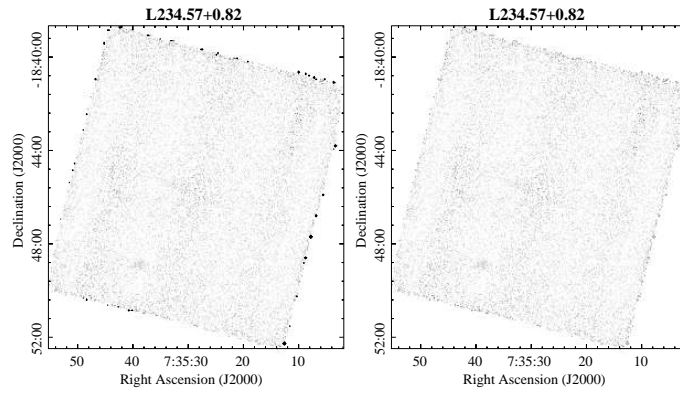


(B.1.74) L213.71-12.62 map,  $\sigma_{rms} = 421 \text{ mJy beam}^{-1}$ .

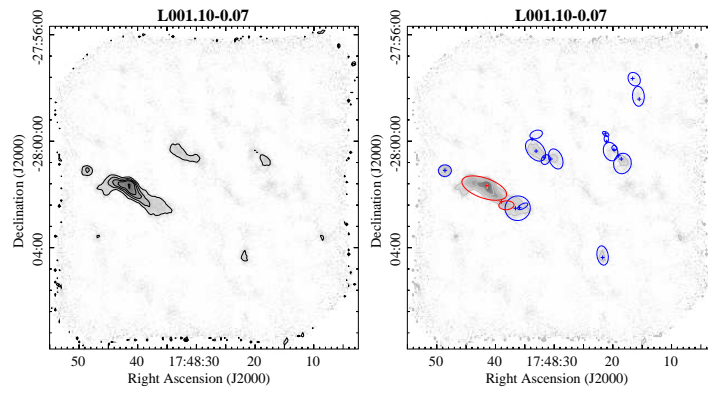


(B.1.75) L217.37-0.07 map,  $\sigma_{rms} = 704 \text{ mJy beam}^{-1}$ .

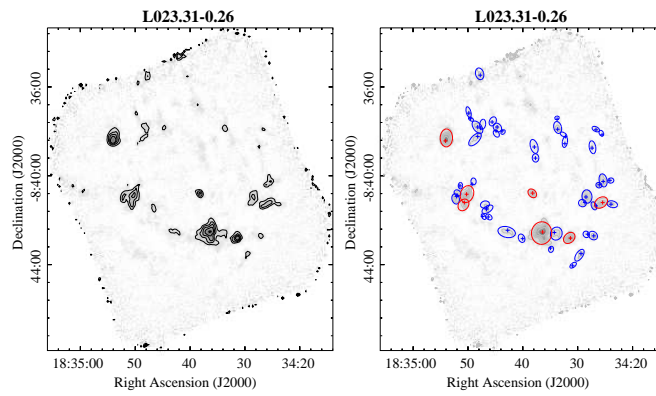
Figure B.1 Continuation



(B.1.76) L234.57+0.82 map,  $\sigma_{rms} = 1051 \text{ mJy beam}^{-1}$ .

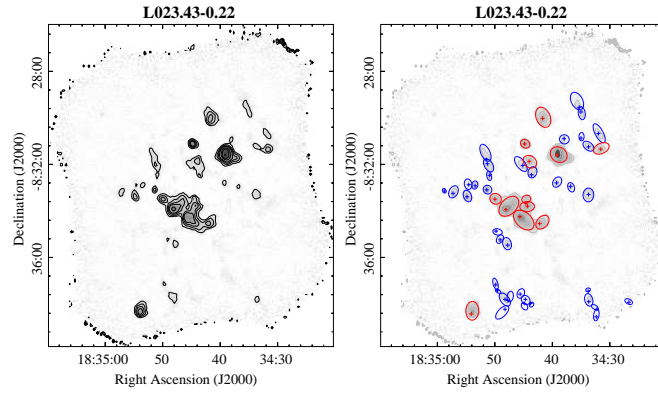


(B.1.77) L001.10-0.07 map,  $\sigma_{rms} = 849 \text{ mJy beam}^{-1}$ .

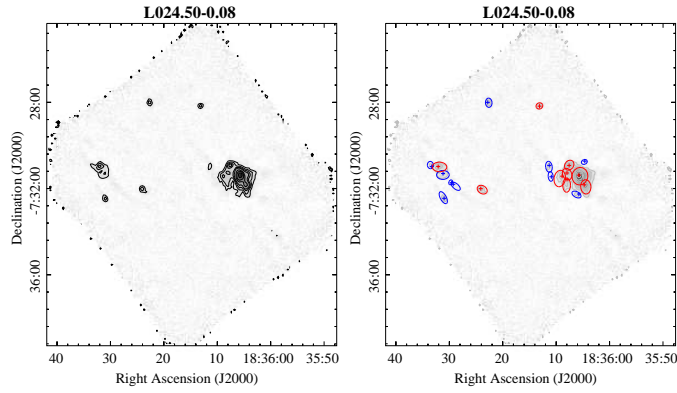


(B.1.78) L023.31-0.26 map,  $\sigma_{rms} = 379 \text{ mJy beam}^{-1}$ .

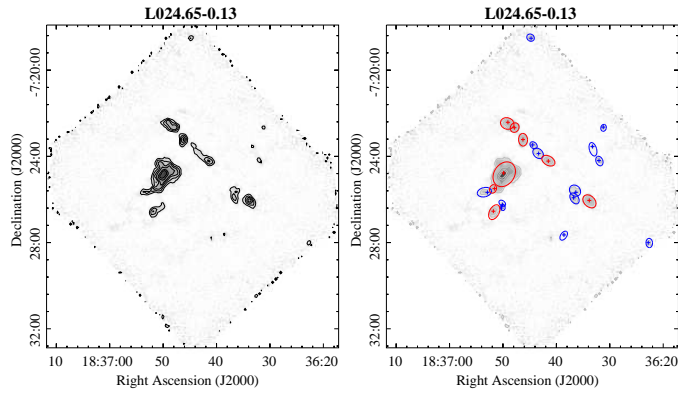
Figure B.1 Continuation



(B.1.79) L023.43-0.22 map,  $\sigma_{rms} = 375 \text{ mJy beam}^{-1}$ .

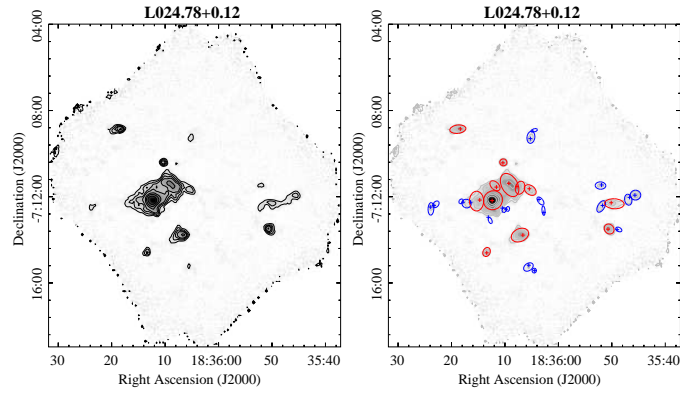


(B.1.80) L024.50-0.08 map,  $\sigma_{rms} = 306 \text{ mJy beam}^{-1}$ .

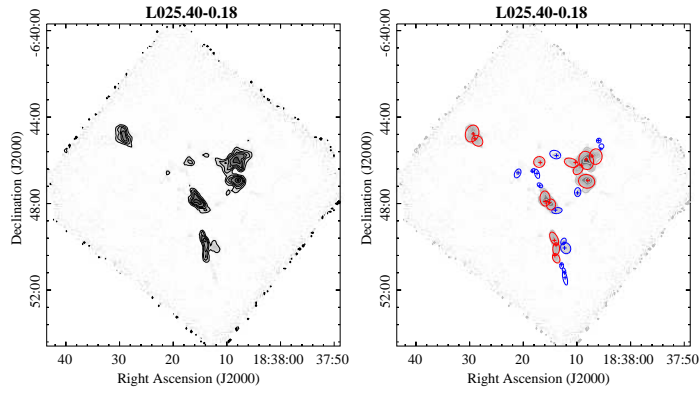


(B.1.81) L024.65-0.13 map,  $\sigma_{rms} = 357 \text{ mJy beam}^{-1}$ .

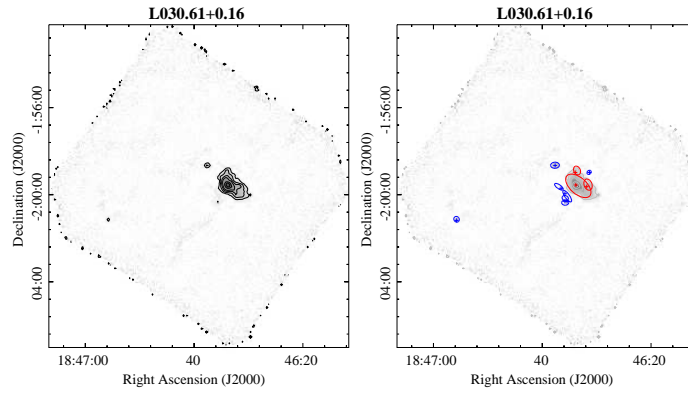
Figure B.1 Continuation



(B.1.82) L024.78+0.12 map,  $\sigma_{rms} = 363 \text{ mJy beam}^{-1}$ .

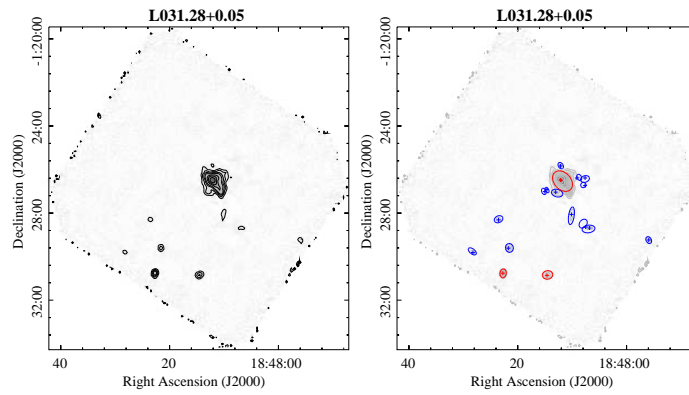


(B.1.83) L025.40-0.18 map,  $\sigma_{rms} = 482 \text{ mJy beam}^{-1}$ .

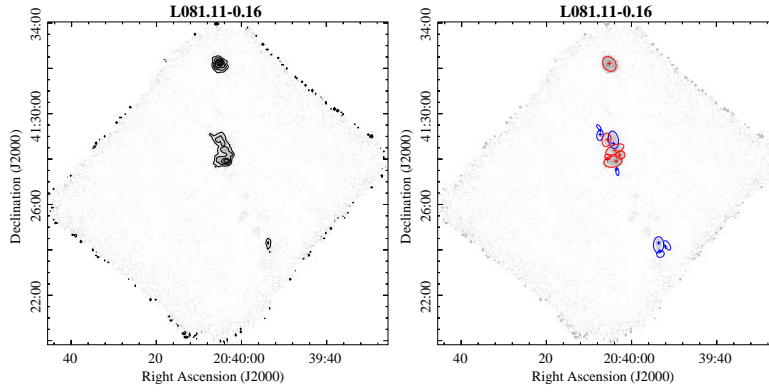


(B.1.84) L030.61+0.16 map,  $\sigma_{rms} = 349 \text{ mJy beam}^{-1}$ .

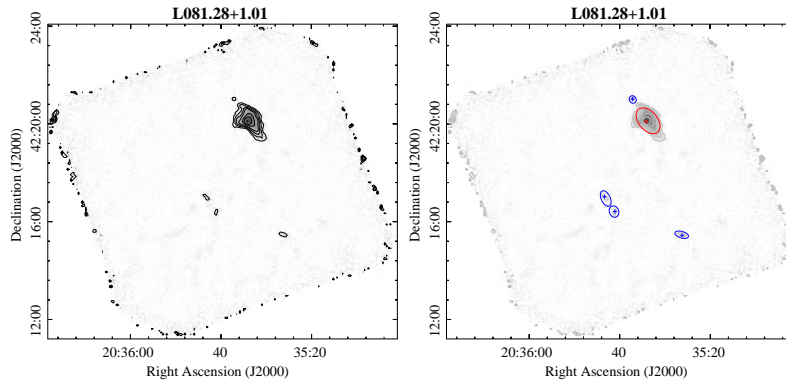
Figure B.1 Continuation



(B.1.85) L031.28+0.05 map,  $\sigma_{rms} = 303 \text{ mJy beam}^{-1}$ .



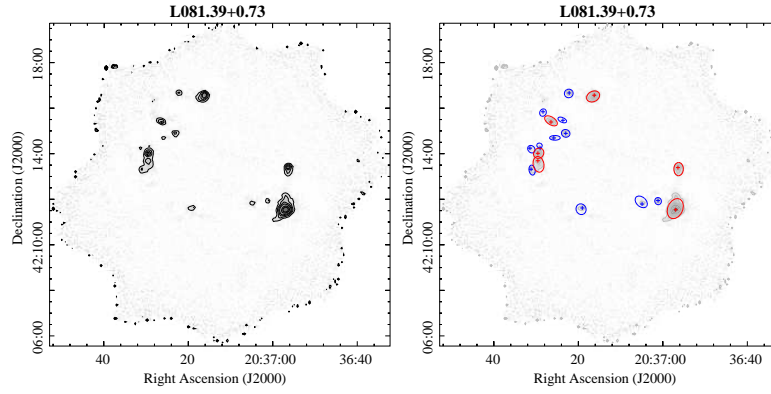
(B.1.86) L081.11-0.16 map,  $\sigma_{rms} = 341 \text{ mJy beam}^{-1}$ .



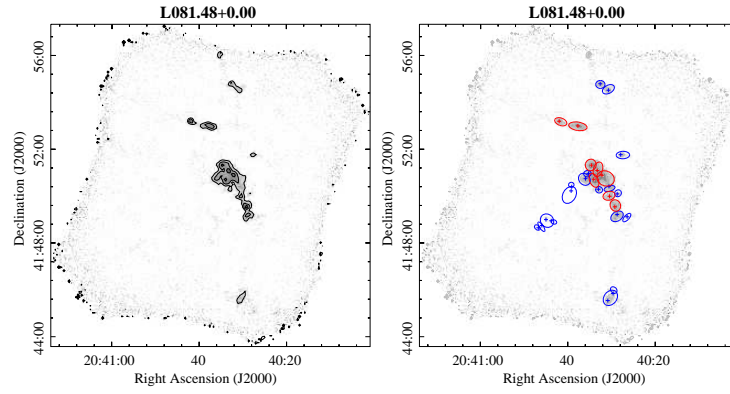
(B.1.87) L081.28+1.01 map,  $\sigma_{rms} = 250 \text{ mJy beam}^{-1}$ .

Figure B.1 Continuation

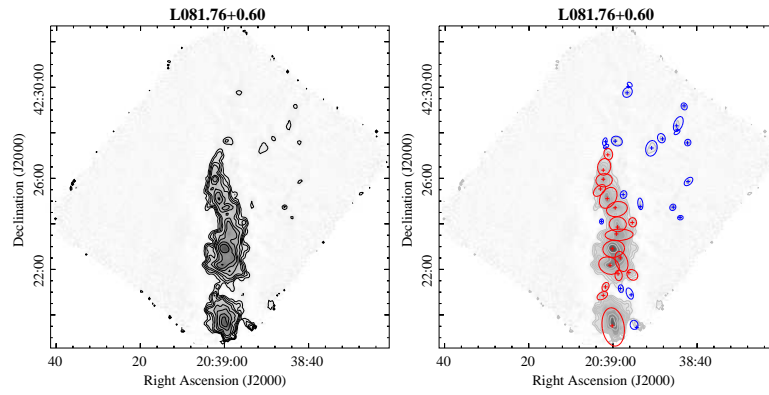




(B.1.88) L081.39+0.73 map,  $\sigma_{rms} = 341 \text{ mJy beam}^{-1}$ .

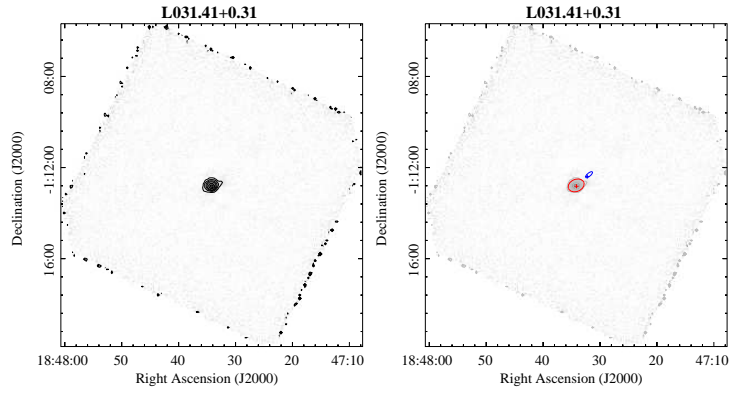


(B.1.89) L081.48+0.00 map,  $\sigma_{rms} = 353 \text{ mJy beam}^{-1}$ .

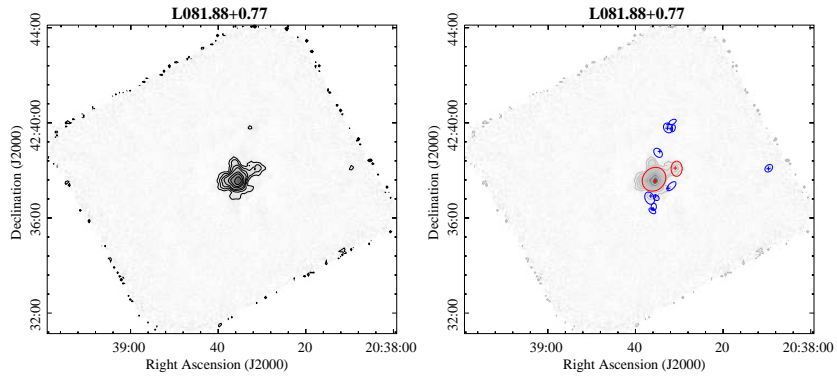


(B.1.90) L081.76+0.60 map,  $\sigma_{rms} = 329 \text{ mJy beam}^{-1}$ . Additional contour is drawn at  $200\sigma$ .

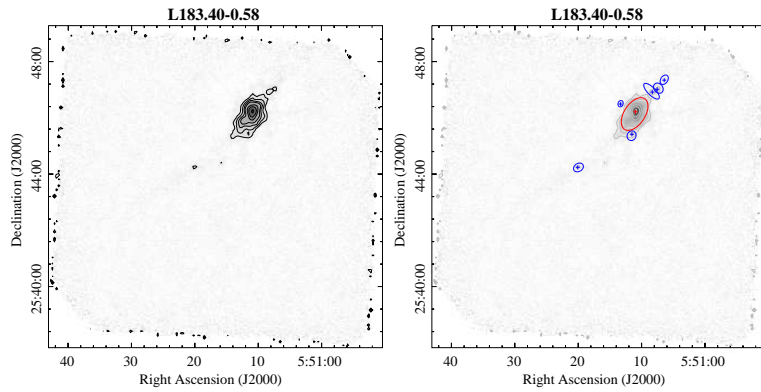
Figure B.1 Continuation



(B.1.91) L031.41+0.31 map,  $\sigma_{rms} = 791 \text{ mJy beam}^{-1}$ .

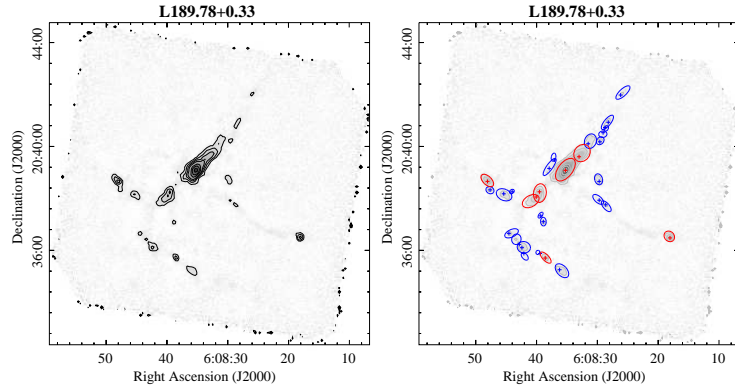


(B.1.92) L081.88+0.77 map,  $\sigma_{rms} = 717 \text{ mJy beam}^{-1}$ .

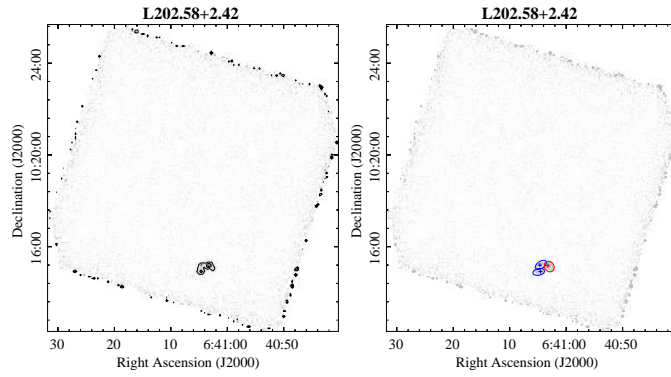


(B.1.93) L183.40-0.58 map,  $\sigma_{rms} = 255 \text{ mJy beam}^{-1}$ .

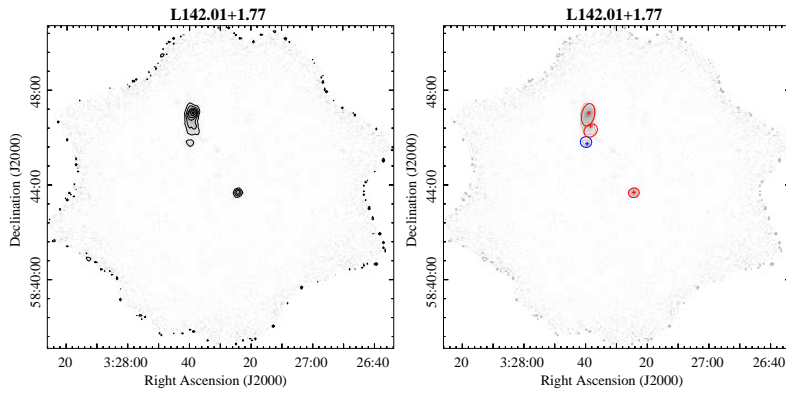
Figure B.1 Continuation



(B.1.94) L189.78+0.33 map,  $\sigma_{rms} = 294 \text{ mJy beam}^{-1}$ .

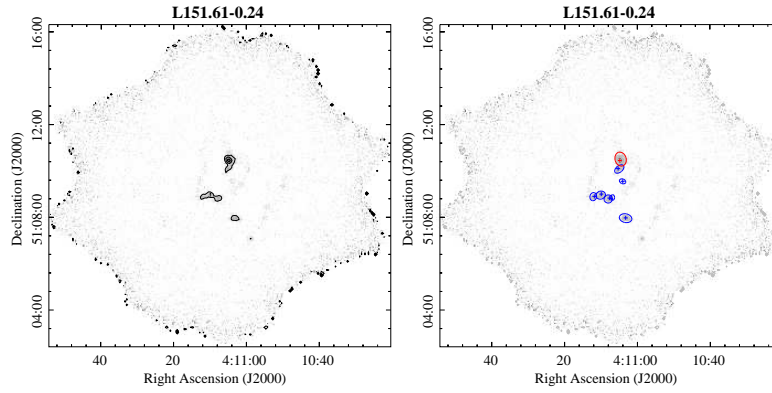


(B.1.95) L202.58+2.42 map,  $\sigma_{rms} = 370 \text{ mJy beam}^{-1}$ .

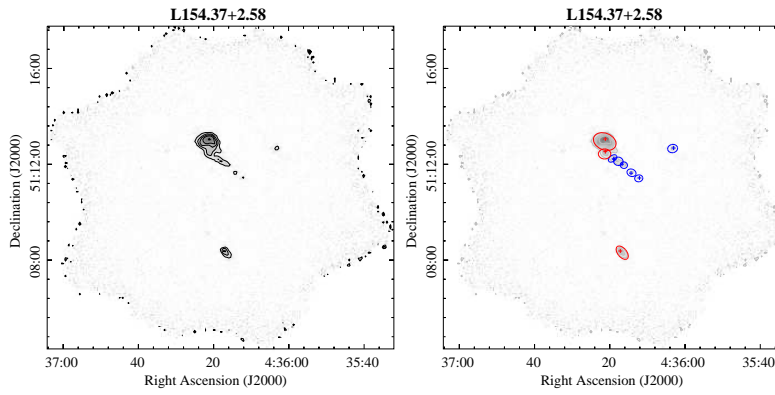


(B.1.96) L142.01+1.77 map,  $\sigma_{rms} = 305 \text{ mJy beam}^{-1}$ .

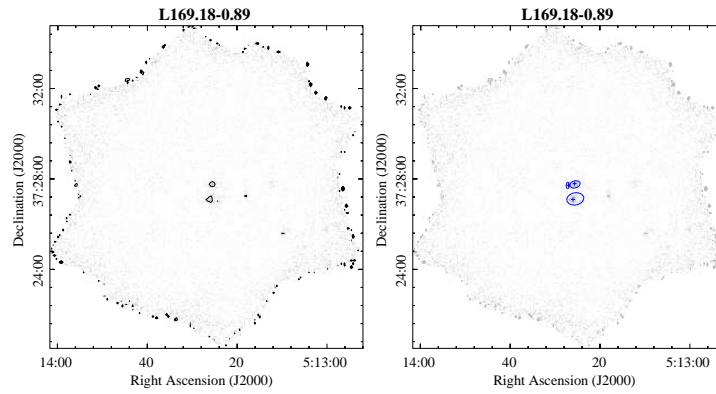
Figure B.1 Continuation



(B.1.97) L151.61-0.24 map,  $\sigma_{rms} = 266 \text{ mJy beam}^{-1}$ .

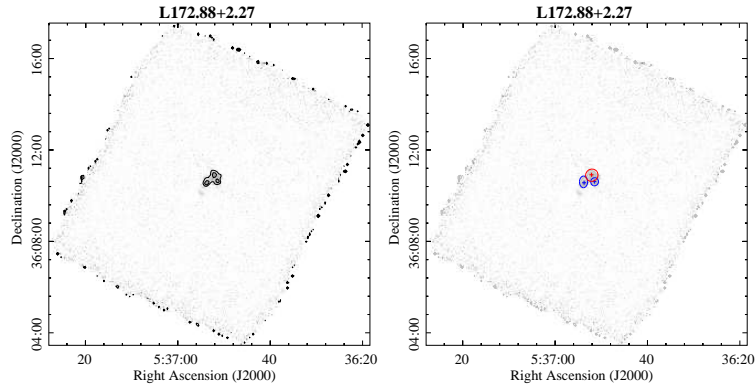


(B.1.98) L154.37+2.58 map,  $\sigma_{rms} = 266 \text{ mJy beam}^{-1}$ .

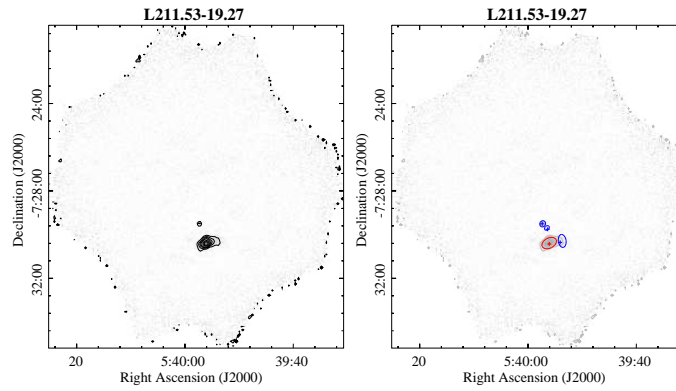


(B.1.99) L169.18-0.89 map,  $\sigma_{rms} = 232 \text{ mJy beam}^{-1}$ .

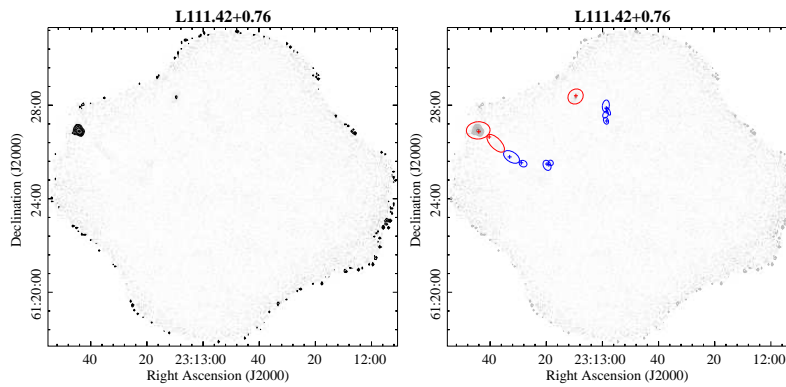
Figure B.1 Continuation



(B.1.100) L172.88+2.27 map,  $\sigma_{rms} = 315 \text{ mJy beam}^{-1}$ .

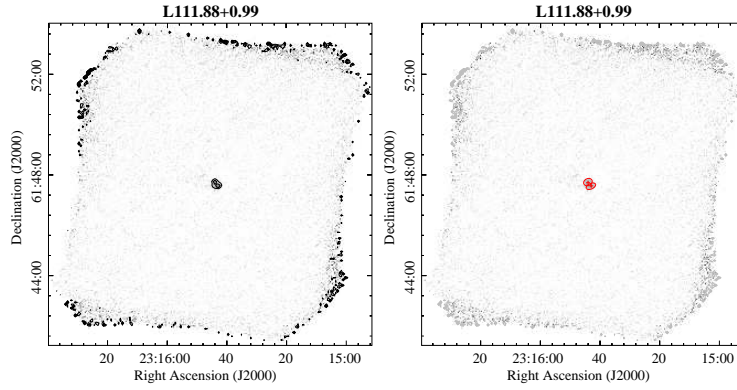


(B.1.101) L211.53-19.27 map,  $\sigma_{rms} = 254 \text{ mJy beam}^{-1}$ .

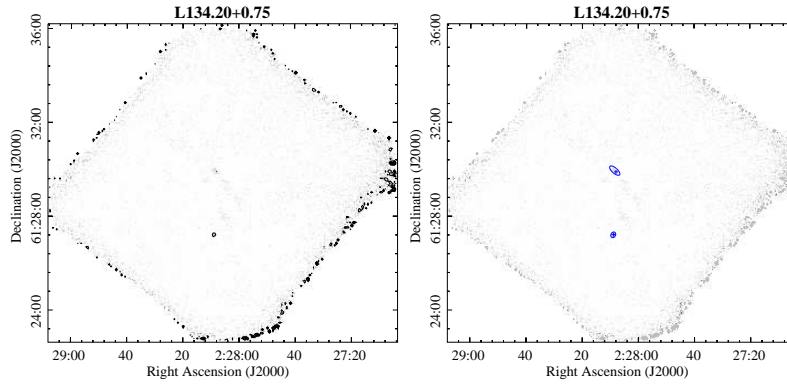


(B.1.102) L111.42+0.76 map,  $\sigma_{rms} = 375 \text{ mJy beam}^{-1}$ .

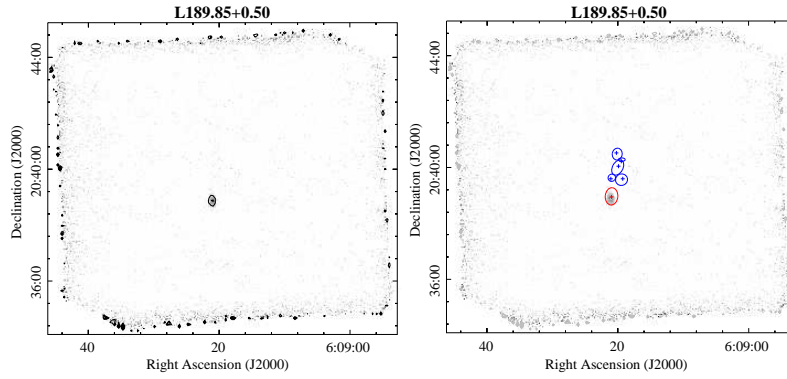
Figure B.1 Continuation



(B.1.103) L111.88+0.99 map,  $\sigma_{rms} = 226 \text{ mJy beam}^{-1}$ .

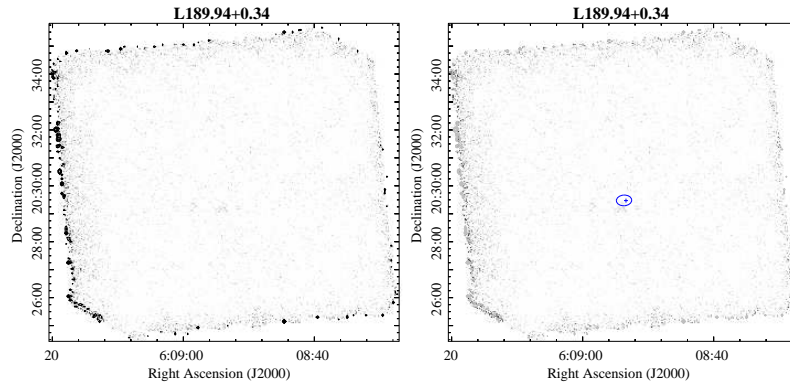


(B.1.104) L134.20+0.75 map,  $\sigma_{rms} = 525 \text{ mJy beam}^{-1}$ .

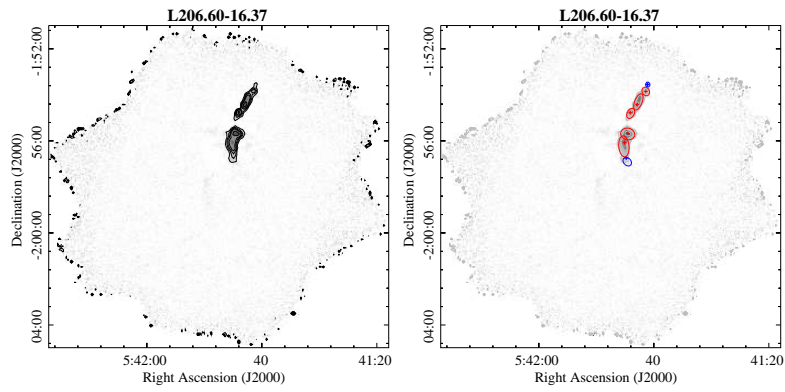


(B.1.105) L189.85+0.50 map,  $\sigma_{rms} = 506 \text{ mJy beam}^{-1}$ .

Figure B.1 Continuation



(B.1.106) L189.94+0.34 map,  $\sigma_{rms} = 590 \text{ mJy beam}^{-1}$ .



(B.1.107) L206.60-16.37 map,  $\sigma_{rms} = 563 \text{ mJy beam}^{-1}$ .

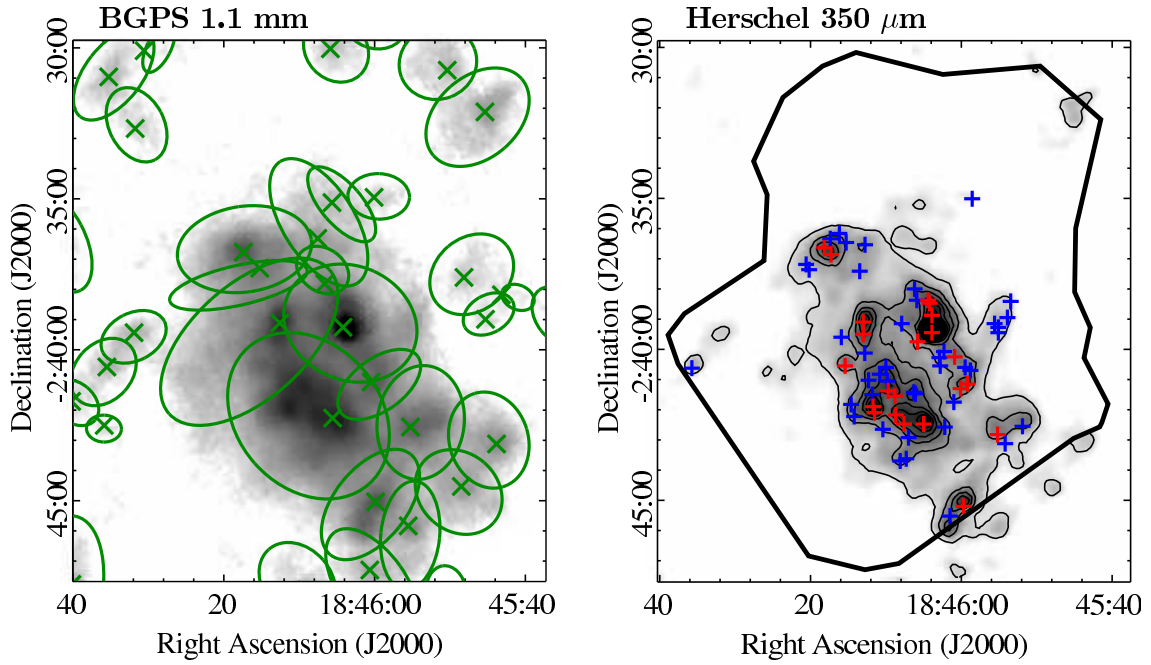
Figure B.1 Continuation

## Appendix C

### Hi-Gal SPIRE images at $350 \mu m$ for $l = 30^\circ$

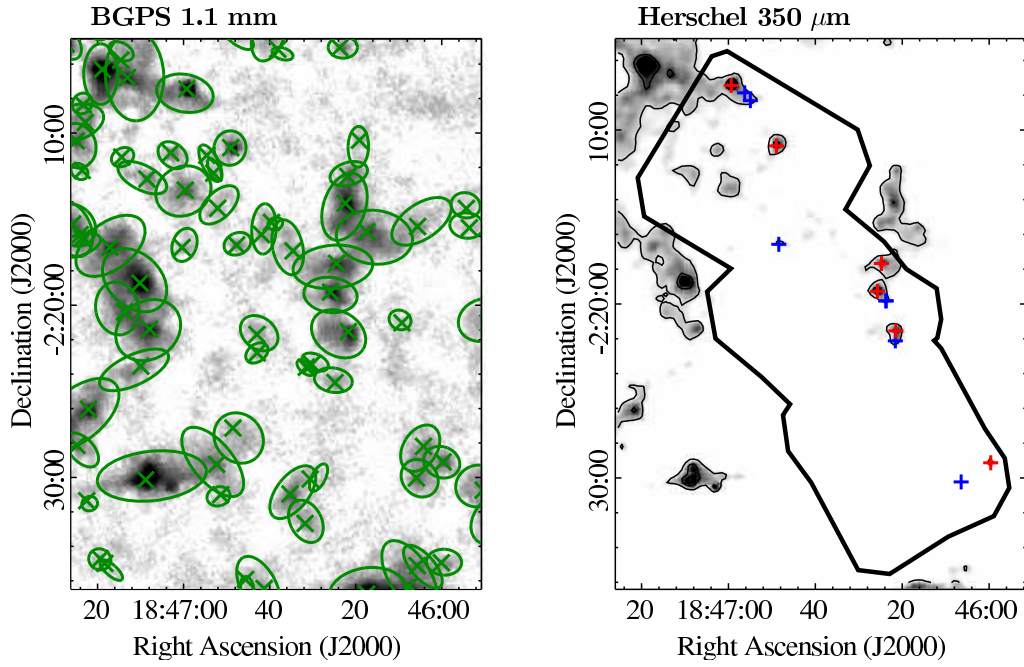
In this section we indicate the locations of the high-resolution sources identified in the  $350 \mu m$  SHARC-II maps ( $8.5''$  beam size) toward  $l = 30^\circ$ , and their comparison with structures observed at lower resolution ( $24.9''$ ) in the corresponding *Herschel*/SPIRE maps at the same wavelength and BGPS maps at  $1.1 \text{ mm}$  at a resolution of  $33''$ . Figure C.1 shows  $1.1 \text{ mm}$  continuum gray scale maps with green contours representing sources from the BGPS catalog, and *Herschel* grey scale maps with contours representing the emission at  $10\sigma$ , and increasing steps of  $5\sigma$ , with  $\sigma=164 \text{ MJy ster}^{-1}$ . The thick black line on each map represent the area covered by the SHARC-II maps, with the name of those maps indicated for each region. Peak positions of detected high-resolution sources from SHARC-II maps are overlaid in red and blue crosses, representing sources with signal-to-noise above and below a value of 10, respectively. Most sources with high signal-to-noise are well associated with strong emission in the *Herschel* maps, but several of the low signal-to-noise sources are not individually identified and they are part of extended background emission detected in *Herschel* maps but not recovered in SHARC-II maps.



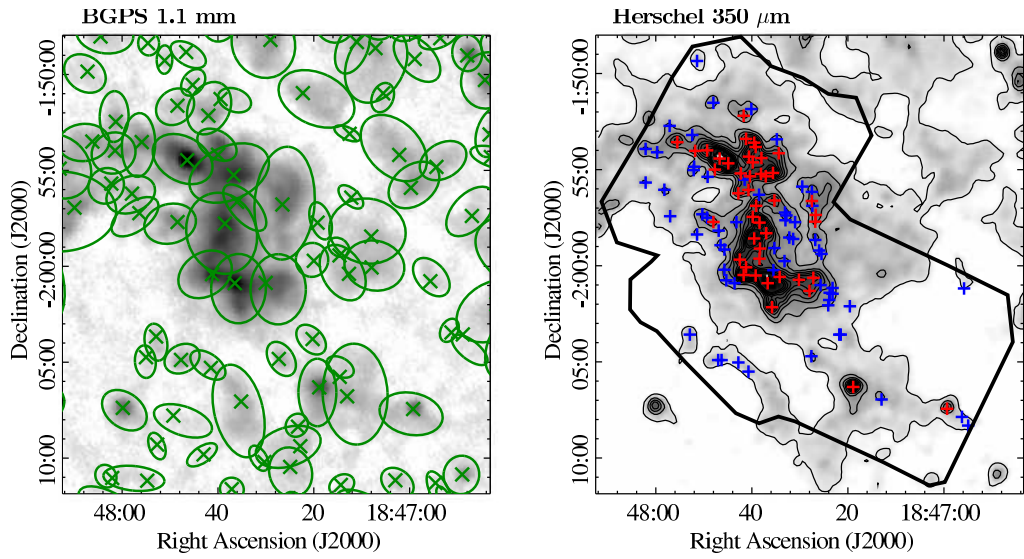


(C.1.1) Thick black contour in Herschel map represents the area covered by maps L029.95-0.05 and L030.00+00.

Figure C.1 Left: BGPS maps at 1.1 mm toward  $l = 30^\circ$ . The ellipses show the recovered sources from the BGPS catalog. Right: Corresponding 350  $\mu\text{m}$  maps from *Herschel* SPIRE. Contours start from  $10\sigma$ , with increasing steps of  $5\sigma$  ( $\sigma=164 \text{ MJy ster}^{-1}$ ) The crosses show the peak position of the high-resolution sources recovered in SHARC-II map. Red and blue crosses show substructures with peak signal-to-noise above and below 10, respectively. The area covered by SHARC-II maps, indicated under each figure, is represented by the thick black contour. Figures 28.128.5 are available in the online version of the Journal.

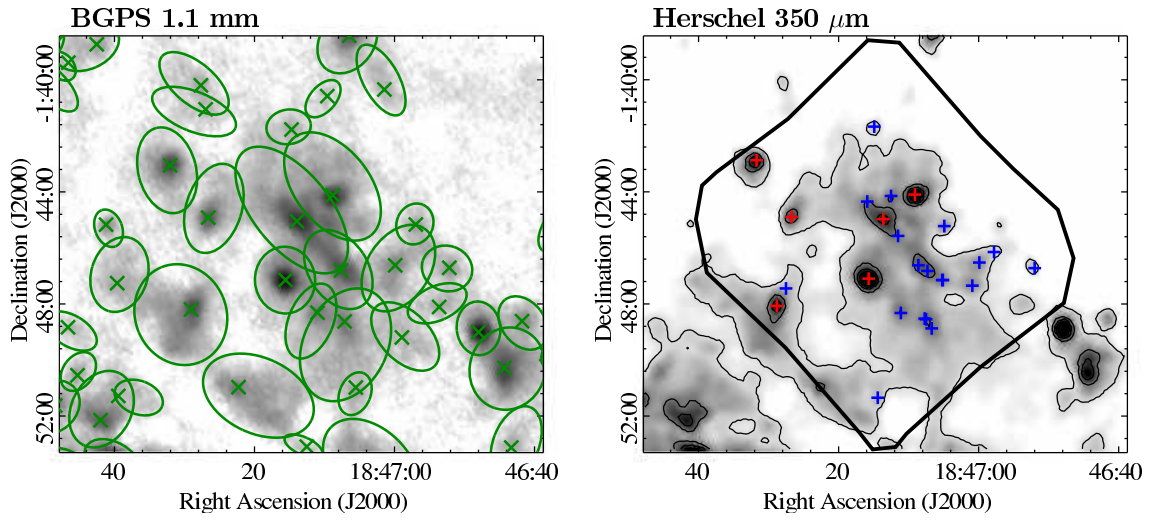


(C.1.2) Thick black contour in Herschel map represents the area covered by maps L030.15+0.00, L030.30+0.00 and L030.45+0.00.

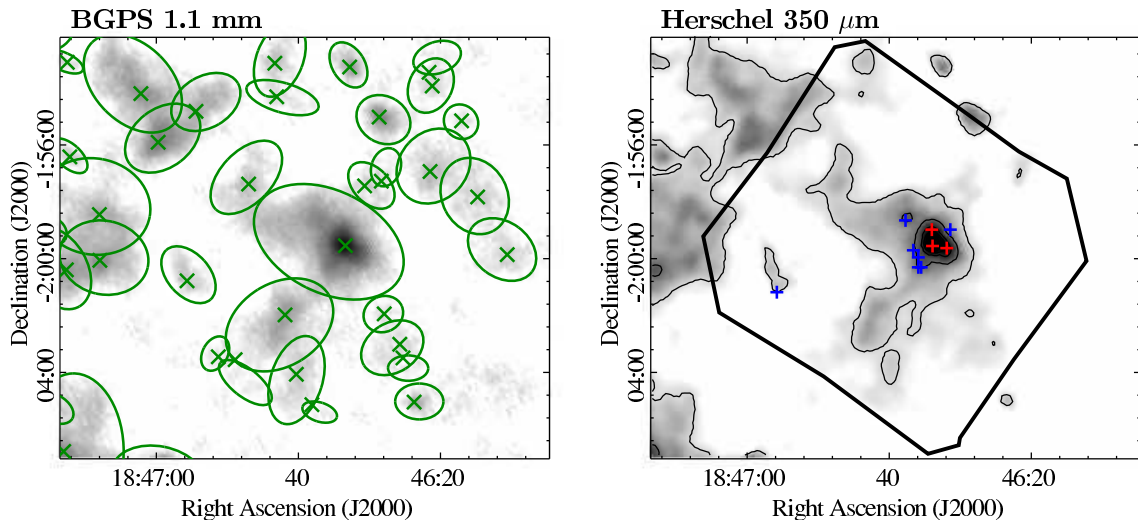


(C.1.3) Thick black contour in Herschel map represents the area covered by maps L030.60+0.00, L030.70-0.07 and L030.80-0.05

Figure C.1 Continuation.



(C.1.4) Thick black contour in Herschel map represents the area covered by map L030.88+0.13.



(C.1.5) Thick black contour in Herschel map represents the area covered by map L030.61+0.16.

Figure C.1 Continuation.

## Bibliography

- Acord, J. M., Walmsley, C. M., & Churchwell, E. 1997, *ApJ*, 475, 693
- Acord, J. M., Churchwell, E., & Wood, D. O. S. 1998, *ApJ*, 495, L107
- Aguirre, J. E., Ginsburg, A. G., Dunham, M. K., et al. 2011, *ApJS*, 192, 4
- Alvarez, H., May, J., & Bronfman, L. 1990, *ApJ*, 348, 495
- Arce, H. G., & Sargent, A. I. 2006, *ApJ*, 646, 1070
- Arce, H. G., Shepherd, D., Gueth, F., et al. 2007, *Protostars and Planets V*, 245
- Aurière, M. 1982, *A&A*, 109, 301
- Bally, J., Moeckel, N., & Throop, H. 2005, *Chondrites and the Protoplanetary Disk*, 341, 81
- Bally, J., Aguirre, J., Battersby, C., et al. 2010, *ApJ*, 721, 137
- Bally, J., & Zinnecker, H. 2005, *AJ*, 129, 2281
- Bartkiewicz, A., & van Langevelde, H. J. 2012, *IAU Symposium*, 287, 117
- Battersby, C., Bally, J., Ginsburg, A., et al. 2011, *A&A*, 535, A128
- Beckwith, S. V. W., & Sargent, A. I. 1991, *ApJ*, 381, 250
- Beelen, A., Cox, P., Benford, D. J., et al. 2006, *ApJ*, 642, 694

- Benjamin, R. A., Churchwell, E., Babler, B. L., et al. 2003, PASP, 115, 953
- Bergin, E. A., & Tafalla, M. 2007, ARA&A, 45, 339
- Bertin, E., & Arnouts, S. 1996, A&AS, 117, 393
- Bertoldi, F., & McKee, C. F. 1992, ApJ, 395, 140
- Beuther, H., Schilke, P., Sridharan, T. K., et al. 2002, A&A, 383, 892
- Beuther, H., Schilke, P., & Gueth, F. 2004, ApJ, 608, 330
- Beuther, H., Schilke, P., & Wyrowski, F. 2004, ApJ, 615, 832
- Beuther, H., Leurini, S., Schilke, P., et al. 2007, A&A, 466, 1065
- Blake, G. A., Sutton, E. C., Masson, C. R., & Phillips, T. G. 1987, ApJ, 315 621
- Blitz, L. 1993, Protostars and Planets III, 125
- Blum, R. D., Damineli, A., & Conti, P. S. 1999, AJ, 117, 1392
- Bonnell, I. A., & Bate, M. R. 2006, MNRAS, 370, 488
- Bourke, T. L., Garay, G., Lehtinen, K. K., et al. 1997, ApJ, 476, 781
- Bronfman, L., Cohen, R. S., Thaddeus, P., & Alvarez, H. 1985, The Milky Way Galaxy, 106, 331
- Bronfman, L., Alvarez, H., Cohen, R. S., & Thaddeus, P. 1989, ApJS, 71, 481
- Bronfman, L., Nyman, L.-A., & May, J. 1996, A&AS, 115, 81

- Bronfman, L., Casassus, S., May, J., & Nyman, L.-Å. 2000, *A&A*, 358, 521
- Bronfman, L., Garay, G., Merello, M., Mardones, D., May, J., Brooks, K. J., Nyman, L.-Å., Güsten, R. 2008, *ApJ*, 672, 391
- Butler, M. J., & Tan, J. C. 2012, *ApJ*, 754, 5
- Calzetti, D., Kennicutt, R. C., Engelbracht, C. W., et al. 2007, *ApJ*, 666, 870
- Calzetti, D., Wu, S.-Y., Hong, S., et al. 2010, *ApJ*, 714, 1256
- Carey, S. J., Noriega-Crespo, A., Mizuno, D. R., et al. 2009, *PASP*, 121, 76
- Carlhoff, P., Nguyen Luong, Q., Schilke, P., et al. 2013, *A&A*, 560, A24
- Caswell, J. L., & Haynes, R. F. 1987, *A&A*, 171, 261
- Caswell, J. L., Haynes, R. F., & Goss, W. M. 1980, *AuJPh*, 33, 639
- Caswell, J. L., Vaile, R. A., Ellingsen, S. P., Whiteoak, J. B., & Norris, R. P. 1995, *MNRAS*, 272, 96
- Caswell, J. L., Fuller, G. A., Green, J. A., et al. 2011, *MNRAS*, 417, 1964
- Caswell, J. L. 1997, *MNRAS*, 289, 203
- Caswell, J. L. 1998, *MNRAS*, 297, 215
- Caswell, J. L. 2009, *PASA*, 26, 454
- Cesaroni, R., Walmsley, C. M., Koempe, C., & Churchwell, E. 1991, *A&A*, 252, 278

Charnley, S. B. 1997, *ApJ*, 481, 396

Churchwell, E., Walmsley, C. M., & Cesaroni, R. 1990, *A&AS*, 83, 119

Contreras, Y., Schuller, F., Urquhart, J. S., et al. 2013, *A&A*, 549, A45

Csengeri, T., Urquhart, J. S., Schuller, F., et al. 2014, *A&A*, 565, A75

Dame, T. M., Elmegreen, B. G., Cohen, R. S., & Thaddeus, P. 1986, *ApJ*, 305, 892

Dowell, C. D., et al. 2003, *Proc. SPIE*, 4855, 73

Draine, B. T., & Lee, H. M. 1984, *ApJ*, 285, 89

Dunham, M. K., Rosolowsky, E., Evans, N. J., II, et al. 2010, *ApJ*, 717, 1157

Dunham, M. K., Rosolowsky, E., Evans, N. J., II, Cyganowski, C., & Urquhart, J. S. 2011, *ApJ*, 741, 110

Edgar, R., & Clarke, C. 2004, *MNRAS*, 349, 678

Elia, D., Schisano, E., Molinari, S., et al. 2010, *A&A*, 518, L97

Ellsworth-Bowers, T. P., Glenn, J., Rosolowsky, E., et al. 2013, *ApJ*, 770, 39

Evans, N. J., II 1999, *ARA&A*, 37, 311

Fazio, G. G., Hora, J. L., Allen, L. E., et al. 2004, *ApJS*, 154, 10

Faúndez, S., Bronfman, L., Garay, G., et al. 2004, *A&A*, 426, 97

- Fontani, F., Caselli, P., Bourke, T. L., Cesaroni, R., & Brand, J. 2008, *A&A*, 477, L45
- Fukui, Y., Sakakibara, O. 1992, *Mitsubishi Electronic Advance* 60, 11
- Fukui, Y., Ogawa, H., Kawabata, K., Mizuno, A., & Sugitani, K. 1991, *The Magellanic Clouds*, 148, 105
- Furuya, R. S. 2003, *Galactic Star Formation Across the Stellar Mass Spectrum*, 287, 367
- Garay, G., Reid, M. J., & Moran, J. M. 1985, *ApJ*, 289, 681
- Garay, G., & Lizano, S. 1999, *PASP*, 111, 1049
- Garay, G., Köhnenkamp, I., Bourke, T. L., Rodríguez, L. F., & Lehtinen, K. K. 1998, *ApJ*, 509, 768
- Garay, G., & Lizano, S. 1999, *PASP*, 111, 1049
- Garay, G., Brooks, K. J., Mardones, D., Norris, R. P., & Burton, M. G. 2002, *ApJ*, 579, 678
- Garay, G., Mardones, D., Rodríguez, L. F., Caselli, P., & Bourke, T. L. 2002, *ApJ*, 567, 980
- Garden, R. P., Hayashi, M., Hasegawa, T., Gatley, I., & Kaifu, N. 1991, *ApJ*, 374, 540
- Ginsburg, A., Glenn, J., Rosolowsky, E., et al. 2013, *ApJS*, 208, 14



- Goss, W. M., Manchester, R. N., & Robinson, B. J. 1970, *AuJPh*, 23, 559
- Goss, W. M., Radhakrishnan, V., Brooks, J. W., & Murray, J. D. 1972, *ApJS*, 24, 123
- Gottlieb, C. A, Gottlieb, E. W., Litvak, M. M., Ball, J. A., & Penfield, H. 1978, *ApJ*, 219, 77
- Groesbeck, T. D. 1995, Ph.D. Thesis
- Harvey, P. M., & Forveille, T. 1988, *A&A*, 197, L19
- Hatchell, J., & Dunham, M. M. 2009, *A&A*, 502, 139
- Heiderman, A., Evans, N. J., II, Allen, L. E., Huard, T., & Heyer, M. 2010, *ApJ*, 723, 1019
- Hill, T., Thompson, M. A., Burton, M. G., et al. 2006, *MNRAS*, 368, 1223
- Hirano, N., Liu, S.-Y., Shang, H., et al. 2006, *ApJ*, 636, L141
- Hirota, T., Bushimata, T., Choi, Y. K., et al. 2007, *PASJ*, 59, 897
- Hoare, M. G., Kurtz, S. E., Lizano, S., Keto, E., & Hofner, P. 2007, *Protostars and Planets V*, 181
- Holland, W. S., Robson, E. I., Gear, W. K., et al. 1999, *MNRAS*, 303, 659
- Hunter, T. R., Brogan, C. L., Megeath, S. T., et al. 2006, *ApJ*, 649, 888
- Johnstone, D., & Bally, J. 2006, *ApJ*, 653, 383

- Jones, C., & Dickey, J. M. 2012, ApJ, 753, 62
- Kahn, F. D. 1974, A&A, 37, 149
- Kennicutt, R. C., Jr. 1998, ARA&A, 36, 189
- Kennicutt, R. C. 2005, Massive Star Birth: A Crossroads of Astrophysics, 227, 3
- Kennicutt, R. C., & Evans, N. J. 2012, ARA&A, 50, 531
- Kerr, F. J., & Knapp, G. R. 1970, AuJPA, 18, 9
- Koda, J., Scoville, N., Sawada, T., et al. 2009, ApJ, 700, L132
- Kovács, A., *SHARC-2 350  $\mu$ m Observations of Distant Submillimeter-Selected Galaxies and Techniques for the Optimal Analysis and Observing of Weak Signals*, PhD Thesis, Caltech, 2006.
- Kramer, C., Richer, J., Mookerjee, B., Alves, J., & Lada, C. 2003, A&A, 399, 1073
- Kristensen, L. E., van Dishoeck, E. F., Bergin, E. A., et al. 2012, A&A, 542, A8
- Krumholz, M. R., & McKee, C. F. 2008, Nature, 451, 1082
- Kuiper, R., Klahr, H., Beuther, H., & Henning, T. 2010, ApJ, 722, 1556
- Kuno, N., Nakai, N., Handa, T., & Sofue, Y. 1995, PASJ, 47, 745
- Lada, C. J., Lombardi, M., & Alves, J. F. 2010, ApJ, 724, 687
- Larson, R. B., & Starrfield, S. 1971, A&A, 13, 190

- Linke, R. A., Frerking, M. A., & Thaddeus, P. 1979, *ApJ*, 234, L139
- Longmore, S. N., Rathborne, J., Bastian, N., et al. 2012, *ApJ*, 746, 117
- Louvet, F., Motte, F., Hennebelle, P., et al. 2014, arXiv:1404.4843
- Machida, M. N., & Hosokawa, T. 2013, *MNRAS*, 431, 1719
- Martin-Pintado, J., Bachiller, R., & Fuente, A. 1992, *A&A*, 254, 315
- Masson, C. R., & Chernin, L. M. 1993, *ApJ*, 414, 230
- Mathis, J. S., Mezger, P. G., & Panagia, N. 1983, *A&A*, 128, 212
- Matzner, C. D., & McKee, C. F. 2000, *Bulletin of the American Astronomical Society*, 32, #135.07
- McKee, C. F., & Ostriker, E. C. 2007, *ARA&A*, 45, 565
- McMullin, J. P., Waters, B., Schiebel, D., Young, W., & Golap, K. 2007, *Astronomical Data Analysis Software and Systems XVI (ASP Conf. Ser. 376)*, ed. R. A. Shaw, F. Hill, & D. J. Bell (San Francisco, CA: ASP), 127
- Megeath, S. T., Townsley, L. K., Oey, M. S., & Tieftrunk, A. R. 2008, *Handbook of Star Forming Regions, Volume I*, 264
- Menten, K. M., Walmsley, C. M., Henkel, C., et al. 1986, *A&A*, 169, 271
- Merello, M., Bronfman, L., Garay, Nyman, L.-Å., Evans, N. J., Walmsley, C. M. 2013, accepted by *ApJ*

- Miettinen, O., Harju, J., Haikala, L. K., & Pomrén, C. 2006, *A&A*, 460, 721
- Mill, J. D., O'Neil, R. R., Price, S., et al. 1994, *JSpRo*, 31, 900
- Molinari, S., Pezzuto, S., Cesaroni, R., et al. 2008, *A&A*, 481, 345
- Molinari, S., Swinyard, B., Bally, J., et al. 2010, *PASP*, 122, 314
- Moore, T. J. T., Bretherton, D. E., Fujiyoshi, T., et al. 2007, *MNRAS*, 379, 663
- Motte, F., Bontemps, S., Schilke, P., Schneider, N., Menten, K. M., & Broguière, D. 2007, *A&A*, 476, 1243
- Mueller, K. E., Shirley, Y. L., Evans, N. J., II, & Jacobson, H. R. 2002, *ApJS*, 143, 469
- Myers, P. C. 1995, *Molecular Clouds and Star Formation*, 47
- Myers, P. C., Evans, N. J., II, & Ohashi, N. 2000, *Protostars and Planets IV*, 217
- Nakamura, F., & Li, Z.-Y. 2007, *ApJ*, 662, 395
- Neugebauer, G., Habing, H. J., van Duinen, R., et al. 1984, *ApJ*, 278, L1
- Nguyen Luong, Q., Motte, F., Schuller, F., et al. 2011, *A&A*, 529, A41
- Ogawa, H., Mizuno, A., Ishikawa, H., Fukui, Y., & Hoko, H. 1990, *IJIMW*, 11, 717
- Ossenkopf, V., & Henning, T. 1994, *A&A*, 291, 943
- Panagia, N. 1973, *AJ*, 78, 929

- Pestalozzi, M. R., Minier, V., & Booth, R. S. 2005, *A&A*, 432, 737
- Plambeck, R. L., Wright, M. C. H., Welch, W. J., et al. 1982, *ApJ*, 259, 617
- Plume, R., Jaffe, D. T., & Evans, N. J., II 1992, *ApJS*, 78, 505
- Ragan, S. E., Henning, T., & Beuther, H. 2013, arXiv:1308.6157
- Rand, R. J., & Kulkarni, S. R. 1990, *ApJ*, 349, L43
- Rand, R. J. 1993, *ApJ*, 404, 593
- Reid, M. J., et al. 2009, *ApJ*, 700, 137
- Reipurth, B., & Bally, J. 2001, *ARA&A*, 39, 403
- Reynolds, S. P. 1986, *ApJ*, 304, 713
- Rivera-Ingraham, A., Martin, P. G., Polychroni, D., et al. 2013, *ApJ*, 766, 85
- Rosolowsky, E., Dunham, M. K., Ginsburg, A., et al. 2010, *ApJS*, 188, 123
- Rydbeck, O. E. H., Hjalmarson, A., Rydbeck, G., et al. 1980, *ApJ*, 235, L171
- Sadavoy, S. I., Di Francesco, J., Johnstone, D., et al. 2013, *ApJ*, 767, 126
- Santiago-García, J., Tafalla, M., Johnstone, D., & Bachiller, R. 2009, *A&A*, 495, 169
- Sault, R. J., Teuben, P. J., & Wright, M. C. H. 1995, *Astronomical Data Analysis Software and Systems IV*, 77, 433

- Schilke, P., Walmsley, C. M., Pineau des Forets, G., & Flower, D. R. 1997, *A&A*, 321, 293
- Schlingman, W. M., Shirley, Y. L., Schenk, D. E., et al. 2011, *ApJS*, 195, 14
- Schnee, S., & Goodman, A. 2005, *ApJ*, 624, 254
- Schnee, S., Enoch, M., Noriega-Crespo, A., et al. 2010, *ApJ*, 708, 127
- Schuller, F., Menten, K. M., Contreras, Y., et al. 2009, *A&A*, 504, 415
- Scoville, N. Z. 1990, *The Evolution of the Interstellar Medium*, 12, 49
- Shaver, P. A., & Goss, W. M. 1970, *AuJPA*, 14, 133
- Shetty, R., Kauffmann, J., Schnee, S., Goodman, A. A., & Ercolano, B. 2009, *ApJ*, 696, 2234
- Shirley, Y. L., Evans, N. J., II, Rawlings, J. M. C., & Gregersen, E. M. 2000, *ApJS*, 131, 249
- Shirley, Y. L., Evans, N. J., II, Young, K. E., Knez, C., & Jaffe, D. T. 2003, *ApJS*, 149, 375
- Shirley, Y. L., Nordhaus, M. K., Grcevich, J. M., et al. 2005, *ApJ*, 632, 982
- Shirley, Y. L., Huard, T. L., Pontoppidan, K. M., et al. 2011, *ApJ*, 728, 143
- Shirley, Y. L., Ellsworth-Bowers, T. P., Svoboda, B., et al. 2013, arXiv:1308.4149
- Shu, F. H., Adams, F. C., & Lizano, S. 1987, *ARA&A*, 25, 23

- Siringo, G., Kreysa, E., De Breuck, C., et al. 2010, *The Messenger*, 139, 20
- Stahler, S. W., Palla, F., & Ho, P. T. P. 2000, *Protostars and Planets IV*, 327
- Su, Y.-N., Liu, S.-Y., Chen, H.-R., & Tang, Y.-W. 2012, *ApJ*, 744, L26
- Swade, D. A. 1989, *ApJ*, 345, 828
- Szymczak, M., Kus, A. J., Hrynek, G., Kępa, A., & Pazderski, E. 2002, *A&A*, 392, 277
- Tan, J. C., Beltran, M. T., Caselli, P., et al. 2014, arXiv:1402.0919
- Traficante, A., Calzoletti, L., Veneziani, M., et al. 2011, *MNRAS*, 416, 2932
- Urquhart, J. S., Hoare, M. G., Lumsden, S. L., Oudmaijer, R. D., & Moore, T. J. T. 2008, *Massive Star Formation: Observations Confront Theory*, 387, 381
- Urquhart, J. S., Moore, T. J. T., Schuller, F., et al. 2013, *MNRAS*, 431, 1752
- Wakelam, V., Ceccarelli, C., Castets, A., et al. 2005, *A&A*, 437, 149
- Ward-Thompson, D., André, P., & Kirk, J. M. 2002, *MNRAS*, 329, 257
- Watson, C., Churchwell, E., Zweibel, E. G., & Crutcher, R. M. 2007, *ApJ*, 657, 318
- Welch, W. J., Wright, M. C. H., Plambeck, R. L., Bieging, J. H., & Baud, B. 1981, *ApJ*, 245, L87
- Wienen, M., Wyrowski, F., Schuller, F., et al. 2012, *A&A*, 544, A146
- Williams, J. P., deGeus, E. J., & Blitz, L. 1994, *ApJ*, 428, 693

- Williams, J. P., Blitz, L., & McKee, C. F. 2000, *Protostars and Planets IV*, 97
- Wilson, T. L., & Rood, R. 1994, *ARA&A*, 32, 191
- Wilson, T. L., Rohlfs, K., Hüttemeister, S. 2009, *Tools of Radio Astronomy*, by Thomas L. Wilson; Kristen Rohlfs and Susanne Hüttemeister. ISBN 978-3-540-85121-9. Published by Springer-Verlag, Berlin, Germany, 2009.,
- Wolfire, M. G., & Cassinelli, J. P. 1987, *ApJ*, 319, 850
- Wright, E. L., Eisenhardt, P. R. M., Mainzer, A. K., et al. 2010, *AJ*, 140, 1868
- Wu, Y., Wei, Y., Zhao, M., et al. 2004, *A&A*, 426, 503
- Wu, J., Dunham, M. M., Evans, N. J., II, Bourke, T. L., & Young, C. H. 2007, *AJ*, 133, 1560
- Wu, J., Evans, N. J., II, Shirley, Y. L., & Knez, C. 2010, *ApJS*, 188, 313
- Wynn-Williams, C. G., Becklin, E. E., & Neugebauer, G. 1972, *MNRAS*, 160, 1
- Yorke, H. W., & Kruegel, E. 1977, *A&A*, 54, 183
- Zhang, Q., Hunter, T. R., Beuther, H., et al. 2007, *ApJ*, 658, 1152
- Zinnecker, H., & Yorke, H. W. 2007, *ARA&A*, 45, 481



## Vita

Manuel Antonio Merello Ferrada was born in Santiago, Chile, on December 24, 1983. He attended high school at the Instituto Nacional José Miguel Carrera. He received two Bachelor of Science degrees, one in Physics and one in Astronomy, from Universidad de Chile in 2005. He obtained from the same institution his Master of Science degree in 2008, working under the supervision of Prof. Leonardo Bronfman and Prof. Guido Garay.

He was awarded with a Fulbright fellowship to continue his studies in United States of America, enrolling in the Astronomy program of the University of Texas at Austin on 2008. During his candidacy, he was supervised by Prof. Neal J. Evans II, working on the study of the formation of massive stars, and characterization of star-forming regions across the Galactic plane.

He had the opportunity to spend many nights observing at the Caltech Submillimeter Observatory at Mauna Kea, Hawaii, spending the nights on a rotating dome and murmuring Pablo Neruda's "Poema 20" under "the infinite sky".

He married his beautiful wife Victoria Gamonal on January, 2014. Upon obtaining his Doctoral degree, he will start a Postdoctoral research position at the Istituto di Astrofisica e Planetologia Spaziali (IAPS-INAF) at Rome, Italy.

Permanent address: 3200 1/2 Tom Green  
Austin, Texas 78705

This dissertation was typeset with L<sup>A</sup>T<sub>E</sub>X<sup>†</sup> by the author.

---

<sup>†</sup>L<sup>A</sup>T<sub>E</sub>X is a document preparation system developed by Leslie Lamport as a special version of Donald Knuth's T<sub>E</sub>X Program.